Tip Based Automated Nanomanipulation using Scanning Probe Microscopy

Submitted in partial fulfillment of the requirements for

the degree of

Doctor of Philosophy

in

Mechanical Engineering

Onur Ozcan

B.S., Mechatronics Engineering, Sabanci University
M.S., Mechanical Engineering, Carnegie Mellon University

Carnegie Mellon University
Pittsburgh, PA

March, 2012

Keywords: Nanomanipulation, Nanofabrication, Scanning Probe Microscopy, Control, Automation

To my beloved parents, Ali and Bahar.

Acknowledgments

I wish to express my gratitude to everyone who contributed in any way to the completion of this thesis. Among all, I must single out my advisor, Prof. Dr. Metin Sitti, who never withheld his support; academically, mentally or financially.

Two of the people I owe thanks to is Prof. David Ricketts and Prof, James Bain, whom I know through TFAN project. They developed a researcher's approach in me in addition to their valuable mentorship, patience, and understanding. It has always been nice and enlightening to work with them.

I would also like to thank my committee members Prof. James Bain, Prof. Tomasz Kowalewski, and Prof. Fred Higgs, for finding time in their busy schedule to serve as my jurors and Prof. Metin Sitti for being the chair of my committee.

I also owe thanks to NanoRobotics Lab members and TFAN project members for their invaluable discussions suggestions throughout my PhD studies.

I must acknowledge my friends, who have been very supportive and kind to discuss and exchange many ideas throughout the thesis. Among them, the ones that really made a difference for me could be counted as: Guzide Atasoy, whose love and support always make things easier; Dr. Cagdas Onal, who was my TA, my project partner, my roommate and my confidant, Dr. Burak Aksak, who helped me understand how things work, in or out or the lab; Dr. Bilsay Sumer, who is the most important person to know in Pittsburgh if you are Turkish; Dr. Ozgur Unver, who helped me settle down in US in my first year; Weihua Hu, with whom I shared significant number of nights running experiments in TFAN lab; Yigit Menguc and Eric Diller, whom I have been sharing a house with in the last two years which I enjoyed much; Emrecan Soylemez, who helped me with experiments, discussions or things unrelated to work whenever I needed and Turkish Mafia (Turkish graduate students in CMU) whose friendships made PhD much more bearable.

Finally, I would like to thank my family for the backup and understanding they provided me through my entire life. I wouldn't have achieved what I have without their neverending support.

This thesis work and my PhD study is partially funded by National Science Foundation CAREER Award program (NSF IIS-0448042), DARPA Tip Based Nanofabrication Program (Grant #N66001-08-1-2039) and personal and family savings.

Abstract

The promise to build structures atom by atom that would lead to devices or materials with tuned properties that surpass any material we encounter in the macroscale world inspires more researchers everyday to study nanotechnology. As a direct result of this interest in nanotechnology, manipulation systems with nano or sub-nano scale precision are required to position or pattern matter in smaller scales to study it. However, this manipulation task is not straightforward due to small scale physics, which reduces the effect of weight and inertia, the dominant forces in macroscale, and promotes other forces such as adhesion or electrostatic interactions. Hence, to understand nanoscale physics, the first step to take is to model and characterize the underlying principles. In this context, scanning probe microscopes (SPMs) are suitable tools for experimenting on nanoscale physics, in addition to being good candidates as nanomanipulation systems due to their ability to locally interact with the substrate using the end-effector that they utilize on the order of a few nanometers or below. On the other hand, using SPMs for nanomanipulation has drawbacks as well. Since they utilize a single end-effector to interact with the substrate, the manipulation process is serial hence slow with low throughput. Furthermore, having no real-time visual feedback and the non-linearity of the actuators decrease the precision and the repeatability of the positioning, hence decreasing the reliability of the manipulation. In order to consider SPMs as viable nanomanipulation tools, these challenges of speed and reliability should first be tackled by utilizing smarter algorithms and mechanisms.

In this work, we demonstrate two case studies that are used for tackling the speed and reliability challenges of nanomanipulation. As the first case study, an AFM is utilized to position nanoparticles. In the AFM based mechanical contact manipulation of nanoparticles, we demonstrate automated control to increase speed and reliability. In order to achieve the automation, we present models to investigate the physics of nanoparticle manipulation using an AFM cantilever, and use these models to investigate the effect of cantilever selection to manipulation success. We demonstrate particle detection using line-scans and a contact loss detection algorithm using cantilever normal deflection data to decrease the number of images taken during manipulation. We also demonstrate through experimental results that it is possible to push and pull particles on a flat surface into defined patterns autonomously, using an AFM probe tip, and with an error less than the particle diameter, and with success rates as high as 87%.

Moreover, an STM is utilized to manipulate surfaces using electrical pulses and high electric fields as a second case study of this thesis. During the STM based electrical non-contact manipulation, utilizing conductive AFM probes as STM end-effectors as a step towards a multiple probe approach is suggested to improve the speed and throughput of the STM manipulation. STM imaging of surfaces using STM tips and conductive AFM probes are demonstrated and algorithms for STM based electrical manipulation of surfaces is presented and experimentally verified. Furthermore, models for STM operation and manipulation using STM tips and AFM probes as end-effectors are developed and the effects of several design parameters on STM based imaging and manipulation that utilizes AFM probes and STM tips are investigated. In addition, a faster and more flexible controller is designed and implemented which allows instant switching between AFM and STM modes, when conductive AFM probes are utilized.

Contents

List of Figures

List of Tables

Chapter 1

Introduction

1.1 Motivation

Richard Feynman's famous talk in 1959, entitled "There is plenty of room at the bottom", is the pioneer speech for the idea of Nanotechnology, and as years passed we have witnessed more and more researchers become inspired by Feynman's ideas and start studying smaller scale physics and engineering. One of the overarching visions of these researchers is enabling the construction of structures or devices atom by atom. Building from the "bottom-up" will lead to materials or structures with extraordinary properties compared to conventional manufacturing techniques due to the possibility of creating defect-free structures. For instance, a typical mechanical structure can fail under a load propagating a crack created during the manufacturing process or present in the initial materials. If we were able to remove the defect or create defect-free structures, the yield load of the mechanical structure would increase dramatically. Eliminating defects and impurities would also have a significant effect on material conductivity. Metal conductivity increases with decreasing temperatures, but never reaches infinity because of these issues; with perfect materials, this superconductivity is theoretically possible.

Besides Feynman's ideas, another motivation for the nanotechnology is the decrease in the miniaturization rate of MEMS fabrication techniques. Throughout the years, MEMS fabrication has achieved lower and lower sized structures, though researchers agree that the MEMS fabrication techniques are reaching their size limits. On the other hand, there are virtually no size limits to the bottom-up fabrication approach, as long as we can successfully manipulate atoms. In addition, with the change to bottom-up manufacturing would come a significant decrease in further development costs. Every time MEMS fabrication lowers its fabrication size limit, MEMS factories must change several pieces of fabrication equipment, costing them millions of dollars. However, with the advances in bottom-up approach, nanotechnology researchers only need to change software, end-effectors, sensors or positioning tools which cost much less than MEMS fabrication equipment.

Despite of all the advantages given above, creating structures using a bottom-up approach seems to be infeasible with the current available nanomanipulation techniques due to the speed and throughput problems. The source of these problems stem from the fact that current tools for bottom-up fabrication allow only serial processes, i.e. one manipulation action at a time, and that the only actuators.

Given the motivations above, this thesis focuses on utilizing scanning probe microscopes (SPM) as a viable bottom-up manufacturing and nanomanipulation tool. To achieve this, we study physics, control and automation of tip based nanomanipulation using atomic force microscopes (AFM) and scanning tunneling microscopes (STM) to suggest solutions to the speed and throughput problems of nanomanipulation.

1.2 Previous Works

1.2.1 Scanning Probe Microscopy

Research on nanoscale electrical and mechanical measurements in 1980s at IBM Zurich laboratories lead to a Nobel prize in physics and two significant inventions for nanotechnology: the scanning tunneling microscope (STM) and the atomic force microscope (AFM). Both microscopes, although is also used for manipulation purposes several years after their invention, were designed for characterization, spectroscopy and imaging in small scale up to atomic resolution.

The STM, invented in 1981, is one of the first SPMs that promised sub-nanometer to atomic resolution three-dimensional topography images of surfaces [14]. The working principle of STM was simply to apply a bias voltage between a sharp metal tip and a conductor or semi-conductor surface that are placed within a nanometer distance, which leads a current, called tunneling current, to form between the tip and the surface. When the bias voltage is held constant, a control loop is formed to hold the current constant while doing raster movements on the surface. The output of this control loop has to be almost identical to the topography of the surface in order to keep the distance between the metal tip and the surface hence the tunneling current constant.

The formation and the amplitude of this current is so sensitive to the distance between the tip and the surface, STM enabled researchers to acquire topography images down to atomic scale to examine the atomic structures of the materials [13, 79]. Topography imaging can also be carried on sub-micron scales to examine the topography of the surfaces [34].

The AFM, invented in 1986 by the inventors of STM, is also designed to take sub-nanometer resolution topography images of surfaces. It, however, has a purely mechanical working principle [15]. Instead of a sharp metal tip, AFM uses a microscale cantilever as the end-effector with a very sharp tip on its free end. This cantilever bends up and down with respect to the attractive and repulsive forces acting on its tip due to the interaction with the surface. The deflection of this cantilever is sensed using a laser and a position sensitive photo diode (PSPD). In contact mode operation, this cantilever tip is pressed into the surface, creating a contact force on the cantilever and a corresponding deflection. A control loop is formed to hold the deflection constant, and the surface is imaged with raster movements.

The other two operation modes of the AFM are known as non-contact mode and tapping mode. In the non-contact mode, the cantilever is excited slightly above its natural frequency and as the tip of the cantilever gets closer to the surface, the phase of the oscillations of the cantilever shifts. A phase lock loop (PLL) controller is formed to hold the phase of the oscillations constant, and the surface is imaged [96]. In the tapping mode, the cantilever is excited slightly below its natural frequency with the amplitude of the oscillations often controlled for imaging [74]. Researchers that study biological entities or fragile surfaces often use non-contact or tapping mode AFM because the low interaction force between the tip and the surface does not damage the substrate [30, 99].

Instead of imaging with atomic resolution, AFM is a tool that is mostly used for taking small scale images [30, 96, 128]. Since the tip of the AFM cantilever is often in contact with the surface while imaging, the smallest feature that is detectable in an image is determined by the contact area between the tip and the surface, which is often significantly bigger than a single atom [104]. However, even though the process is significantly harder than STM, researchers have shown that imaging with atomic resolution is possible using AFM using non-contact mode AFM under ultra-high vacuum (UHV) [124].

In addition to taking topography images of materials at small scales, characterizing materials for their physical properties is a necessary step to be able to accurately understand and model their behavior. Characterization in the nanoscale has an additional importance, since it is predicted that with a reduction in scale, material properties may change. Every material we encounter in the macroworld has some imperfections. Due to these imperfections, what is perceived becomes an average behavior and does not necessarily reflect the material properties of just a given structure. However, in the nanoscale, these imperfections start to become less pronounced. Moreover, in small scales dominant factors start to change, generally yielding nonlinear behavior [10] or even new discoveries [117].

Utilizing SPMs to measure physical properties in nanoscale is widely used due to the ability of SPM to interact with different types of materials in very small scales. The sharp AFM or STM tip enables operators to locally take measurements, or “images”, of material properties with few changes in the technique and the equipment. Often referred as different SPM techniques, the techniques like friction force microscopy (FFM) [20], electrostatic force microscopy (EFM) [86], magnetic force microscopy (MFM) [40], or piezoelectric force microscopy (PFM) [44] are "images" of material properties like friction, dielectric constant, magnetic or piezoelectric constant and are actually derivations of AFM or STM imaging.

Rather than "imaging" the material properties, another way to investigate physical properties of materials is to apply SPM based spectroscopy techniques. Researchers, soon after the invention of the STM, realized that electrical characteristics of the surfaces can also be examined by holding the tip at a constant position, and increasing the bias voltage gradually while recording the change in the tunneling current. This method is called a current-voltage spectroscopy or I-V spectroscopy. I-V spectroscopy is widely used by researchers to characterize the electrical properties of the surfaces like the band-gap [27, 79]. Another widely used spectroscopy technique is current-distance spectroscopy, also known as I-d spectroscopy, in which the distance between the tip and the surface decreased or increased gradually while keeping the bias voltage constant and recording the tunneling current. Like I-V spectroscopy, I-d spectroscopy is also widely used for electrical characterization of surfaces [34, 69].

Similar to STM spectroscopy techniques, there are spectroscopy techniques for AFM that are used to measure some mechanical properties of the surface. For instance, to measure the surface energy of a sample, one can use force-distance spectroscopy, also known as F-d curves, in which the cantilever is driven into the surface from a position that the tip and the sample were not in contact. The cantilever than is pulled back to terminate the contact again and the deflection of the cantilever is recorded [19, 99]. The point where the tip and the surface lost contact is dependent on the cantilever stiffness and the work of adhesion between the two materials, hence surface energy. Researchers can also characterize resistance, elastic modulus or strength of objects lying on the surface, such as nanotubes [103, 127], nanoparticles [110] or nanowires [130].

A recent study on particle friction utilized pushing spherical particles on a flat surface with the AFM tip, while monitoring the forces [119]. Results of these experiments yielded findings on three different particle motion modes (rolling, sliding, and spinning) and theoretical predictions of particle motion from the force data.

1.2.2 Nanomanipulation Techniques with SPM

Mechanical manipulation using AFM

As powerful a tool as it is for imaging, AFM also has significant importance for mechanical manipulation in nanoscale because of its capability of working with all types of materials and being able to apply force on the surface with the tip of its cantilever. Among several manipulation techniques, we can group AFM based manipulation techniques into 3 major categories: indentation, lithography, and pushing/pulling.

Indentation typically means making notches, recesses, or sharp depressions on a surface. Using an AFM for mechanical nanoindentation tasks has become increasingly popular for characterizing surfaces and thin films of many different types of materials. To achieve mechanical nanoindentation, the tip is first brought into contact with the substrate, then pressed into the surface to induce plastic deformation, and finally lifted off the sample, leaving a negative impression of the tip geometry. During this process, the normal deflection of the cantilever can be measured concurrently using the optical lever detection system to determine the amount of load on the substrate. Naturally, a higher load yields a larger indentation depth. The tip can be pressed onto the surface at different displacements or forces, with different speeds, and with different waiting times at maximum penetration to achieve different size and depth indentation marks.

AFM can be used as a purely mechanical nanoindenter to characterize mechanical properties [11, 55], as well as it can be employed with resistors to heat a small surface area around the tip and make small indentations in a thermo-mechanical sense [132]. Other approaches to leave small marks on a surface include electrostatic [72] and magnetic [45, 46] methods. As an application to nanoindentation using AFM, magnetic data storage experiments were carried as a proof of concept by Hosaka *et al.* [45, 46]. Data is written on the magnetic film substrate using voltage pulses. Then the recorded data is read using the MFM mode of an SPM. The advantages of magnetic indentation allow the easy reading of recorded data and the compactness of the storage. The spatial resolution in AFM based nanoindentation can be on the order of nanometers, which make it an ideal candidate for high density data storage systems, exceeding 1 Tb/in^2 limit [45].

Other than nanoindentation tasks, AFM is employed to conduct nanolithography on surfaces. In modern technology, patterning photoresists with light at a certain wavelength (photolithography) and using this as a mask to transfer the pattern to an underlying structure, is widely employed for microfabrication of small components and circuits. With the ever increasing demand for miniaturization towards nanoscale, limits of photolithography are constantly being pushed. However, the minimum achievable feature size from photolithography is obviously limited by the diffraction limit of light, which is due to its wavelength. One solution researchers pursue is utilizing the wave property of light to create high and low intensity regions by the addition or subtraction of light waves from separate sources, or namely the interference lithography. While interference lithography has the ability to generate structures below the diffraction limit, it usually gives an array of such features like grating patterns, which may not be useful for some applications. Among other possibilities, a promising method is charged-particle-beam lithography, which includes electron-beam (EBL) and ion-beam lithography. In this method, especially for EBL, very small features can be generated, but with the disadvantage of high system cost [73].

An alternative for nanolithography may be utilizing an AFM tip to pattern surfaces in a serial manner. The nature of this patterning can be mechanical (adding or removing material) or electrical. Since the AFM tip diameter can be on the order of tens of nanometers, this method has the potential to provide high spatial resolution at a cheap price. Material removal from the substrate, by scratching the surface with the tip, is the simplest method of AFM based nanolithography.

Several mechanical lithography examples are tried in [65, 68, 123]. The main problem addressed in these applications was the lack of real time feedback during the use of AFM cantilever tip as an end effector. Using a haptic interface [123], modeling of forces during manipulation [65] or adjusting the oscillation set point to control the interaction of tip with surface [68] can be used in mechanical nanolithography to prevent applications from suffering from uncertainties of nanoscale physics.

A very popular method, called dip-pen lithography (DPN), to add material on a surface is covering the tip with “ink” and then moving on the substrate to “write” by transferring the “ink” material to the surface. DPN is a relatively new AFM-based soft-lithography technique where an AFM tip is used to deliver molecules (ink) to a surface via a solvent meniscus, which forms naturally in the ambient atmospheric conditions. As with other AFM based nanopatterning approaches, it offers high-resolution capabilities for a number of (bio)molecular “inks” on a variety of substrates (metals, semiconductors, monolayer functionalized surfaces). Nevertheless, due to its nature of patterning, it has certain selectivity over which materials that can be used [63, 93].

As another nanolithography technique, local anodic oxidation (LAO) is an electrical counterpart for AFM based nanolithography. This procedure, invented by Dagata [26], is one of the early developed techniques based on a direct oxidation of the sample by a negative potential applied to the AFM tip. The oxidation process utilizes the presence of a water-bridge between the tip and the sample under ambient conditions [36]. For high local electric fields, water molecules dissolve into H+ and OH- ions. OH- ions get transported toward the positively charged substrate and react with surface atoms to induce oxidation. Oxide layers in forms of lines, dots can be created with nanoscale feature sizes.

The third main AFM based mechanical manipulation technique is pulling/pushing where AFM tip is utilized to position relatively small particles (compared to bulk materials that are often used in other manipulation types) with high precision using mechanical, electrical, or chemical principles to create more complex structures. Particles that are often used in particle manipulation systems have specific geometric shapes (mostly spherical) with usually well determined dimensions. Nanoparticles are defined as particles that can be described as above with the largest dimension of 100 nanometers. This dimension limit of 100 nanometers is a commonly accepted limit by several sources; on the other hand, the limit is still subject to change in different sources with different nanoparticle definitions.

In this context, AFM based nanoparticle manipulation is reasonable as a bottom-up approach to manufacturing systems. It is theoretically possible to use nanoparticle manipulation in applications where particles can be precisely positioned to create miniature sensors, actuators, and man-made materials, or to fix protein or DNA type biological samples on the surface for enabling characterization. Nano-particle manipulation systems can be utilized for soldering or gluing applications for micro/nano scale structures or devices. An electrical connection can be established using conductive nanoparticles; on the other hand, polymer nanoparticles can be used as glue droplets for fixing a substrate on a surface at a specific location. Plasmonics is another area that researchers are trying to use nanoparticles as wave-guides or wave-generators which would require high precision in positioning. Stamps or mask templates can be generated for micro/nano manufacturing purposes; similarly nanoparticle manipulation systems can be used for prototyping for micro/nano scale devices.

The nanoparticles that are positioned in nanoparticle manipulation systems are smaller than the wavelength of the visible light; therefore, they cannot be seen under optical microscope. Due to this lack of real-time visual feedback, nanoparticle manipulation with AFM stood as a grand challenge for several years.

Several groups have worked on AFM based manipulation, to show its feasibility and to acquire more control on the manipulation process. Schaefer *et al.* published one of the earlier works of this research field, showing that 9-20 nm gold nanoparticles can be manipulated to form clusters using AFM [105].

The most common approach to the nanoparticle manipulation tasks usually involves a few steps. First the user takes the image of the nanoparticle sample, selects the particle that would be manipulated and a target position for the nanoparticle. The tip is then moved on a line which passes through the center position of the nanoparticle and the target position for the manipulated nanoparticle. In the meantime, servo feedback control is usually turned off or the voltage set point of the signals are set to a lower value in order to decrease the distance between the substrate and the AFM tip, so that particles can be mechanically manipulated rather than the tip of the AFM probe jumping over the particles. In most applications shown in literature there is no other control applied on the process other than decreasing the set point or the turning servo feedback off. Therefore, this manipulation procedure is often referred as “blind” or “push-and-look” type approach since there is no or little control during manipulation. There are several publications on nanoparticle manipulation (with particles 15-100 nm in diameter) applications with this “blind” pushing technique. These publications can be claimed to be the earlier works showing the feasibility of the idea [5, 47, 53, 65, 68, 96].

There have been several groups who have worked on improving the “blind” approach for AFM based nanomanipulation systems. Several efforts are conducted on modeling the physics of manipulation. The effects of the tip shape and dimensions on nanomanipulation systems have been investigated [39], as well as the effect of the interaction between the substrate and the surface on the manipulation, with the conclusion that some substrates interact more with specific surfaces which can cause particles to form assemblies more likely and easily [98]. Besides these attempts on understanding the underlying physics better, some groups have investigated new approaches to enable better control over manipulation. The cantilever deflection signals, normal and lateral force measurements, or oscillation amplitude during manipulation are among the possible candidates that might enable the researchers to manipulate the nanoparticles in a more controlled fashion. One of the first attempts on controlled manipulation was to inspect the oscillation amplitude of the AFM cantilever during manipulation operation which decreases to zero when the tip is in contact with the particle [75].

Beside the manipulation systems that are designed to manipulate a single particle in a user controlled manner, several groups have demonstrated automated AFM based nanomanipulation systems [66, 84]. The automated manipulation system in Michigan State University [66] uses the pushing force data to implement a virtual reality system for the user. Results show that, the system is working successfully enough for coarse positioning of 100 nm particles, with some mismatches between the actual template and the desired one. Another automated manipulation system [84] uses a drift compensator for piezoelectric x-y stages of AFMs [83], and is able to manipulate 28 particles in a total of 40 min. approximate time. The results were impressive for the reliability of the system; on the other hand, success rates of the manipulation attempts are not included in the publication.

Besides these works on nanomanipulation, force feedback controlled micromanipulation [134], modeling of friction forces in nanoworld [28], and a combination of these two works with a resulting force model of AFM based nanomanipulation [120] are published and presented the question of whether force controlled nanomanipulation is possible or not.

Electrical manipulation using STM

Even though there are a few studies that show the possibility of mechanical manipulation using STMs [122], due to the high possibility of tip deformation, STM is often employed as an atomic scale imaging and electrical manipulation tool on semi-conductor and conductor surfaces. The ability of STM to work in distances below a nanometer and deliver electrical power to the surface by applying electric fields makes STM an invaluable tool for electrical manipulation. In addition, it also has the ability to image the manipulated surface and conduct electrical characterization to provide the exact difference among the original and the manipulated surface. Although many research groups use STMs for several different manipulation techniques the most common types of STM based manipulation are: single atom manipulation, surface modification and inducing chemical reactions on surface.

The pioneering work in STM based manipulation is conducted by researchers from IBM in

1990, by showing manipulation of single xenon atoms at low temperatures (4^o K) in UHV STM environment. [32]. After this proof-of-concept demonstration, many researchers showed similar results on different materials such as silicon [71], germanium [31], or copper [4, 80]. All of these demonstrations that show the possibility of single atom manipulations laterally or vertically have been conducted at low temperatures. To achieve single atom manipulations, the procedure often involves stopping the tip on the selected atom for manipulation and applying short electrical pulses by either increasing the bias voltage between the tip and the surface or decreasing the tip-sample distance. In both cases, the tunneling current increases 2-3 orders of magnitude, which causes an increase in the electrical power delivered to the surface resulting the termination of the bond between the selected atom and the neighboring atoms on the surface. In addition to these studies, Moresco *et al.* demonstrated that manipulation of single molecules at low temperatures can be utilized as working devices as they showed a molecular reversible on/off type switch on copper surface at 15^o K temperature. The results showed that manipulating a single molecule can result in a drastic resistance change acting like a switch [85].

Due to the difficulty in operating and managing a low temperature STM, many researchers tried similar experiments at room temperature, using UHV or ambient STMs and demonstrated surface manipulations at slightly larger scales; therefore, these studies are grouped as surface modification. The procedure for surface modification is often the same as single atom manipulation studies, the electrical powered delivered by the tip to the surface is increased by applying sharp pulses on the bias voltage or by decreasing the tip-sample distance, only difference being the operating temperature. Cesium [126], gold [41], highly oriented pyloritic graphite [7], tungsten-selenium [35], and silicon [102] are among several surfaces that surface modification using the method described above is demonstrated. It should also be noted that the surface modification process is often subtractive, i.e. it removes material from surface other than depositing material. The size of the marks left on the surface using this method can be as small as sub-nanometers [35] and can increase up to tens of nanometers [102].

Another method for surface modification is demonstrated by Lyding *et al.* on silicon surface using UHV STM. In this method, the tip-sample distance is kept constant by turning the control loop off during the manipulation attempt and the bias voltage used is increased a few times to deliver more power to the surface. The method does not employ any pulsing, hence is easier to implement. On the other hand, the resulting structures are at least a few nanometers wide. In his demonstration, silicon surface is first covered by hydrogen atoms and the surface modification method is employed on selected lines or areas resulting with the desorption of hydrogen on modified regions. Following the modification step, oxygen is induced in the chamber causing the oxidation of the regions without hydrogen coverage. The technique demonstrated a possible way to use hydrogen as a mask for fabrication [70].

In addition to single atom manipulation and surface modification, STM can also be used to change the surface chemically by inducing a reaction. A demonstration of this technique was the formation of a bond between a carbon monoxide molecule and an iron atom embedded in a copper surface. The experiment is carried at low temperature under UHV and two carbon monoxide molecules are bonded to the iron atom, forming one bond at a manipulation [62]. Another demonstration of inducing chemical reactions using an STM is carried on titanium surface under ambient conditions. In the experiment, the water vapor in the room is ionized by the tunneling current between the tip and the surface. The bias voltage is increased to achieve ionization however pulsing is not employed. The resulting oxygen ions chemically attached to titanium surface atoms, hence caused the oxidation of the titanium surface at selected locations. Using this oxidation technique, a single electron transistor is built as another demonstration of utilizing STM based manipulation techniques to build functioning devices [78]. This method is identical to LAO studies done using AFMs, with the only difference of the operation mode being STM.

1.2.3 Current Nanomanipulation Challenges and Solutions for SPM

Even though it has fewer limitations than MEMS fabrication techniques and despite the several successful manipulations listed above that scientists achieved in the last three decades, SPM based nanomanipulation is still not counted as a viable nanoscale fabrication technique. This viability assessment on SPM based manipulation is fair, considering the existing problems including: actuator non-linearities and lack of sensor feedback, vibrations, and, speed/throughput problems.

Piezoelectric actuators are widely used for nanopositioning systems, including SPMs, because of their capability of high precision positioning. However these actuators are highly non-linear in nature; they have hysteresis in their voltage-displacement relation and they suffer from creep phenomena, i.e. they continue to move with rapid changes in their input voltages. In addition to these hysteresis and creep, since the parts of SPMs are built from many different materials, they have thermal drift problems as well. However the non-linearity of the nanopositioner is often not considered to be a significant problem for imaging because it does not only depend on the precision of the actuator. Since the distance between atoms are well characterized, the images taken with atomic resolution also have position data embedded to the image. On the other hand, the non-linearity problem of the nanopositioners is very significant for nanomanipulation because mostly the manipulation and imaging are accomplished in different steps.

The easiest way to solve the hysteresis and creep problems is to use a charge amplifier to drive the piezoactuator since the piezoactuators are linear in charge but not in voltage. This method, however, can cause saturation of the actuator and the charge amplifier is an expensive solution [9, 23, 33]. Another possibility for non-linearity compensation is to employ feedback control techniques. Many different feedback controllers are employed to solve the nonlinearity problem, however, it is known that even the simplest PI controller can solve this problem [2, 38, 81, 101]. On the other hand to improve tracking, several groups employed optimal controllers [1, 57, 101, 106, 108] and iterative learning methods [22, 49, 61], as well.

Although the nonlinearity problem is easy to solve using feedback, in most cases feedback is not available. Most of the commercial SPMs do not have positioning feedback sensors either because the resolution of the sensors is limited, or the sensors adequate for nanoscale positioning are expensive. In addition, having a feedback control loop will limit the bandwidth of the operation that already has speed problems. Most commercial SPMs employ a linear fit to the hysteretic voltage-displacement curve and find the voltage needed for a desired position. Due to this lack of positioning sensor feedback, in most systems compensating for non-linearities are not straightforward.

Several groups studied the possibility of a model based open-loop control of the piezoelectric actuators to compensate for the nonlinearities. There are known models for hysteresis and creep phenomena that researchers tried and successfully implemented. To be able to employ this open-loop control, the procedure includes characterization of the nonlinearities, inverse modeling of voltage-displacement relationship and solving the inverse model to find the necessary voltage input for a desired displacement [17, 24, 52, 88, 107, 113, 114, 115, 121, 136]. Attempts have also been made to iteratively improve these models in some studies using adaptive or iterative learning techniques [29, 43, 59, 135]. The biggest down side of the inverse model based open-loop control solutions is however the need of positioning feedback sensors for characterization step.

On the other hand, one group has demonstrated the ability to correct for non-linearities using topography data from images taken by the SPM [25], however the method employed was applied offline to correct images that are already taken, hence it was not useful for manipulation purposes directly.

Drift is a more complicated problem than hysteresis and creep because of its stochastic behavior. It cannot be modeled and corrected, and with the lack of positioning feedback, it cannot be solved by feedback controllers. However, Kalman filter based [83] and particle filter based [54] solutions have been suggested in literature that depend only on image data for compensation.

In addition to these lateral positioning problems from literature, the vibrations caused by the dynamics of the vertical nanopositioners in SPMs are also a problem. The problem arises from the resonance of the vertical nanopositioners; increasing the speed of the SPM operation will often excite the natural frequency of the vertical nanopositioner, causing the vertical positioner to oscillate. Not only the image quality will significantly decrease, but the scanner itself can break because of the oscillations.

To increase the speed of the SPM operation, several researchers tackled this problem to ensure stability along vertical axis. Among many solutions, using shunt damping [3, 33], Q-control [8, 58], adaptive robust control techniques [49], and optimal control techniques have been demonstrated to solve the problem [91, 108].

Last but not least, speed and throughput is another problem that SPM based nanomanipulation suffers. SPM has a single end-effector, a sharp metal tip with a (for all modeling purposes) "infinitely" stiff backing layer for STM case or a compliant cantilever with a sharp tip for AFM case. Having a single end-effector and imaging and manipulating objects with this effector makes the SPM based manipulation a serial process which decreases the significance of SPM as a manipulation tool.

For AFM operation, the solution is either to accelerate the process by automation or by employing an array of cantilevers that carries manipulation in a parallel fashion [60, 94]. The increase of the throughput by adding more end-effectors will not directly increase the speed of the movement however it will decrease the time spent for multiple number of manipulations. Dip-pen lithography is a very good example of this solution, where the researchers show writing multiple patterns on a surface on different locations at the same time, hence parallelizing the manipulation and increasing the throughput and the speed [18].

However, the choice is more limited for STM case, because parallel end-effectors require parallel vertical positioning and this is not available for STM tips because of their "infinitely" stiff backing layer. So far, no solution is suggested for this problem in literature.

1.3 Research Objectives

To explore SPM based manipulation in depth, we will be using two case studies, AFM based nanoparticle manipulation and STM based surface modification. For AFM based nanoparticle manipulation, we use a commercial AFM whose positioning is done using a three degree-of-freedom stage with nanoscale resolution. For STM based surface modification studies, we use a commercially available SPM that operates in ambient conditions and UHV without any positioning sensors.

The manipulation processes in these two case studies are modeled to understand the mechanics of the processes better. The modeling step allows us to examine the effects of the manipulation design parameters like cantilever stiffness, tip radius, bias voltage or tunneling current during the imaging and manipulation operations. In addition to the modeling, we designed and implemented a new controller for both cases to increase the reliability and speed of the processes. Specific manipulation techniques that we investigated include: automated nanoparticle manipulation using AFM, surface modification using short electrical pulses via STM and surface modification using high electric fields via STM which employs compliant AFM cantilevers as end-effectors. In all these techniques, by using the models and the experiments, we discovered the limitations of the systems and suggest design parameters for end-effectors and the operations and implement a control system that would increase the speed and the precision of the manipulation system.

The main objectives of this thesis work are:

- Understanding the mechanics of SPM based manipulation, as well as investigating the forces experienced by the end-effector of the SPM due to imaging and manipulation.
- Designing algorithms and controllers that will increase the reliability of SPM based manipulation
- Developing automated SPM based manipulation processes to increase the speed of SPM based manipulation.

- Investigating the possibility of STM imaging and surface modification using AFM cantilevers as end-effectors in order to operate on electrically heterogeneous surfaces and as a step towards a multiple probe array manipulation approach.

1.4 Contributions

The major contributions of this thesis lie in the development of mechanical models of SPM based nanomanipulation and control strategies and algorithms that will increase the speed of the SPM based manipulation. We incorporate contact mechanics theories, control techniques, and system dynamics to achieve the objectives outlined above that will improve the SPM based manipulation techniques. The findings from this work, including the control methods and mechanical modeling, can be applied to future generation SPM based manipulation systems towards the development of a feasible SPM based nanomanipulation/nanofabrication system.

In summary, this work presents many contributions to the field of nanomanipulation and nanotechnology:

- We demonstrated the model of the forces experienced during AFM based particle manipulation using contact mechanics theories that enabled us to choose cantilevers with appropriate stiffness and tip radius values.
- We demonstrated the model of the dynamics for STM imaging and manipulation using AFM cantilevers. This model is used to identify the effects of several imaging and design parameters for the system on imaging and manipulation, such as bias voltage and cantilever stiffness. We verified this model through experiments.
- We presented a particle detection algorithm that would provide us the location of the particles during manipulation without taking a complete image of the workspace, hence speeding up the process.
- We presented a contact-loss detection algorithm that would provide us the force data during

manipulation and enable us to form a control loop during particle pushing and pulling.

- We demonstrated automated AFM based nanoparticle manipulation scheme that shortens the manipulation time significantly and decreases the user dependence of conventional particle pushing techniques.
- We demonstrated a control system design for electrical manipulation, that allows us to operate faster and switch between AFM and STM operation modes. This controller allows us to work on electrically heterogeneous surfaces where we image the sample in AFM mode and manipulate the surface in STM mode using the same end-effector without doing any drastic changes.
- We demonstrated imaging and manipulation using conductive AFM probes in STM mode for a potential multi-probe approach for STM based nanomanipulation, that would increase the throughput of STM based manipulation technique. This will be a step towards parallel operation in STM based electrical nanomanipulation.
- We investigated the effects of set-point normal force and manipulation voltage on the properties of written features for conductive AFM mode and STM mode electrical manipulation of surfaces using conductive AFM probes.

1.5 Thesis Outline

In this work, Chapter 2 introduces the mechanical model of an AFM and STM. The case studies and specific approaches to solve SPM based manipulation problems will also be introduced. Chapter 3 will introduce the first case study, automated nanoparticle manipulation using AFM, in which force models for particle manipulation are introduced, optimal design parameters of cantilevers for AFM based particle manipulation are investigated and controllers and algorithms that would enable automation are explored. The second case study, STM based surface modification, is introduced in Chapter 4, where results for STM based surface modification are presented, possibility of STM imaging with AFM cantilevers are demonstrated and mechanics of STM operation and surface modification using STM tips and AFM cantilevers are modeled and the models are verified. Finally, conclusions and future directions are presented in Chapter 5.

Chapter 2

Approach and Scanning Probe Microscopy Models

2.1 Introduction

In this chapter, I introduce our specific approach to tackle the challenges of SPM based nanomanipulation. I will discuss basic AFM and STM principles and present detailed models of the SPM based imaging and manipulation system, including: several contact mechanics models from literature, simple PI control loop employed by commercial SPMs, and beam mechanics for the deflection of the cantilever. I will also be exploring the tip-sample interaction forces, associated with the presence or absence of contact between the tip and the surface. In addition, I will introduce the two case studies that I am conducting to demonstrate our approach on SPM based manipulation and talk about challenges and approaches specific to the case studies.

2.2 Proposed Solutions for SPM Based Nanomanipulation Challenges

To solve the aforementioned challenges in SPM based nanomanipulation, we need to demonstrate that more reliable SPM based manipulation is possible while increasing throughput. These challenges are the most significant obstacles to an SPM based nanomanipulation system becoming a viable fabrication tool.

To tackle the speed and throughput problems, automation of the manipulation systems are required. A manipulation system that depends on operator interaction will always be prone to errors and speed problems. Implementing automation will simply eliminate the human response time in the manipulation cycle and will yield a faster system. However, to achieve automation, smart algorithms and controllers should be developed that can respond to and compensate for several disturbances that will often exist in the nanoworld due to its stochastic properties. We will suggest some smart algorithms and controllers that will increase the reliability of the SPM based manipulation systems in AFM based nanoparticle manipulation case study and demonstrate automated operation.

In addition to automation, multiple probe techniques are another possibility that can be employed to increase the throughput of an SPM based nanomanipulation system by simply parallelizing a serial process. Although some studies showed the possibility of this approach using an AFM for mechanical manipulation of the surfaces, to the best of our knowledge, electrical manipulation of surfaces using an STM with multiple end-effectors has never been demonstrated before and is a field open for exploration. In order to achieve STM operation and manipulation using multiple probes, compliant structures that can be actuated independently are required; hence the structures will be similar to AFM cantilevers. In this work, we will demonstrate that STM imaging using AFM cantilevers is possible and model the dynamics of this STM based electrical manipulation system that employ AFM cantilevers as end-effectors.

Another challenge SPM based nanomanipulation suffers from is the nonlinear nature of the actuators, which causes uncertainties in lateral positioning during SPM based imaging and manipulation. However, there are several studies in literature that is presented to solve these problems. These precision problems in lateral positioning of an SPM scanner, due to hysteresis and creep can easily be solved using feedback control methods and drift problem is often solved by Kalman or particle filters. Therefore I will be ignoring these problems for this thesis.

Last but not least, the success rate of SPM based manipulation methods hence the reliability of these techniques should be improved. To increase the reliability, complete modeling of the SPM based manipulation system should be performed and the effects of cantilever design parameters such as the stiffness and the tip radius, and operation parameters such as bias voltage, manipulation voltage, and manipulation time as they relate to manipulation and positioning should be investigated. In order to investigate these effects, we will model the forces that SPM end-effectors experience during imaging and manipulation. Using this model, we will also try to identify optimal or sub-optimal parameters for SPM based manipulation tasks. In addition, we will present smarter algorithms for AFM based nanomanipulation, such as particle detection and contact-loss detection algorithms in a control loop to improve the reliability of SPM based manipulation.

2.3 Modeling of SPM Mechanics

2.3.1 AFM Mechanics

An AFM simply consists of: a cantilever with a very sharp tip, a nanoscale (often sub-nanoscale) resolution 3-D positioning system, and a device that detects cantilever deflection at the free end. The most common method to detect the cantilever deflection is to use a laser beam. The beam is positioned and often manipulated by mirrors to reflect off the back side of the free end of the cantilever and then shine on a four quadrant position sensitive photo detector (PSPD), which can detect the vertical and lateral movements of the laser spot. A drawing of the laser, cantilever and PSPD system is shown in Fig. 2.1(a).

There are two voltage signals that are generated from a four-quadrant PSPD. The first one of these signals show the voltage difference between the top half and the bottom half of the PSPD, which corresponds to the difference between the amount of laser shined on these two halves. Hence, this signal reflects the vertical displacement of the laser beam, and called V_{A-B} for historical reasons. As shown in Fig. 2.1(c), both F_y (longitudinal) and F_z (normal) forces cause cantilever bending and therefore a change in the V_{A-B} signal. As a result, this V_{A-B} signal is a coupled signal and cannot be used directly to measure the normal force F_z, or longitudinal force F_y.

Similar to V_{A-B}, the second signal, often referred as V_{LFM}, shows the difference of the laser strength between the left and right halves of the PSPD, showing the torsion of the cantilever. As shown in Fig. 2.1(e), only the force acting on the cantilever in lateral direction with respect to the cantilever length causes a torsion on the cantilever, therefore V_{LFM} is not a coupled signal and the relation between the lateral force acting on the cantilever and the V_{LFM} signal is defined by the relation:

$$F_x = \frac{k_{lat}}{s_{lat}} V_{LFM} \tag{2.1}$$

where k_{lat} and s_{lat} are cantilever lateral stiffness and sensitivity, respectively.

On the other hand, finding the relation between the normal and longitudinal forces and the deflection of a cantilever, hence the V_{A-B} signal is not straightforward. Using small deflection beam theory, the relation between the deflection at the end of the cantilever δ, and the normal force F_z and longitudinal force F_y can be written as:

$$\delta = \frac{1}{k_n}(F_z + \frac{3L_{tip}}{2L} F_y) \tag{2.2}$$

where $k_n = \frac{3EI}{L^3}$ is the normal stiffness, L and L_{tip} is the length of the cantilever and the height

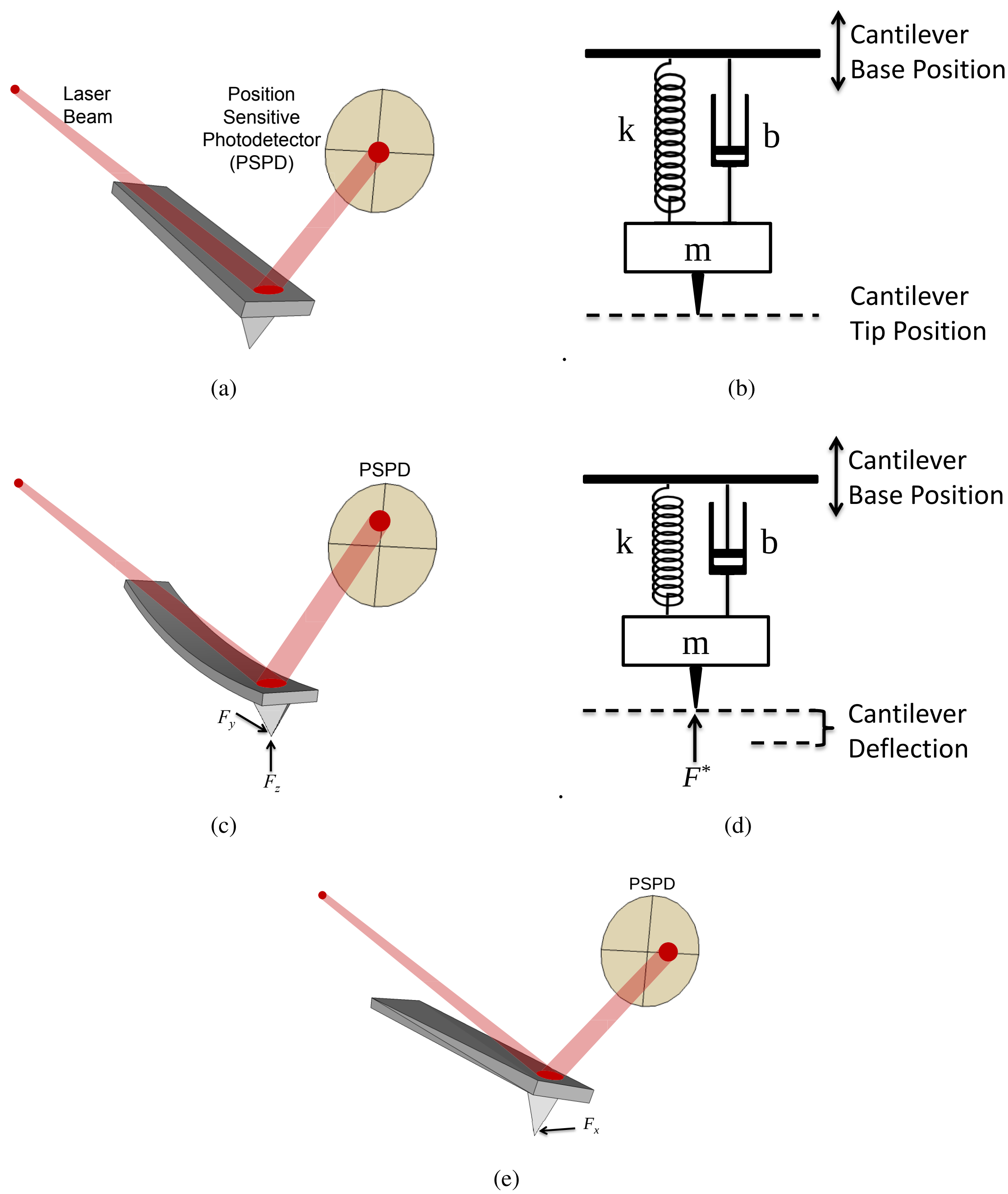

Figure 2.1: (a) An AFM cantilever at rest. A laser spot reflects off the free end of the cantilever and is collected on a PSPD, which measures the position of the spot and hence the deflection of the cantilever. (b) Mechanical equivalence of an AFM cantilever at rest. (c) AFM cantilever normal deflection measurement. When a vertical and/or a longitudinal force acts on the tip, the free end of the cantilever bends and the laser spot moves vertically on the PSPD. (d) Mechanical equivalence of an AFM cantilever with a coupled force $F*$. (e) AFM cantilever lateral deflection measurement. When a lateral force acts on the tip, the free end of the cantilever twists and the laser spot moves horizontally on the PSPD.

of the tip, respectively; E is the Young's modulus and I is the moment of inertia. Since the laser beam shines off at the back of the cantilever, the position of its reflection on the PSPD is effected directly by the slope of the end of the cantilever, other than the deflection. This slope at the end of the cantilever is:

$$\alpha = \frac{L^2}{2EI}(F_z + \frac{2L_{tip}}{L}F_y) \tag{2.3}$$

V_{A-B} is directly proportional to α, which is difficult to measure. However, a common practice is to push the tip against the surface with a motion in vertical (z) direction and plot V_{A-B} with respect to z position. The slope of this 'force-distance' curve gives the normal sensitivity $s_n = V_{A-B}$ of the cantilever. Then, from the same experiment, the relation between the A-B signal and the slope can be found, assuming that the laser is shined on the very end of the cantilever, as:

$$\alpha = V_{A-B}\frac{3L_{tip}}{2Ls_n} \tag{2.4}$$

which translates as:

$$F^* = V_{A-B}\frac{k_n}{s_n} = (F_z + \frac{2L_{tip}}{L}F_y) \tag{2.5}$$

Here, F^* is the coupled force reading and is impossible to decouple unless any further information on the surface geometry is gathered.

As a first step to form a complete system model, we need to model AFM cantilevers. We can model the cantilever, simply, as an ideal mass-spring-damper system, as shown in Fig. 2.1(b), where the spring constant k will be equal to k_n, the normal stiffness of the cantilever, mass m will be equal to the effective mass of the cantilever and the damping constant b will be the total damping the cantilever experiences due to the air damping and the inherent damping of the cantilever. Unlike normal stiffness, the mass and the damping constant of the cantilever are not often advertised or specified by the manufacturers however the values can be obtained using the frequency response of the cantilever as:

$$m = \frac{k_n}{\omega_n} \tag{2.6}$$

$$b = 2m\frac{\omega_n}{2Q} \tag{2.7}$$

where ω_n is the natural frequency of the cantilever in radians/sec and Q is the quality factor of the cantilever which is the full width of the amplitude versus frequency curve at half of the resonance amplitude. Using this mass-spring-damper model as the cantilever, the normal deflection of the cantilever with respect to any value of the coupled force F^* will be equal to the deflection of the mass-spring-damper system. Figure 2.1(d) shows the mechanical equivalent system.

During AFM operation, the sharp tip of the AFM cantilever interacts with the surface causing the cantilever to experience attractive and repulsive forces. These forces will be defined in detail in following chapters. The presence of the forces lead to the two main imaging modes of an AFM, which are the contact mode and the dynamic mode.

Contact mode operation is simpler. In this mode, the cantilever is pressed onto the surface at a given set-point force and the measured errors are regulated by the linear feedback controller. The linear controller drives the vertical positioner which is often a piezoelectric stack-type actuator. The output of this controller is also read by the data visualization PC and is recorded as the topography image of the surface. Figure 2.2(a) illustrates contact operation mode. One drawback of this method is that it can cause wear on the tip and/or the substrate. Due to this effect, dynamic mode is generally preferred for soft or fragile substrates, such as cells, or specimens not sufficiently immobilized on the surface, such as nanoparticles.

Dynamic mode uses a dynamic measurement technique, where the AFM cantilever is oscillated at a frequency around its first normal resonant frequency by either the vertical positioner or a second actuator that is capable of higher bandwidth actuation. The amplitude or the phase

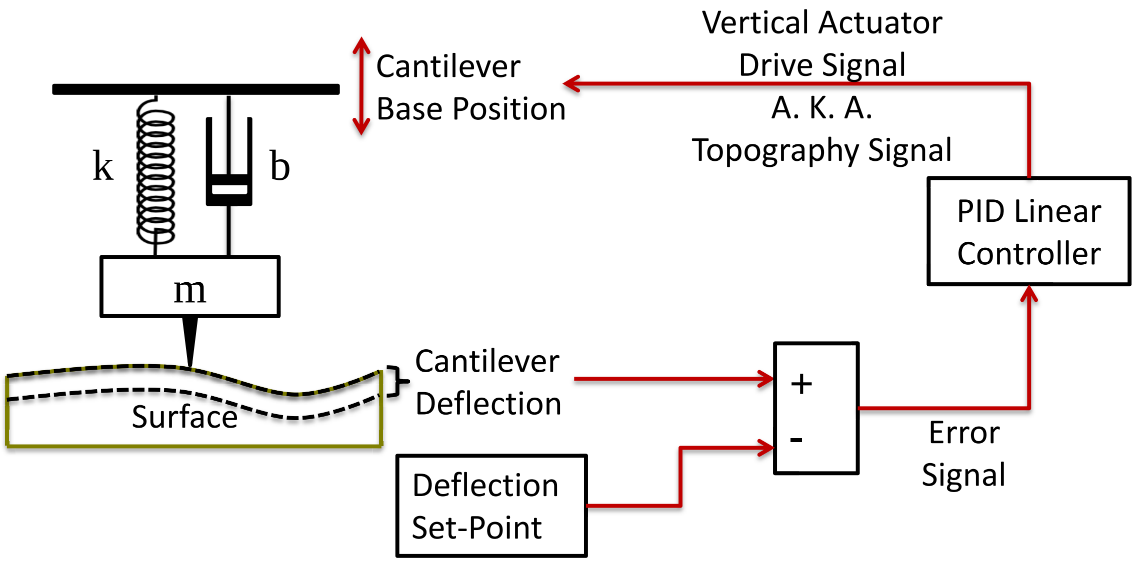

(a)

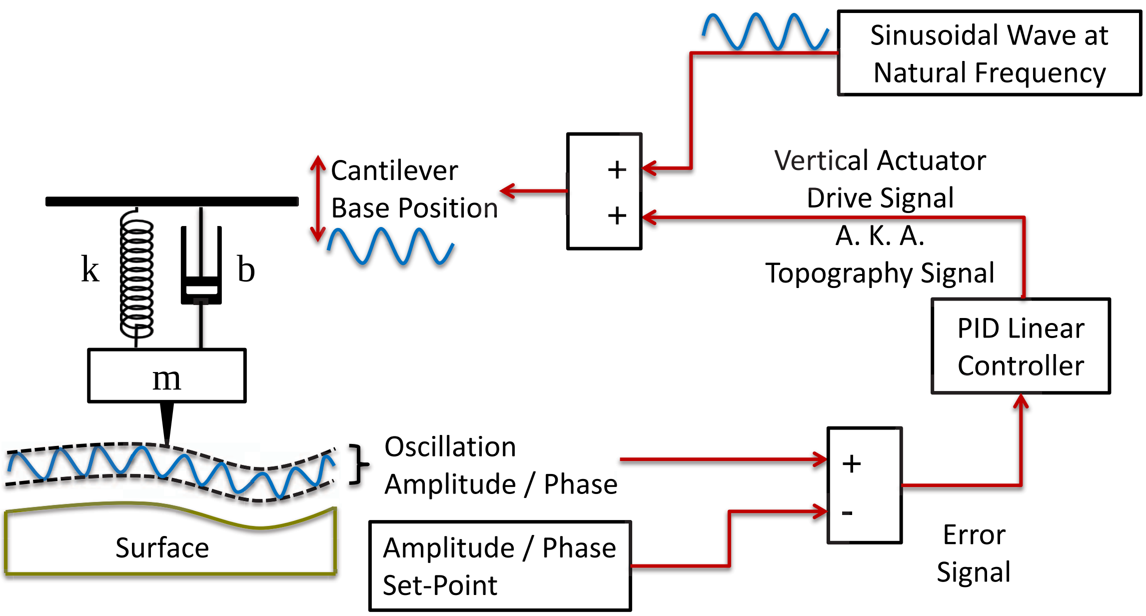

(b)

Figure 2.2: (a) Contact mode AFM operation. Cantilever is pressed to the surface until the its deflection reaches the deflection set-point. The deflection is held constant via a linear controller while the cantilever is moved on the surface. The output of this controller is the so-called topography image of the surface in contact-mode. (b) Dynamic mode AFM operation. Cantilever is oscillated above the surface, and either the oscillation amplitude or the phase is held constant at the set-point via a linear controller while the cantilever is moved on the surface. The output of this controller is the so-called topography image of the surface in dynamic mode.

of vibration is detected by the optical measurement system. As the tip is brought close to the surface, attractive forces cause the resonant frequency to decrease, yielding a different vibration amplitude and a different phase. The controller in this mode is set to keep the amplitude or phase of the oscillation constant. As in contact mode, the controller drives the vertical positioner in dynamic mode as well, and the controller output is recorded as the topography image data as illustrated in Fig. 2.2(b).

2.3.2 STM Mechanics

An STM simply consists of: a conductive end-effector, a nanoscale (often sub-nanoscale) resolution 3-D positioning system, and a device that can measure currents as small as tens of picoamperes. The device for measuring the tunneling current is often referred to as a trans-impedance amplifier (TIA) since it converts the current readings to voltage readings for the data acquisition system to read the signal. This current signal is also often amplified by a secondary amplifier to strengthen the small current signal.

The most common choice for an STM end-effector is a sharp metal wire, often Tungsten (W) or Platinum-Iridium (Pt-Ir). These tips are commercially available, however, they are also easy to fabricate. The most common ways to prepare an STM tip from metal wires is either to etch the wire to form a needle shape (for W tips) or to cut the wire diagonally while pulling the two ends of the wire, causing a pointy tip (for Pt-Ir tips). These tips are then mounted on a bulk metal holder and inserted to a socket on the vertical actuator of the STM via tight mechanical fitting or locking mechanisms. The tip, holder and the actuator becomes a single body in terms of mechanics, and body formed by the tip and its holder is assumed to be "infinitely stiff" for modeling purposes. Since the tip is not allowed to deflect, it cannot be directly modeled as a mass-spring-damper system however, the body formed by the tip, holder and the actuator can be modeled as a mass-spring-damper system. This system can be characterized by conducting a frequency sweep in actuator voltage and measuring the tip displacement, and then fitting a second order system model to the bode plot of the displacement behavior. The results will yield higher stiffness values (on the order of hundreds of kN/m) and higher mass (hundreds of grams) compared to AFM cantilever properties.

In addition to the metal wire tips, conductive AFM cantilevers can also be used to image the surface; however they will result in lower quality images and often instability in vertical positioning due to snap-into-contact phenomenon. This is because of the high attractive forces the cantilever experiences. This problem will be investigated in detail in following chapters. For the case where AFM cantilevers are used as STM end-effectors, as discussed in the previous subsection, the cantilever can be modeled as a mass-spring-damper system.

During STM operation, the sharp tip of the STM end-effector is brought close to the surface as the tunneling current increases. When the tunneling current reaches the current set-point, the approach is achieved and the tip-sample distance is kept constant at that position. Often the distance between the tip and the surface is within a nanometer. Using the model in [109], the tunneling current density can be defined as:

$$J_{TC} = \frac{e}{4\pi\hbar z^2}\left[2\bar{\phi}\exp[-(4\pi z m_e^{0.5}/\hbar)(2\bar{\phi})^{0.5}] - 2\bar{\phi}\exp[-(4\pi z m_e^{0.5}/\hbar)(2\bar{\phi}+2eV)^{0.5}]\right], \quad (2.8)$$

where $\bar{\phi}$ is the difference between the work functions of the tip and the sample, e is the charge of an electron, $\hbar$ is the Planck's constant, and m_e is the mass of an electron, z is the distance between the tip and the surface and V is the bias voltage. Using (2.8), the tunneling current can be obtained by simply integrating it on the surface of the conical tip in Fig. 2.3:

$$I_{TC} = \int_{z}^{z+L_t} J_T(z_0)(2\pi z_0 \tan\theta_t)\,\mathrm{d}z_0. \quad (2.9)$$

A sample tunneling current plot for different bias voltages is shown in Fig. 2.4(a). After finding the tunneling current, we also need to determine the maximum and minimum tunneling

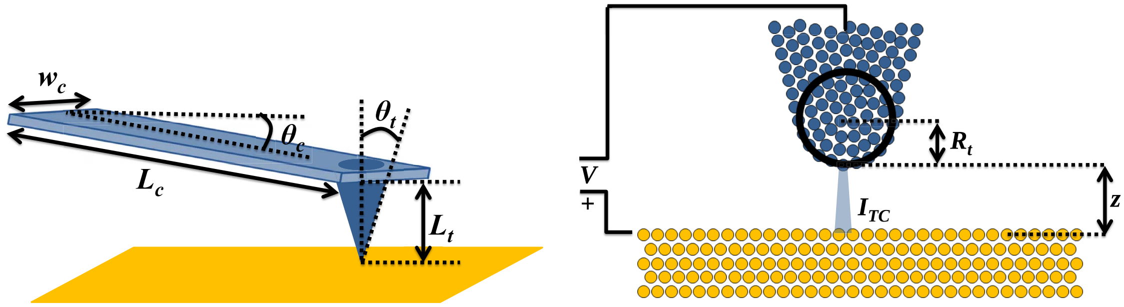

Figure 2.3: (a) A schematic of the system where the conductive atomic force microscope (CAFM) probe and tip dimensions used in the model are shown. (b) A zoomed-in schematic of the cantilever tip and the surface. Each circle represents an atom.

currents that can be used for the STM operation. We define the maximum tunneling current as 2 nA as we never used a higher tunneling current for imaging or fabrication in our system. The minimum tunneling current is defined as 0.5 nA as this is 100 times the resolution of the trans-impedance amplifier used in our system. The maximum tunneling current will define the minimum tunneling distance of the cantilever, since if the cantilever comes any closer to surface, this will only increase the tunneling current. In a similar fashion, the minimum tunneling current will define the maximum tunneling distance. The maximum and minimum tunneling distances as a function of bias voltage can be seen in Fig. 2.4(b).

As can be seen from equations 2.8 and 2.9, the tunneling current depends on the distance between tip and the surface and the bias voltage as well as the material properties of the tip and the surface. The relation between the distance and the tunneling current is exponential, which makes it hard to use conventional linear controllers. Since the tips used in commercial STM are “infinitely stiff”, there is no deflection on the position of the tip, hence linear proportional integral (PI) controllers can be used to control tip-sample distance. As the end-effector becomes compliant, another degree-of-freedom is added to the system, hence making the system harder to control with a conventional linear controller.

Despite several different imaging modes, the most widely used and the easiest to operate STM imaging mode is constant current mode. This mode is available in any commercially available

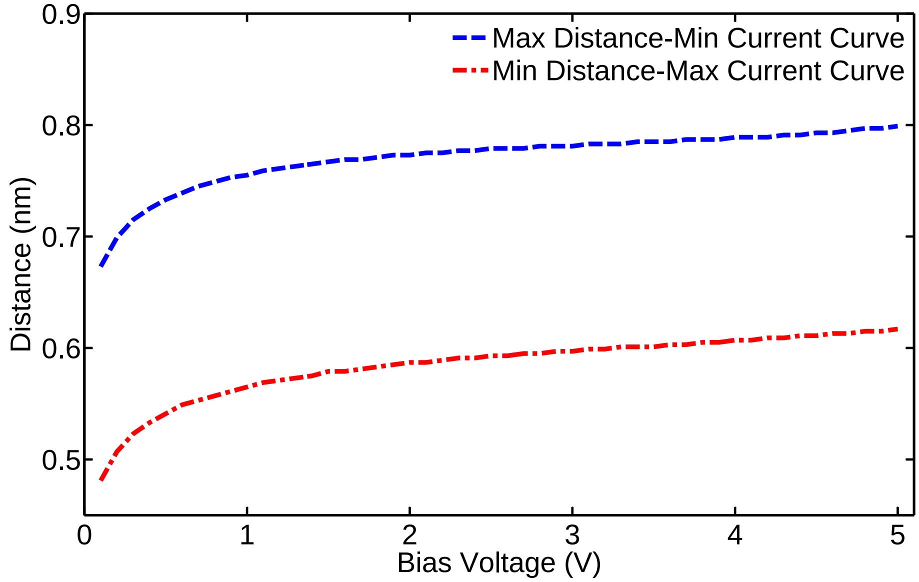

(a)

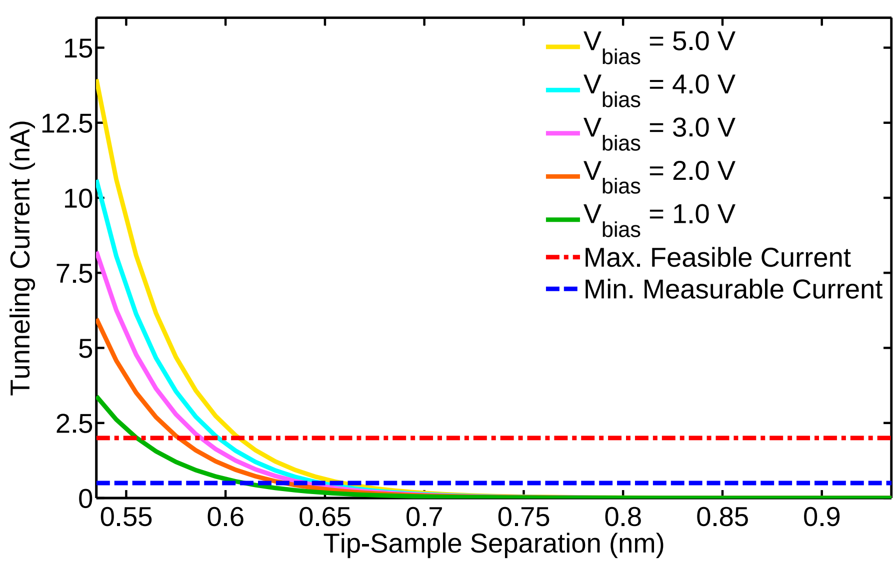

(b)

Figure 2.4: (a) Sample tunneling current curves for varying bias voltages. (b) Sample maximum and minimum tunneling distance curves for varying bias voltages. These maximum and minimum distances are found simply by finding the distances between the tip and the surface where the tunneling current value is equal to minimum measurable (for maximum distance) and maximum feasible (for minimum distance) tunneling current values.

STM, and is the mode that is of interest for this thesis.

During the constant current mode STM, the end-effector of the STM is brought toward the surface, until the tunneling current is equal to the current set-point. While the current is equal to the set-point, the tip is often within 1 nm distance away from the surface. During imaging, the tunneling current flowing between the tip and the surface is detected by the TIA and the controller is set to keep this current constant. Similar to AFM imaging, the controller drives the vertical positioner in constant current STM and the controller output is recorded as the topography image data as illustrated in Fig. 2.5.

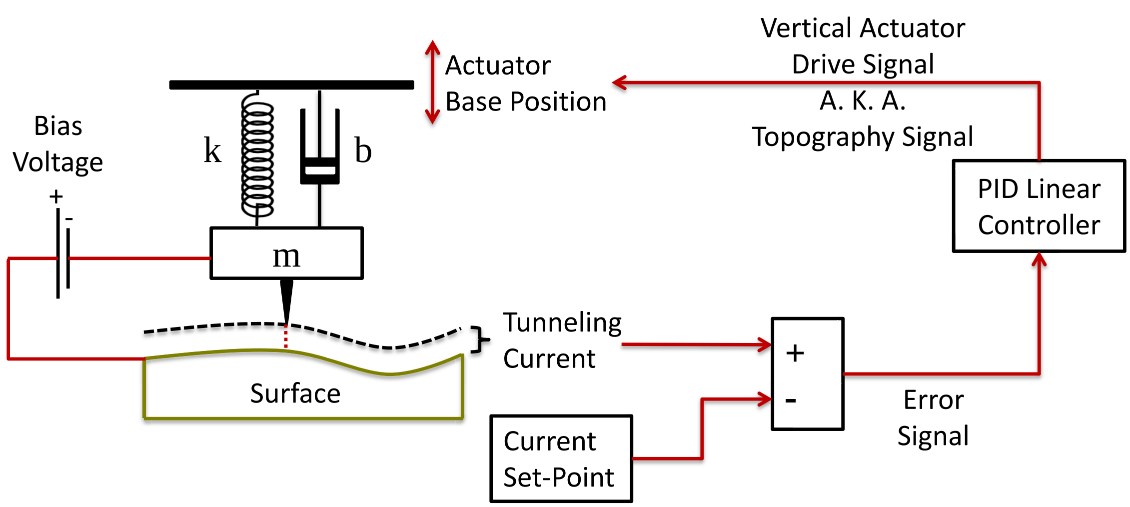

Figure 2.5: Constant current mode STM operation. STM end effector, which can be a conductive cantilever or an STM tip, is brought very close to surface until the tunneling current reaches the current set-point. The tunneling current is held constant via a linear controller while the end effector is moved on the surface. The output of this controller is the so-called topography image of the surface in constant current mode STM.

2.4 Probe-Sample Interaction Model

In order to create a complete model of SPM based manipulation, accurate modeling of the interaction forces between the end-effector of the SPM and the sample is essential. This interaction can be investigated as two parts: non-contact forces and contact forces. The non-contact forces, for SPM operation, simply consists of van der Waals interaction, that exists for every material in every environment, electrostatic interaction, that exists for STM operation due to the applied bias voltage between the tip and the surface, and the surface tension forces, that exist in interactions in ambient conditions where there is humidity. The contact forces exist when the tip and the surface are touching, due to the stiffness of the two bodies.

For the AFM based nanoparticle manipulation, we are only interested in contact forces since the imaging part of this operation is conducted using dynamic mode AFM and the non-contact forces are controlled by AFM's own controller. However accurate modeling of the forces experienced during contact manipulation of particles via pushing or pulling, is necessary to find the conditions that effect contact manipulation.

On the other hand, for STM based electrical manipulation, we are interested in both contact and non-contact forces, since we are proposing to carry out STM imaging and manipulation of the surfaces using conductive AFM probes. However, this operation can be conducted under UHV, i.e. without humidity; therefore, modeling of the surface tension forces is not a part of this work. The only modeled forces will be van der Waals, electrostatic, and contact forces for this manipulation type.

The van der Waals forces are caused by the interaction between two bodies that are close to each other. This force exists due to the polar interaction of the atoms close to each other and a weak interaction. However, because of the proximity of the tip and the surface, these forces have a dominant role in this interaction. The van der Waals interaction is governed by the Lennard-Jones potential between two surfaces [51], and this interaction force can be written as the derivative of the Lennard-Jones potential. Hence, the van der Waals interaction between a tip and a surface is:

$$F_{vdW} = \frac{A_H R_e}{6\sigma^2} \left[\frac{\sigma^2}{z^2} - \frac{1}{30} \frac{\sigma^8}{z^8} \right] \tag{2.10}$$

where A_H is the Hamaker constant of the surface material, $R_e = (R_t + R_s)/R_t R_s$ is the effective radius, R_t and R_s is the radius of the tip and the sample, respectively, σ is the inter-atomic distance and z is the separation between the tip and the sample.

The other non-contact force that we are interested in is the electrostatic attraction between two charged bodies. Although this force is unavoidable for any two surfaces with different work functions that are not in contact, they become more significant when an extra bias voltage is applied on the surfaces that electrically charge them with opposite signs, i.e. during STM operation. We choose to divide the electrostatic attraction between the probe and the surfaces into two parts: electrostatic attraction between the probe tip and the surface and the electrostatic attraction between the probe cantilever and the surface.

There are several models in literature to calculate electrostatic forces between the probe tip and the surface, however we will be using a specialized model that is proposed for the electrostatic attraction between a flat surface and a conical AFM tip [50]. In this model, the electrostatic force between the AFM cantilever tip and a flat surface is shown to be:

$$F_{el} = \pi\epsilon_0 V_b^2 \left[\frac{AR_t^2}{z[z + AR_t]} + B^2\left(\ln\frac{L_t}{z + AR_t} - 1 + \frac{R_t\cos^2\theta_t\sin\theta_t}{z + AR_t}\right)\right] \tag{2.11}$$

where $A = 1 - \sin\theta_t$ and $B^2 = \frac{1}{[\ln(\tan\theta_t/2)]^2}$, ϵ_0 is the permittivity of free space, V_b is the bias voltage, R_t is the tip radius, L_t is the tip length, z is the distance between the SPM end-effector and the surface and θ_t is the tip cone angle.

Using the model in [16], the electrostatic attraction between the conductive cantilever and the conductive sample can be defined as:

$$F_{El-c} = h(z', L_c, L_t, \theta_c)\frac{\epsilon_0 V^2 w_c}{2}\frac{L_c\cos\theta_c}{z'^2 - z' L_c\sin\theta_c}, \tag{2.12}$$

where $h(z', L_c, L_t, \theta_c)$ is the correction factor to modify the distributed force on the cantilever to a point load on the tip and is defined as

$$h = \frac{z'}{L_c \cos^3\theta_c \sin^3\theta_c}\left[(2z' - L_c \sin\theta_c) L_c \sin\theta_c ... \right.$$
$$\left. ... + 2z'(z' - L_c \sin\theta_c)\log(1 - \frac{L_c \sin\theta_c}{z'})\right]. \tag{2.13}$$

z' is the distance between the cantilever and the sample and defined as $z' = z + L_t \cos\theta_c + L_c \sin\theta_c$. In these equations, w_c, L_c, and θ_c are the width, length, and angle of the cantilever, respectively.

The total non-contact attractive force is calculated by simply adding the van der Waals and the electrostatic attraction forces. All of these non-contact forces are negative by definition (attractive forces are defined negative and repulsive forces are defined positive) and the attractive force exponentially increases while it is approaching the inter-atomic distance σ, which is the minimum energy distance between two atoms of a surface, hence the equilibrium distance. If the distance between two surfaces is decreased any further than σ, the two surfaces are considered in contact, therefore, the non-contact force plots are calculated down to this distance. To calculate the forces the SPM end-effector experience below this distance, contact mechanics theories should be used.

There are several contact mechanics theories in literature that deals with forces between two bodies touching. Among these theories, Hertz theory deals with idealistic contacts between infinitely hard surfaces with no adhesion, Johnson-Kendall-Roberts (JKR) theory deals with contact between soft surfaces with adhesion, Derjaguin-Muller-Toporov (DMT) theory deals with contact between hard surfaces with adhesion, and Maugis-Dugdale (MD) theory deals with the intermediate regime contacts, i.e. contacts whose hardness is between JKR and DMT suggests. In order to decide which contact mechanics theory should be used, one needs to calculate the non-dimensional Tabor parameter, μ, which defines the "softness" of the contact. Tabor parameter is defined as:

$$\mu = \left(\frac{16R_e\gamma^2}{9\kappa^2\sigma^3}\right)^{1/3} \tag{2.14}$$

where R_e is the effective radius of tip and the surface, γ is the effective surface energy, κ is the effective Young's modulus of the tip and the surface and σ is the inter-atomic distance. κ is defined as:

$$\kappa = \left[\frac{3}{4}\left(\frac{1-\nu_t^2}{E_t} + \frac{1-\nu_s^2}{E_s}\right)\right]^{-1} \tag{2.15}$$

where ν_t and ν_s are the Poisson ratio of the tip and the surface, respectively and E_t and E_s are the Young's modulus of the tip and the surface respectively. Using the Eq. 2.14 and the parameters listed in Tables 2.1 and 2.2, the tabor parameter for AFM based nanoparticle manipulation, μ_{AFM} and STM based surface modification, μ_{STM}, both using a silicon AFM tip is calculated as: 0.3856 and 0.0849, respectively.

To interpret these results, the meaning of Tabor parameter should be explained in more detail. The tabor parameter defines the adhesiveness and the softness of the contact between two surfaces. If the value of Tabor parameter is low, the contact is hard and not very adhesive, if it is high the contact is soft and more adhesive. For $\mu < 0.1$, DMT theory approximates the forces better than the other theories, whereas for $\mu > 5$, JKR is the appropriate theory to estimate the forces. The μ values between 0.1 and 5 suggest intermediate regime in terms of softness and MD theory should be used [131]. Therefore, to model the forces for STM based surface modification DMT theory should be used, however AFM based nanoparticle manipulation should be modeled using MD theory.

To model the tip-sample interaction for AFM based nanoparticle manipulation, instead of MD theory, we used the Pietrement model, which gives the relation between the indentation depth and the force experienced as a generalized equation and is a very close approximation to MD theory [92]. We selected using this theory because the MD model is not practical for SPM purposes, the model is not easy to solve analytically, and hence numerical techniques should be employed. Pietrement model suggest an easily solvable polynomial equation for contact radius and force. Using this model, maximum adhesion force between a tip and the surface can be approximated as:

$$F_a = \pi R_e \gamma \left(0.267\alpha^2 - 0.767\alpha + 2\right) \tag{2.16}$$

where γ is the effective surface energy, R_e is the equivalent radius, and α is a parameter that is defined by Pietrement to build the approximate model to MD theory. α can be found as:

$$\alpha = \frac{1 - e^{\left(\frac{-\lambda}{0.913}\right)}}{1.018} \tag{2.17}$$

where λ is the Maugis parameter which can be calculated from Tabor parameter, μ directly using $\lambda = 1.1570\mu$. The Pietrement model also gives the contact radius between the surface and the tip as:

$$a = a_0 \left(\frac{\alpha + \sqrt{1 + \frac{F_n}{F_a}}}{1 + \alpha}\right)^{2/3} \tag{2.18}$$

where a_0 is the contact radius between the tip and the surface under 0 normal force and F_n is the normal force applied on the surface by the cantilever. a_0 can be calculated as:

$$a_0 = \left(\frac{\pi \gamma R_e}{\kappa}\right)^{1/3} \left(-0.451\alpha^4 + 1.417\alpha^3 - 1.365\alpha^2 + 0.95\alpha + 1.264\right) \tag{2.19}$$

These general equations will be used in Chapter 3 while the interaction forces between the AFM cantilever tip, surface and the nanoparticle are modeled.

On the other hand, to model the forces in STM based surface modification, DMT contact mechanics theory is used as suggested before. DMT theory suggests the force between two hard surfaces with the presence of adhesion is governed by:

$$F_{DMT} = \frac{4a^3}{3\pi R_e \kappa} - 2\pi R_e W \tag{2.20}$$

where a is the contact radius between the tip and the sample and W is the work of adhesion between the two surfaces. The relationship between the contact radius a and indentation d is given by DMT as $r = \sqrt{dR_e}$. Since indentation can be defined as $d = z - \sigma$, combining these two relationships with Eq. 2.20 yields:

$$F_{DMT} = \frac{4\sqrt{R_e}(z-\sigma)^3/2}{3\pi\kappa} - 2\pi R_e W \tag{2.21}$$

An extra step should be taken here to protect the continuity of the total force equation. At $z = \sigma$, the contact starts and the electrostatic force disappears since the charges between the tip and the surface are equilibrated. However both the non-contact van der Waals force and DMT contact mechanics force can be defined at $z = \sigma$ using Eqs. 2.10 and 2.21, and these two forces should be equal at inter-atomic distance. Hence the equality:

$$\frac{29 A_H R_e}{180\sigma^2} = -2\pi R_e W \tag{2.22}$$

should hold, which will yield:

$$W = -\frac{29 A_H}{360\pi\sigma^2} \tag{2.23}$$

The values of the general and material dependent model parameters defined in this section are listed in Tables 2.1 and 2.2, respectively. These stated values are used for all of the simulations in this work, unless a parameter is varied during the simulation.

Using the Eqs. 2.10, 2.11, 2.12, 2.21 and 2.23, the total force, contact force and non-contact force on the STM end-effector due to its sample interaction during imaging and surface modification can be calculated. Using these equations and parameters defined in Tables 2.1 and 2.2, a sample simulated force vs. tip-sample distance plot using a platinum coated silicon cantilever

Table 2.1: General parameters used for sample plots and CAFM probe analysis for STM operation

Parameter (Unit)	Value	Parameter (Unit)	Value
σ_0 (nm)	0.288	ϵ_0 (F/m)	8.854×10^{10}
θ_t (degrees)	22.5	θ_c (degrees)	15
L_t (μm)	12.5	L_c (μm)	225
R_s (nm)	∞	R_p (nm)	50
R_t (nm)	20	W_c (μm)	28
V (V)	1	e (C)	1.602×10^{-19}
$\hbar$ (m^{2}kg/s)	6.626×10^{-34}	m_e (kg)	9.109×10^{-31}

Table 2.2: Material dependent parameters used for sample plots and CAFM probe analysis for STM operation

Parameter (Unit)	Platinum Tip	Platinum-Iridium Tip	Diamond Tip	Gold Surface
E (GPa)	168	184	1220	79
ν	0.38	0.38	0.2	0.44
A_H (zJ)	400	224 *	296	400
W (J/m^2)	0.124	0.069	0.092	0.124
ϕ (eV)	5.65	5.65	4.80	4.52

* Fitted from experimental data.

with 20 nm of tip radius and a gold surface at 1 V bias can be seen in Fig. 2.6(c). As can be seen from the figure, electrostatic attraction between the tip and the surface and the intermolecular forces between the tip and the surface are the two major forces. The electrostatic attraction between the cantilever and the surface is a few magnitudes of order smaller than these forces, hence does not play a major role. The reason for this is the length of the tip. The electrostatic interaction between the tip and the surface occurs from a distance of a few new nanometers. On the other hand, the same interaction between the cantilever and the tip occurs from the same tip-sample distance added to tip length, i.e. approximately 10 μm for commercial cantilevers. It should also be noted that if a CAFM probe with a shorter tip length is used, the electrostatic force between the cantilever and the surface would increase. The jump of the force at the interatomic distance ($z = 0.288$ nm) occurs because the electrostatic force will go to 0 due to the redistribution of the charges shortly after tip-sample contact.

The last relation that needs to be defined is the snap-into contact distance of the cantilevers. This is modeled using the relation given in [12], where the snap-into contact distance is taken as the distance where the following equation holds:

$$\frac{\mathrm{d}f_{\text{total}}}{\mathrm{d}z} = k_{\text{cantilever}}. \tag{2.24}$$

This force model will be used in Chapter 4, to analyze the possibility of using AFM cantilevers for STM operation. Using the equations above, probes viable for STM operation are found as those for which the calculated snap-into contact distance of a cantilever is lower than the maximum tunneling distance.

2.5 Case Study Specific Approaches

The general models presented above in this chapter are used to create full system models, and the challenges reported in the first section of this chapter are attempted to be tackled on the

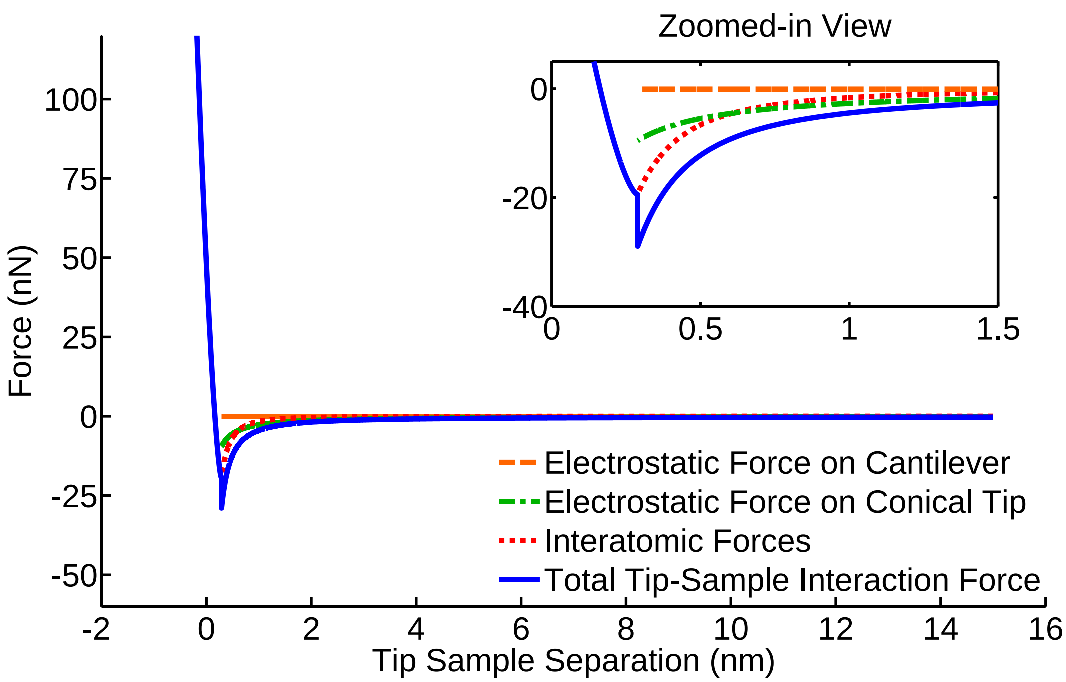

Figure 2.6: A sample force-distance relation between a CAFM probe and surface for a bias voltage of 1 V. When the distance between the tip and the cantilever reaches 0.288 nm which is defined as the inter-atomic distance, the surfaces become in contact, the electrostatic forces disappear, and contact mechanics theories take over. The contact part of this force curve is governed by the DMT contact mechanics model since the contact is hard, tabor parameter $\lambda = 0.0835$. The plot is generated for a cantilever with a tip radius of 20 nm, tip angle of 22.5^o, tip height of $12\mu m$, bias voltage of $1V$, the surface is gold and the probe is platinum.

following two case studies: automated mechanical contact manipulation of nanoparticles and automated electrical non-contact manipulation of surfaces.

2.5.1 Automated mechanical contact manipulation of nanoparticles

As the first case study of this thesis, an AFM is utilized as a nanoparticle manipulation tool. To achieve this, nanoparticles with 100 nm diameter are positioned into assemblies and patterns using an AFM, by mechanically pushing or pulling the particles. During this case study, the physics behind the AFM based nanoparticle manipulation are investigated using Pietrement contact mechanics model and the choice of appropriate cantilevers are discussed. The non-linear behavior of the lateral actuators is solved by employing feedback control. The lack of real-time feedback during manipulation is solved by utilizing the force and image data that is available when AFM is employed in such a task. Finally, to tackle the low throughput problem of SPM based manipulation systems, automated particle manipulation is demonstrated which does not require user interaction and images taken in between manipulation steps. In order to achieve automation, particle detection, contact-loss detection and task planning algorithms are presented. The performance of the AFM based nanoparticle manipulation system is also discussed and quantified with experiments.

2.5.2 Automated electrical non-contact manipulation of surfaces

The second case study of this thesis is utilizing an STM to manipulate surfaces using electrical pulses or high electric fields between the STM probe tip and surface. During this demonstration, an STM end-effector images the surface and at the regions where modification is desired, the bias voltage is pulsed or switched to a high value to create features using electrical principles. This manipulation technique is demonstrated in literature before; however, the novelty of our approach is investigating the possibility of utilizing a conductive AFM probe to perform the STM imaging and surface manipulation as a first step towards a multi-probe electrical manipulation approach.

In addition, utilizing a conductive AFM probe enables us to implement a dual mode SPM system, where it can image with the more stable and electrically non-selective AFM mode and it can manipulate the surface with STM mode, where the feature sizes are smaller. The advantage of such a system is its ability to work on electrically heterogeneous surfaces which is a requirement for most device applications. In order to achieve this, the mechanics of the system is examined by creating a full system model of the system dynamics using DMT contact mechanics theory, and equations presented above on non-contact interaction forces. The dynamics of the system is also modeled as a mass-spring-damper system, which is also discussed in previous sections of this chapter. A more flexible and faster SPM controller is also designed and implemented which allows us to switch between AFM and STM modes instantaneously.

Chapter 3

Automated Mechanical Contact Manipulation of Nanoparticles

3.1 Introduction

Due to its purely mechanical working principle described in previous chapters, AFMs have the capability of performing several manipulation techniques on all types of materials as well as imaging them. The most common two-dimensional (2-D) AFM based manipulation tasks are lithography [65, 67, 123], dissection [56, 116] and particle positioning. Several groups have worked on AFM based particle manipulation to show its feasibility [5, 47, 53, 65, 66, 67, 83, 96, 105]. In these applications from the literature, servo feedback is turned off so the vertical actuator does not respond to particle topography and the set-point for the dynamic mode is decreased or the manipulation is carried out in contact mode in order to decrease the tip-sample distance. These two minor changes enable the AFM tip to manipulate particles mechanically rather than allowing the tip of the AFM probe to jump over the particles. With no or little control during the manipulation, these applications can be referred as push-and-look type, or blind manipulation. This behavior leads to three notable problems in existing AFM based nanomanipulation: lack of reliability, speed and precision.

Due to the lack of real-time visual feedback, automated nanomanipulation with AFM stood as an unsolved problem for several years. Recently, however, several groups [21, 66, 82] have demonstrated AFM based automated nanoparticle manipulation. In one study [84], a drift compensation method is used to autonomously position 28 nanoparticles with 15 nm diameter in a total of 40 minutes. The images of manipulated particles were impressive; however, force feedback of the AFM probe was not utilized during nanomanipulation for control and success rates of the manipulation attempts were not investigated in depth.

To increase the speed and control of AFM based nanoparticle manipulation, this chapter focuses on developing an automated 2-D nanomanipulation system. The AFM tip is utilized to push 100 nm diameter gold nanoparticles on a flat mica substrate covered with Poly-L-Lysine (PLL) in 2-D. The success rate of each automated manipulation operation is improved using a contact loss algorithm that continuously tracks the real-time force feedback of the AFM probe, rather than the standard blind, push-and-look approach. The contact loss algorithm dramatically increases the reliability of the system because errors in positioning and pushing can be prevented, as suggested but not demonstrated in [6].

In addition to the contact-loss detection, particle pulling is shown to be possible, which can be a more stable manipulation method compared to pushing. To compare the different manipulation types such as pulling, pushing, sliding, spinning, or rolling, a force model for the nanomanipulation system is built.

To increase the speed of the AFM based nanoparticle manipulation techniques, a multiple particle manipulation scheme is introduced, which does not require a new image before each single manipulation operation. Since taking images consumes significant amount of time, this scheme increases the manipulation speed drastically.

Another problem arises due to the drift in the AFM system. Thermal and piezoelectric drift (creep) cause the particle positions to change over time, and the positions extracted from the reference image will become incorrect. However, there are several methods in literature that is shown to compensate for drift using Kalman or particle filters. Therefore, hereafter in this section, drift problems will be neglected.

The performance of these control methods are investigated through a statistical study to form a quantifiable basis of development and comparison. One of the strengths of this technique is that it can be generalized to different materials and known geometries, and does not require the particles to be separated from each other.

3.2 System Description

Figure 3.1 displays the overall layout for the automated nanomanipulation system. An AFM (Veeco, Autoprobe M5) with an AFM cantilever (Veeco, RTESPA-M, normal stiffness:1-2 N/m) is used as the nanomanipulator, which is accessed by a Windows 95-based PC (AFM PC). A client-server program is created on the AFM PC, which allows an external PC to connect to the AFM through TCP/IP Ethernet (the Veeco SPMAPI is used to interface with the AFM). The main control PC uses real-time Linux (RTAI 3.3, Ubuntu Linux 2.6.15) and an interface program written in C++. It interfaces with the AFM PC through a direct Ethernet connection. A 3-DOF piezoelectric nanopositioning stage (Physik Instruments P-753, 12 μm range, sub-nm precision) is used as the positioner in the AFM, which allows for a faster control bandwidth compared to actuating the AFM's nanopositioner through TCP/IP. The three axes of the piezo stage are controlled through its dedicated controller (Physik Instruments E-612) by the main control PC using three D/A outputs (Adlink PCI-6208). Positions are read from the amplifier using an A/D converter (National Instruments PCI-6024E). In addition, the AFM's normal-deflection signal (A-B voltage signal) is read directly from the AFM with the A/D converter. The total control bandwidth is 1 kHz, which is limited by the data acquisition system.

For operation, a sample is placed on the nanopositioner and the AFM probe is automatically positioned to the sample with a short distance from the surface, where dynamic mode AFM (the type of dynamic mode used is non-contact mode (NCAFM)) is used to avoid inadvertently

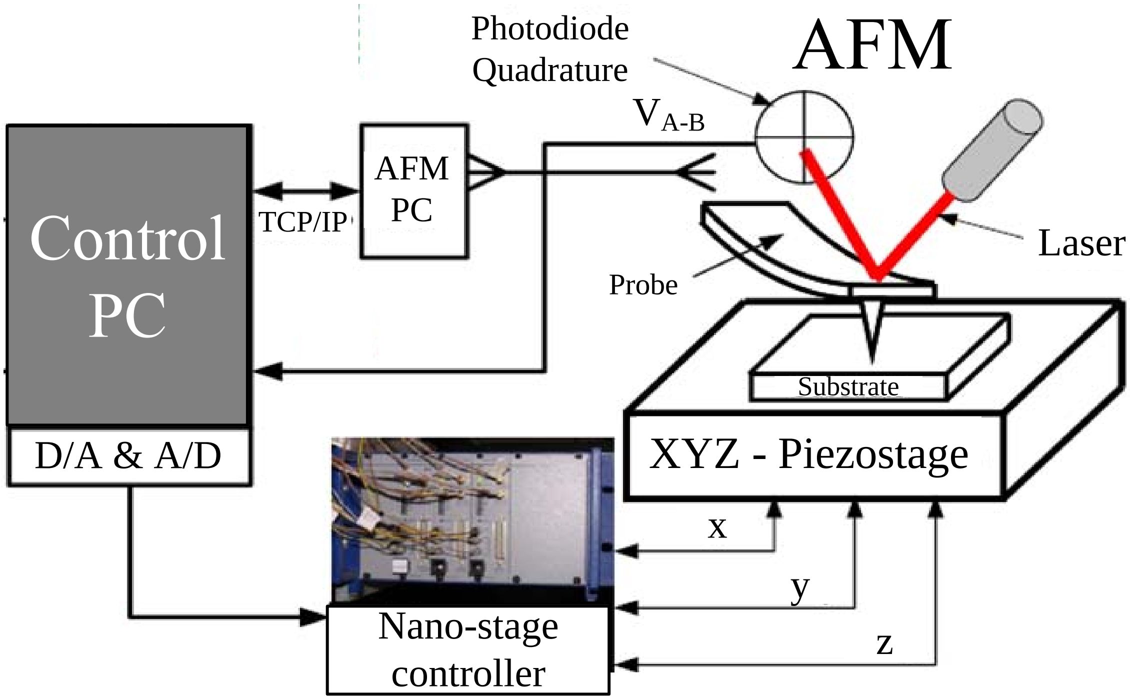

Figure 3.1: Overall system structure of the autonomous nanoparticle manipulation setup

moving particles during imaging. By default, the AFM servo positions the probe with an offset over the surface to maintain a constant vibration amplitude upon the substrate. The software in the main control PC has the capabilities of turning the servo feedback control on and off, position the tip with a high precision, change the set point of NCAFM tip vibration magnitude, take non-contact images of the substrate and make single line scans or line travels on a given line with a given length. Before beginning the experiments, we wait for any drift in the system to dissipate.

The 100 nm gold colloid nanoparticle samples are prepared with the procedure by Baur *et al.* [5]. Commercially available nanoparticle samples, often used for SPM calibration tasks, are used. The overall procedure consists of adsorbing 20 μl of 0.1% Poly-L-Lysine (PLL) onto freshly cleaved mica for 20-60 seconds, rinsing with de-ionized water and drying with nitrogen. Immediately after drying, 20 μl of gold colloidal solution is adsorbed onto the treated mica for 5 minutes or more, depending on the surface concentration needed. The sample is then rinsed again with de-ionized water. After drying with nitrogen it is finally incubated in a 60 ^{o}C oven for at least 1 hour. The positive charge of PLL and the negative charge of Au nanoparticles create an electrostatic bond between the mica surface and the particles, temporarily fixing them on the surface for imaging. A scanning electron microscope (SEM) image of the resulting sample is shown in Fig. 3.2.

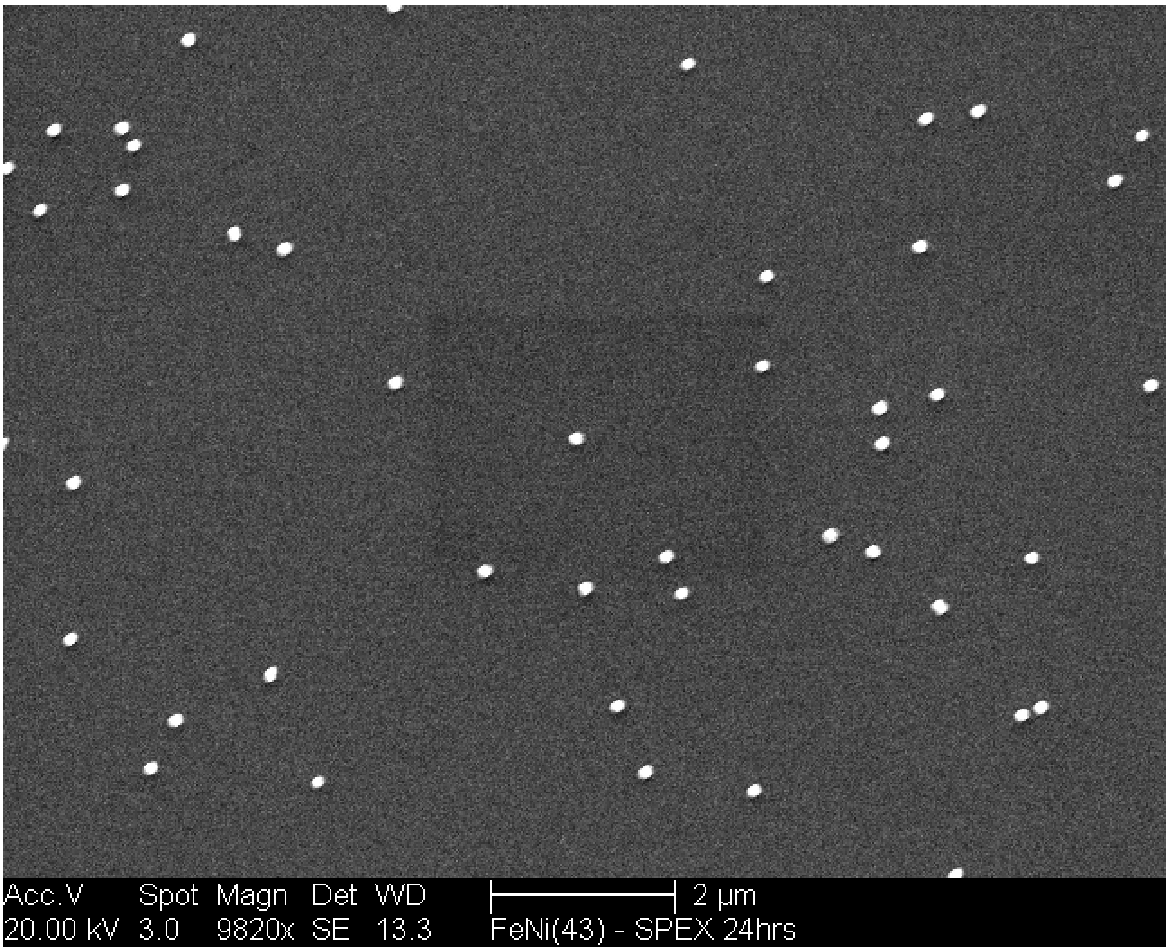

Figure 3.2: Scanning electron microscope (SEM) image of 100 nm gold nanoparticles on Poly-L-Lysine (PLL) covered mica surface. The particles are fixed due to the electrostatic attraction between the gold nanoparticles and PLL.

3.3 Nanoparticle Imaging and Manual Manipulation

As the electrostatic forces holding the nanoparticles on the surface are relatively weak [5], small contact forces from conventional contact mode imaging might disturb and move the particles.

To eliminate this possibility, dynamic-mode scans are used for particle imaging. Dynamic mode imaging works with a similar principle as the contact-mode. In dynamic-mode, the cantilever is oscillated with a certain amplitude near its resonance frequency, as the tip interacts with the surface, the natural frequency of the cantilever shifts and the oscillation amplitude and phase changes. Using a feedback loop to enforce a set-point oscillation amplitude or phase, the tip traces the surface without ever touching it. Often the cantilevers used in dynamic mode imaging have high stiffness values (30-60 N/m), but for nanoparticle imaging in dynamic mode the stiffness of the cantilevers used is selected in intermediate range (1-5 N/m). This decreases the interaction forces between the particles and the surface. Because the tip is not in contact with dynamic mode, the resolution is decreased as opposed to the contact mode.

A sample 3 μm $\times$ 3μm AFM image of the gold nanoparticles is shown in Fig. 3.3. As seen in this image, the nanoparticle size is artificially inflated due to tip convolution effects.

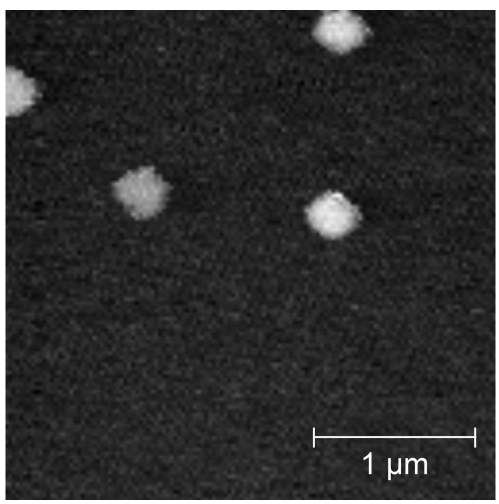

Figure 3.3: A sample 128 $\times$ 128 pixels^2, 3 μm $\times$ 3 μm dynamic-mode AFM image of 100 nm gold nanoparticles

As mentioned previously, the method for moving the nanoparticles to their respective target positions is mechanical pushing with the AFM tip. A sequence of pushing operations, performed by manual tip positioning commands, is given in Fig. 3.4. The simple blind procedure of manipulation is to take a 'before' image, position the tip behind the particle, turn the z-servo off, and move the tip on a straight line passing through the center of the particle to the target position. After this tip motion, the z-servo is turned on, and an 'after' image is taken.

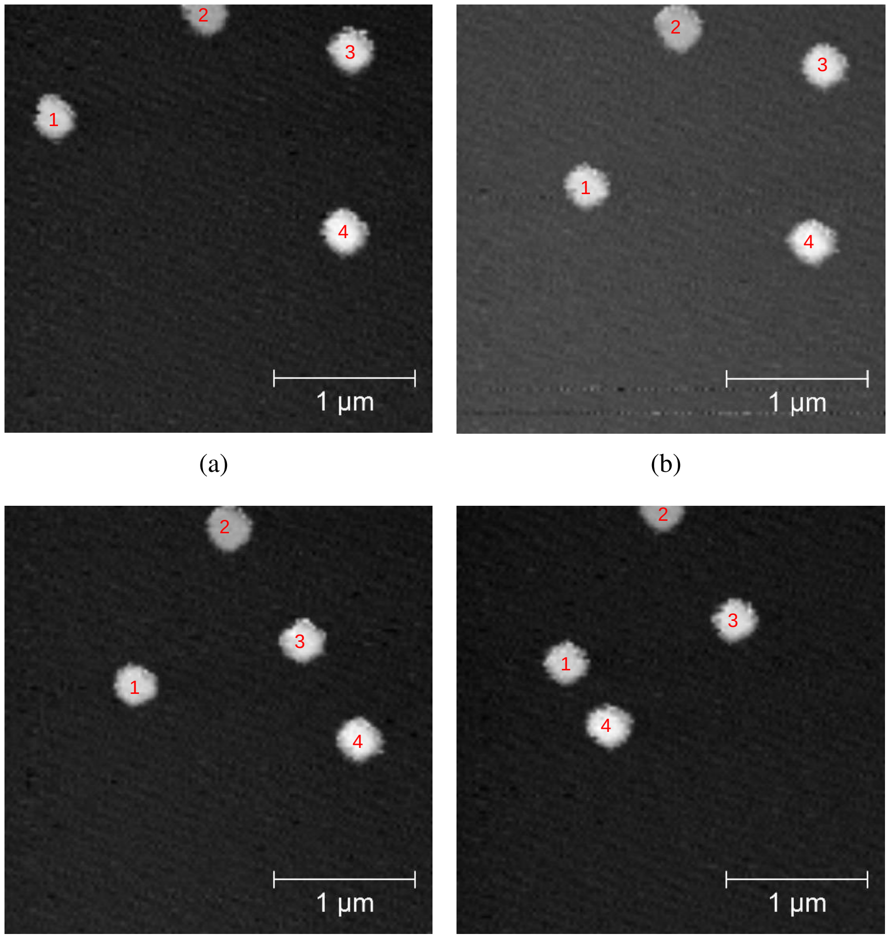

(a) (b) (c) (d)

Figure 3.4: 3 μm $\times$ 3 μm dynamic-mode AFM images of a sequence of manual manipulation tasks on 100 nm gold nanoparticles

Even for non-automated trials, not all attempts of particle pushing are successful. The most prominent source of error is the tip trajectory not passing through the particle center. The amount of offset seems to be critical for the success of this operation as mechanical pushing, in essence, is critically stable. Any small offset might cause the particle to spin around the tip, resulting in failure.

3.4 Force Modeling

Forces encountered in particle-surface and tip-particle interfaces during tip-particle contact were modeled previously for tribological characterization [110, 119], and manipulation experiments [66, 89, 111] on microscale or for teleoperated systems. In this section, we apply a similar force modeling approach to investigate the nanoparticle manipulation mechanism. This investigation involves an analysis of possible particle motion modes (rolling, spinning, and sliding) for the pushing and pulling cases.

Our main variable in this model is the cantilever normal stiffness since it can be chosen almost freely. A second reason to focus on stiffness is that our initial experimental results showed a preferred stiffness range for successful particle manipulation. Very low stiffness values failed to move the particle whereas high stiffness values moved the particle even during imaging. Although the results of this analysis will not be used directly in the automated particle manipulation procedure, they will provide a basis for discussion when combined with experimental results in the following sections. This analysis will help us understand why there is a preferred cantilever normal stiffness range for manipulation.

3.4.1 Assumptions

1. Manipulation while the tip is in contact with the surface is not considered for any experiment or simulation. Since this case study focuses on the design of a more controllable way to manipulate nanoparticles, all of the experiments and modeling are for dynamic mode AFM, where the tip and surface are not in contact. A few drawbacks of manipulation while the tip is in contact with the surface include:

    - Tip becomes blunt after several manipulations due to wear. This changes the geometry of interaction.

    - The particle force feedback signal from the AFM becomes corrupted for some directions because of the high interaction force between the surface and the tip.

2. Servo feedback control of the AFM should be disabled just before starting manipulation. If it is kept on, the tip would respond to the change in topography data during manipulation trial, which would result the tip jumping over the particle instead of pushing it. Therefore, for experiments, the servo control is turned off and, for simulations, the tip height is assumed to be constant prior to and at the beginning of manipulation.

3. For the cantilever used in the experiments with normal stiffness of approximately 3 N/m, regardless of the manipulation direction, the V_{A-B} signal always increases, whereas the mean of the V_{LFM} signal stays nearly constant during the failed manipulation trials. This observation can be interpreted as the failure of the manipulation occurs due to the tip jumping over the particle instead of moving around the particle. Since the normal stiffness of the cantilever is around one order of magnitude lower than the lateral stiffness, this argument seems to be valid.

4. During experiments, the snap-in distance of the tip is observed as about 10 nm in dynamic AFM. In addition, the very end of the tip is approximated as a sphere in the nanometer scale. When we consider a spherical tip with radius of 130 nm, a spherical particle with radius 50 nm and a snap-in distance of 10 nm, using geometrical relations, the contact angle between the tip and the particle would be at least 30 degrees.

5. Tip velocities relative to the substrate are slow in comparison to dynamics at the nanoscale. Due to this fact, a quasi-static assumption of force balance during tip-particle contact is employed.

3.4.2 Modeling of Tip-Surface-Particle Interactions

The interaction forces during manipulation can be examined at the tip-particle and particle-surface interfaces. At both of these interfaces there are friction and normal forces that are caused by the interaction. In addition, there are adhesive forces which are a limiting effect to the normal force component in the interface. Figure 3.5 shows the interaction forces between the tip, particle, and the surface.

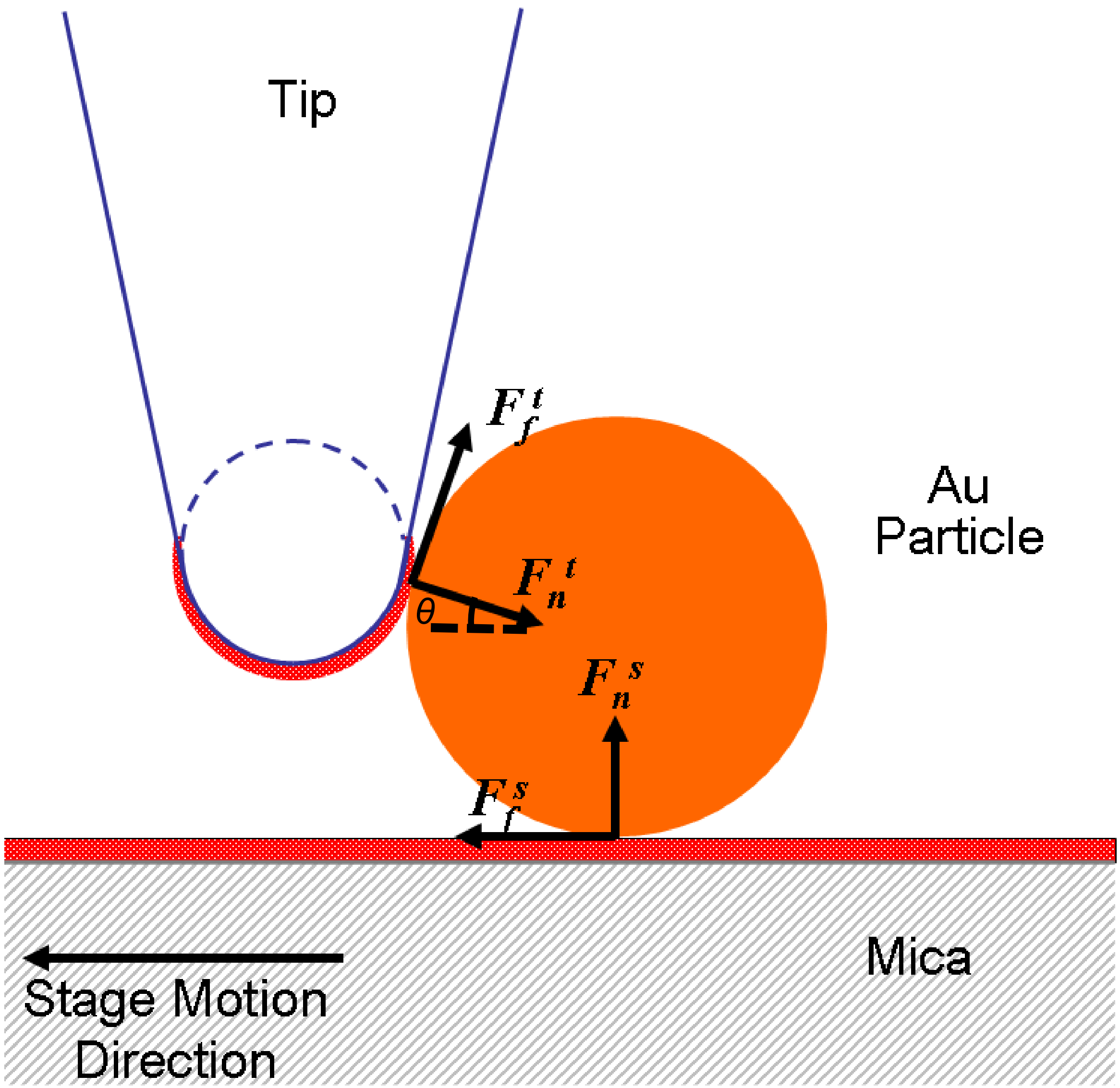

Figure 3.5: Interaction forces during pushing-sliding type manipulation. Tip and substrate are covered with a (red) PLL layer. Only relevant forces are shown for brevity.

Let F_n^s and F_f^s be the normal and friction force applied on the particle due to the interaction with the surface.

The adhesive force F_a^s, between the particle and substrate, is defined as the maximum normal force that can be applied to the particle in the negative direction that would not pull the particle off the surface. This adhesive force keeps the particle on the surface even for negative loads. F_a^s can be a combination of electrostatic, Van der Waals and capillary forces. We will use the Pietrement contact mechanics model [92] to calculate the adhesive force and contact radius as we suggested before in Chapter 2 Section 2.4.

The adhesive force F_a^s can be calculated using Eq. 2.16. The nanoscale friction force is dominated by the shear friction and for particle manipulation it can be calculated as:

$$F_f^s = \tau_s \pi a_s^2 \tag{3.1}$$

where τ_s is the interfacial shear strength of the particle substrate interface and a_s is the contact radius of particle substrate interface that can be calculated using Eq. 2.18.

Since F_n^s is the normal force applied on the particle from the surface due to the interaction with the tip, it is directly related to the cantilever stiffness and the contact angle of the particle with the tip. Assuming θ is the instantaneous contact angle of the tip with the particle, θ_0 is the initial contact angle and k_n is the normal stiffness of the cantilever, the following geometric relation can be obtained:

$$F_n^s = k_n \delta = 2 k_n R_p \left(\sin\theta - \sin\theta_0\right) \tag{3.2}$$

where R_p is the particle radius.

The friction between the particle and the tip can be calculated in the same way as the particle surface interaction. F_n^t is the pushing/pulling force of the tip applied on the particle and should be calculated from the force balance equations. In what follows, a theoretical analysis of 100 nm gold nanoparticle manipulation with an AFM tip on a mica surface is made for different particle manipulation modes. The parameters used for this analysis are given in Table 3.1. Note that the effective surface energy (γ) and interfacial shear strength (τ) values for both interfaces are taken to be equal. The reason for this is the fact that PLL-like polymers cover the tip as soon as any tip-substrate contact occurs [87], which means that both interfaces consist of Au-PLL contact. The tip radius (R_t) is calibrated using the convolution effect of the particles in AFM images. As the actual particle size is known, the tip radius is extracted from the apparent particle size as:

$$2R_p = 2R_{p\,\text{apparent}} - 2R_t \tag{3.3}$$

where $R_{p\,\text{apparent}}$ is the particle radius observed from an AFM line-scan or image.

Table 3.1: Parameters Used For Nanoparticle Manipulation Analysis

Parameter	Value	Unit	Description
R_p	50	nm	Particle radius
R_t	65	nm	AFM cantilever tip radius
E_t	170	GPa	Young's modulus of the tip
E_p	78	GPa	Young's modulus of the particle
E_s	15	GPa	Young's modulus of the surface
ν_t	0.17		Poisson's ratio of the tip
ν_p	0.44		Poisson's ratio of the particle
ν_s	0.5		Poisson's ratio of the surface
γ_t	0.304	N/m	Surface energy of the tip
γ_s	0.304	N/m	Surface energy of the sample
σ_t	0.3	nm	Inter-atomic distance of the tip
σ_s	0.3	nm	Inter-atomic distance of the surface
τ_t	0.326	GPa	Interfacial shear strength of the tip
τ_s	0.326	GPa	Interfacial shear strength of the surface

3.4.3 Pushing-Sliding Case

For successful pushing-sliding of the particle along the mica surface, the following inequalities should hold:

$$F_f^{smax} \leq cos\theta F_n^t + sin\theta F_f^t \tag{3.4}$$

$$F_f^{tmax} \geq sin\theta F_f^s - cos\theta F_n^s \tag{3.5}$$

This inequality is impossible to solve since there is no way to determine simultaneous force values for normal and friction forces. However, the following worst case scenario can be found:

$$F_f^{smax} \leq cos\theta F_n^t \tag{3.6}$$

$$F_f^{tmax} \geq sin\theta F_f^{smax} - cos\theta F_n^s \tag{3.7}$$

Here the inequalities signify that, for successful manipulation, the horizontal components of the particle-tip interaction forces should be higher than the friction force between the particle and surface and the friction force between the tip and particle should be high enough so that the particle does not jump over the particle during pushing. However, this second relation in Eq. 3.7 is actually the necessary condition for sliding, for if the tip does not jump over the particle, the necessary horizontal deflection would eventually be satisfied to push the particle on the surface (as the particle substrate friction is not strong enough to break the cantilever).

Here, it should be noted that it is possible to describe each force in terms of F_n^s for successful manipulation; therefore we can find optimal values for cantilever normal stiffness k_n and contact angle θ for different surfaces, materials and sizes. Such an analysis is made for different stiffness values in Fig. 3.6. As expected, there is a lower limit of cantilever stiffness values ($k_n \approx 2.6$ N/m) to initiate sliding by pushing. This result is in line with our experimental findings.

3.4.4 Pushing-Spinning Case

Spinning is directly related with the center detection error and the spinning resistance moment. The relations for the no-spin case are given below:

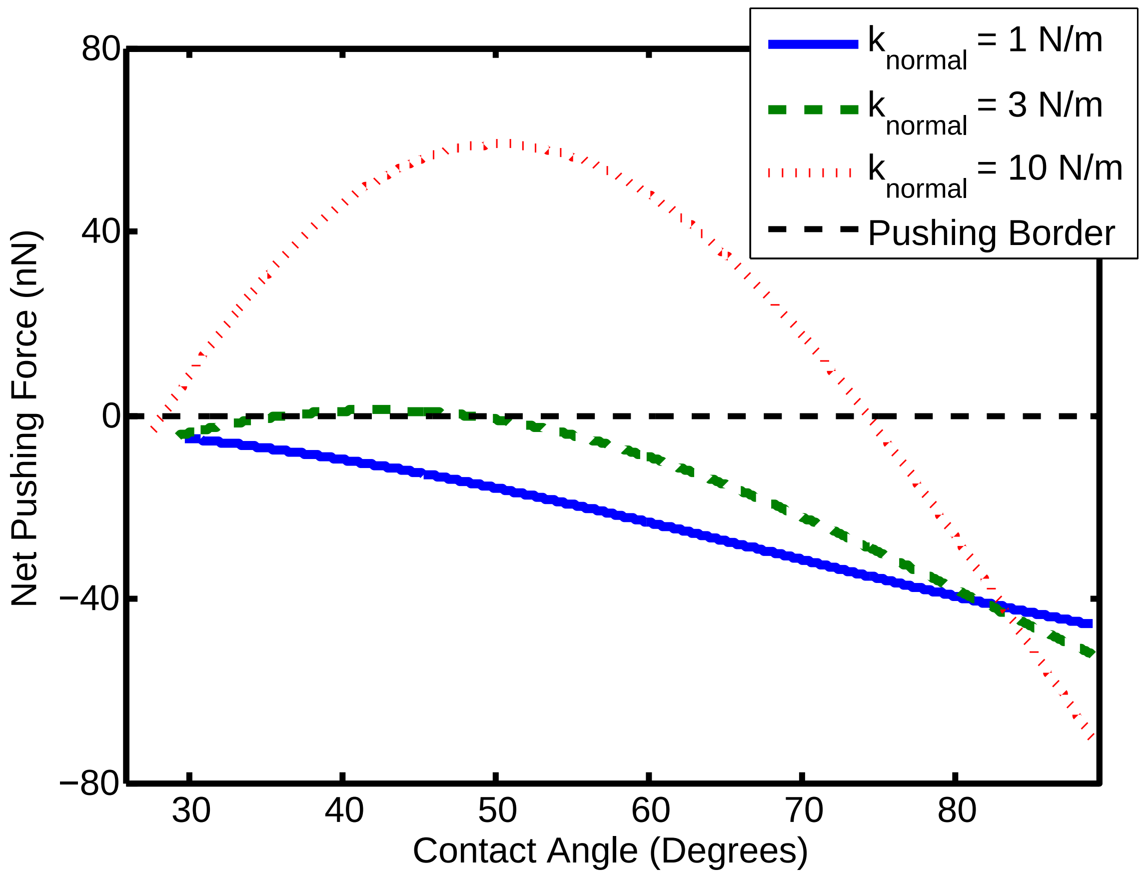

Figure 3.6: The net force ($F_f^{tmax} - sin\theta F_f^{smax} + cos\theta F_n^s$) acting on the particle for different cantilever normal stiffness (k_n) values.

$$
\begin{aligned}
\Gamma^{max} &= \frac{2\pi}{3}\tau_s a_s^3 && (3.8)\\
F_{spin}^{max} &= \frac{2\pi}{3x_0}\tau_s a_s^3 = F_f^s \frac{2}{3x_0} a_s && (3.9)\\
cos\theta F_n^t + sin\theta F_f^t &\leq F_{spin}^{max} && (3.10)\\
F_f^s &\leq F_f^s \frac{2}{3x_0} a_s && (3.11)\\
3x_0 &\leq 2a_s && (3.12)
\end{aligned}
$$

Here, a_s is the contact radius of particle and surface and x_0 is the offset of the tip from the center, due to particle center detection and positioning errors. Since these errors during particle center detection and positioning are believed to be very low ($x_0 \leq 5$ nm) in our experiments, the spinning inequality is very likely to hold. Indeed, a theoretical analysis of the required offset for spinning, shown in Fig. 3.7, indicates that spinning is unlikely to happen.

3.4.5 Pushing-Rolling Case

The interaction forces and moment during a successful rolling operation is shown in Fig. 3.8. For a successful pushing-rolling type manipulation of the particle along mica surface, the following inequalities should hold:

$$
\begin{aligned}
M_{roll} &\geq M^{max} && (3.13)\\
F_f^{t\,max} &\leq cos\theta F_n^s - sin\theta F_f^s && (3.14)
\end{aligned}
$$

In these inequalities M_{roll} is the instantaneous rolling moment applied on the particle by the tip. This rolling moment can be calculated as:

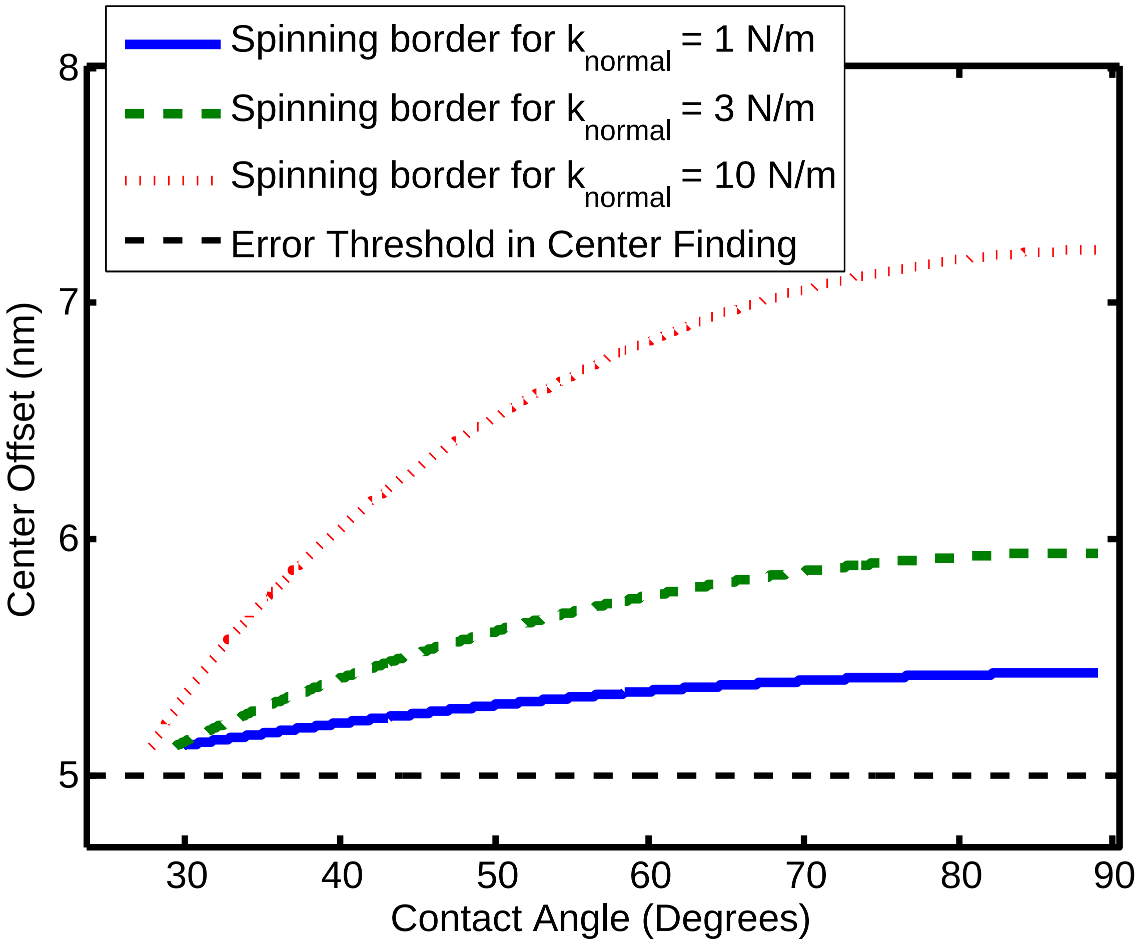

Figure 3.7: The required offset values for spinning for different cantilever normal stiffnesses. The dashed line indicates an estimated maximum center detection error. According to this analysis, if error in particle center detection is less than border, spinning is not a problem.

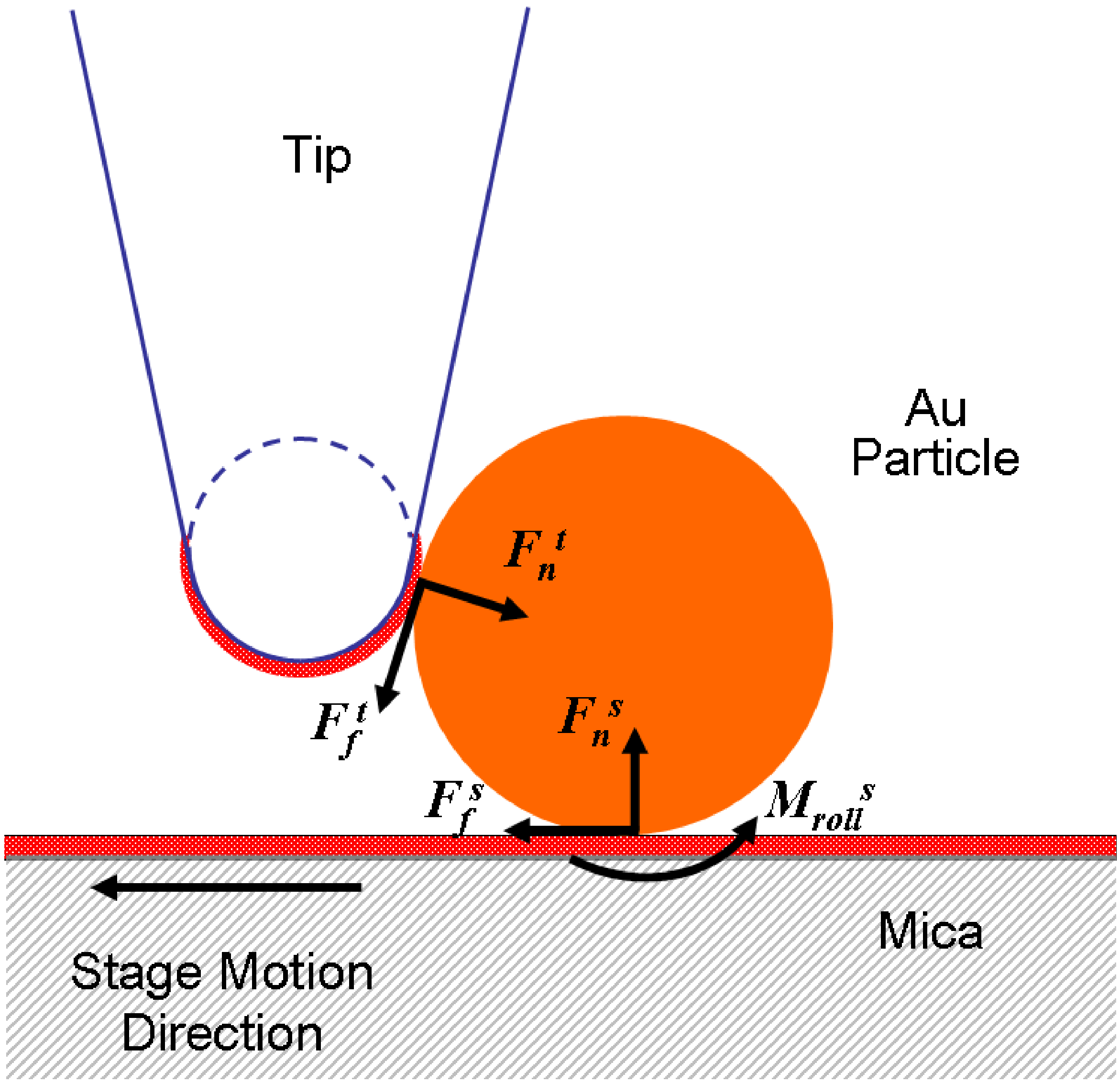

Figure 3.8: Interaction forces and moments during a successful pushing-rolling operation. Tip and substrate are covered with a (red) PLL layer.

$$M_{roll} = -(sin\theta F_n^t + cos\theta F_f^t)cos\theta R_p$$
$$+ (cos\theta F_n^t - sin\theta F_f^t)(1 + sin\theta)R_p \quad (3.15)$$

The maximum resistance moment of an interface (M^{max}) can be calculated as:

$$M^{max} = 6\pi R_s \gamma_s \xi \quad (3.16)$$

where ξ is the critical rolling distance and its value should be: $\sigma_s \leq \xi \leq a_s$

A theoretical analysis of the rolling condition for different cantilever stiffness values is shown in Fig. 3.9. As seen in this figure, the net moment acting on the particle is not enough to initiate rolling for soft cantilevers. Therefore, rolling is not possible for our cantilever stiffness value, $k_n = 3$ N/m.

3.4.6 Pulling-Sliding Case

The interaction forces during a regular pulling operation is shown in Fig. 3.10.

For a successful pulling type manipulation, the following inequalities should hold:

$$F_f^s \leq F_n^t cos\theta + F_f^t sin\theta \quad (3.17)$$
$$F_n^s \geq F_n^t sin\theta - F_f^t cos\theta \quad (3.18)$$

As the worst case scenario, the friction between the particle and the tip could be neglected which would mean:

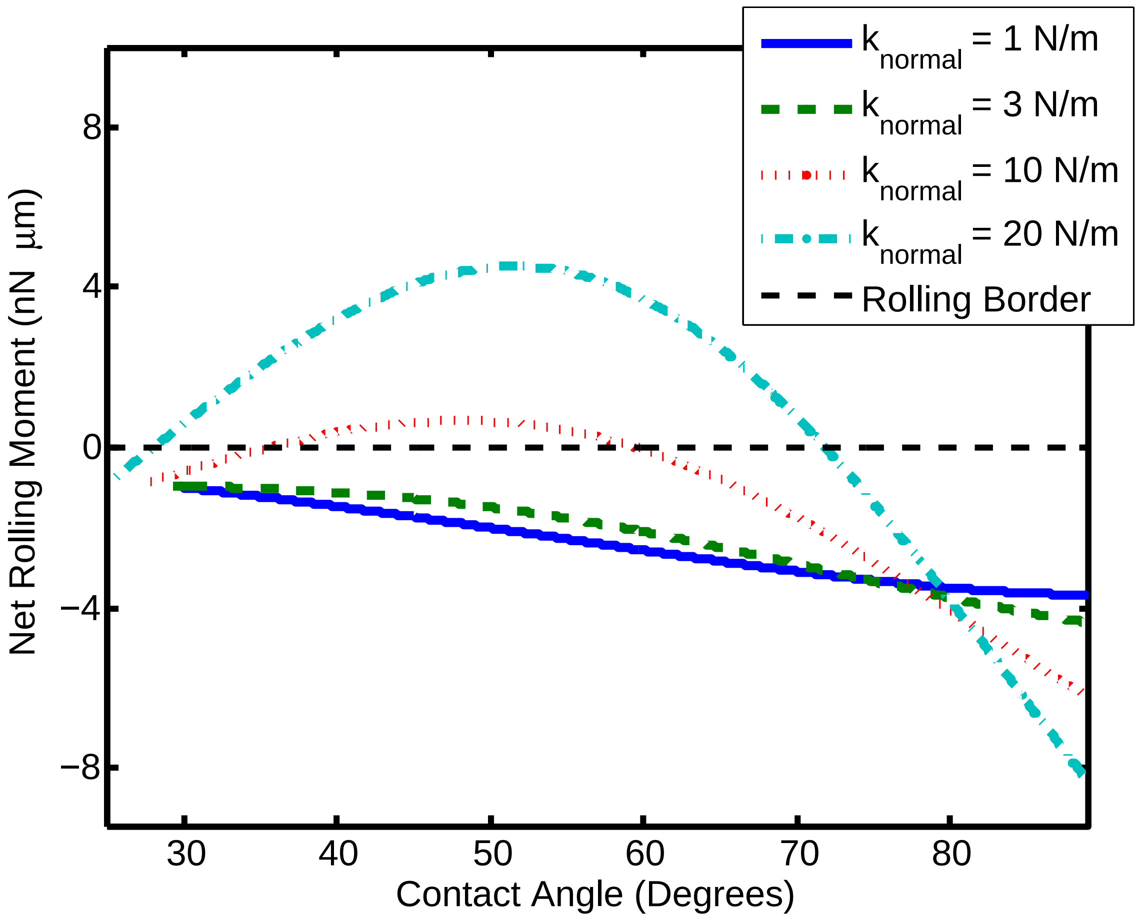

Figure 3.9: The net rolling moment ($M_{net} = M_{roll} - M^{max}$) acting on the particle for different cantilever normal stiffnesses. Higher stiffness cantilevers are more suitable to roll a particle by pushing.

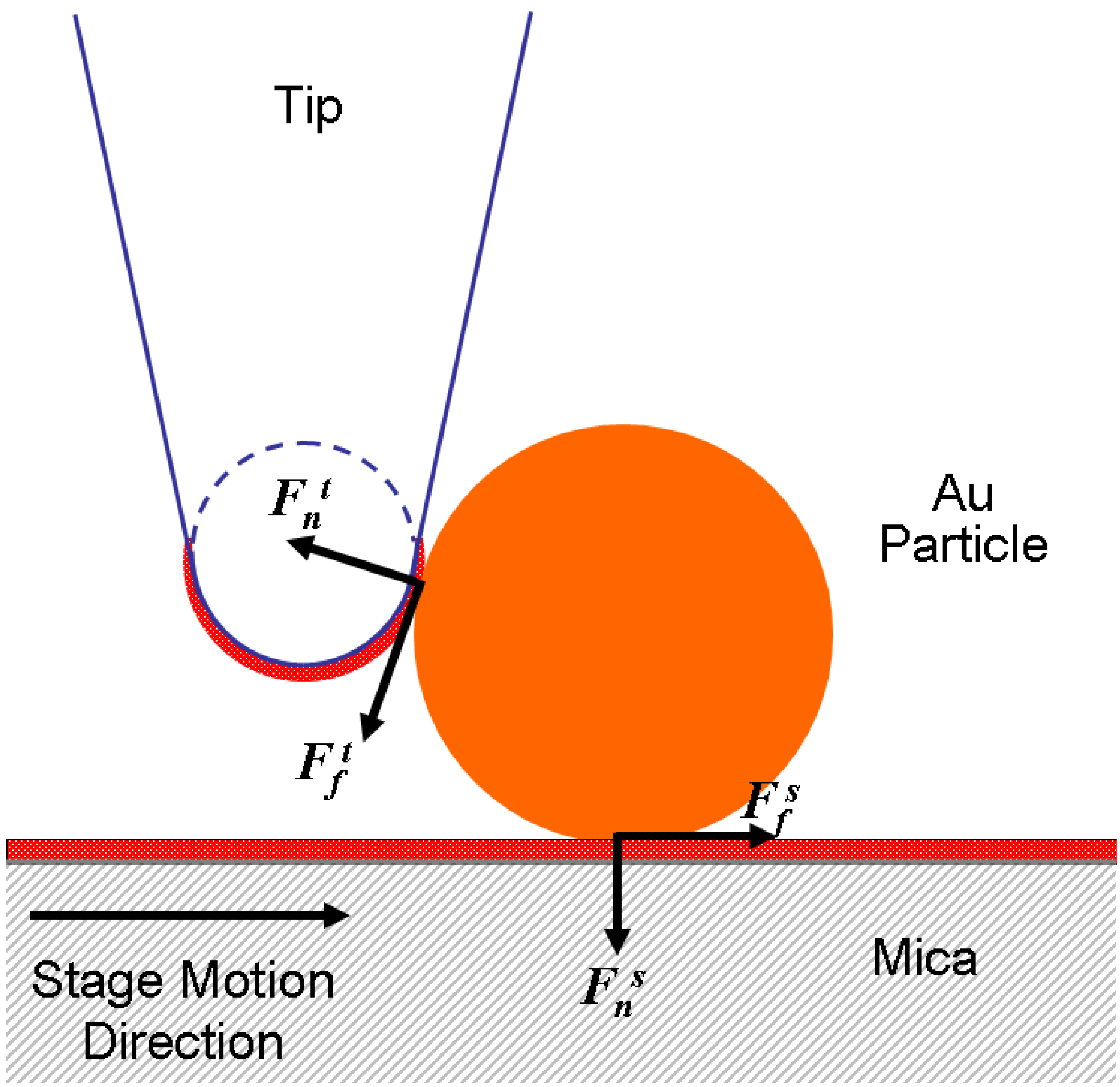

Figure 3.10: Interaction forces during a successful pulling operation. Tip and substrate are covered with a (red) PLL layer. Only relevant forces are shown for brevity.

$$F_f^s \leq F_n^t cos\theta \tag{3.19}$$

$$F_n^s \geq F_n^t sin\theta \tag{3.20}$$

Here, maximum F_n^s can be equal to the adhesive force (F_a^s) between the particle and the surface. Therefore the inequalities mean that the tip should be pulling the particle with a force whose lateral component is greater than the surface-particle friction, but the normal component of the force should be less than the adhesive force between the surface and particle.

The interaction forces can be calculated the same way as they were in the pushing case, but it should be noted that the normal forces changed sign in both interfaces, which would result in a negative effect to the contact radius in the interfaces (*i.e.* decrease the friction force in both interfaces). Since the normal force acting on the AFM tip is negative, we can deduce that the cantilever should bend down to achieve the necessary forces for pulling. While pulling, the tip-substrate separation is smaller than the initial separation. Defining this initial separation as δ_o, we can perform an analysis of the required deflection for successful pulling and find a lower bound of δ_o according to a changing cantilever normal stiffness value. Figure 3.11 displays results of this analysis. Since a $\delta_o > 100$ nm would not initiate contact with the particle, we are interested in the minimum stiffness value that allows pulling, theoretically.

According to these results the pulling-sliding case is also a candidate for nanoparticle manipulation, which supports our experimental results indicating that if the tip cannot push a particle, pulling can occur. Also it should be noted that spinning and rolling forces are not created with pulling.

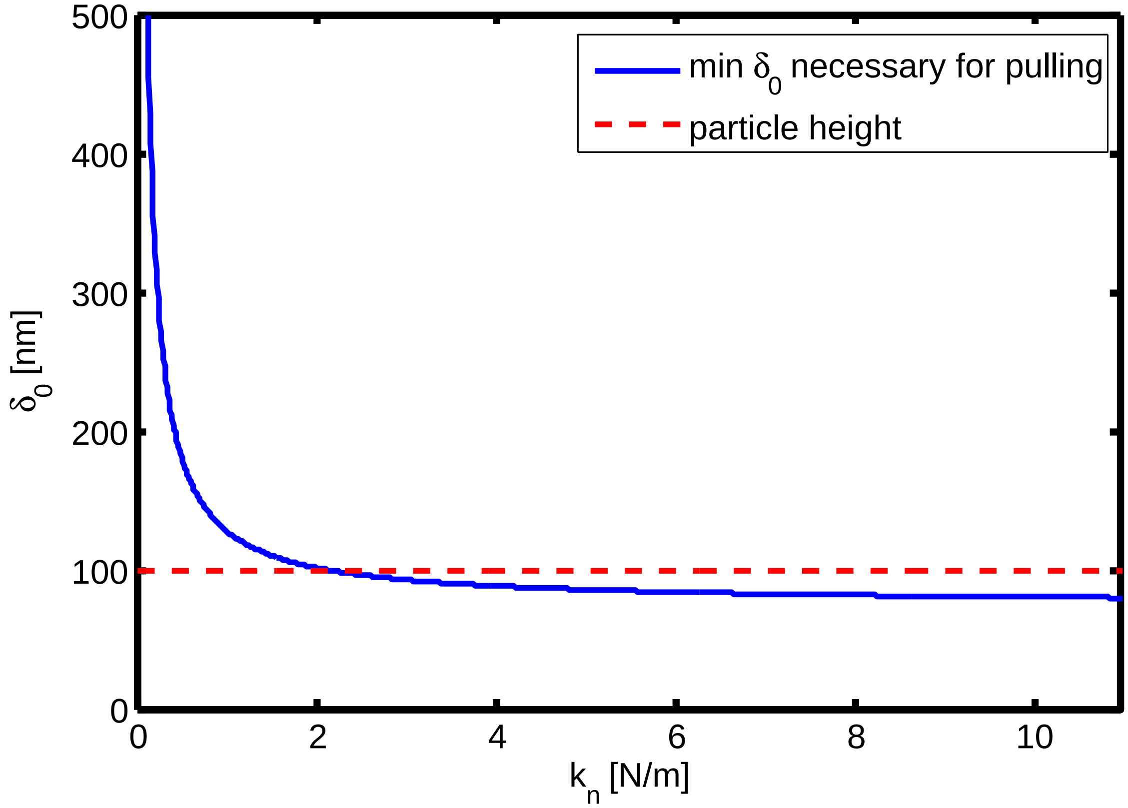

Figure 3.11: Simulated relation of the initial tip-substrate separation to the cantilever normal stiffness for successful pulling.

3.5 Automated Single Particle Manipulation Scheme and Experiments

The general algorithm to autonomously manipulate nanoparticles is outlined in a flowchart in Fig. 3.12. The procedure starts with an initial 10 μm $\times$ 10 μm area non-contact image of the sample. On this image, the operator clicks on a particle and a target position. The program takes an additional fast, low resolution 1 μm $\times$ 1 μm image around the particle and finds the highest point of this image as an initial guess for the particle center. Then, the particle center detection algorithm, described in Algorithm 1 is used, on successive line scans in two orthogonal directions over the estimated center position, to converge to the actual particle center position.

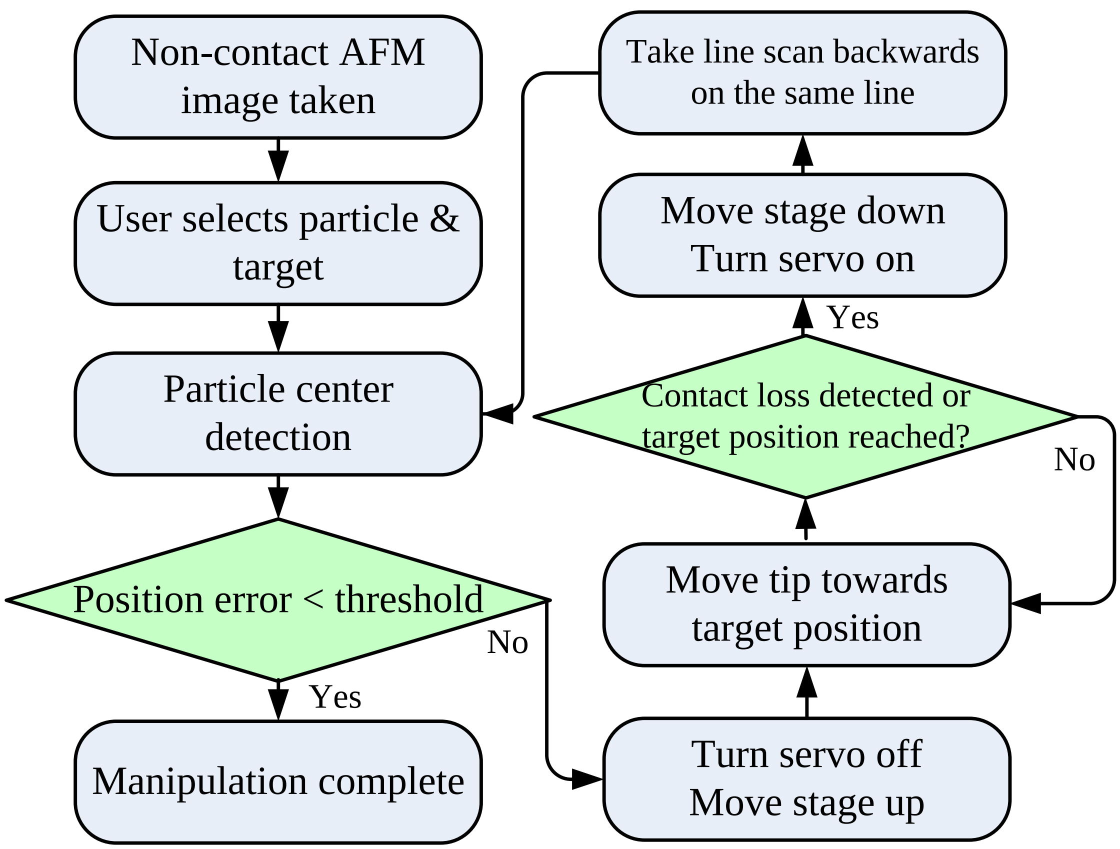

Figure 3.12: A flowchart description of the automated single nanoparticle manipulation algorithm.

This algorithm is an altered version of the watershed algorithm [37] widely used in image

Algorithm 1 Particle Center Detection from Linear Topographic Data

1: Low-pass filter and take derivative of topography data.
2: Take the points of absolute derivative values larger than a threshold as initial guesses.
3: Iterate guess points according to their corresponding derivative values until convergence (*i.e.* $x_k = x_{k-1} + K_x dz/dx$, $y_k = y_{k-1} + K_y dz/dy$ and $K_x, K_y \in \Re^+$).
4: Remove one of the guesses closer to each other than a threshold.
5: Take weighted averages of data points around the remaining guesses.

processing. Its main principle is to use the edges of a particle as initial guesses and move these estimates according to the derivative information to converge on local maxima. The operation detects all of the particles that appear on the same line scan data as seen in Fig. 3.13. Then, the program decides which particle is to be manipulated and takes line scans over this particle in two orthogonal directions to converge to the actual center of the particle. Figure 3.13 shows an arbitrary initial line scan data that does not pass through the center of the particles, yet the center detection algorithm can still find an estimate for the centers of the particles from this data even though there is a high slope and the maximum data point is not 100 nm higher than the surface.

During tip travel, contact loss can be detected using the algorithm described in Algorithm 3. As seen in Fig. 3.14, V_{A-B} is almost zero, with minimal deviation when the tip and the particle are not in contact. However, for tip-particle contact during manipulation, V_{A-B} starts to oscillate with a higher magnitude around a non-zero offset. The contact loss detection algorithm uses this fact as its basis. It continuously checks for contact loss, during manipulation, using the mean and the standard deviation values of the normal deflection signal. Note that the normal forces acting on the cantilever are there regardless of the manipulation direction, which gives us a robust means to add control to nanoparticle manipulation without the complication of 3-D force decoupling.

Algorithm 2 Contact Loss Detection from Normal Deflection Signal

1: Wait for contact.
2: Take the latest N cantilever normal deflection signal data points; calculate their mean and standard deviation.
3: If mean and the standard deviation values are both close to 0, contact is lost.

If contact loss is detected, the tip travels on the same trajectory backwards to relocate the

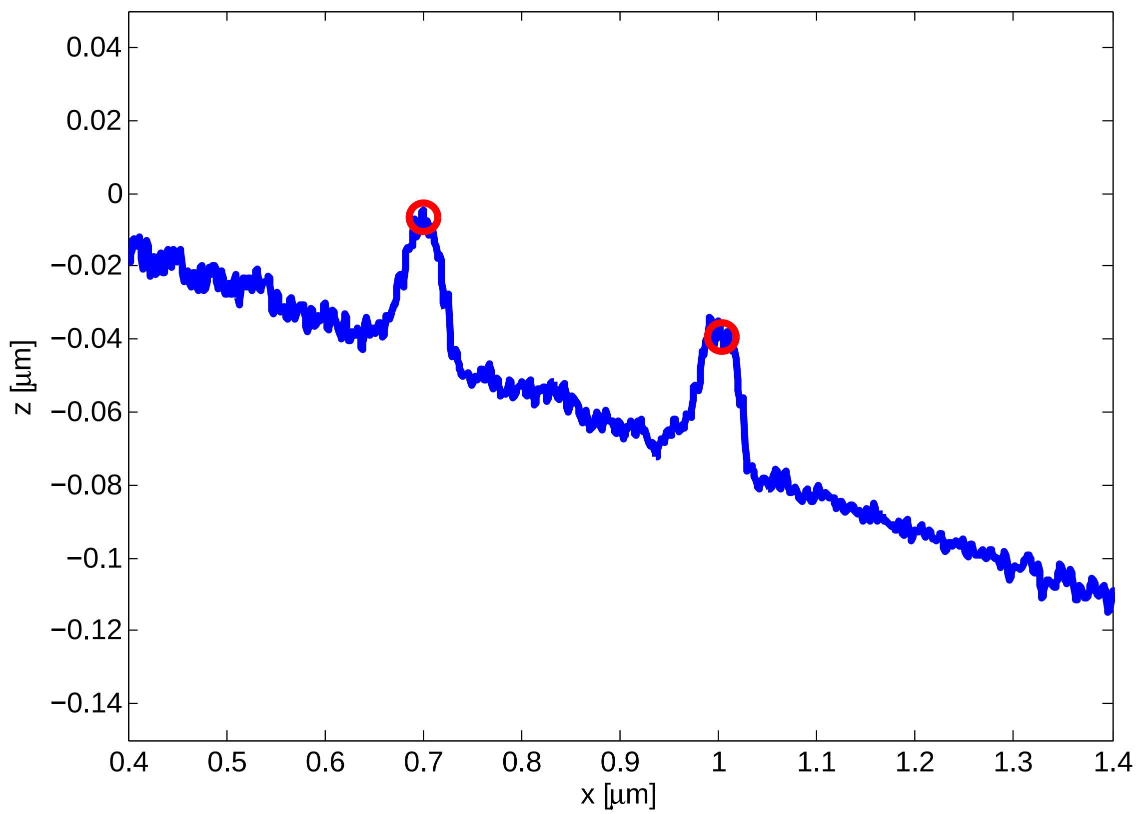

Figure 3.13: Sample experimental AFM line scan data of two close particles; circles indicate the centers of the particles detected using the center detection algorithm. From all detected centers, the one closer to the previous estimate is taken as the actual particle to be manipulated and others are discarded.

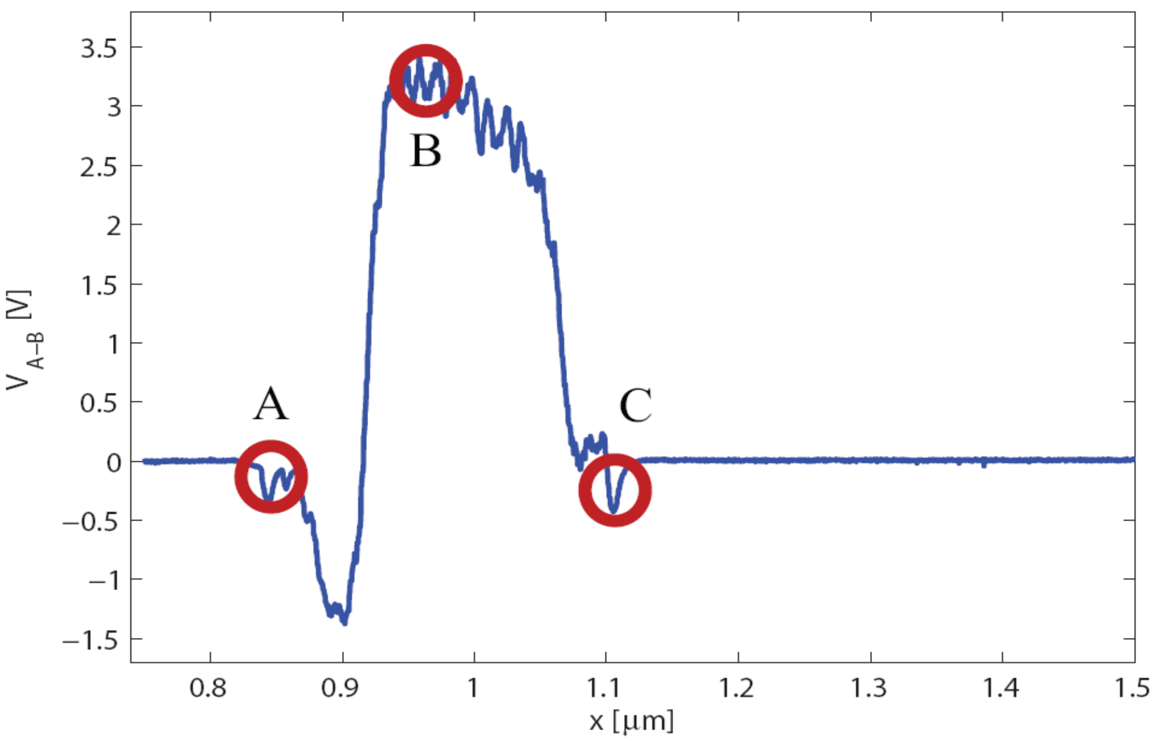

Figure 3.14: A sample experimental AFM normal force data during a particle pushing operation: point A is where the tip and nanoparticle snaps into contact, point B is where tip is jumping over the particle and point C is where the contact loss occurs.

lost particle. This search method is used since the probable reason of contact loss is due to the tip jumping over the particle and not the particle spinning off the tip. Therefore, the particle is likely to be left on the trajectory. In all our experiments, we never encountered a case where the particle is not found on the backwards manipulation trajectory. The overall algorithm runs in a loop until the final particle positioning error drops below a threshold value, which is defined as 100 nm in this case study.

Manipulation experiments are conducted using this procedure. Figures 3.15 and 3.16 show sample 10 μm x 10 μm AFM images demonstrating results of the autonomous nanoparticle manipulation method. As seen from Fig. 3.16, it is possible to manipulate nanoparticles one by one to target positions and achieve patterns. The problem with this approach is that it has an implicit requirement to take another AFM image (about 2 minutes) after each manipulation operation, which slows down the overall speed, considerably.

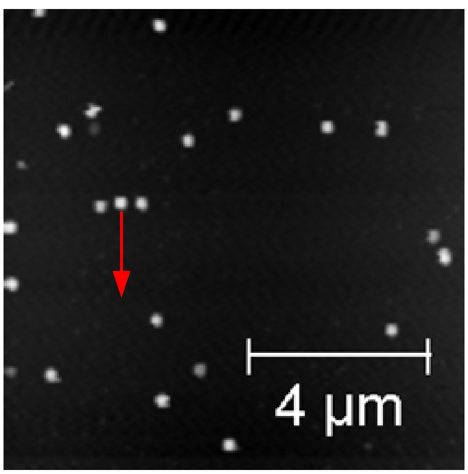

(a)

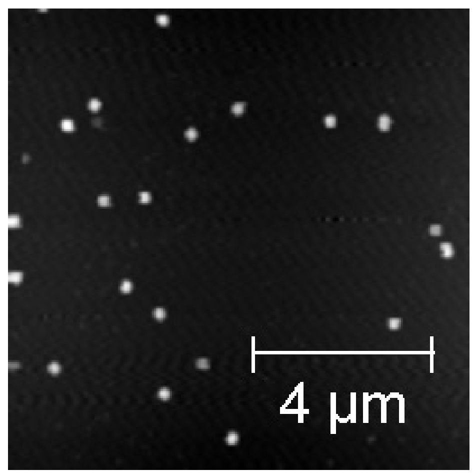

(b)

Figure 3.15: (a) Before and (b) after manipulation of a 100 nm diameter gold nanoparticle indicated by the arrow. It is possible to manipulate a particle without disturbing the close neighbor particles.

During preliminary experiments, it is realized that the manipulated particles are sometimes pulled instead of being pushed. During the manipulations that are achieved by pushing, the final tip positions are behind the particles. The V_{A-B} signal has a positive offset during pushing which

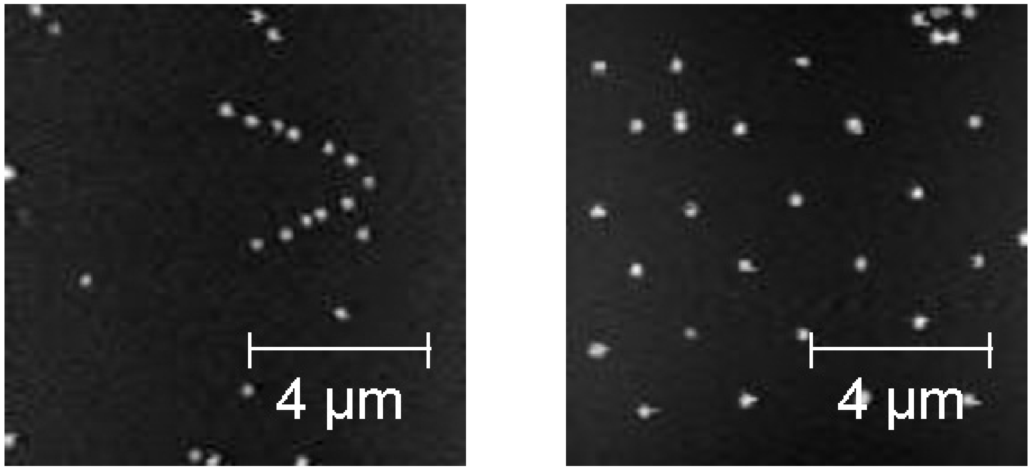

Figure 3.16: Two resulting sample patterns after a sequence of autonomous single particle manipulations.

simply means that the cantilever is pushed up by the particle.

On the other hand, during the manipulations that are achieved by pulling, the final tip positions are in front of the particles that are being manipulated. The V_{A-B} signal has a negative offset in these cases which simply means that the cantilever is pulled down by the particle. Figure 3.17 shows sample V_{A-B} data for pushing and pulling type manipulations.

One significant aspect of pulling is that it is a more stable manipulation technique than pushing. During pushing, the tip can jump over the particle which decreases the stability of the contact between the tip and the nanoparticle. Pulling is a more stable alternative to pushing for manipulation, where it is easier to define the trajectory and final target position of tip to decrease the final positioning error.

3.6 Automated Multiple Particle Manipulation Scheme and Experiments

In Fig. 3.16, it is shown that a sequence of single particle manipulations can be performed to achieve complex patterns of particles. Building upon this individual nanoparticle manipulation

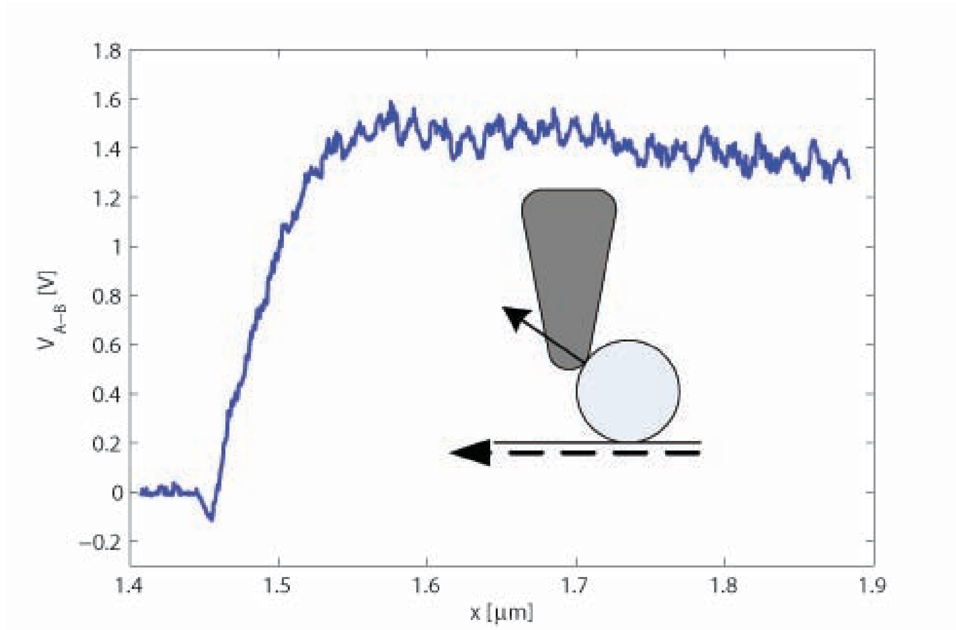

(a)

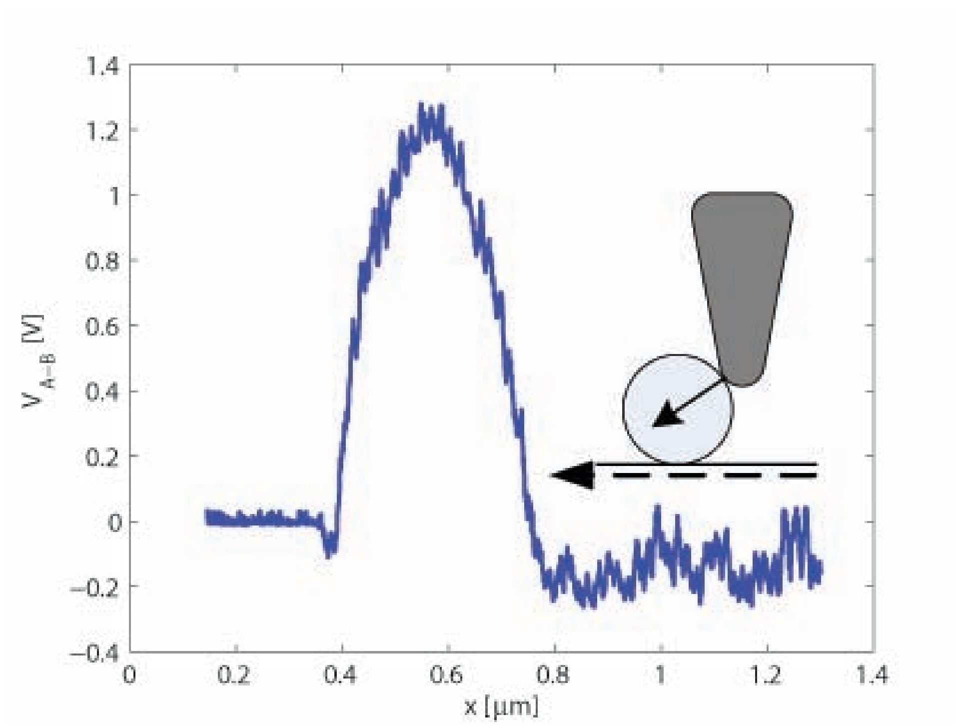

(b)

Figure 3.17: V_{A-B} signal during (a) pushing and (b) pulling. Sample is moving left to manipulate the particle to the right. For pushing, particle exerts on the tip a force directed upwards on the normal direction; for pulling particle exerts on the tip a force directed downwards on the normal direction.

scheme, we perform experiments of multiple particle manipulations. In these operations a commanding task planner [89] is utilized to order individual manipulation operations for maximum efficiency.

Briefly, the task planner assumes linear manipulation trajectories of individual particles and has the objective of minimizing obstacles to these trajectories. Calculating the number of blockages each particle and target position cause to all potential trajectories, the planner pairs the particle that intersects the most number of trajectories to the target position that cuts the minimum number of potential trajectories. This approach takes the most "problematic" particle to the least interfering position. If there are two candidate particles to a target position, the closer one is manipulated.

Figure 3.18 displays the flow of our multiple nanoparticle manipulation procedure. First, a non-contact mode AFM image of the sample is taken and the particles are detected. Next, the user inputs the target positions. The task planner assigns the particles to be manipulated and the target positions at this time and the program starts to form a loop. The single nanoparticle manipulation procedure is run for each particle-target pair and the target positions that are filled are deleted from the target positions array.

However, nanoparticle manipulations are not always successful. If the manipulation fails due to strong adhesion of particle to the sample or to the tip, the particle is discarded and the task planner assigns a new particle for that target position. The program realizes the strong adhesion problem between the tip and the particle if the particle vanishes from the images or line-scans when the tip was in contact with the particle. The particles that get stuck to the surface are detected if the particle would not move more than 20 nm in 4 manipulation trials and is taken as just an obstacle after that. The manipulation program finishes after all of the target positions are successfully filled with nanoparticles.

The addition of a task planner for multiple particle manipulation allows us to remove the overhead of taking intermediate AFM images between each manipulation operation. All particles are

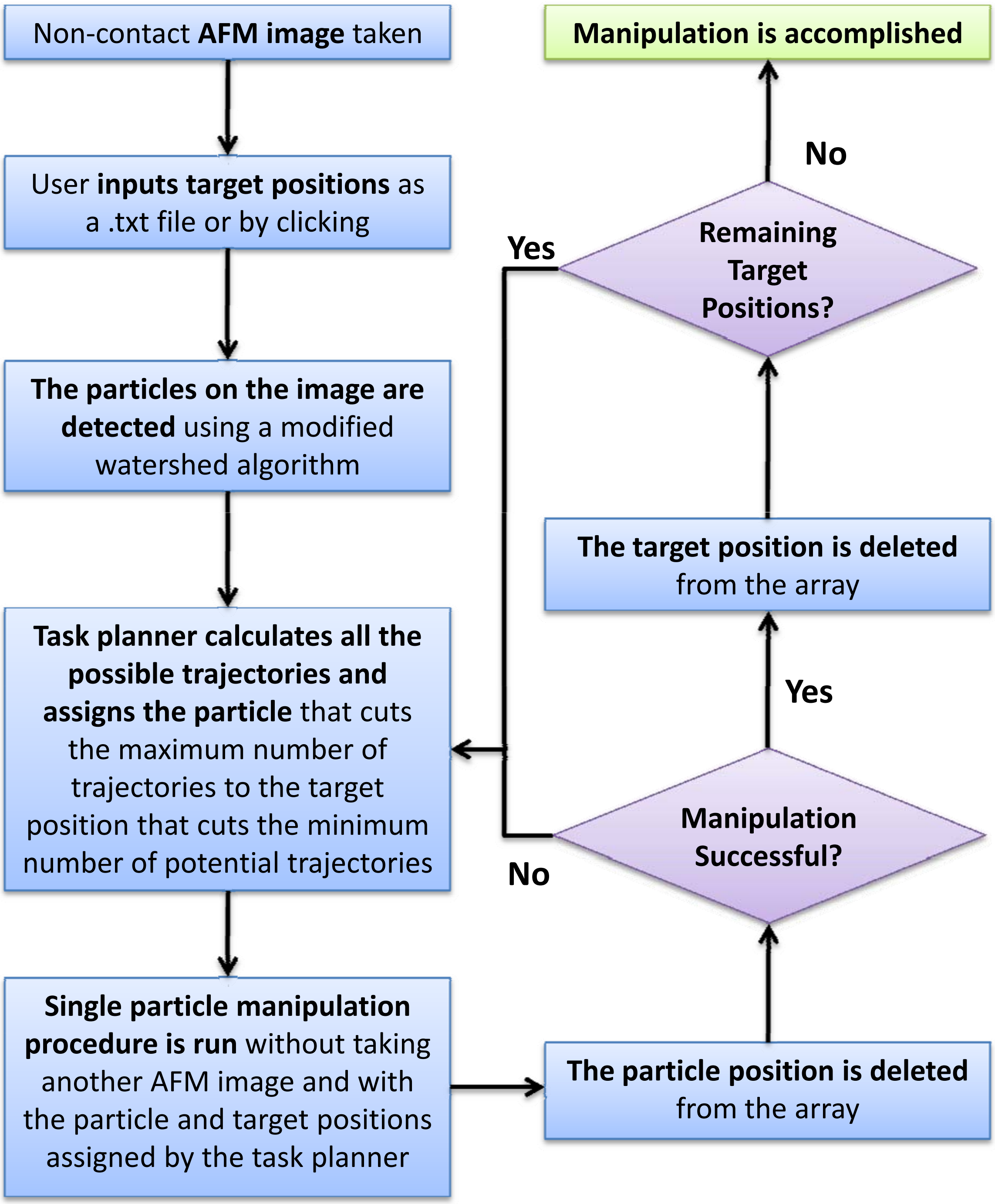

Figure 3.18: A flowchart description of the automated multiple nanoparticle manipulation algorithm.

detected using a modified watershed algorithm [37], autonomously paired with target positions, and individual manipulations are performed in order. Figures 3.19 and 3.20 demonstrate results of proof-of-concept multiple particle manipulation experiments. Five and six nanoparticles are autonomously positioned in a line assembly and a pentagonal arrangement, respectively. Average manipulation time is about 1 minute per particle.

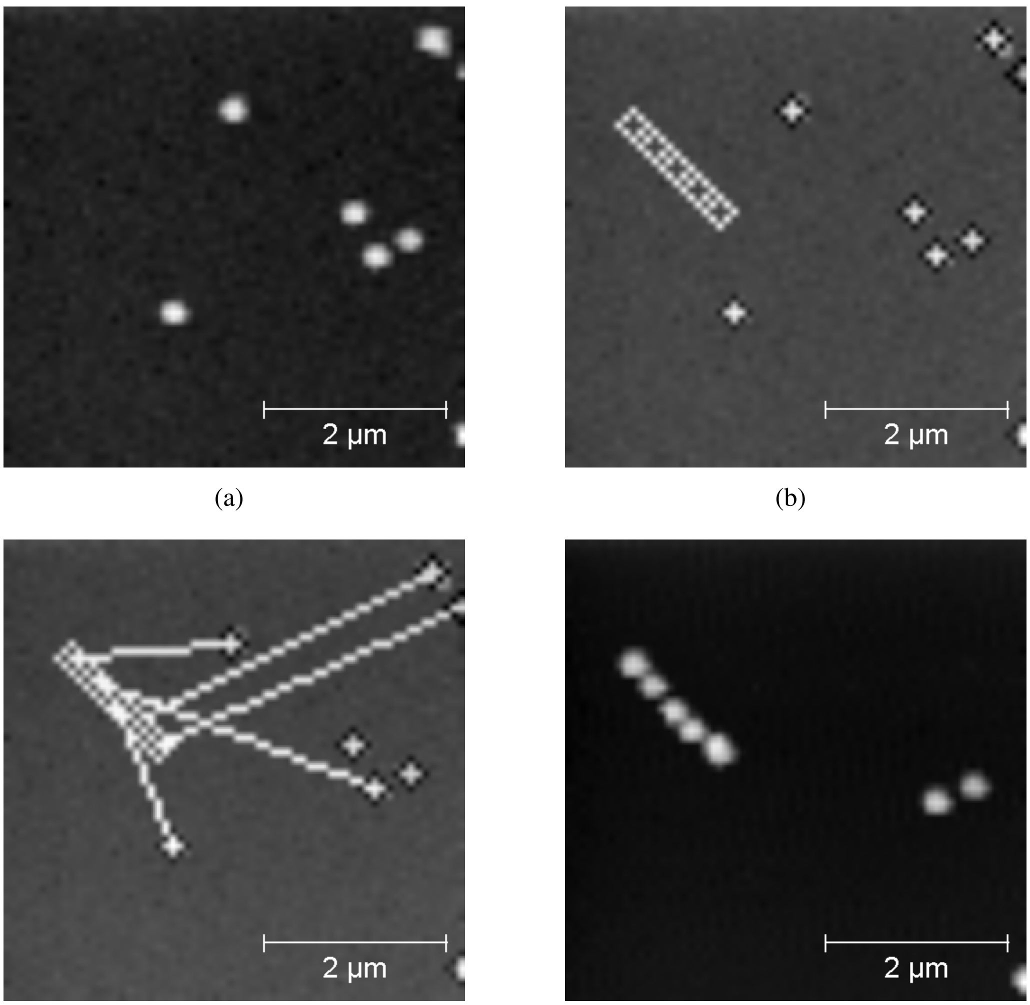

(a) (b) (c) (d)

Figure 3.19: Automated manipulation of five nanoparticles to form a linear assembly. An initial image is taken in (a). All particles are detected using a watershed algorithm and the target positions are given to the program in (b). Task planner decides which particle will be manipulated to which target position in (c). A final image after the experiment is shown in (d).

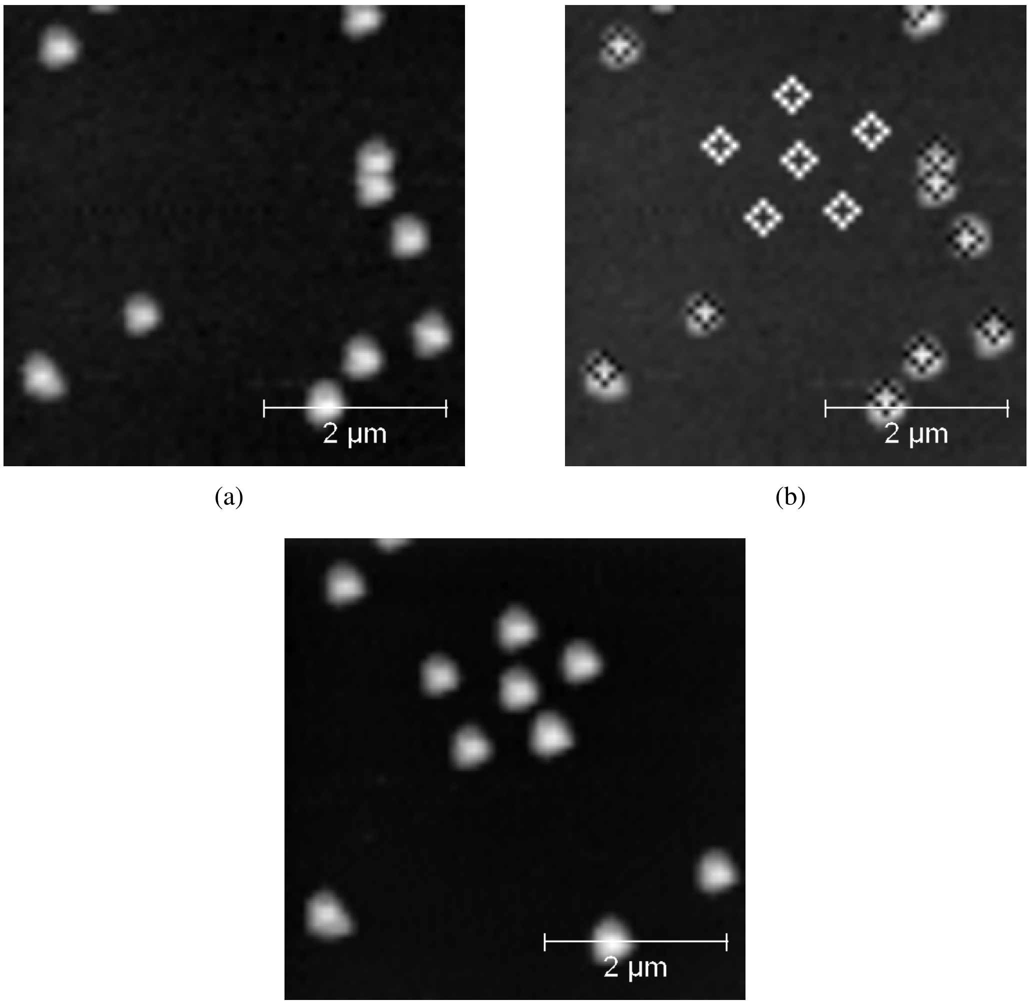

(a) (b) (c)

Figure 3.20: Automated manipulation of six nanoparticles to form a pattern that cannot be formed with a distance based planner. An initial image is taken in (a). All particles are detected using a watershed algorithm and the target positions are given to the program in (b). Task planner decides which particle will be manipulated to which target position. A final image after the experiment is shown in (c).

3.7 Performance Analysis

In addition to the discussions above, the performance of an autonomous manipulation system should be investigated; therefore, an experiment plan is established to observe the performance under two metrics. First of all, the overall success rate of the system is determined. 50 different nanoparticles are tried to be manipulated and the outcomes are grouped into 3 categories. 86% of all manipulation trials ended up with success. The particles in this category are positioned with a final error lower than the positioning error threshold of 100 nm. In 6% of the manipulation trials, the particles cannot be moved at all. In 8% of the trials, nanoparticles got stuck on the tip, which resulted with the loss of the nanoparticle and the contamination of the tip, which causes distortions in the successive images due to tip convolution. The tip is mechanically cleaned after those trials to continue experiments.

The particles that cannot be moved at all were observed to be smaller than the manipulated ones. Particles with 90-120 nm height can be manipulated easily whereas particles whose height is between 50 nm and 70 nm cannot be moved at all.

Besides overall success rate, the performance of the successful manipulations is also evaluated by calculating the speed and final positioning error of the manipulations with different angles and different distances. Final positioning error is defined as the actual distance between the target position and the particle center position after the last run of manipulation. Speed is defined as the ratio between the distance of the manipulation and the time elapsed during the manipulation. Since there is a finite amount of jobs to do before manipulating a particle, the speed was expected to increase as manipulation distance increases.

Figure 3.21 shows the variation of positioning error and speed for different pushing angles. As can be seen from the plots, positioning error and speed have no correlation with the pushing angle, as expected. Figure 3.22 shows the variation of final positioning error and speed for different manipulation distance. As seen from the plots, the speed increases with the distance due to the overhead operations but positioning error has no correlation with manipulation distance.

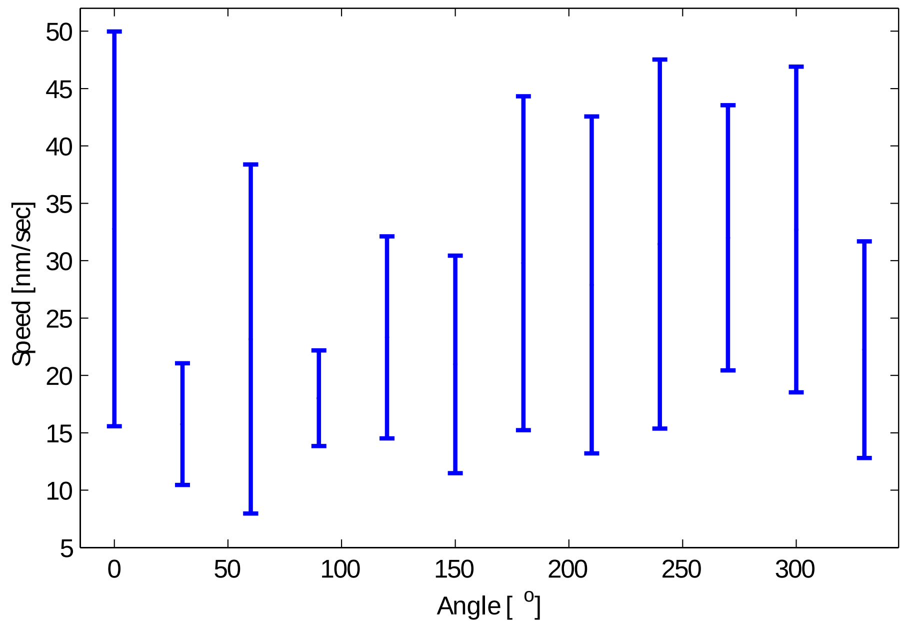

(a)

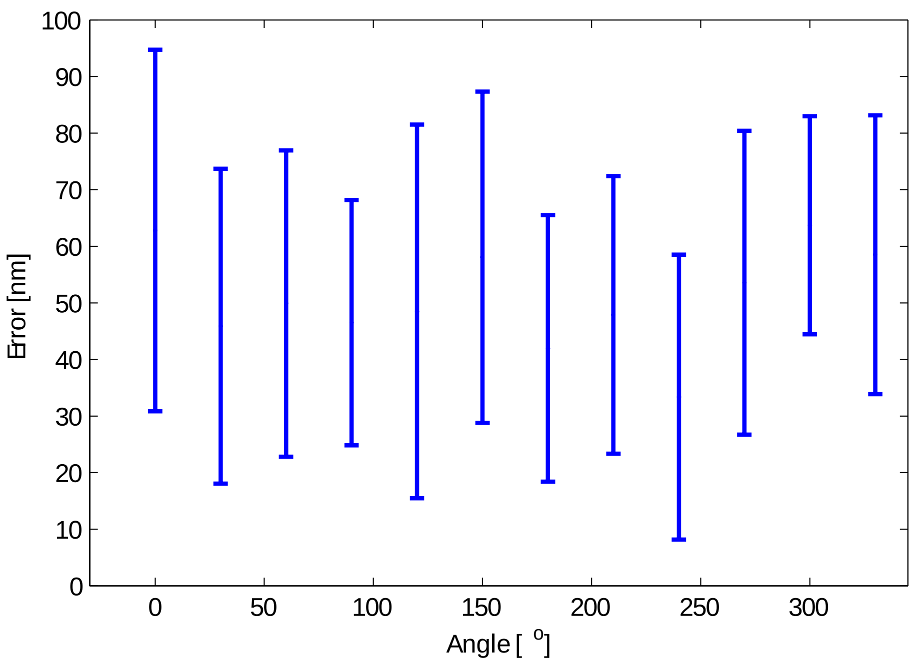

(b)

Figure 3.21: Average manipulation speed (a) and final positioning error (b) results for 12 different manipulation angles using 5 data points for each angle.

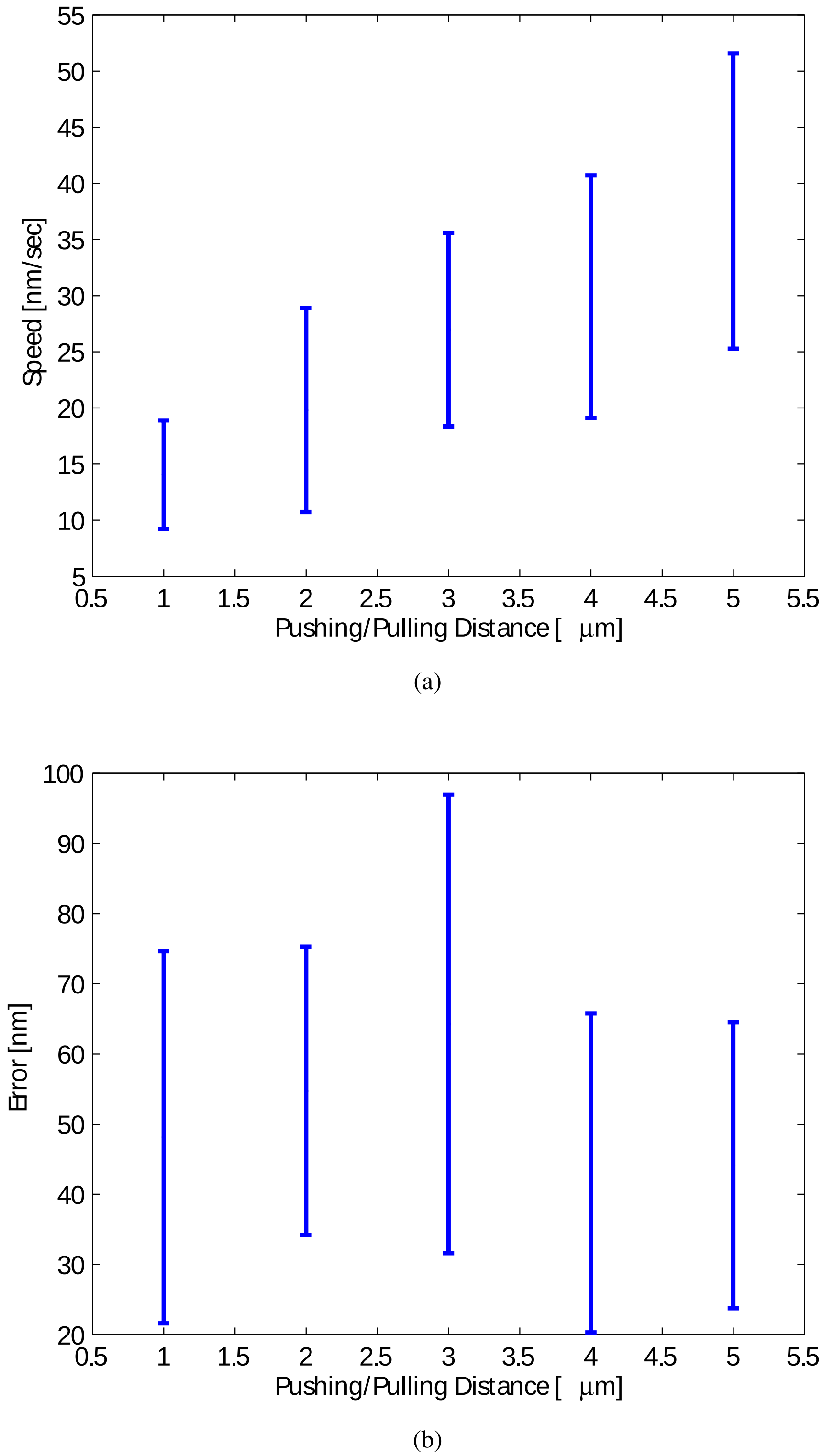

Figure 3.22: Average manipulation speed (a) and final positioning error (b) results for 5 different manipulation distances using 12 data points for each distance.

The absence of correlation between the pushing angle and the performance parameters shows the reliability of manipulation procedure for all angles. The speed increase in longer manipulations is due to overhead operations and demonstrates that the manipulation procedure does not need to divide a long manipulation into smaller steps. This is a direct outcome of detecting the contact loss between the tip and the particle in comparison to blind manipulation.

3.8 Tip Contamination

As the AFM probe gets used more and more, it gets contaminated from the PLL and nanoparticles and it becomes blunter due to the interaction forces it experiences during AFM operation and manipulation. This contamination and becoming blunt affects the manipulation in two ways: it enables pulling operation and it makes the tip harder to lose contact with the particle after the manipulation is conducted.

Figure 3.23(a) shows the AFM probe tip after it is used for 6 months for nanoparticle manipulation operation. The accumulation extending from the probe tip is a combination of PLL and nanoparticles collected by the tip during manipulation procedure. This accumulation changes the geometry and material properties of the tip, causing it to become blunter and stickier. Figure 3.23(b) shows an AFM image of the nanoparticle sample using a new, sharp probe tip. As a result, the nanoparticles look small and spherical. On the other hand, after the contamination, the particles appear larger and non-spherical, as can be seen in Fig. 3.23(c). This is due to the fact that the AFM image is a convolution of the probe tip and the surface topography other than only being topography. Hence, the result in the tip geometry reflects itself on the topography images.

Other than its effects on imaging, contamination also results in positive and negative effects on manipulation. The first major problem is its effects on modeling the manipulation. Our model takes into account the change of probe material after contamination. The contamination causes the probe tip to be covered with PLL and our model assumes the tip material is PLL in terms of adhesion. However the model does not take into account the change in the geometry.

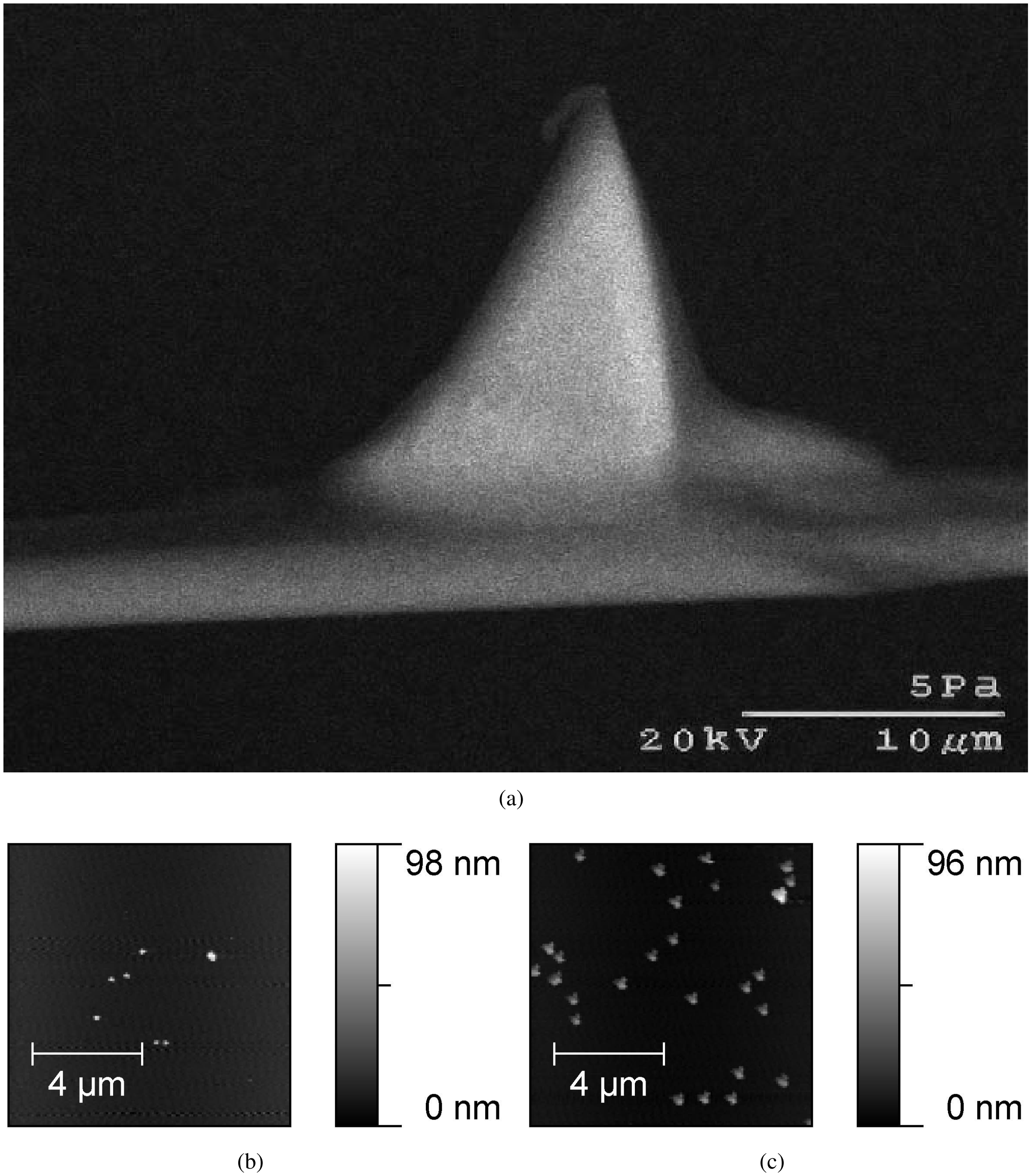

Figure 3.23: (a) SEM image of a AFM probe tip that is used for nanoparticle manipulation for 6 months. (b) A 10 μm x 10 μm non-contact mode AFM image of nanoparticle samples deposited on PLL covered mica taken with a clean AFM probe tip. (c) A 10 μm x 10 μm non-contact mode AFM image of nanoparticle samples deposited on PLL covered mica taken with a contaminated AFM probe tip.

The geometry of the probe tip assumed in the model is conical, hence can be approximated with a sphere. However the contamination is unpredictable and the shape of the tip after the contamination will no longer be conical. We believe this is not a very significant problem since smooth shapes can be approximated with spheres and contamination will likely result in a smooth shape.

A second problem arises from the increase in the adhesion force between the probe tip and the particle. For a successful manipulation, the adhesion between the tip and the particle should be lower than the adhesion between the particle and the surface, so that the tip can pull-off contact from the particle after positioning is finished. However, the contamination results in tip getting stickier and blunter, which results at a higher adhesion force between the particle and the tip. Hence, more particles get stuck to the tip during manipulation processes when contaminated probes are used.

On the other hand, contamination has one advantage on the manipulation process. When started with a clean sharp tip, the adhesion between probe tip and the nanoparticle is not strong enough to cause pulling. Our pulling trials became more and more successful in time, mainly due to the increase in the adhesion between the tip and the particles caused by this contamination. Therefore, a slight amount of contamination on the probe tip, which causes enough adhesion between the tip and the particle for pulling is desired as long as the adhesion does not become too high to prevent loss of contact between the particle and the tip after manipulation.

3.9 Summary

This chapter demonstrated an automated 2-D nanoparticle manipulation procedure using an AFM system. Particles are imaged using dynamic mode AFM. A particle and a target position are selected by the user and the particle is manipulated autonomously. Robust particle center detection and contact loss detection algorithms are developed to overcome speed and reliability issues of AFM based nanomanipulation. Unlike blind manipulation techniques, manipulation distances are not divided into parts artificially to increase the reliability. The physics behind this manipulation system is investigated by modeling the system using contact mechanics. Possible manipulation types and their required cantilever normal stiffness ranges are shown.

Moreover, a fully automated multiple particle manipulation program that does not need to take AFM images in between individual nanoparticle manipulation attempts is demonstrated. A task planner, which minimizes the number of obstacles for efficiency is utilized for these experiments. The performance of the designed manipulation system is presented with statistical data.

Designing and implementing a fast and reliable technique for multiple particle manipulation could increase the use of AFM for micro/nano-manufacturing applications where AFM might be less expensive than other techniques that are currently used for nanofabrication. Although AFM based nanoparticle manipulation is slow for mass fabrication or manipulation, we believe that forming nanofabrication masks and templates for plasmonic, optoelectronic or MEMS/NEMS devices would be possible using these types of procedures. Manipulating nanoparticles into predefined positions could also potentially be used for gluing or soldering at the nanoscale.

The work performed on automated AFM based nanoparticle manipulation that is presented in this chapter of this thesis is considered to be complete. At this point, we are not proposing any future work on this topic.

Chapter 4

Electrical Non-contact Manipulation of Surfaces

4.1 Introduction

Modification of the surfaces through non-contact electrical interactions results in smaller structures compared to mechanical contact manipulation, but limits the substrate to semi-conductors or conductors. Manipulation of single atoms have been demonstrated in literature [32] using an STM in low temperature environment that presented the possibility of nanometer, or even sub-nanometer scale manipulation, which cannot be achieved using AFM based contact manipulation techniques. However, single atom manipulation techniques require low temperature environments, hence adding another selectivity criterion which is not desired in a viable manipulation technique. On the other hand, performing such a manipulation technique in ambient environment results in structures that are still often smaller than the ones AFM based contact manipulation can achieve [70], which forms the main topic of this chapter.

The conventional techniques for electrical surface manipulation often utilize standard STM tips and scanners for manipulation. During the operation, the sample is imaged using constant current mode STM, and then various gaseous species are introduced to the environment and adsorbed onto the substrate surface, if needed. After this dosing, the surface is often imaged a second time, in order to ensure global coverage. Following this scan, a desired pattern and manipulation parameters are inputted to the control software by the operator. A series of short consecutive voltage pulses or a constant high bias voltage is applied between the STM tip and the surface while the tip scans the desired pattern to manipulate the surface. This last step is often carried out without the vertical feedback to ensure that the scanner will not respond to the manipulation operation and the tip-surface distance stays constant. As the last step the surface is imaged again to verify the manipulation. This sequence is repeated until the surface changes as required. This process is slow due to the large number of images taken and requires significant input from the user. Long processing times and significant user input required make this process industrially not viable.

The case study presented in this chapter aims to create a viable system for electrical non-contact manipulation of surfaces using STM and conductive AFM (CAFM) principles with different end-effectors. In order to solve the problems of electrical manipulation stated above, we will model the underlying principles of the STM operation and manipulation, and use this model to design algorithms and techniques to increase manipulation speed of electrical manipulation. We will present a complete model of the STM based manipulation system that includes contact mechanics models and non-contact van der Waals and electrostatic force models, scanner dynamics, tunneling current model and a control system that uses the tunneling current to control the end-effector position. Beyond modeling current STM based nanomanipulation systems, non-contact, electrical nanomanipulation is proposed using stiff, conductive AFM cantilevers as STM end-effectors. This will enable parallel manipulation using multiple probe tip arrays, thereby decreasing processing time and possibly eliminating a hurdle to industrialization. A schematic of this operation is shown in Fig. 4.1.

Another advantage of utilization of conductive AFM probes as electrical manipulation end-effectors is the ability to image in AFM mode. Most electrical manipulation systems suffer

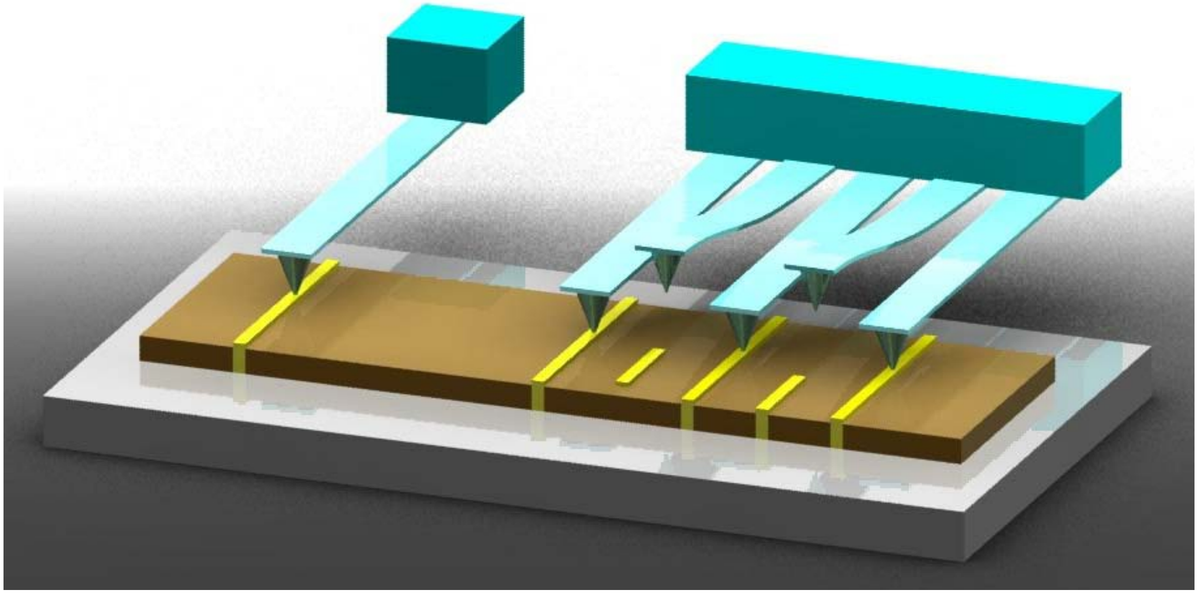

Figure 4.1: Imagined electrical manipulation operation using compliant cantilever probe arrays.

from the selectivity of their end-effectors. When STM tips are utilized, the surfaces imaged and manipulated has to be conductors or semi-conductors. On the other hand, when CAFM probes are used, a heterogeneous surface that has insulators, conductors and semi-conductors on the same sample can also be imaged and manipulated using electrical principles because imaging can be conducted in AFM mode and manipulation can be carried in CAFM or STM mode.

In order to enable the utilization of AFM cantilever as STM end-effectors, the model will be extended to include cantilever dynamics and feasibility of this utilization will be demonstrated on simulation results and STM images. The model will be verified with experiments and manipulation using high electric fields and short electrical pulses will be demonstrated. Moreover, the effects of set-point force and bias voltage on written features will be investigated through experiments. We believe the models and experiments in this work will provide enough information to achieve multiple probe array operation for electrical nanomanipulation of surfaces.

4.2 System Description

In this case study, two identical SPM systems are used with the single difference of operation environment. For manipulation of silicon surfaces using short electrical pulses, a RHK brand ultra high vacuum SPM is used. For manipulation of titanium surfaces using high electric fields, a RHK brand ambient SPM is used. These two SPMs are identical for all controls purposes; therefore the microscope will only be presented once. A custom control system is also designed and a software to control the SPMs are written which is also discussed in this section.

4.2.1 RHK SPM1000 Scanning Probe Microscope

Figure 4.2 shows the UHV-SPM system that will be used for electrical non-contact manipulation of surfaces case study. This system is designed and built by RHK Technology, Inc. Troy/MI in cooperation with researchers from Institute for Complex Engineered Systems (ICES) of Carnegie Mellon University (CMU). This system consists of four chambers: load lock, analysis, preparation and SPM chambers, that are all operating under UHV. The system is on a pneumatic table, which supplies vibration isolation to the system from outside environment. The gases in the chambers are pumped out by a three stage pumping system which consists of rough pumps, which lower the gas pressure inside the chambers down to 10^{-3} – 10^{-4} Torr, turbo pumps, which lower the gas pressure down to 10^{-7} – 10^{-8} Torr, and ion pumps, which lower the gas pressure down to UHV values that are 10^{-9} – 10^{-11} Torr. The samples are loaded inside the UHV system from the load lock and stored in the preparation chamber. The preparation chamber is also used for some of the sample cleaning procedures. The sample surfaces are chemically analyzed in the analysis chamber using several different spectroscopy techniques like Auger electron spectroscopy or X-ray photoemission spectroscopy. In addition to these chambers, the SPM chamber has an SPM which can perform as an STM or AFM, capable of atomic resolution UHV SPM imaging of sample surfaces.

Figure 4.3(a) shows the picture of the assembled system. The chamber marked by the red

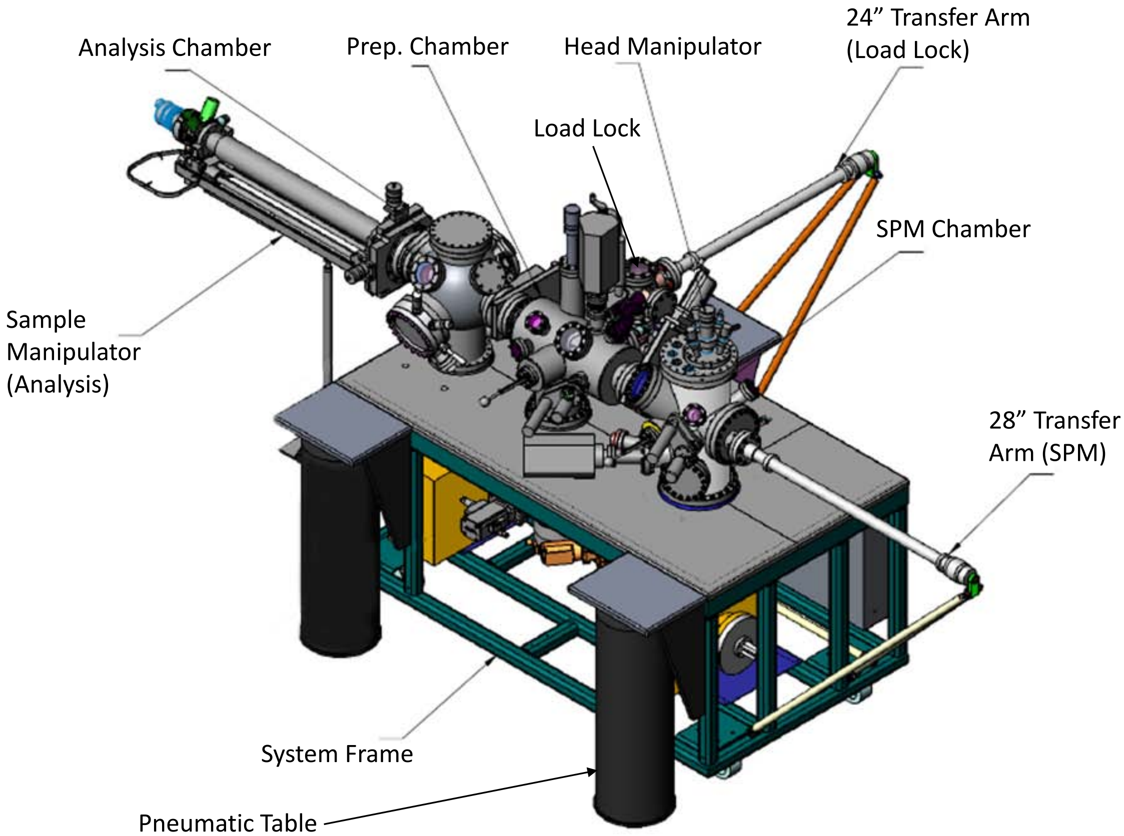

Figure 4.2: Schematic of the UHV-STM System that will be used in this case study. The chambers are sealed and the gases inside the chambers are pumped using rough, turbo and ion pumps to decrease the pressure to UHV levels (10^{-9} Torr and below). The load lock chamber is where the samples and tips are loaded inside the UHV chamber, prep. chamber is where the sample preparation procedures executed, analysis chamber is where the samples are analyzed using several surface chemistry analysis tools such as X-Ray Photoemission or Auger spectroscopy and SPM chamber is where the images of the sample are taken and the manipulation operations are carried using STM. The transfers between the chambers are conducted using the transfer arms. The chambers are suspended on pneumatic legs to isolate the system from outside vibrations.

oval is the SPM chamber, the chamber that is of interest for our work. The view of the SPM inside this chamber from a window of the UHV system is shown in Fig. 4.3(b). The part hanging from the ceiling of the SPM chamber is the SPM scanner and marked by red oval. The sample stage is marked by green rectangle and is the stationary part in the chamber where the sample holders, which are shown in Fig. 4.3(d) are putted on. This part is connected to the ceiling of the SPM chamber via springs which provides extra vibration isolation. Figure 4.3(c) shows a close-up view of the SPM scanner. The tip holder, which is the part where the SPM end-effector is assembled, is inserted in the piezoelectric stack actuator of the scanner. The tip holder is held in the stack actuator by mechanical fittings. This stack actuator provides the vertical motion necessary for scanning. During SPM operation, the SPM scanner is lowered down until its legs are touching to the ramps on the sample holder. The scanner legs are piezoelectric tube scanners that can bend to move the tip. During imaging, the three legs bend synchronously to create the small raster scan motion. The range of this motion is 5 μm. To position the tip coarsely in lateral and vertical directions, the legs "walk" on the ramp by using a stick-slip motion generated by a saw tooth wave type voltage input. This coarse movement of the scanner is observed through a camera view and remotely controlled from outside by an operator. This scanner does not have any positioning sensors.

The ambient SPM used in this case study is identical to the SPM chamber of this UHV SPM, without any pumps assembled to its chamber. They are mechanically the same and can be controlled using the same RHK controller without any changes to parameters.

4.2.2 Custom Control System and Oscan V2.0

The RHK SPM systems will be controlled using two controllers: RHK's own XPM100 controller and custom design, control system. XPM100 is a regular SPM controller with good resolution however it lacks flexibility, random path generation functions and speed. It is designed for SPM imaging but it does not allow users to input arbitrary paths for manipulation and it does not have

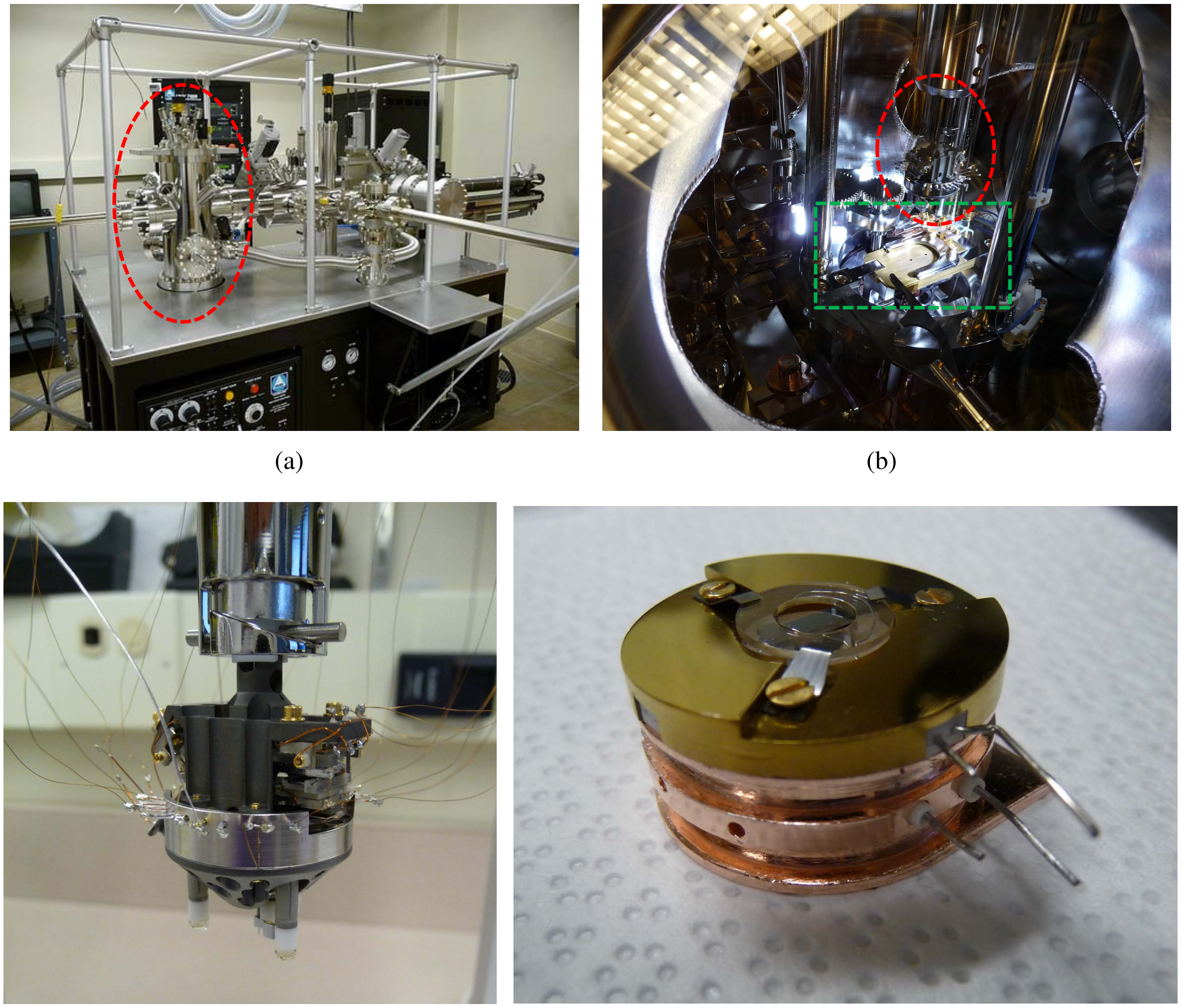

(a) (b) (c) (d)

Figure 4.3: Pictures of RHK make UHV-STM system. (a) The completed UHV-STM system. The chamber inside the red oval is SPM chamber. (b) A view of the SPM from a window of SPM chamber. The part enclosed with green rectangle is the sample stage where the samples in specifically designed sample holders (picture (d)) are held during operation. This part is suspended in air using springs attached to the chassis of the chamber to improve vibration rejection. The part enclosed with a red oval is the SPM scanner. (c) Close-up view of the SPM scanner. The legs underneath the scanner with glass sphere ending are tube scanners which produces the motion of the scanner. (d) Specifically designed sample holders. The SPM scanner is released on the sample holder during operation. The glass spheres on the end of the tube scanners are in contact with the ramps on the sample holder. To achieve coarse positioning in x, y and z directions, the scanner “walks” on the ramps via stick-slip type motion.

an application programming interface or scripting language that would allow users to generate their own procedures. In addition, its control loop bandwidth is not high enough to support tip speeds higher than 2 $\mu m/s$. In order to solve problems of speed and flexibility, we designed our custom controller whose schematic is shown in Fig. 4.4.

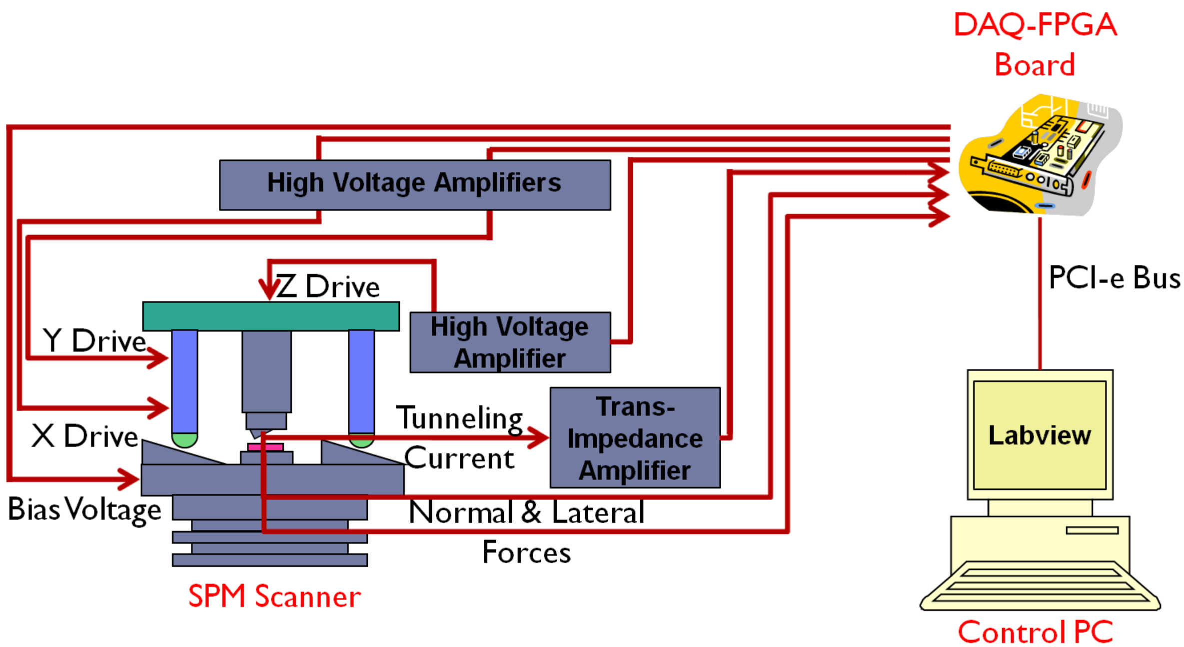

Figure 4.4: Schematic of the custom SPM control system. The SPM will be commanded using a windows based PC that runs LabView. The signals are read and written from a data acquisition board (DAQ) connected to the computer. The DAQ also has a Field Programmable Gate Array (FPGA) on it for on-board processing, to increase control speed. The maximum data acquisition speed achieved is around 400 kHz. The control signals are generated using this FPGA board and sent to the piezoscanner after being amplified at the analog high-voltage amplifiers. The resulting tunneling current, normal force and lateral force data is read and sent as feedback to the FPGA. The bias voltage is also output from the DAQ board.

In the custom control system, the SPM stages and the bias voltage are driven by the signals that high voltage amplifiers are outputting. The high voltage amplifiers have a bandwidth of 30 kHz with a gain of 20 (A.A. Lab Systems A301). The signals going into the amplifiers are generated from a Field Programmable Gate Array (FPGA) that is on an FPGA based DAQ board (National Instruments PCIe-7852R). This board is connected to a Windows 7-based 64 bit PC (Control PC) via PCI-express slot, and is programmed using LabView 2009 and LabView FPGA module. Z-scan and z-offset signals coming out of high voltage amplifiers are sent directly to the scan head whereas x and y voltage signals are sent to a programmable relay box (RHK PPC200) that generates all the signals required to run x and y actuators. The tunneling current is measured by using a trans-impedance amplifier (TIA) built by RHK, and is read by the FPGA based data acquisition board to form the feedback loop necessary for the STM operation. In addition to this, normal force and lateral force signals generated by the laser and the photo diode is read by RHK PLLPro AFM controller and sent to the DAQ board. These signals are used to form the AFM operation mode controller. The total data acquisition rate of the system is 400 kHz. The control bandwidth of the RHK STM system is expected to be around 30 kHz which will be limited by the bandwidth of its high voltage amplifiers.

Custom control system is commanded via SPM software that we have coded in LabView and named after its creator as Oscan V2.0. As promised, the new custom control system and its software can operate at faster speeds (upto 36 $\mu m/s$) with no to very little degradation on image quality. Figures 4.5(a) and 4.5(b) shows an AFM image taken at 4 $\mu m/s$ and 36 $\mu m/s$ speeds with almost no difference in image quality. In addition, the new control system can switch between the AFM mode and STM mode instantaneously which allow us to work on electrically heterogeneous surfaces. Figure 4.5(c) shows imaging and manipulation on a titanium structure deposited on silicon dioxide. Imaging is done in AFM mode since the silicon dioxide part of the surface cannot be imaged in STM mode; however STM mode is used for oxidizing the box on titanium. Both operations are conducted back to back using a conductive AFM probe, RHK ambient SPM, custom control system and Oscan V2.0. In addition to these superiorities over RHK controller, our custom controller can also conduct manipulation operation on arbitrary paths. Figure 4.5(d) shows “DARPA TBN” letters oxidized on a titanium film using STM mode manipulation and AFM mode imaging. Total operation takes around 80 seconds. RHK controller was not able to generate these arbitrary paths but can write single lines. Same pattern can be oxidized using RHK controller by dividing the pattern into linear paths, but the operation takes around 30 minutes.

All of the experimental results presented in this chapter are taken using RHK SPM, specified above. During these experiments, the RHK system is controlled either with its dedicated controller and software or custom control system and Oscan V2.0 software. More information on the SPM, custom control system and Oscan V2.0 can be found in Appendix A.

4.3 STM Imaging with Atomic Resolution

Si(100) is the main substrate that is used throughout this case study. Before loading the Si(100) samples in the UHV system, the samples are cleaned by submerging the substrate inside acetone, isopropyl alcohol (IPA) and methanol for 5 minutes. However, Si(100) is not stable in ambient conditions, i.e. the surface layer atoms of Si(100) bonds with the oxygen in the air and forms native oxide on the surface instantaneously, disabling atomic resolution imaging on Si(100). In order to solve this problem, the samples should be cleaned one more time in the UHV chamber prior to imaging. This last cleaning step is called “flashing” the sample [70]. “Flashing” is a cleaning technique that consists of heating the sample to high temperatures for the oxygen, hydrogen and carbon bonded on the surface atoms to desorb, and cooling the sample slowly following the heating step for the atoms to reconstruct the surface. The change of the sample temperature in time during this procedure is shown in Fig. 4.6.

During “flashing” the temperature of the sample is increased to 1250^o C while trying to keep the pressure of the UHV chamber low to prevent contamination of the surface. In order to achieve this dual control, several stops can be made while increasing the temperature. After reaching 1250^o C, the sample temperature is held at this temperature for 1 minute, causing the sample to anneal, release all the oxygen, hydrogen and carbon bonds from the surface atoms, and start reconstructing the surface. After annealing step, the sample temperature is immediately decreased to 900^o C, then the temperature is ramped down slowly until the temperature reaches 700^o C. The time spent at this step is around 12 minutes. This time allows the silicon atoms,

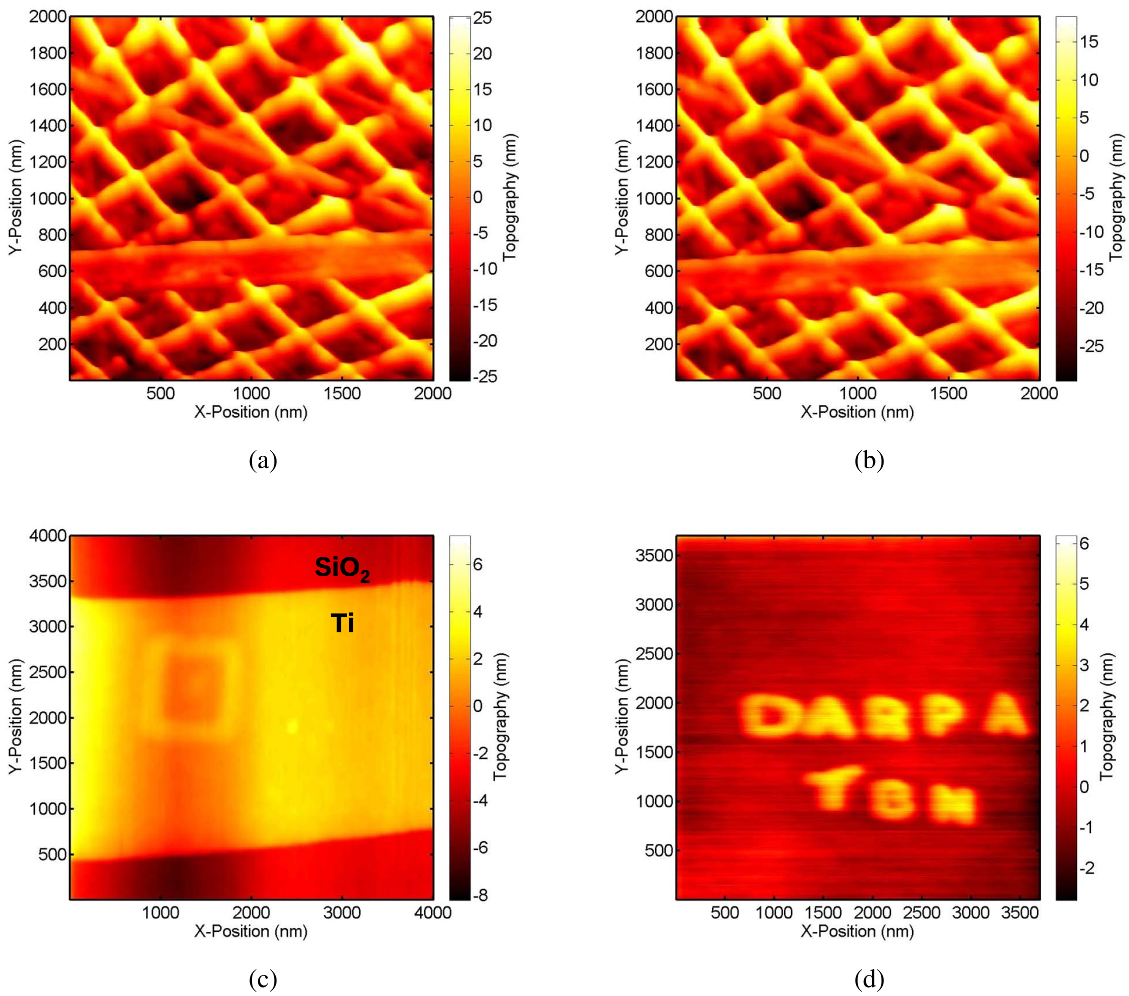

Figure 4.5: Trial images and manipulations conducted using custom control system and Oscan V2.0. (a) An AFM image of a calibration sample taken at 1 Hz/line speed. (b) An AFM image of the same calibration sample taken at 9 Hz/line speed. (c) A box oxidized on a Titanium sample deposited on SiO_2. The box is oxidized in STM mode whereas imaging is conducted in AFM mode because the sample is electrically heterogenous. (d) “DARPA TBN” letters are written on a Titanium film using local anodic oxidization. Oxidization is conducted in STM mode and the surface is imaged in AFM mode.

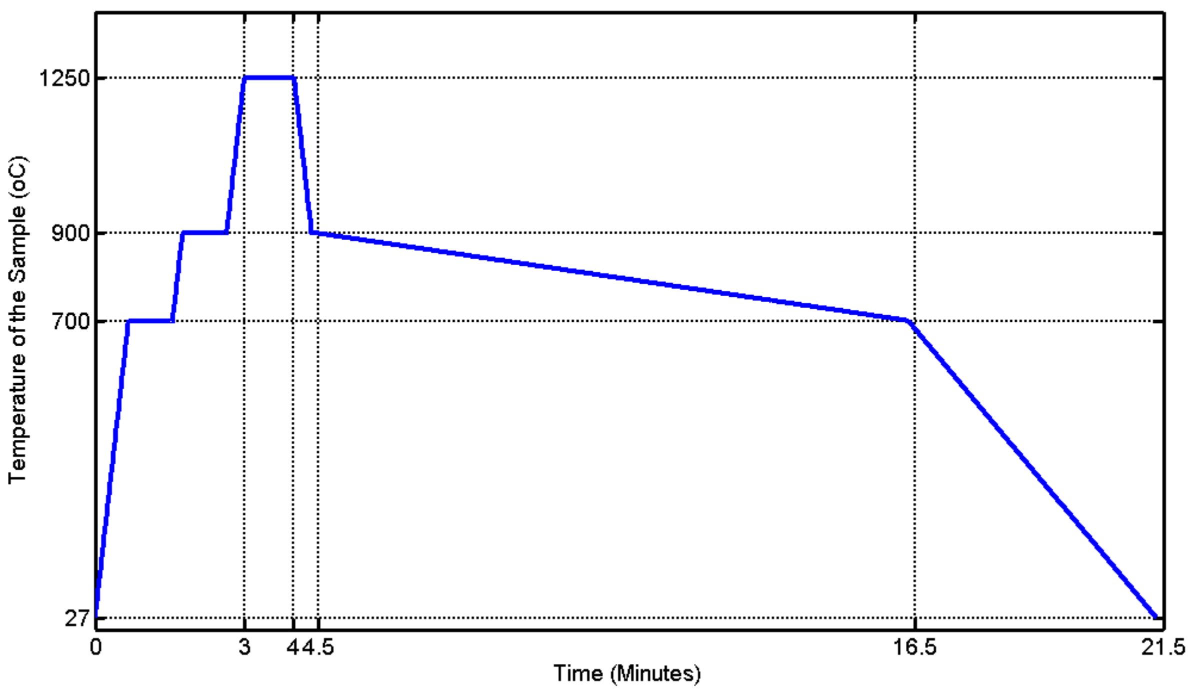

Figure 4.6: Plot showing how the temperature of the sample is changed during the flashing operation. The flat portions at 700^{o}C and 900^{o}C are waiting times for the pressure of the chamber to stabilize below $10^{-}9$ Torr. Then the temperature of the sample is increased up to 1250^{o}C and flashed for 1 minute to clean the silicon surface from hydrogen, oxygen and carbon bonds. The temperature of the sample is then decreased slowly to allow more time for the reconstruction of the surface.

which are mobile due to the sample's temperature, to complete the surface reconstruction. The speed of the ramp is then increased, and the temperature is decreased to room temperature in 5 minutes. The total time spent in the "flashing" process is 20 minutes.

After "flashing" the sample, it is transferred to the SPM sample stage and the SPM scanner is engaged with the sample. During atomic resolution image of a sample, the bias voltage values used are lower than normal scanning voltages in order to decrease tip-sample distance, hence decrease the effective beam radius of the tunneling current. Sharp STM tips should also be used to image in order to prevent suffering from tip convolution effects. An atomic resolution image of Si(100) taken in RHK STM using STM tips is shown in Fig. 4.7(b).

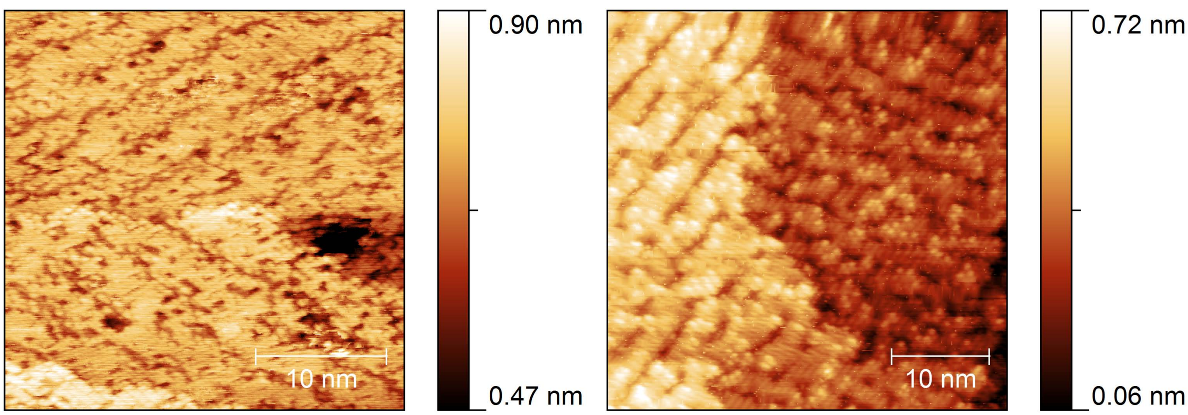

(a) (b)

Figure 4.7: (a) 30 nm × 30 nm STM image of Si(100) surface under UHV with atomic resolution. The image is taken using a diamond coated conductive AFM cantilever with a normal stiffness of 42 N/m and tip radius 35 nm, at bias voltage of 1 V and set-point current of 100 pA. (b) 40 nm × 40 nm STM image of Si(100) surface under UHV with atomic resolution. The image is taken using a Pt-Ir STM tip, at bias voltage of 1 V and set-point current of 150 pA.

The image show dimer rows, the surface construction of Si(100) atoms. A dimer is a pair of atoms that share a bond hence are closer to each other than any other neighboring atoms. Therefore surface construction of Si(100) is often referred as 2×1. These dimer atoms form dimer rows that run all the way on the surface. The image also shows neighbor terraces and atomic steps that form due to the misalignment of the sample while it is prepared by the vendor. The dimer rows in two neighbor terraces are perpendicular to each other which help us recognize atomic resolution images.

To show the feasibility of using conductive AFM cantilevers for STM imaging, we have used diamond coated conductive AFM cantilevers (Bruker AFM Probes, DDESP-10, $k_n = 42$N/m, $R_t = 35$nm) to image Si(100) surface using STM mode of the RHK SPM. The resulting image is shown in Fig. 4.7(a).

To succeed in using AFM cantilevers as STM end-effectors, the cantilever stiffness is chosen very high to avoid snap-into contact with the surface and the tunneling current is decreased slightly to increase the distance between the tip and the surface during operation. As can be seen from resulting images, the dimer rows are observable; however the quality of the image is significantly lower compared to the images taken with an STM tip. On the other hand, this is one of the first images that show atomic resolution STM images can be taken using AFM cantilevers, to the best of our knowledge.

4.4 Electrical Manipulation of Surfaces Using Electrical Principles

Not every surface is electrically modifiable; hence the material selection is important for electrical manipulation. On the other hand, the work presented in this chapter is not about how to modify the surfaces but how to control the manipulation better. Therefore, we chose two standard surface manipulation techniques from literature, hydrogen passivation and tip directed depassivation of Si(100) surfaces, and local anodic oxidation of Ti surfaces. These techniques might be used as alternative methods to MEMS manufacturing techniques for patterning silicon or titanium surfaces or they can be used in tandem with MEMS techniques to create hybrid manufacturing methods, if they are perfected.

4.4.1 Manipulation of Silicon Surfaces Using Short Electrical Pulses

In order to create structures on silicon, it should first be masked, and then the desired structures should be written on the mask at desired locations. Consequently, desired material for the structures should be introduced to the chamber, which would cause deposition of new layers at the desired locations, whereas the non-patterned parts of the mask will protect the silicon underneath it. To achieve this deposition, one needs to satisfy the dangling bonds on the Si(100) surface to stabilize the substrate, i.e. prevent it making bond with other atoms or molecules in its environment. This is considered to be the first step of creating a mask and is called passivation.

In order to passivate the surface, hydrogen gas (H_2) is introduced to the UHV chamber and is broken to atomic hydrogen (H) using a filament at 1500^{o}C. The resulting atomic hydrogen bonds with the surface silicon atoms and satisfies the dangling bonds of Si(100) surface. Any other material introduced the chamber after this step will not bond with the silicon since its dangling bonds are satisfied. After the passivation step, Si(100) surface becomes harder to image since its conductivity drops because of the lack of dangling bonds, however it can still be imaged at atomic resolution. But the resulting image, as can be seen in Fig. 4.8, will be lower quality compared to cleaned and reconstructed silicon surface.

Another detail that should be noted for imaging passivated Si(100) surface is the significance of the bias voltage polarity. While a clean, reconstructed Si(100) surface with dangling bonds is being imaged, the current flows from the tip, passes through the dangling bonds, and flows into the surface. The bias voltage used at this operation should be positive (+), so that the electrons should be tunneling from the tip into the surface. However, when the surface is passivated, the dangling bonds are satisfied and the electron transfer occurs between the tip and the bond between adjacent pairs of silicon atoms. The bias voltage used at this operation should be negative (-), so that the electrons would be tunneling from the surface into the tip [125]. However during patterning the surface, the desired action for the hydrogen atoms on the Si(100) surface is to receive an electron and leave the Si(100), hence, the bias voltage during surface modification

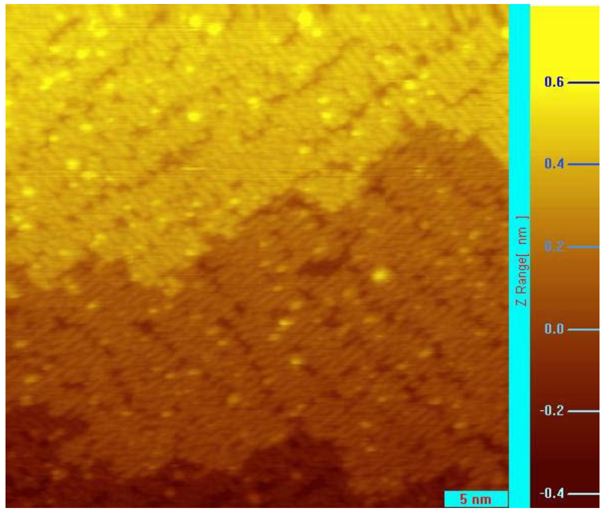

Figure 4.8: 40 nm $\times$ 40 nm STM image of hydrogen passivated Si(100) (Si(100) 2×1:H) surface under UHV with atomic resolution. The image is taken using a Pt-Ir STM tip, at bias voltage of -1 V and set-point current of 150 pA.

should be positive (+).

While the set-point values for the tunneling current used during imaging are around hundreds of picoamperes, the currents required for depassivating the surface are significantly higher, often around tens of nanoamperes. These high current values can be achieved in two ways: using very large bias voltages or using short pulses on moderate bias voltages that would enable the tip to act like a capacitor that is discharging. Using pulses has the advantage of eliminating extra cost for a high voltage power supply, hence this method is chosen for writing operation. Figure 4.9 is a schematic of the electrical manipulation using voltage pulses. During scanning, pulses on bias voltage are set to occur at the desired locations, which cause the hydrogen bond at the pulsed location to break. As a result, the Si(100) surface at those pulse locations are depassivated.

The general algorithm to electrically manipulate surfaces using STM is outlined in a flowchart in Fig. 4.10. After the passivation of the surface, an initial image of the surface is taken. The operator then inputs the desired pattern to the software and specifies the pulse time and voltage. Following this user interaction, the scanner starts scanning the surface as if it is imaging. At the desired pulse locations the imaging and the scanner is stopped, the feedback is turned off so as to not cause the tip to move due to the instantaneous change in the current,

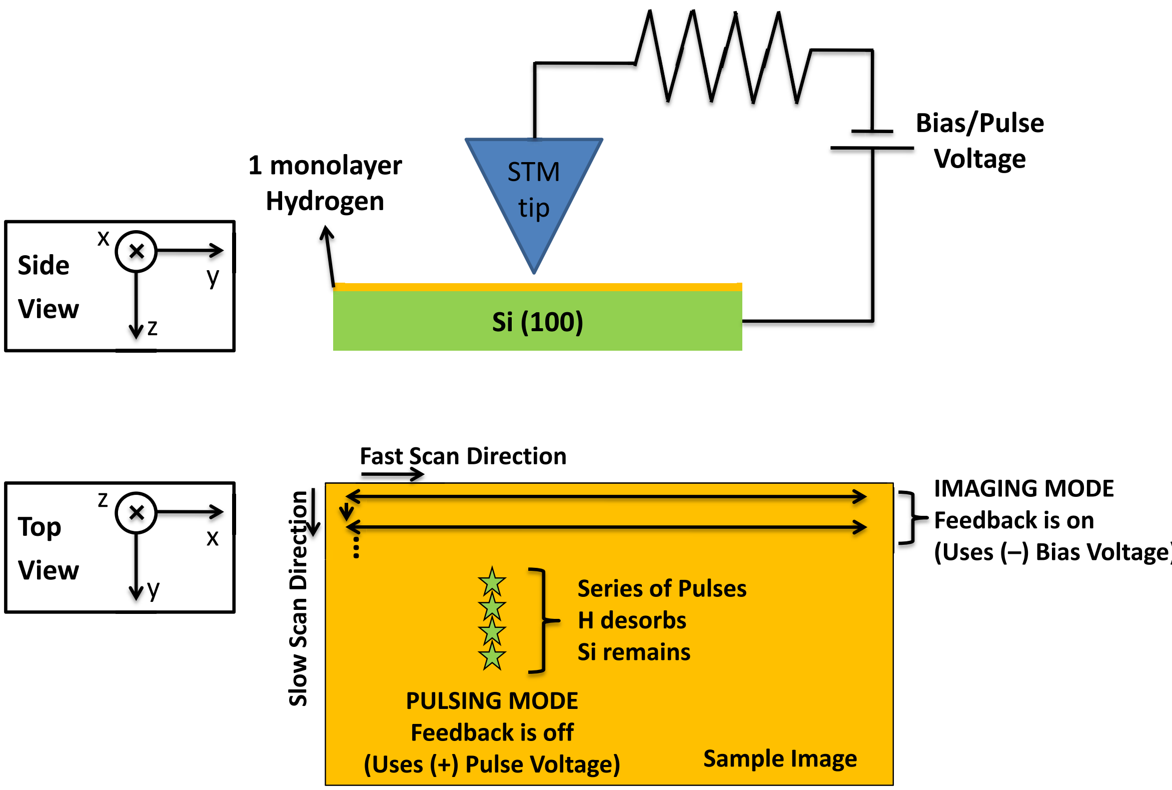

Figure 4.9: The schematic of short electric pulse based surface manipulation. The imaging and manipulation are conducted at the same time. In the top drawing, Si(100) surface (green) is covered with a monolayer of hydrogen atoms (yellow) that are forming bonds with the surface Si(100) atoms, hence passivating them. The tip is positioned directly above this surface during imaging and manipulation. In the below drawing, the tip is raster scanning the surface and imaging it using negative bias voltage. A series of pulses (denoted by stars) induced at the desired locations. These pulses causes desorption of the hydrogen at the pulse locations and the Si(100) surface is imaged. The pulse voltages used are positive.

and the bias voltage is increased to the pulse voltage during the pulsing time. After this image is completed, the pulsing mode is turned off and the sample is imaged for a second time to verify that the surface is changed as desired. If the manipulation attempt is not successful, the operator updates writing parameters such as the pulsing time and the voltage, and the same operation is repeated. This flow continues until the desired change of the surface is acquired.

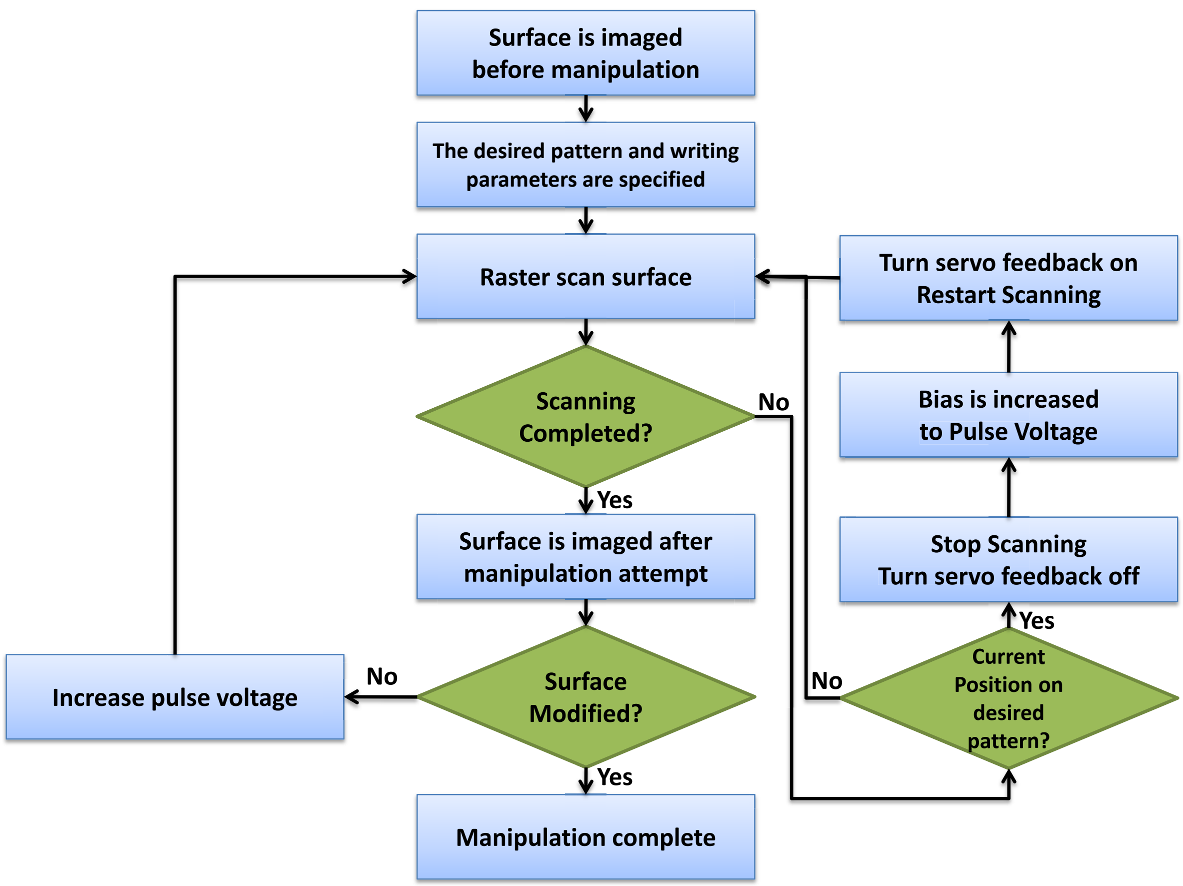

Figure 4.10: The flow of operation for manual STM based surface manipulation.

Using this manipulation technique, we have written several lines on a silicon surface whose widths were on the order of a few nanometers. These results are presented in the experiments section.

4.4.2 Manipulation of Titanium Surfaces Using High Electric Fields

The mechanism for manipulation of titanium surfaces are much less complicated compared to silicon. The manipulation process is referred as local anodic oxidation (LAO) in literature, it is done with a sharp tip, often using STM tips or AFM cantilevers. The only requirement for LAO to be successful is the humidity of the environment. Since LAO uses the water vapor, the humidity should be above 30%, so the process can only be done under ambient conditions.

During local anodic oxidation, the titanium sample is biased positive with respect to a counter- electrode, which is the scanning probe microscope tip. Water meniscus on the surface caused by the humidity of the environment serves as the electrolyte. Our process starts with a clean titanium surface. The surface is imaged either using AFM mode or STM mode. Then, selective regions are oxidized using a high electric field applied between the probe tip and the titanium surface. During the oxidation process, the CAFM probe tip acts as a negative biased electrode with respect to the sample surface and the water meniscus between the probe tip and sample acts as the electrolyte producing the oxidation reaction. There are several parameters that affect the oxidation width and the resistivity such as tip radius, oxidation current, i.e. current flowing between tip and the sample during oxidation process, and the electric field strength, i.e. bias voltage during oxidization. The process can be done in STM or CAFM mode, which will also result in different oxide widths and resistances. A schematic of this operation is shown in Fig. 4.11.

Since the native oxide layer of titanium is a few layers thick, no additional cleaning is necessary before oxidation. The chemical reactions during local anodic oxidation of titanium can be simplified as [42]:

The water meniscus between the probe tip and the titanium surface dissociates into H^+ and $(OH)^-$:

$$2\,H_2\,O \rightleftharpoons 2\,H^+ + 2\,OH^-.$$

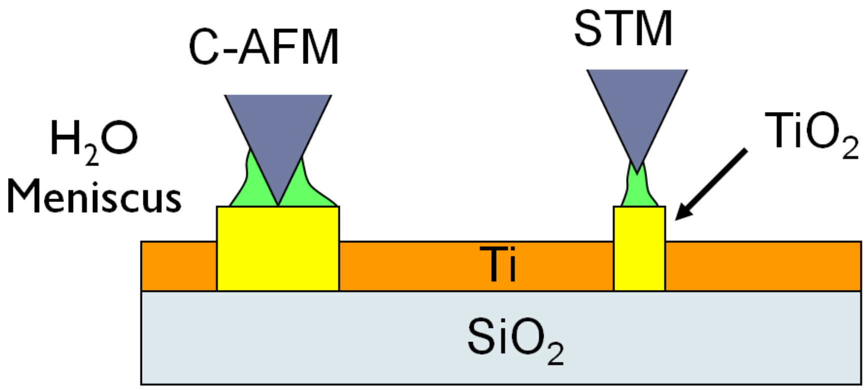

Figure 4.11: The schematic of high electric field based surface manipulation. A titanium film is deposited on silicon dioxide. The sample is imaged under ambient conditions and a high electric field between the titanium film and tip is applied. High electric field causes the water meniscus on the surface to ionize. Oxygen ions are diffused through titanium, changing the material to titanium dioxide. The same oxidization process can be done using STM or AFM mode.

Applied electric field causes the Ti^{2+} ions to accumulate at titanium film surface:

$$\mathrm{Ti} + 2\,\mathrm{H}^{+} \rightarrow \mathrm{Ti}^{2+}.$$

These reactions cause a charge transfer between the two electrodes until equilibrium is established. Ions migrate through the oxide, driven by the potential drop, and combine to form the rather unstable $Ti(OH)_2$ which disintegrates under the formation of TiO_2:

$$\mathrm{Ti(OH)}_2 \rightarrow \mathrm{TiO}_2 + \mathrm{H}_2.$$

Using the physical principle described above, it has been shown that features with sizes of tens of nanometers can be fabricated using CAFM operation [48]. The size of these features can even be decreased to a few nanometers using STM principles, where the end-effector operates a few angstroms above the surface instead of touching or indenting the surface [48]. In addition, it is proposed in literature that LAO can be used to manufacture nanodevices such as diodes or single electron transistors [77]. On the other hand, using STM operation with CAFM probes to obtain smaller features is not shown in literature. Therefore, manipulation using LAO process in STM mode with CAFM probes and characterization of these features is an important step in achieving dual mode and multiple probe array manipulation of surfaces using electrical principles.

Using this manipulation technique, we have written several features on titanium surfaces and characterized their properties such as width and resistivity. These results are presented in the experiments section.

4.5 Modeling of STM Operation and Manipulation

In order to understand the dynamics of the STM operation and manipulation, the mechanics of the system should be modeled. Performing STM operation and manipulation using STM tips and AFM cantilevers are conducted in this case study; hence there will be two separate models for these two operation modes. The use of AFM cantilevers as STM end-effectors is not a common technique; therefore, this case needs specific attention during modeling. The models presented this section will be used to show the feasibility of using CAFM probes in STM mode and to determine optimal or sub-optimal values of design and operation parameters for using CAFM probes as STM end-effectors.

4.5.1 Using STM Tips as End-effectors

To investigate the effects of bias voltage, scanner dynamics and pulsing on STM operation using any end-effector, a model of the STM system is needed. For the initial model, the most common end-effector is chosen for the operation: STM tip. Since STM tips are considered to be "infinitely" stiff, modeling of STM operation using STM tips is a more trivial version of the model that will be presented next, model of STM operation using AFM cantilevers.

The STM operation using STM tips is modeled in the Simulink® environment in Matlab®, as can be seen in Fig. 4.12. The tunneling current is calculated using an embedded Matlab function block. The tunneling current is modeled by Eq. 2.9 presented in Section 2.3.2. The noise of the TIA, which is characterized by researchers in ECE, is added to the tunneling current calculation. The error is generated by subtracting this measurement from the set-point current and is fed to the proportional-integral (PI) controller. The output of this controller is saturated to reflect the actual DAQ board and this output signal is inputted to the state-space stage model. The output of this stage model, which is the displacement of the stage, is slightly corrupted with the positioning noise of the stages. This displacement is then subtracted from the initial distance and the topography of the surface and the tip-sample distance is found. The virtual topography of the surface is set to be rectangular bumps; however a square wave is not used directly because the derivative of the square wave signal does not exist. Instead the rising and falling edges of the rectangular topography data are smoothened by using a high slope ramp, which made the signal's derivative existing but discontinuous. After finding the distance, the distance value and the bias voltage is inputted to the tunneling current calculation.

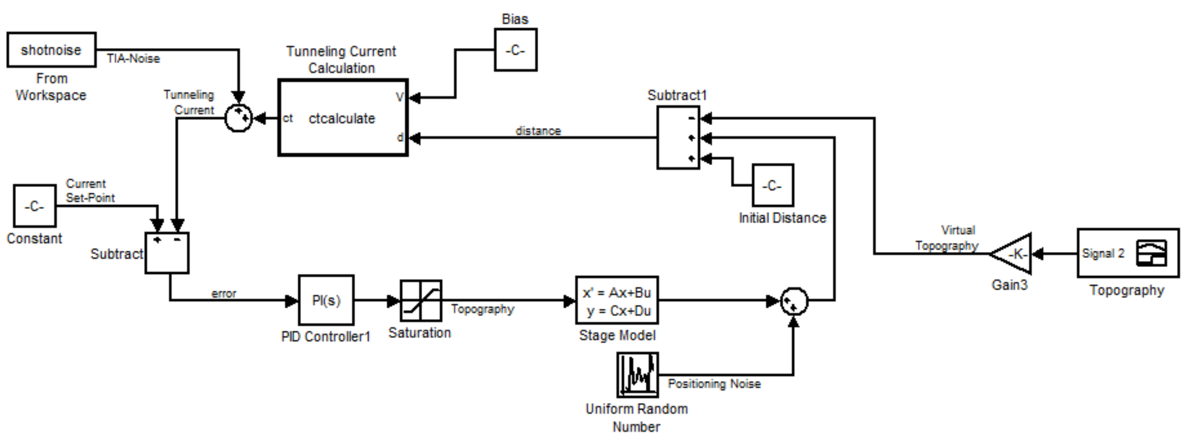

Figure 4.12: The simulation model of the STM operation using STM tips. The tip-sample interaction is not modeled since the STM tip can be modeled as "infinitely" stiff.

It should also be noted here that, STM images are created using the topography signal generated by the controller, which is in fact the output of the controller scaled with a constant calibration value. Since the scanner always tries to keep the tip-sample separation constant during imaging to keep the tunneling current constant, the output of the controller follows the actual topography of the surface. The calibration value is found by scanning a sample, which has features with known heights, and comparing it with the output of the controller.

3 different stage models are used during simulations. The first stage can be referred as an ideal stage, whose bandwidth is ∞. This stage can be considered as "infinitely" fast and is used to isolate the simulations from the effects of the stage speed. A second stage model used, referred as the slow stage model in this study, is the model of the Physik Instrumente P-753 type linear stages. This model reflects a more realistic scenario for a stack type piezo actuator. Its model is acquired by feeding a frequency sweep sinusoidal signal, also known as a chirp signal, to the system and measuring the output. After finding the frequency characteristics of this stage, a first degree second order model is fitted to this experimental data to find an approximate model. The bandwidth of this stage is approximately 4 kHz. The third stage model used, referred as the fast stage model, is a faster version of the slow stage model. To obtain this model, we increased the bandwidth of the slow stage by 100, increasing the bandwidth to around 400 kHz, which is similar to the bandwidth of commercially available tube scanners.

All of the simulations, unless stated otherwise in the figure caption, are performed using a set of nominal parameters to establish fair comparison between simulations. All of these parameters, their descriptions, and the transfer functions used for these three stages are shown in Table 4.1. From this point on, only the parameters that are different in each simulation will be noted. The rest of the parameters can be found from this table, if needed.

In addition to these parameters, a set of parameters is used to calculate the tunneling current via Eq. 2.9. These parameters are never changed during the simulations, and are listed in Table 4.2. Therefore, any tip with any shape is assumed to create the same tunneling current beam that only changes with the tip-sample distance, even when the tip radius is changing. A sample plot of this tunneling current is shown in Fig. 4.13. The non-linearity of this tunneling current with respect to tip-sample separation provides high sensitivity to the small changes in topography, hence enables atomic resolution imaging. On the other hand, to control the vertical actuator

Table 4.1: Nominal Parameters for STM Operation Simulations

Parameter	Value	Unit	Description
k_n	42	N/m	Cantilever Normal Stiffness
R_t	35	nm	Tip radius of a cantilever
Set-Point	80	pA	Tunneling current set-point
Bias Voltage	1	V	Voltage between STM end-effector and surface
f_n	320	kHz	Cantilever's natural frequency
θ_t	22.5	degrees	Cone angle of the tip
L_t	12.5	μm	Tip length
E_t	169	GPa	Young's modulus of tip [Si(111)]
E_s	130	GPa	Young's modulus of sample [Si(100)]
ν_t	0.28		Poisson's ratio of Si(111)
ν_s	0.28		Poisson's ratio of Si(111)
z_0	1	nm	Initial tip-sample separation
A_H	270	zJ	Hamaker constant of Si(111)
σ	0.235	nm	Inter-atomic distance of Si
ϵ_0	8.85×10^-12	$\mathrm{s}^4\mathrm{A}^2/\mathrm{m}^3\mathrm{kg}$	Permittivity of free space
Q_t	100		Quality factor of the cantilever
Scanning speed	0.5	Hz	1/simulation time, defines the lateral speed of the scanner
$\mathrm{TF}_{\mathrm{ideal}}$	1	m/V	Ideal stage transfer function
$\mathrm{TF}_{\mathrm{slow}}$	$\frac{-3.15\times10^{-5}s+0.36}{s^2+2.522s+5.845\times10^6}$	m/V	Slow stage transfer function
$\mathrm{TF}_{\mathrm{fast}}$	$\frac{-3.15\times10^{-3}s+3604}{s^2+2.522\times10^5s+5.845\times10^{10}}$	m/V	Fast stage transfer function

using a linear controller like PI controller becomes more difficult, because tunneling current can have values with a few orders of magnitude difference for small changes in tip-sample distance. Hence, it is hard to stabilize the tunneling current flowing using a linear controller with constant gains.

Table 4.2: Parameters for Tunneling Current Calculation

Parameter	Value	Unit	Description
r_{eb}	0.5	nm	Effective tunneling beam radius
q^e	1.6×10^-19	C	Charge of a single electron
$\hbar$	6.63×10^-34	$\mathrm{m}^2\mathrm{kg/s}$	Planck's constant
m^e	0.91×10^-30	kg	Mass of a single electron
ϕ_{Pt}	5.5	eV	Work function of Platinum
ϕ_{Si}	4.52	eV	Work function of Silicon

Using this model, STM imaging and pulsing using STM tips as end-effectors can be simulated easily, however the images would be on a single line. During STM imaging, the two signals that are most commonly visualized by the control PC are the tunneling current and the topography signals. Therefore, during imaging and manipulation simulations, we use these signals to generate output plots. A sample simulation of STM imaging using STM tips is shown in Fig. 4.14. The height of the bumps in the virtual topography of the surface is set to be 1 nm for this simulation and the set-point current of 500 pA are used. The rest of the parameters are parameters from Table 4.1 (nominal parameters). As can be seen from the figure, the scanner was able to track the change in the topography almost perfectly.

4.5.2 Using AFM Cantilevers as End-effectors

Besides the STM images of Si(100) surface taken with AFM cantilevers, which are presented before, modeling of the STM operation and pulsing using AFM cantilevers as end-effectors is also required to show the feasibility of this idea. After establishing the model of the STM operation using STM tips as end-effectors, modeling of the STM operation using AFM cantilevers requires two additions to the model: cantilever dynamics and tip-sample interaction forces.

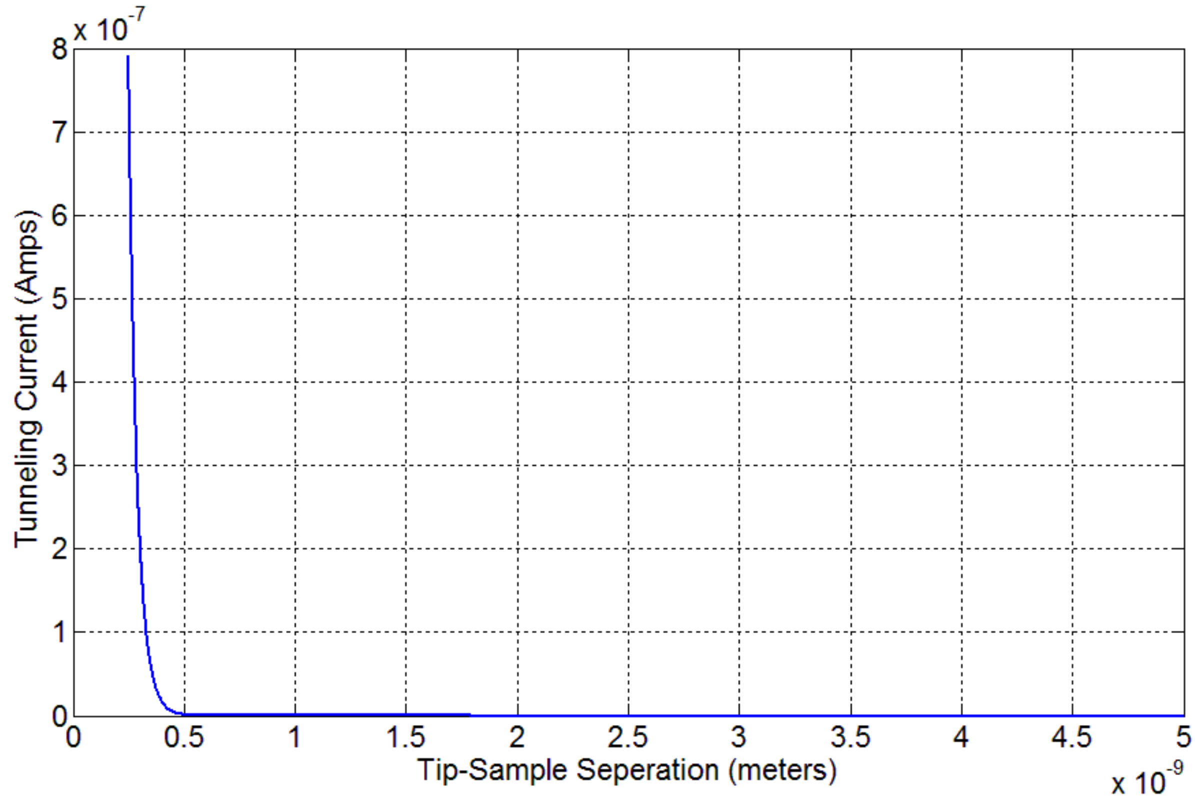

Figure 4.13: The change of tunneling current with respect to the tip-sample separation. Non-linear behavior of the tunneling current makes it easy to detect small topography changes but hard to control the vertical position with a linear controller. The current is simulated for a platinum tip, using the parameters in Table 4.2

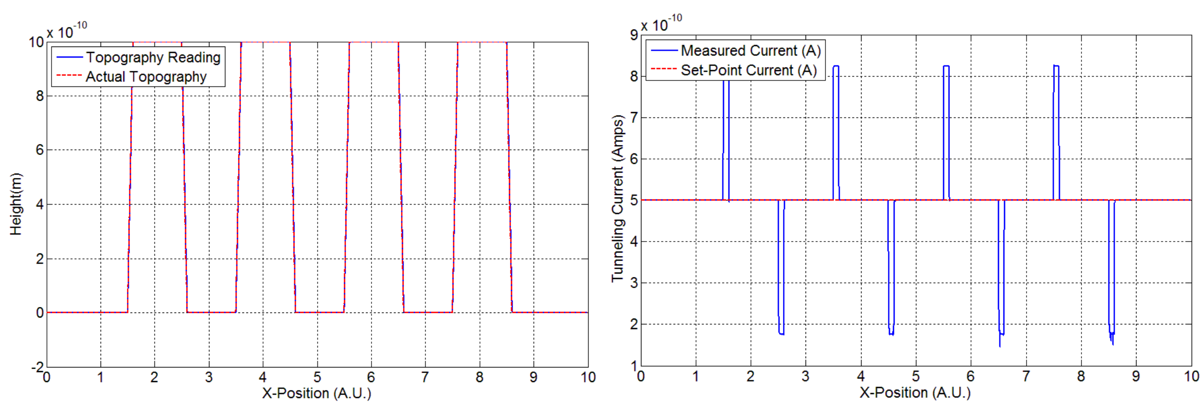

(a) (b)

Figure 4.14: Simulated STM line-scan of a surface using STM tip. The simulation is run using nominal parameters.

As discussed before in Section 2.3.1, AFM cantilevers can be modeled as mass-spring-damper systems. The normal stiffness, being the spring stiffness in this analogy, is a vendor specified value. The natural frequency and the quality factor of the cantilever can be found by utilizing a frequency sweep; on the other hand, these properties are often specified by the vendor as well. The damping and the mass of the mass-spring-damper system can then be found using these parameters and Eqs. 2.6 and 2.7.

In addition to the cantilever dynamics, the probe-sample interaction force should be modeled. The interaction between the probe and the surface is explained before in Section 2.4 and the models for van der Waals attraction, electrostatic attraction between probe tip and surface, electrostatic attraction between probe cantilever and surface, and the contact force are presented. To model the interaction fully, these models are combined and used as the total force acting on the cantilever tip. The resulting overall system model is shown in Fig. 4.15.

There are two major problems for using AFM cantilevers as STM end-effectors: vibrations and snap into contact phenomenon. Since cantilevers, unlike STM tips, are compliant structures, they will vibrate around their natural frequency when small duration forces are induced on them. This is likely to happen during STM operation due to the tip-sample interaction. The vibration of the cantilever due to the sharp tip-sample interaction forces will also cause the tunneling current to oscillate. The snap into contact of the tip to the surface is also a very likely scenario that occurs due to energy balance in the cantilever-surface interaction [11]. At the distance where the contact stiffness between the tip and the surface and the stiffness of the cantilever are equal to each other, the interaction becomes unstable. At this distance, the cantilever either snaps into contact with the surface or pulls off contact from the surface. The contact stiffness is defined as:

$$\begin{aligned} k_{\text{contact}} &= \frac{\delta F_{\text{interaction}}}{\delta z} \\ &= \frac{\delta F_{\text{vdw}}}{\delta z} + \frac{\delta F_{\text{el}}}{\delta z} + \frac{\delta F_{\text{El-c}}}{\delta z} + \frac{\delta F_{\text{DMT}}}{\delta z} \end{aligned} \tag{4.1}$$

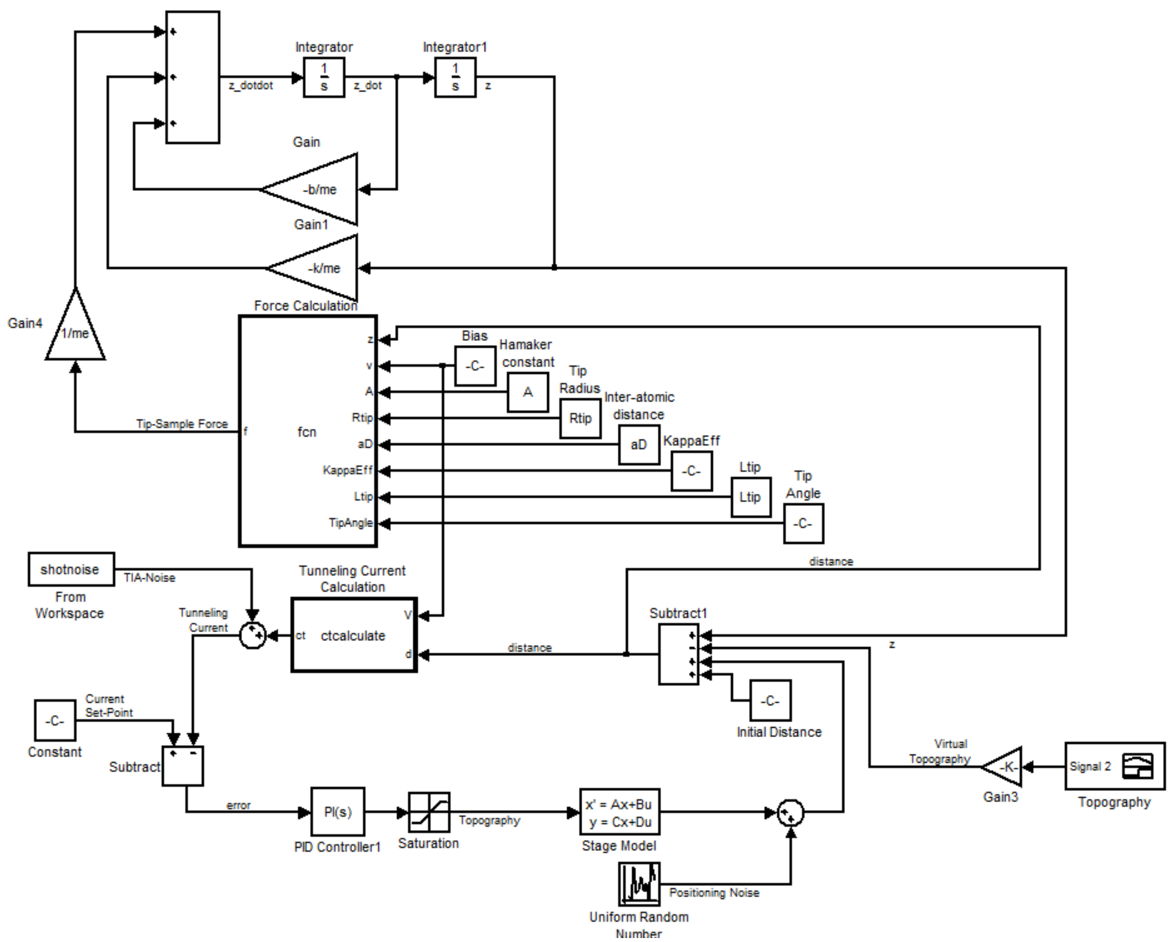

Figure 4.15: The simulation model of the STM operation using AFM cantilevers. Unlike the model for STM operation using STM tips, the tip-sample interaction has to be modeled since AFM cantilever can deflect.

where F_{vdw} is defined as Eq. 2.10, F_{el} is defined as Eqs. 2.11 and 2.12, and F_{DMT} is defined as Eq. 2.21 in Section 2.4. Figure 4.16 is a sample plot that shows $\frac{\delta F_{\text{interaction}}}{\delta z}$, hence the contact stiffness with respect to the tip-sample distance. The red dashed line is the stiffness of a cantilever. The intersection points of these two plots are where the contact is unstable, i.e. the snap into contact and pull off contact distances.

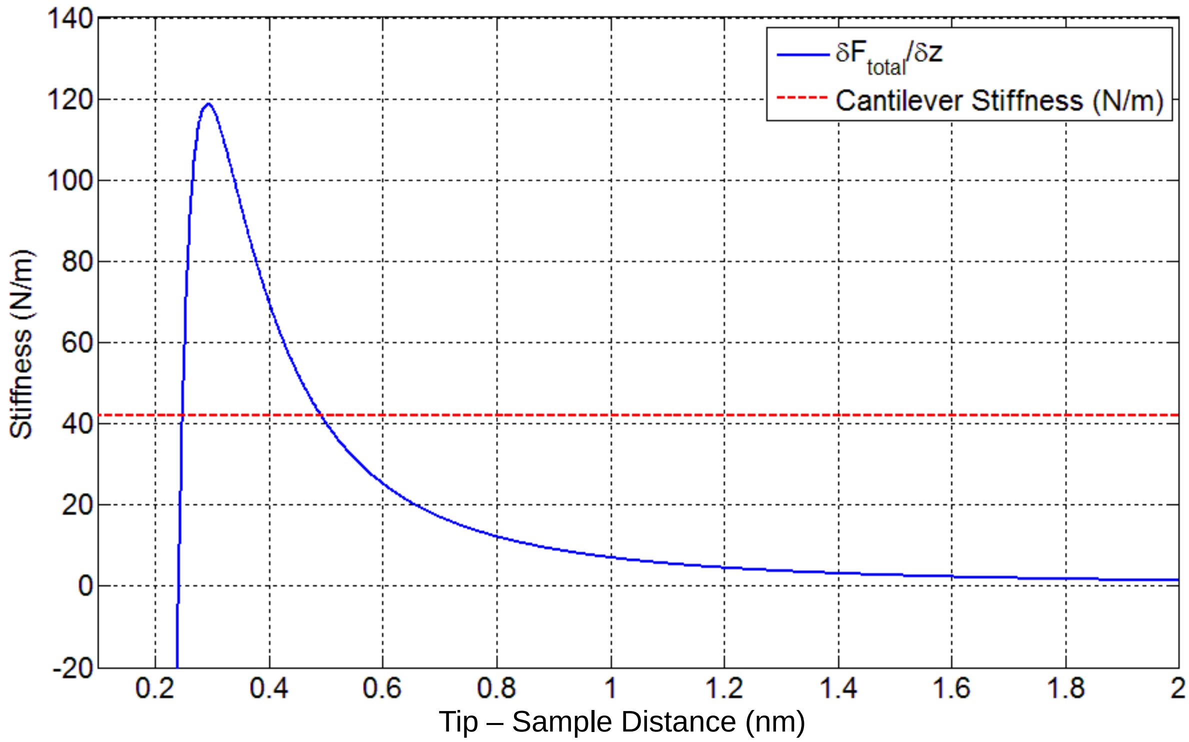

Figure 4.16: Simulated tip-sample interaction force gradient (i.e. contact stiffness) with respect to tip-sample distance. The two points where the contact stiffness intersects the cantilever stiffness are the points of instability. According to this simulation, the cantilever tip will snap-into contact with the surface around 0.5 nm separation and the tip will pull-off contact at 0.23 nm. The simulation is run using nominal parameters.

The dynamic model presented in Fig. 4.15 captures both of these problems, hence is a complete model of the STM system using AFM cantilever, for all simulation purposes. On the other hand, snap into contact behavior of the tip to the surface can also be modeled as in Eq. 4.1. We will use the contact stiffness technique to find the snap into contact points for different cantilevers and compare the results to the values found using the dynamic model to verify that the dynamic model works correct.

Since the model is using AFM cantilevers as end-effectors, force-distance curve simulations can be acquired in addition to image simulations. Figure 4.17 shows a simulated force distance curve. Figure 4.17(a) is a generic plot that can be obtained while taking force distance curves in a commercial AFM. The tip deflection and the force data are the two signals available in AFMs. On the other hand, Fig. 4.17(b) shows the tip-sample distance, which is often not accessible for SPMs, with respect to the base position. Figure 4.17(c) shows a zoomed-in version of the previous plot. The snap-into contact and snap out of contact points are shown on this plot as points A and B, respectively.

Using this dynamic model, STM imaging and pulsing using AFM cantilevers as end-effectors are also simulated and the tunneling current and the topography signals are visualized. A sample simulation of STM imaging using AFM cantilevers is shown in Fig. 4.18. The height of the bumps in the virtual topography of the surface is set to be 1 nm for this simulation and the set-point current of 700 pA are used. The stage is chosen to be ideal and the rest of the parameters are parameters from Table 4.1 (nominal parameters). As can be seen from the figure, the scanner was able to track the change in the topography almost perfectly.

4.6 Simulation Results

To investigate the effect of different parameters on STM operation using AFM cantilevers, we have performed several simulations using the models described in the previous section. All of the parameters except the parameter of interest in every simulation are nominal values of those parameters and can be found in Table 4.1, unless otherwise stated in the simulation plot or the figure caption.

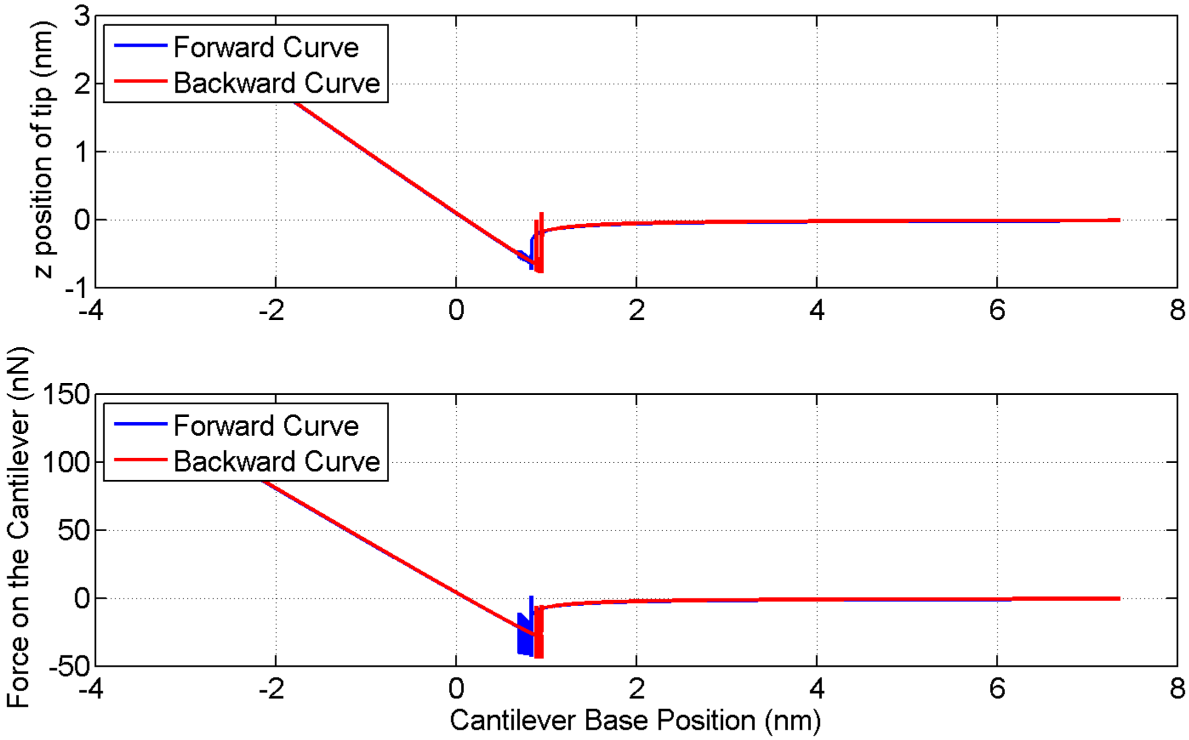

(a)

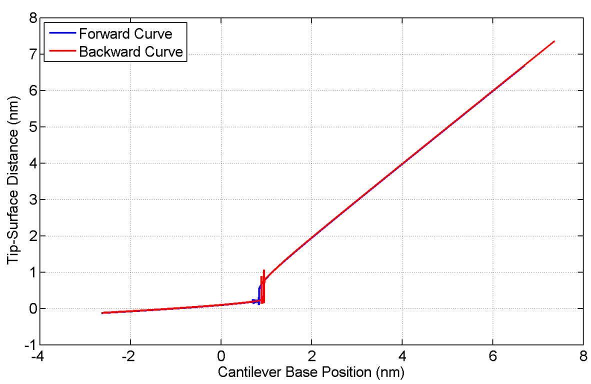

(b)

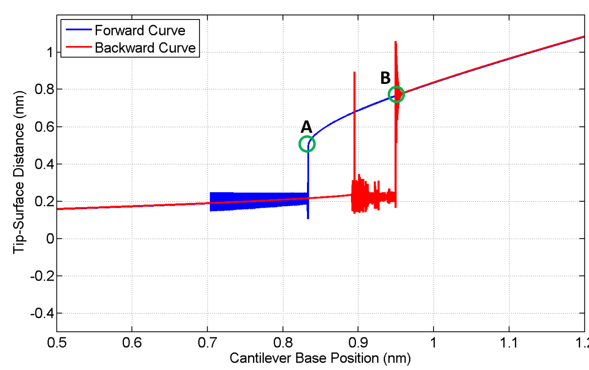

(c)

Figure 4.17: Simulated force-distance curve using an AFM cantilever on Silicon surface. The simulation is run using nominal parameters. (a) The two plots are drawn using the accessible signals of an AFM. These are the plots that commercial AFMs can generate. The bottom plot is force (which is proportional to the deflection of the cantilever) with respect to the cantilever base, and the top plot is the tip position of the cantilever with respect to the cantilever base. (b) This plot shows the tip-sample distance with respect to the base position and this data often cannot be accessed in an AFM. (c) The zoomed plot of distance versus base position. The snap-into contact and pull-off contact points are A and B, respectively. The snap-into contact and pull-off contact distances are simply the y-coordinates of these two points.

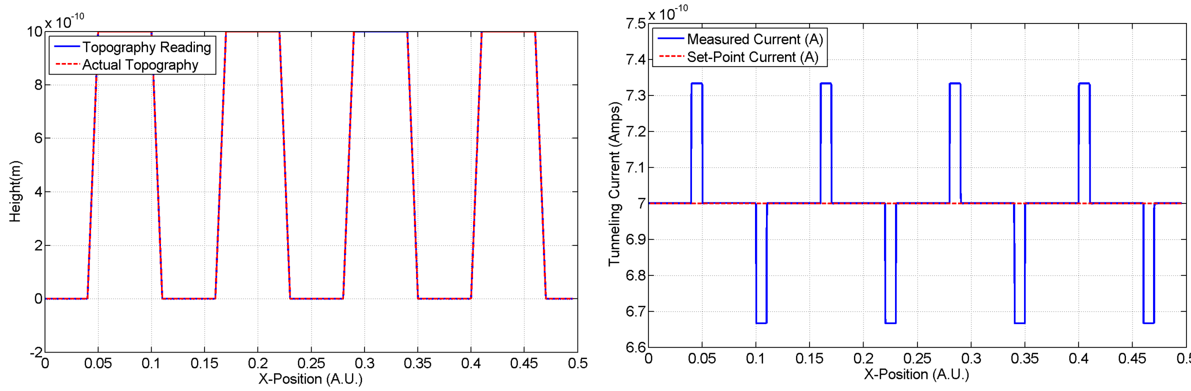

(a) (b)

Figure 4.18: Simulated STM line-scan of a surface using AFM cantilever. The simulation is run using nominal parameters.

4.6.1 STM Operation Using CAFM Probes Under Ultra-High Vacuum

The first set of simulations that we have performed was to define the maximum and minimum tunneling distances for our system. The trans-impedance amplifier used in our system has the upper threshold current value of 100 nA. Hence it can detect, convert to voltage and amplify any current value between 0 and 100 nA. These values are read by the DAQ board from an analog to digital converter channel with 16 bit resolution. Hence the resolution of the current reading is $100\text{nA}/2^{16} = 1.5\text{pA}$. However, most of our successful imaging trials are conducted at 0.5 nA which is set as the minimum tunneling current feasible for our system. On the other hand 2 nA is the highest current value used for imaging and manipulation of surfaces; therefore it is set as the maximum tunneling current feasible. These current values correspond to some distance values for any given bias voltage. During STM operation, the tip of the cantilever should always be between the maximum tunneling distance, which corresponds to 0.5 nA, and the minimum tunneling distance, which corresponds to 2 nA. The change of these distances with respect to bias voltage is simulated and shown in Fig. 4.19. Here, Fig. 4.19(a) is a sample plot that shows the threshold values and the tunneling current with respect to the tip-sample distance and Fig. 4.19(b) shows the resulting relation of minimum and maximum distances with respect to the bias voltage. As can be seen from these figures, for low bias voltages, which are often used during STM operation, the tip sample distance is always below 1 nm.

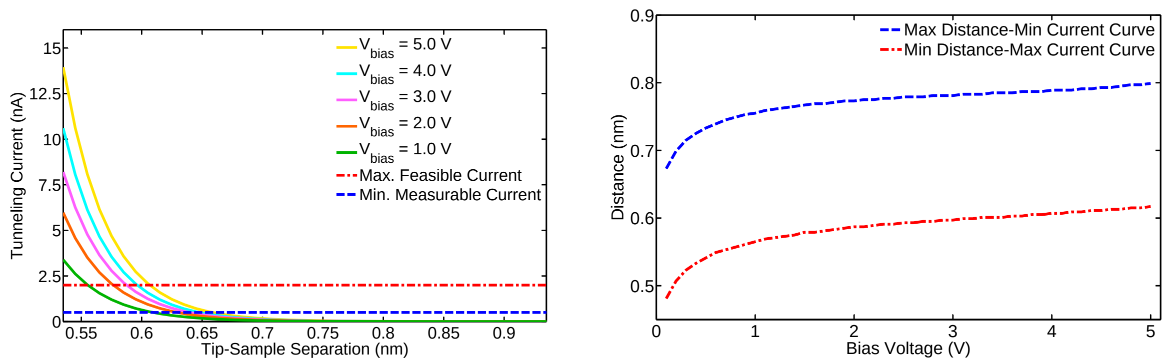

(a) (b)

Figure 4.19: Simulated minimum and maximum distances for tunneling. The simulation is run using nominal parameters. (a) Sample tunneling current with respect to Tip-Sample distance plot where bias voltage is 1 V. Minimum measurable current is 0.5 nA whereas maximum measurable current is 2 nA. (b) Minimum and Maximum tunneling current distances with respect to bias voltage.

In some ideal cases, such as using ideal control loops and stages, the sample could be imaged while the tip is unstable, i.e. below at a distance below the snap into contact distance. On the other hand, to be able to form a more stable feedback loop, it is required for the tip to be positioned below the maximum tunneling distance in a stable way. To enable this, the snap into contact distance of the tip with the surface should be at a lower than the maximum tunneling distance. As the snap into contact distance of the tip decrease, or the maximum tunneling distance increase, the tip is further away from its unstable point during operation, hence is easier to operate the AFM cantilever in STM mode. However since the maximum tunneling distance cannot be changed easily, the next best tactic to employ is to choose an appropriate cantilever for the task.

The two main design parameters of an AFM cantilever which can be specified while purchasing is the cantilever stiffness and the tip radius. Therefore, we performed several simulations using the contact stiffness technique (Eq. 4.1) to define the effect of cantilever stiffness and tip radius to STM imaging, and to analyze which cantilevers would perform better for our system.

The results of these simulations are shown in Fig. 4.20. Figure 4.20(a) shows the snap-into contact distances of different stiffness cantilevers with 20 nm tip radii as a function of bias voltage. The cantilevers that snap-into contact below the maximum tunneling distance curve are viable for STM operation, since they can reach to distances where tunneling is possible. Using this model, it is possible to identify the minimum stiffness values for a given tip radius and bias voltage. Figure 4.20(b) shows such a simulation result. The results show that as the tip radius increases, the minimum stiffness for a given bias voltage will also increase. It also shows that very low and very high bias voltages require a stiffer cantilever than the bias range of 0.5 V - 1.0 V. The reason for high bias voltages requiring a high stiffness is that the electrostatic attraction force is very high. On the other hand, for low bias voltages, it is significantly harder to generate the necessary tunneling current for imaging. Hence, these two factors compete and generate an optimum bias voltage value for STM imaging using CAFM cantilevers. This optimum value depends on the material of the surface and the material of the cantilever, and can be obtained using our model.

We also wanted to verify our dynamic system model, by comparing the snap into contact distance values acquired from the dynamic model to the values acquired from the contact stiffness technique. Finding the snap into contact distance using the contact stiffness technique is straightforward, it is the solution to Eq. 4.1. On the other hand, finding the snap-into contact point using dynamic simulations is not as easy and objective. During the dynamic simulations, the control loop is turned off and the stage position is ramped towards the cantilever tip. At some distance the cantilever starts accelerating towards the stage and snap into contact occurs. However, the snap into contact distance is not explicitly defined in dynamic system model, hence we need to choose the criteria for defining the snap into contact distance for the dynamic model. We have chosen to take the point where the acceleration of the tip movement is greater than its mean acceleration throughout an approach curve. Hence this distance represents the point where the tip start accelerating more towards the surface compared to higher distances and therefore will be very hard to stop the tip after this point, i.e. it will either be or very close to being unsta-

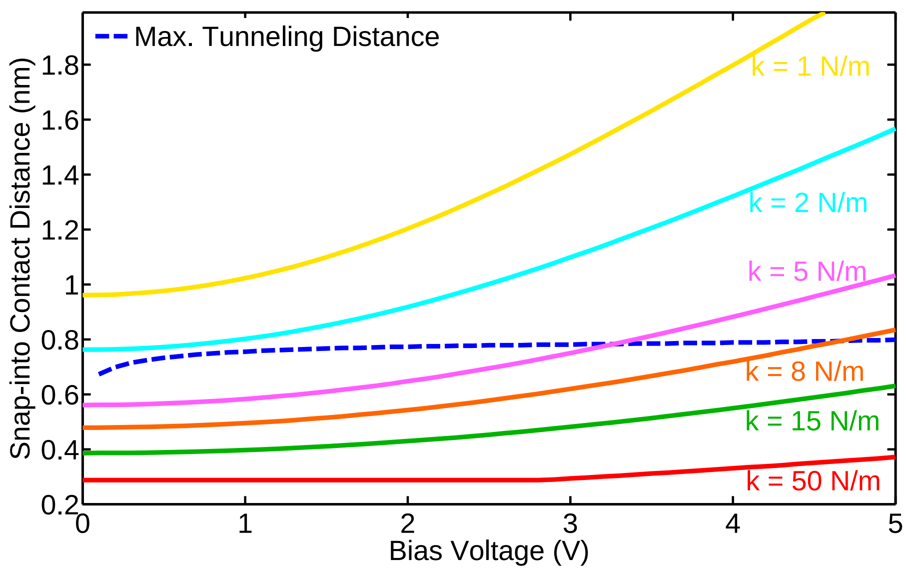

(a)

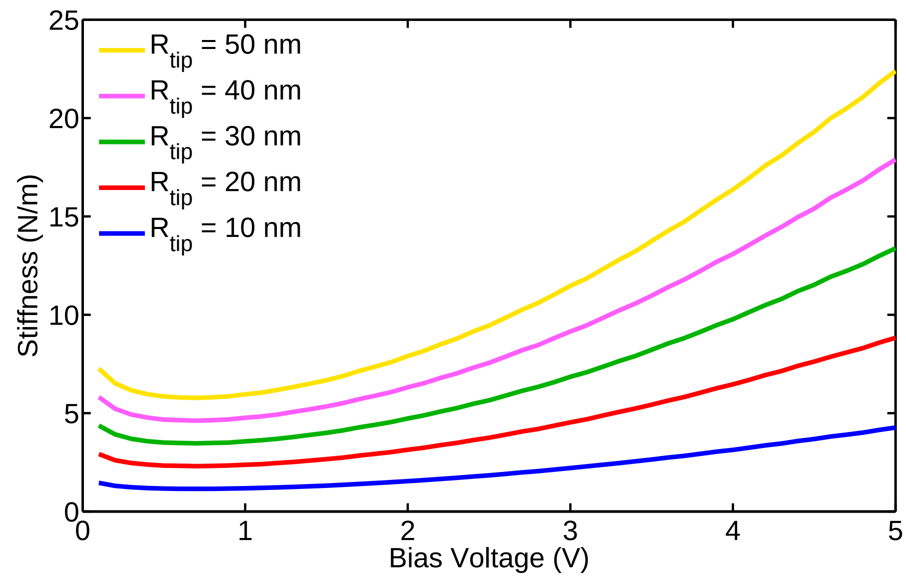

(b)

Figure 4.20: (a) Simulated snap-into contact distances of CAFM probes with different stiffness values for varying bias voltage. (b) Simulated minimum stiffness values for varying bias voltages that STM operation would be viable. The simulation is run using nominal parameters. The results show that STM imaging with AFM cantilevers is possible with stiff cantilevers ($k_n \geq 7$) with small bias voltage values. Decreasing tip radius values also increase the stability.

ble. A sample plot showing one of the dynamic simulations and the snap into contact distance calculated from this simulation is shown in Fig. 4.21.

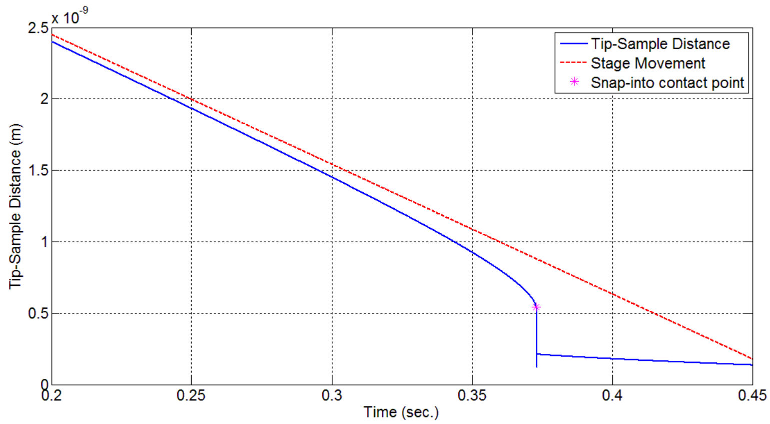

Figure 4.21: Simulated snap-into contact behavior of the cantilever while stage is moving towards the tip. The simulation is run using nominal parameters. The snap-into contact point is defined as the point where the tip starts accelerating towards sample.

After defining the criteria for finding the snap into contact distance between the tip and the surface, several simulations are performed to compare the results with contact stiffness (also known as energy balance) snap into contact results. The results obtain from these two models agree, which verifies that our dynamic simulations work as expected, as can be seen from Fig. 4.22. In both cases, dynamic simulations overshoot the snap into contact point slightly however this is due to the definition of criteria for finding the snap into contact distances in dynamic simulations and can be fixed by changing this selection criteria.

4.6.2 Effect of Stage Speed and Noise on STM Operation Using CAFM Probes

Following the verification of the model, we analyzed the effect of stage speed on the STM imaging with AFM cantilevers. To exaggerate the effect of the stage speed as much as possible, we performed a simulation using the slow scanner. The result of this simulation is presented in Fig. 4.23(a). When compared to the STM imaging with AFM cantilevers using an ideal stage (can

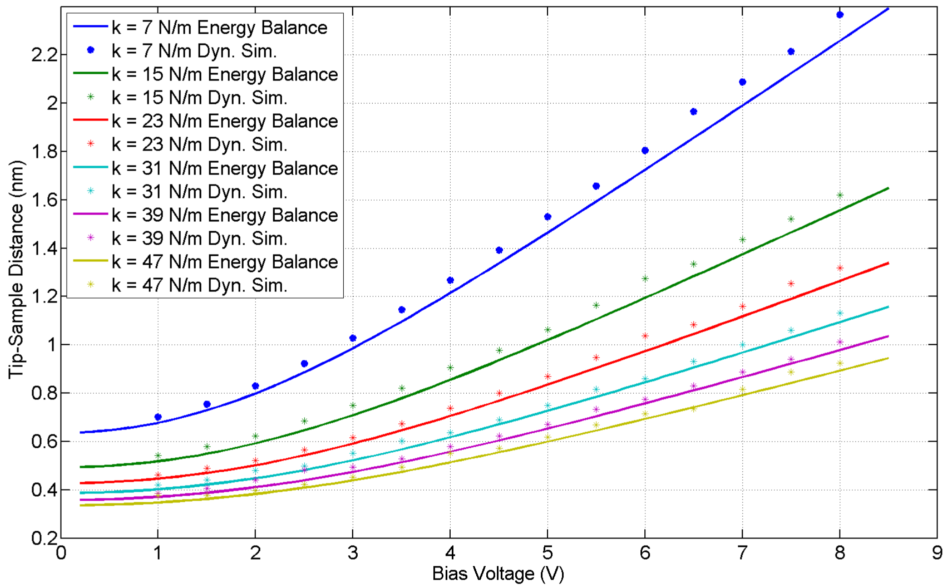

(a)

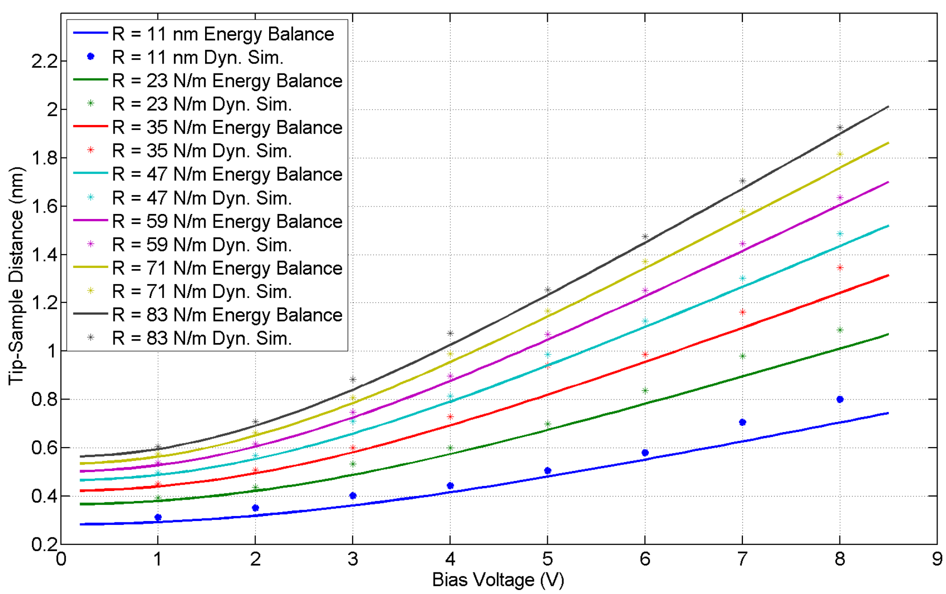

(b)

Figure 4.22: Comparison between the energy balance and dynamic model snap-into contact simulation results. The simulation is run using nominal parameters. The agreement between the simulations verifies that the simulations are valid. The small mismatch between the results is due to the definition of the snap-into contact point in the dynamic model.

be seen in Fig. 4.18), it is obvious that using a slow stage decreases the image quality. The topography cannot be tracked as good as ideal stage case and often overshoot is observed in rising edges of the topography. The falling edges of the topography is tracked slower than the rising edge since the tunneling current error in rising edge is larger than falling edges, as can be seen in Fig. 4.23(b). This is due to the non-linearity of the tunneling current with respect to tip-sample separation.

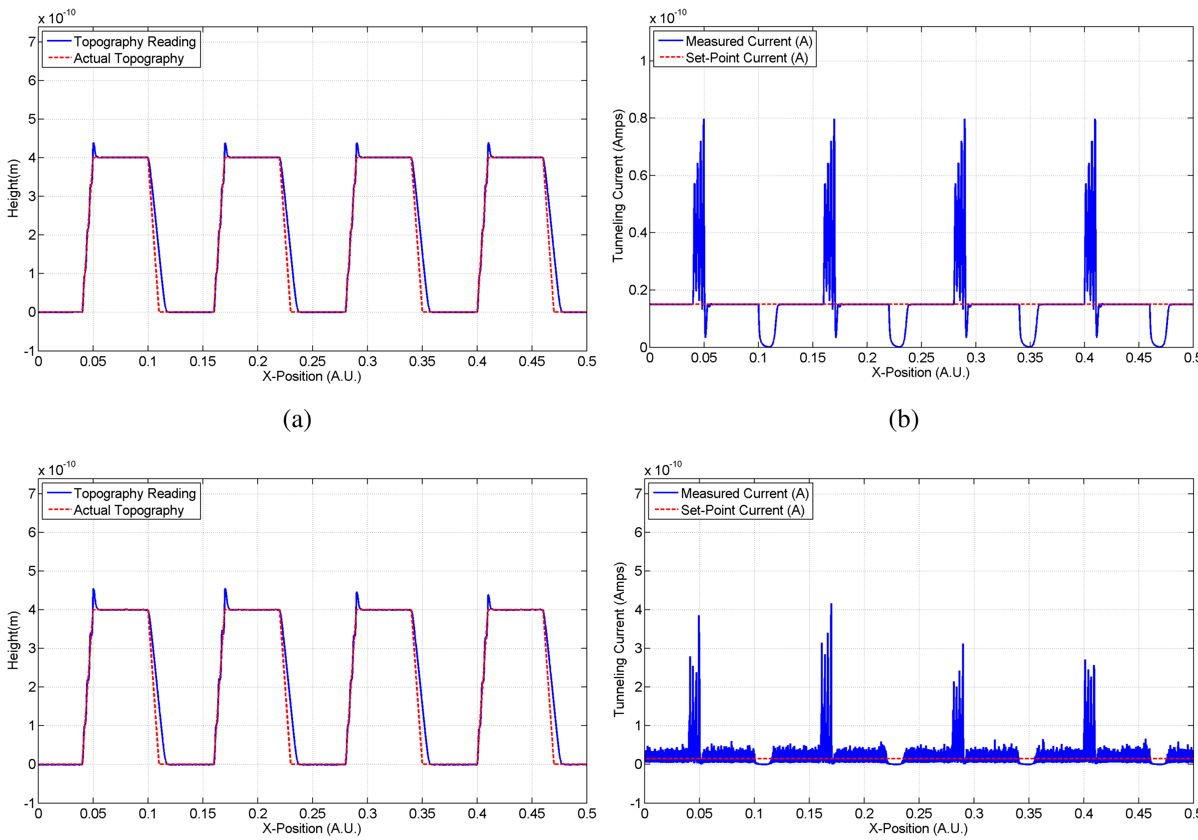

(a) (b)

(c) (d)

Figure 4.23: Sample line-scan simulations that reflect the effect of scanner speed and the noise on STM imaging using AFM cantilevers. As scanner speed decreases STM image quality depreciates. (a) and (b) shows the line-scan simulations using a slow scanner without noise. The scanner cannot keep-up with the speed of imaging. The addition of noise to the simulations also decreases image quality. (c) and (d) shows the effect of noise to the line-scan. The effect of noise is more pronounced on the tunneling current line-scans where the error is increased 700%.

In addition to the stage speed, the qualities of the images are also affected by the noise in the positioning and tunneling current measurement. We modeled the noise in the positioning and the tunneling current measurement as discussed in the previous section and these two possible sources of noise is added to the system. The effect of noise on the imaging is shown in Fig. 4.23. Although the effect of the noise is not very pronounced in topography image simulations, this is due to the fact that the noise values specified for the TIA and the stage used in the system are not very high (50 fA RMS pink (1/f) noise for TIA and 0.02 nm RMS white noise for the stage). On the other hand, the effect of the noise is more obvious from the tunneling current plots due to the non-linearity of the tunneling current. As can be seen from Figs. 4.23(b) and 4.23(d), the error in the tunneling current increased 700%.

A more comprehensive analysis is then performed on the effects of noise and the stage speed to STM imaging using AFM cantilevers. The results of these simulations are shown in Fig. 4.24. For these simulations, the slow stage model with a bandwidth of 4 kHz and the fast stage model with a bandwidth of 400 kHz from Table 4.1 are used. As can be seen from these figures, using a faster stage has a clear advantage on STM based imaging as the distances between the tip and the surface that can be achieved using a fast stage is lower than the distances that can be achieved with a slow scanner. The introduction of noise to the system also decreases the imaging performance as the distance values with noise are higher in this case. It can also be observed from the images that as the cantilever stiffness and the tip radius increases the effect of noise also increases. In addition to this, the effect of noise while using fast scanners are more pronounced compared to the effect of noise while using slow scanners. This is because the fast scanners can achieve lower distance values, hence the cantilever tip is closer to the surface, i.e. the distance between the tip and the surface is closer to the snap into contact distance, and the operation is more prone to positioning and tunneling current measurement errors.

Although not as easy to operate as “infinitely” stiff STM tips, we believe the simulation results presented here when combined with the demonstration of STM imaging using AFM cantilevers with atomic resolution proves the feasibility of STM imaging with compliant AFM can-

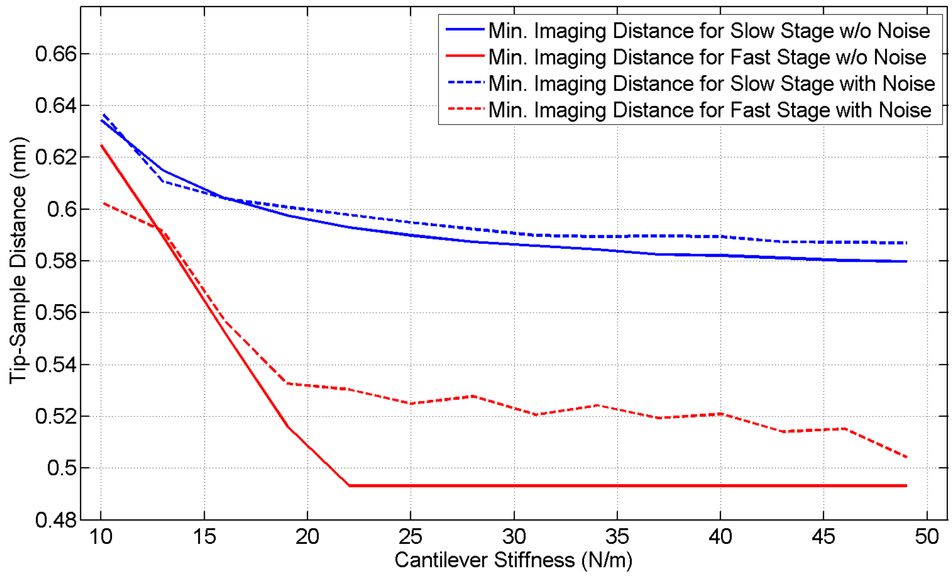

(a)

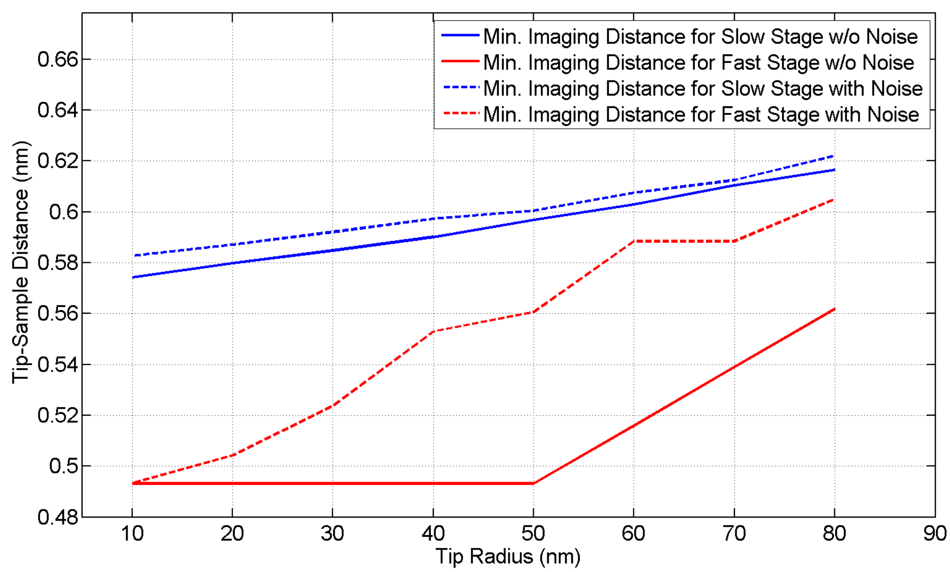

(b)

Figure 4.24: The effect of scanner speed and the noise on STM imaging using AFM cantilevers. Using fast scanners have a clear advantage over using slow scanners. However the effect of noise is more pronounced while using fast scanners. This is due to the fact that, using fast scanners are nearly perfect without noise, whereas the addition of the noise is a minor problem for slow scanners compared to their speed problems. (a) The effect of scanner speed and noise on imaging with respect to various normal stiffness values. (b) The effect of scanner speed and noise on imaging with respect to various tip radius values.

tilevers. However the feasibility of using AFM cantilevers for STM based electrical manipulation of surfaces is another topic and should be investigated more.

4.6.3 Manipulation of Surfaces via Short Electrical Pulses Using CAFM Probes

In order to demonstrate the feasibility of using AFM cantilevers in STM manipulation, we performed pulsing simulations on the system model. During these simulations, we applied a specified pulse on the bias voltage while the tip was imaging the surface in a stable way and checked the deflection of the cantilever as well as if the snap into contact occurred or not. A sample pulse that is applied on the bias voltage is shown in Fig. 4.25(a). The pulse times used in these simulations were all 1 milliseconds long, an easy to achieve time using any DAQ board.

Since we have already demonstrated that pulsing with STM tips is easy to succeed, we first performed a pulsing simulation using the STM operation using STM tip model, to obtain baseline values for the deflection. During these simulations the STM tip, the tip holder and the vertical scanner are assumed to be a single body and the system is modeled as a mass-spring-damper system with values of a similar scanner from literature [97]: $k = 2.8 \times 10^6$ N/m, $b = 13.1$ N-s/m, and $m = 0.6135$ kg. The results show that the deflection of the STM tip with the applied pulse is around 10^{-6} nm, hence negligible. The results of this simulation are shown in Fig. 4.25(b).

On the other hand, when the same pulse is applied on a cantilever, the cantilever starts vibrating at its natural frequency due to the impulse applied from the increase in the electrostatic force. The vibrations dampen in a few microseconds and the tip-sample distance assumes the value corresponding to the increased electrostatic force. When the pulse is over, the electrostatic force decreases to its previous value corresponding to the bias voltage, hence the cantilever oscillates for a second time and then the tip-sample distance assumes its equilibrium value during imaging. Because of the impulse applied on the cantilever, the maximum deflection and the mean deflection of the cantilever during pulsing are not the same value. As can be seen from Fig.

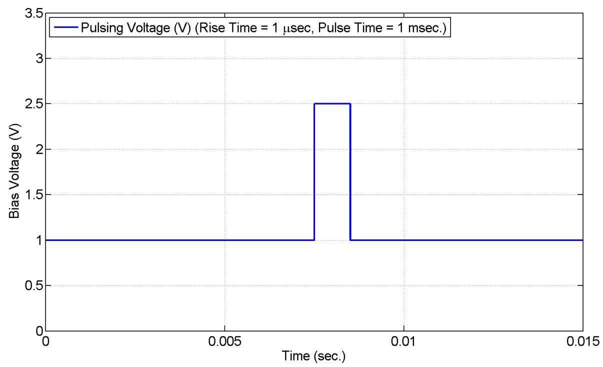

(a)

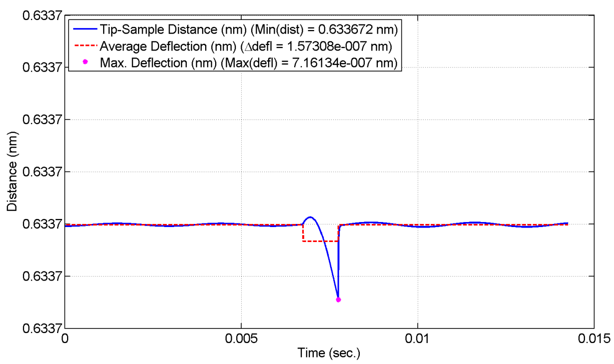

(b)

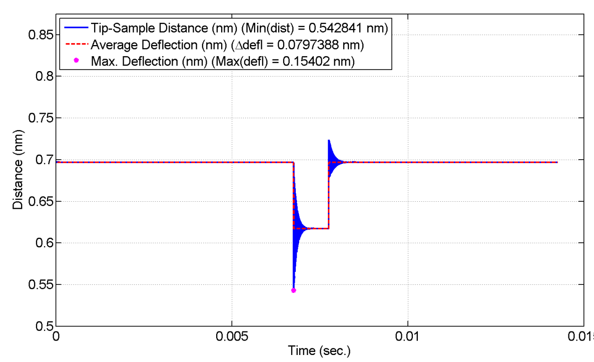

(c)

Figure 4.25: Sample pulsing simulations. (a) The applied bias voltage during imaging. The pulse time is 1 millisecond and pulse voltage is 2.5 V. (b) The deflection of an STM tip during pulsing. The tip deflection is negligible however the damage that can occur during pulsing is not modeled. (c) The deflection of an AFM cantilever during the same pulse. The difference between the deflections is almost 6 orders of magnitude.

4.25(c), the mean deflection of the cantilever is 0.08 nm whereas the maximum deflection is 0.15 nm, almost twice the mean deflection. If the cantilever snaps into contact when the maximum deflection occurs, there is a chance that the cantilever would stay in contact for the remaining of the scan, or the tip might be damaged. In both of these cases STM imaging with the cantilever will no longer be possible.

In order to pulse using a cantilever while keeping it still at the imaging condition, the parameters that affect the maximum cantilever deflection during pulsing should be defined and investigated more in depth. We believe that these parameters are k_n, the normal stiffness of the cantilever, which changes the snap into contact distance of the cantilever; R_t, the tip radius, which changes the force that the cantilever experiences during pulsing; V_b, the bias voltage, which changes the equilibrium distance of the cantilever during imaging; V_p, the pulse voltage, which changes the equilibrium distance of the cantilever during pulsing i.e. the mean deflection; and τ_p, the rise time of the pulse, which changes the sharpness of the pulse, i.e. the similarity of the pulse to an impulse.

To investigate the effects of these parameters listed above, simulations similar to the ones in Fig. 4.25(c) are performed and these results are shown in Fig. 4.26. In these plots, the blue dots denote the equilibrium distance during imaging whereas the maximum deflection during pulsing is denoted by red dots. The purple dashed line is the inter-atomic distance of silicon. A red dot under this purple line means that the cantilever snapped into contact with surface while pulsing with the corresponding parameter. The results suggest that to be able to pulse with cantilevers and continue imaging without damaging the tip, high stiffness cantilevers with sharp tips should be used. The bias voltage, i.e. the starting tip-sample distance prior to pulsing, and the pulse voltage, i.e. the tip-sample equilibrium distance during pulsing, should be high. The rise time also effect pulsing but the effect is not as pronounced as the other parameters.

In addition to the parameters listed above, the pulse time is also a parameter that can affect the maximum cantilever deflection during pulsing as long as the pulse time is lower than 10

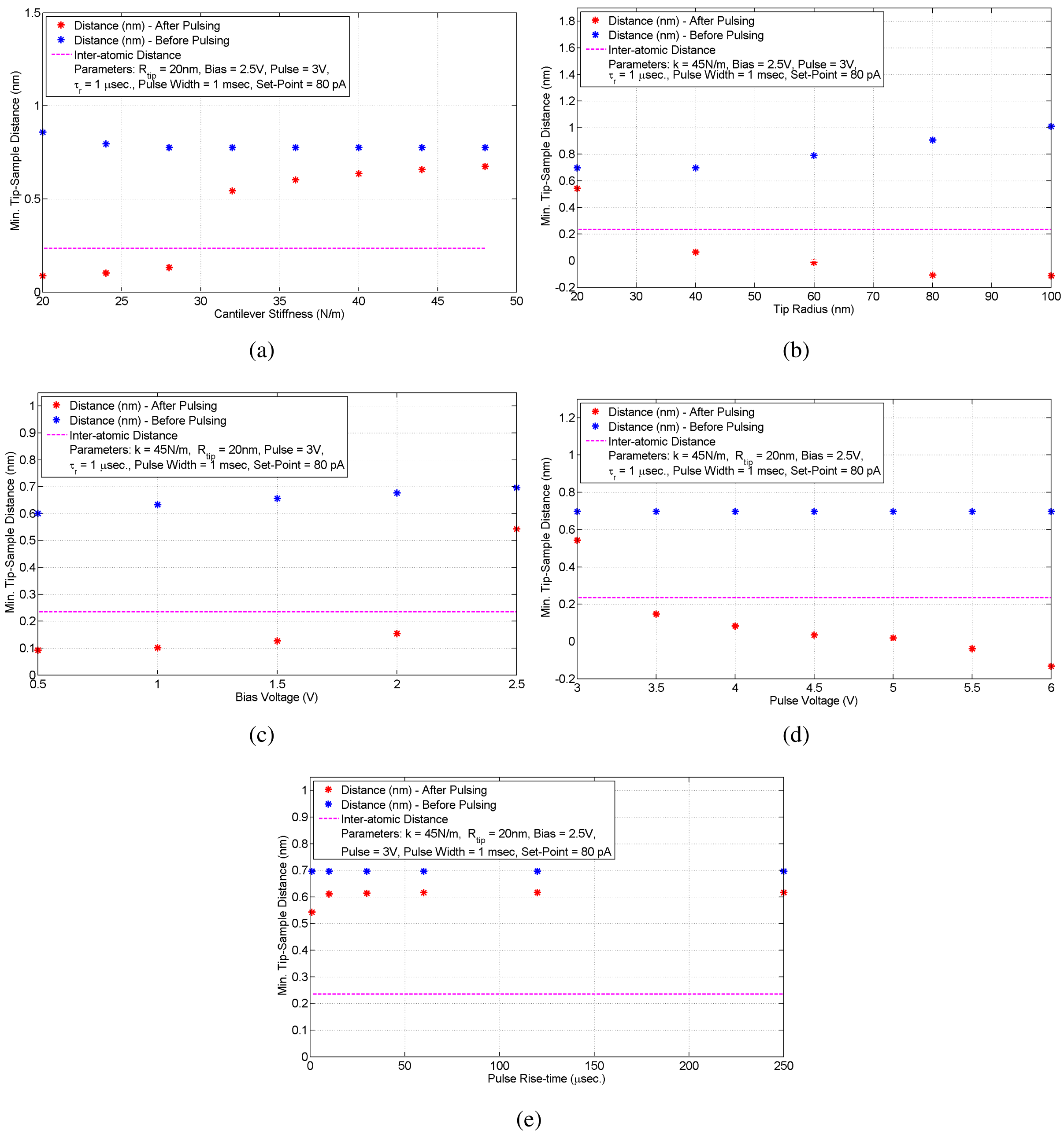

Figure 4.26: The effects of several parameters on pulsing using AFM cantilevers. Blue markers denote the equilibrium distance between tip and the surface during imaging. Red markers denote the minimum distance between tip and the surface during pulsing. Purple dashed line is the inter-atomic distance. If a red marker is under the purple dashed line, the corresponding parameters cause the tip to crash into the sample during pulsing.

microseconds, however this time scale pulses are hard to achieve with a DAQ board. On the other hand, with the compromise of cost and complexity, pulse generators can be used to apply shorter pulses to change the maximum deflection of the cantilever during pulsing. To show this difference, a sample plot of a short pulse of 2 volts for the duration of 100 nanoseconds on the same cantilever is shown in Fig. 4.27. In order to investigate the effect of short pulses in a more comprehensive way, a series of simulations are performed and the results are listed in Table 4.3.

Table 4.3: Simulated Maximum Deflection Values for Short Pulses (nm)

		Pulse Voltage (V)	
		2	8
Pulse Time (nsec)	100	0.005	0.059
	300	0.014	0.315
	600	0.048	0.453*

* Tip snapped into contact

The results of the simulations shown in Table 4.3 reflect that applying very high voltage pulses such as 8 volts are even possible using cantilevers as long as the pulse duration can be kept very short. Hence the equipment used to induce pulses using AFM cantilevers can also be considered as a design parameter of the system and high speed pulse generators can be interfaced with the STM control hardware and the software in order to apply high voltage pulses while using AFM cantilevers as STM end-effectors. We should also note here that, we haven't tried pulsing with CAFM probes due to the expense of the required equipment and change of research plans towards the local anodic oxidation studies. The main reason for the change of focus in the research was the fact that structures that can be made out of pure silicon are useless in a device perspective.

4.6.4 Modeling of Titanium Oxidation Using CAFM Probes

All of the simulation results that have been presented so far assume the operation is carried under ultra-high vacuum. However, titanium oxidation process and local anodic oxidation in general is carried in ambient conditions because of the need to have water meniscus on the surface as the

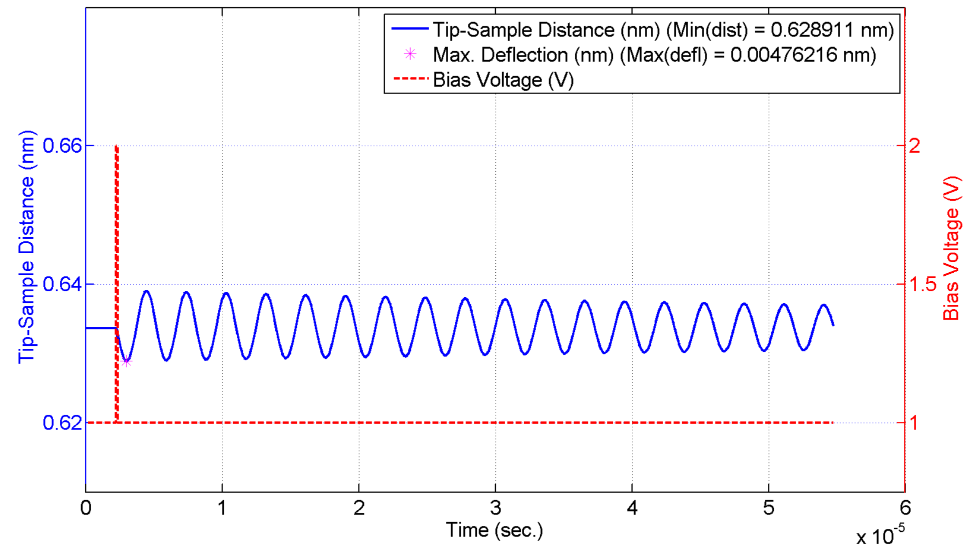

(a)

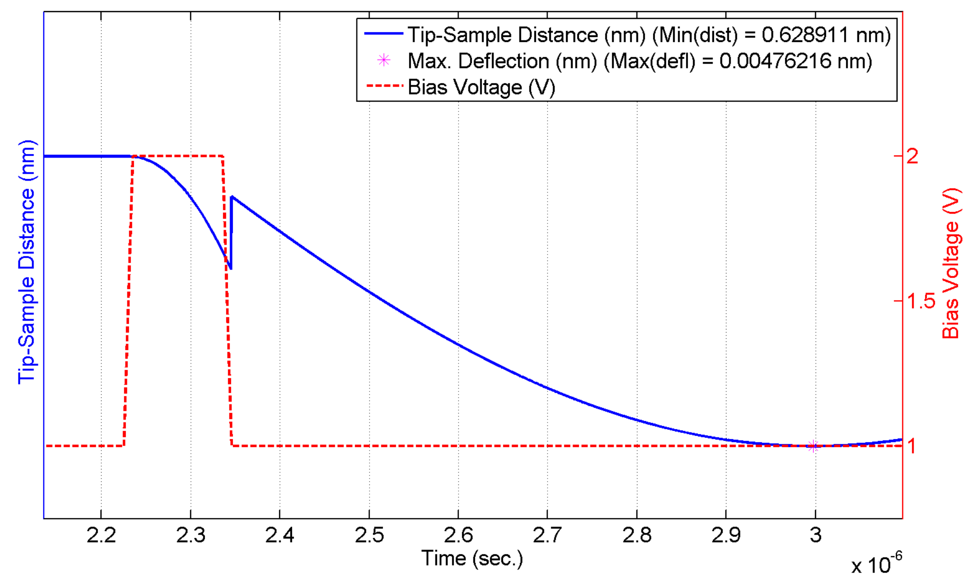

(b)

Figure 4.27: (a) A sample short duration pulse. The deflection of the AFM cantilever is considerably lower compared to long pulses. The oscillations are more pronounced since the simulation time is 2 orders of magnitude shorter compared to long pulses. (b) Zoomed in view of the same plot around the pulse.

electrolyte. This water meniscus causes capillary forces to exist between the CAFM probe tip and the titanium surface during manipulation operation. In order to make the model accurate for titanium manipulation case, this capillary force needs to be modeled as well.

In order to model the capillary forces, we start with finding the water layer thickness on the surface. Since the capillary force only exists when the two meniscuses are touching, this thickness will act as an on/off switch for the existence of this force. The water layer thickness on a surface can be calculated as [112]:

$$r_1 = \frac{2\gamma_L V}{RT\log(RH)}, \tag{4.2}$$

where r_1 is the thickness of the water layer on the surface, γ_L is the liquid surface tension (for our case, surface tension of water $= 0.072$ N/m), V is the liquid volume, R is the universal gas constant ($= 287$J/(kg K)), T is the temperature of the environment and RH is the relative humidity.

Using the $r1$ value, capillary force can be calculated as [112]:

$$F_{\text{Cap}}(z) = -4\pi\gamma_L R_{\text{tip}}\text{cos}\theta \frac{1}{1 + \frac{z}{2r_1\text{cos}\theta}}, \tag{4.3}$$

where z is the tip-sample separation, R_{tip} is the tip radius and θ is the contact angle of the surface.

Using these equations, we calculated the non-contact forces acting on a CAFM probe during operation in ambient conditions as shown below in fig 4.28. The parameters are all nominal parameters stated before in tables 2.1 and 2.2. The new parameters needed for the simulations are given below in table 4.4. Figure 4.28(a) shows the case of a gold sample and platinum/iridium coated tip and Fig. 4.28(b) shows the case of a titanium sample and diamond coated tip.

As can be seen from the force plots, the magnitude of the capillary force during titanium oxidation is comparable to the other forces, therefore it cannot be neglected. Therefore they should be considered when one models the snap-into contact behavior of CAFM probes in ambient conditions. However, one problem arises when this updated force model is implemented to find the

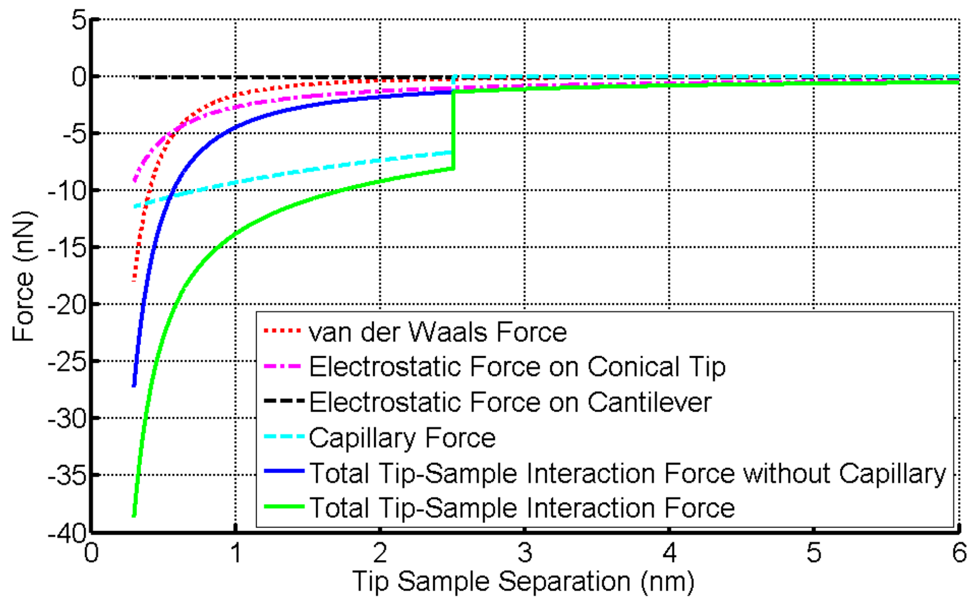

(a)

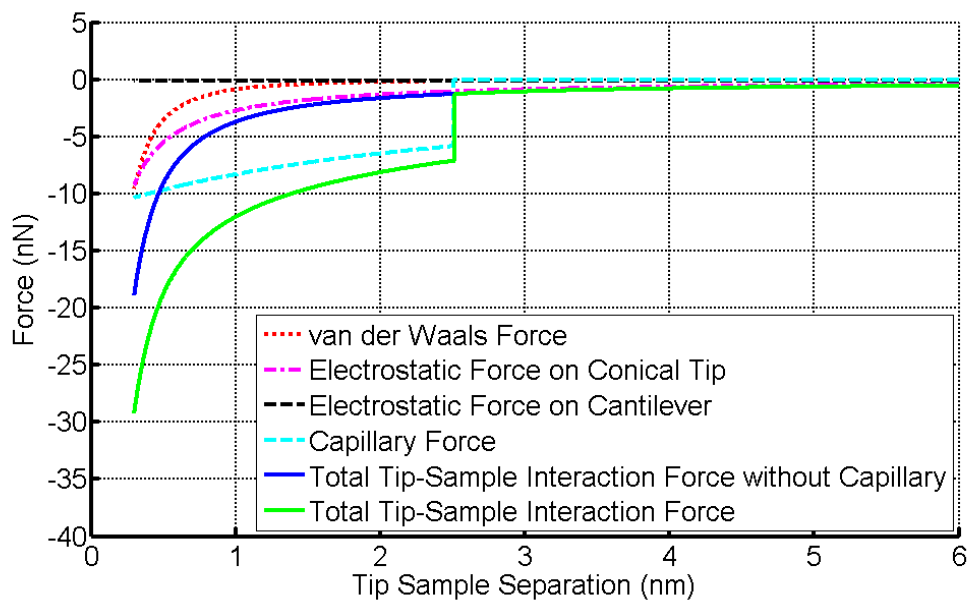

(b)

Figure 4.28: (a) Forces experienced during manipulation operation on a gold surface using a platinum-iridium coated CAFM probe. The capillary force is also included. (b) Forces experienced during manipulation operation on a titanium surface using a diamond coated CAFM probe. The capillary force is also included. Hamaker constant of titanium is taken as $A_H = 153$ zJ [64].

Table 4.4: Parameters for Capillary Force Calculation

Parameter	Value	Unit	Description
θ_{Au}	56 (from [90])	Degrees	Contact Angle of Gold
θ_{Ti}	59.3 (from [95])	Degrees	Contact Angle of Titanium
RH	65%		Relative Humidity

snap into contact distance of the CAFM probe tips. Since the capillary force is not continuous, its derivative does not exist. Therefore, it cannot be compared directly with the cantilever stiffness to find the snap into contact distance. In reality, this discontinuity will result in very high contact stiffness values at the point of discontinuity and probably will cause the probe tips to snap-into contact much before the UHV model predicts.

In order to predict the snap-into contact distances of probes during titanium oxidation, this model should be used. This part of the thesis is left as a future work.

4.7 Experimental Results

To prove the procedures we defined to manipulate silicon and titanium surfaces, we have performed several proof-of-concept experiments using RHK SPM, its own controller and the custom control system. In addition to these manipulation experiments, we conducted experiments to verify the force and snap-into contact model. Moreover, the effect of set-point force during CAFM mode LAO and the effected of manipulation voltage during STM mode LAO are investigated. The results of these experiments are presented in this section.

4.7.1 Silicon Manipulation Using Short Electrical Pulses

Using the manipulation algorithm specified in 4.4.1, we performed several experiments to write lines on the hydrogen passivated silicon surface and observed that the process is repeatable. An image of the patterned area following one of these experiments is shown in Fig. 4.29. To increase the visibility of the written lines in the image, the gradient of the topography image is shown.

During this experiment a total of 48 lines are written (12 long, 36 short) in a 330 nm $\times$ 330 nm area. The lines are written in 6 smaller neighbor regions and a final image of the total region of interest is taken after the lines are written. The time spent to write a line is around 30 seconds.

It should be noted here that, although depassivation is a subtractive patterning method, the written lines are sensed as topographically higher points than the passivated surface. This is due to the conductivity difference between the passivated and depassivated regions. The passivated surface parts are less conductive, leading to a lower topographical image because the flowing current with the same voltage in the passivated areas are lower.

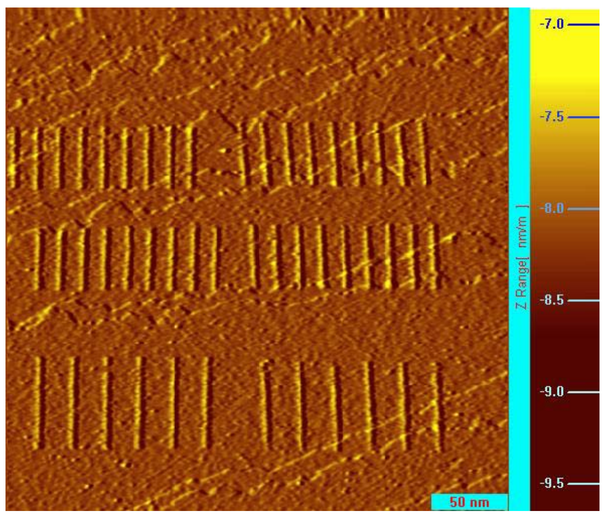

Figure 4.29: 330 nm $\times$ 330 nm gradient STM image of lines written on a hydrogen passivated Si(100) (Si(100) 2$\times$1:H) surface under UHV. The image is taken using a Pt-Ir STM tip, at bias voltage of -1 V and set-point current of 150 pA and the lines are written using +4.5 V, 2 millisecond long pulses on the lines. The distance between two neighboring pulses on the same line is 2 nm.

Although the manipulation is repeatable, passivation of silicon with hydrogen, which is a step needed to prepare the sample is not so repeatable. We suffered during these experiments to reproduce the sample. Adding this problem to the aforementioned problems of not being able to manufacture devices from just silicon and not being able to pulse using conductive AFM probes, we abandoned this manipulation study after these experiments, which proofs that such a manipulation is possible.

4.7.2 Titanium Manipulation Using High Electric Fields

Using the manipulation algorithm specified in 4.4.2, we performed several experiments to write lines on titanium surface and observed that the process is repeatable. To start with, we have deposited rectangular titanium regions whose widths are 2 μm and thicknesses are 5-6 nm on a silicon dioxide surface. We then imaged these surfaces in AFM mode under -1 V bias voltage. We then performed manipulation operation using ambient RHK SPM and custom control system as linear or circular patterns on titanium and imaged the surface in AFM mode to verify manipulation. Figure 4.30(a) shows a line oxidized on titanium region using a CAFM probe in CAFM mode. The manipulation voltage was 10 V and the tip speed was 100 nm/s. The width of the CAFM oxidization line is found to be 253.6 nm.

We have also recorded the current image after the manipulation is done. As can be seen from Fig. 4.30(b), current flows in the regions left of the oxidation line, however after the oxidation line there is no current since the path between the bias port and the sample is broken due to the resistance of the oxidization. We calculate the resistance of the oxidation line using these images by simply subtracting the resistance of the left hand side of the titanium from the right hand side of the titanium with respect to oxidation line. In addition, we record the current data during CAFM mode oxidation to get an idea of the amount of the current flow that occurs during oxidation operation. The current data for this oxidation line is shown in Fig. 4.30(c). The oxidization current is calculated from this data; by simply finding the average current while the tip is over the titanium surface and over the silicon dioxide surface and subtracting these two values. For this oxidization trial, the net oxidization current is 0.12 nA.

Using the same type of sample and conducting AFM probe, ambient RHK SPM, and custom control system, we also performed STM oxidation trials. We imaged the surface in AFM mode since the sample is electrically heterogeneous, then we switched to STM mode while the tip is over the dog bone and conducted the manipulation operation in a circular path and then switched back to AFM mode and imaged the surface one more time to verify manipulation. Figure 4.31(a)

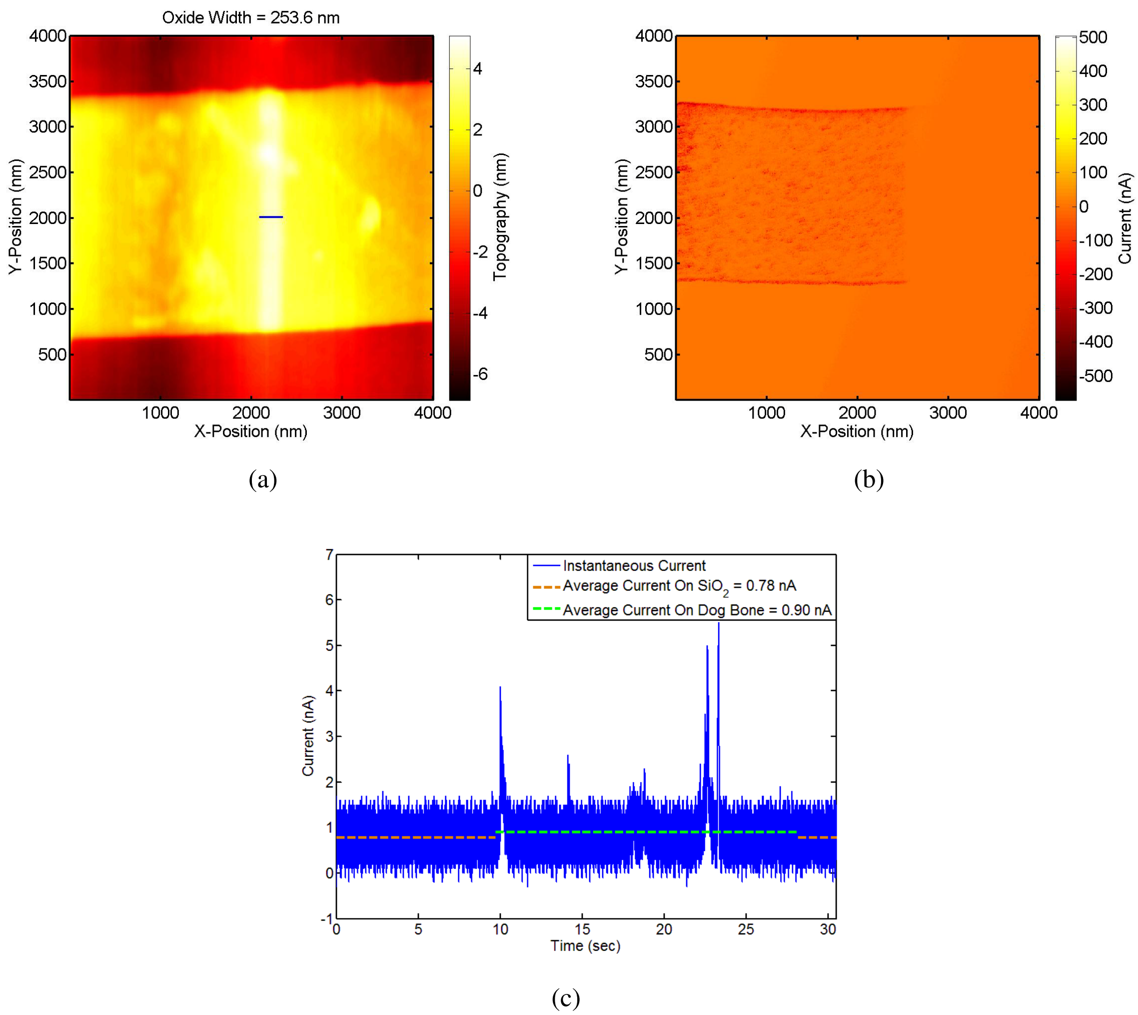

Figure 4.30: AFM image and data of a linear path oxidized in CAFM mode. (a) Topography image. Using this image we calculate the width of the oxide line. (b) Current image. Using this image we calculate the resistance of the oxide line. (c) Current reading during oxidation. This data provides important information regarding the current generated during oxidization procedure.

shows a circular pattern oxidized on titanium region using a CAFM probe in STM mode. The manipulation voltage was 3.5 V and the tip speed was 50 nm/s. The width of the STM oxidization feature is found to be 90 nm this time, which is almost a three times reduction compared to CAFM mode.

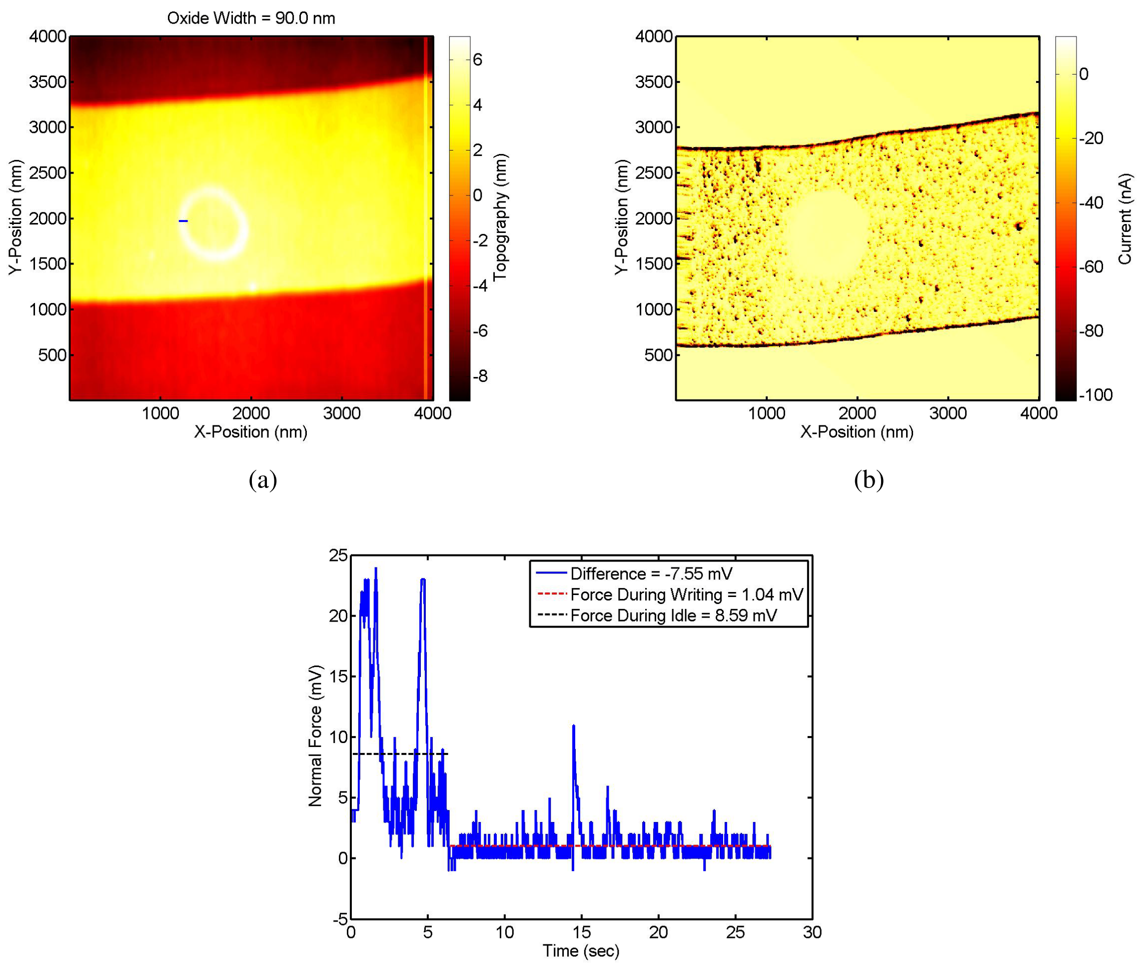

(a) (b)

(c)

Figure 4.31: AFM image and STM data of a circular path oxidized in STM mode. (a) Topography image. Using this image we calculate the thickness of the oxide donut. (b) Current image. Using this image we calculate the resistance of the oxide donut. (c) Force reading during oxidation. This data provides important information regarding the force experienced by the compliant probe during STM mode oxidization procedure.

We have also recorded the current image after the manipulation is done. As can be seen from Fig. 4.31(b), current flows in the regions outside of the oxidation pattern, however there is no current inside the oxide circle since the path between the bias port and that part of the sample is broken due to the resistance of the oxidization. We calculate the resistance of the oxidation line using these current images by simply subtracting the resistance of the outside titanium from the inside titanium with respect to oxidation circle. In addition, we record the force data during STM mode oxidation to get an idea of the forces experienced by the CAFM probe during oxidation operation. The force data for this oxidation line is shown in Fig. 4.31(c). The oxidization force is calculated from this data; by simply finding the average force while the voltage between the tip and the sample is at bias voltage and the voltage between tip and sample is at manipulation voltage and subtracting these two values. For this oxidization trial, the net oxidization force is -7.55 mV which corresponds to an attractive 172.79 nN.

4.7.3 Snap-into Contact of a Compliant Probe under Bias Voltage

In order to verify the force model proposed, we compared the simulated snap-into contact distances for three different stiffness cantilevers (Bruker Probes SCM-PIT, 1-5 N/m, MicroMash NSC14/Pt, 1.8-12.5 N/m, and Bruker Probes DDESP-10, 20-80 N/m) with experimental results. The experiments were conducted with the same SPM the silicon (100) surfaces imaged. For every cantilever, ten force-distance curves were acquired for every bias voltage point (0-4 V with 0.2 V increments) and the distance where the cantilever snapped-into contact with the sample was found. The cantilever stiffness values, calibrated using Sader's method [100], were found to be 4.1 N/m, 6.9 N/m, and 64.8 N/m, respectively.

To obtain the model results for the same set of points, we needed to determine the values of the parameters of the model. The parameters can be divided into two groups: material dependent parameters and geometry dependent parameters. The values of the material dependent parameters were taken from literature with one exception of the Hamaker's constant of Platinum/Iridium and Gold interface, which is not reported in literature. Therefore, we found the value of this parameter by fitting the simulation results to the experimental data using only the 0.0 V and 4.0 V snap-into contact points of the soft probe results which has a tip coating of PtIr. On the other hand, most of the geometry dependent parameters like cantilever width and length are acquired using scanning electron microscope (SEM) images of the cantilevers and the stiffness values of the cantilevers are calibrated using Sader's method, as suggested above. The remaining geometry dependent parameters namely, cantilever angle, tip angle, and the tip radius, are harder to acquire. Among these parameters, we used manufacturer specified values for the cantilever and tip angles. The tip radius values were found by fitting the simulation results to the experimental data using only the 0.0 V and 4.0 V snap-into contact points for all three cantilevers. We chose to fit the tip radius because it affects all of the forces (elastic contact force, inter-atomic force and electrostatic force) whereas tip angle only changes electrostatic force between tip and the sample and cantilever angle only changes electrostatic force between the cantilever and the sample. Therefore, tip radius is the most appropriate parameter to use for this fitting. All of the parameters used in the simulations are listed in tables 2.1 and 2.2. Figure 4.32 shows the result of this comparison.

The tip radii were found as 34.5 nm, 12.9 nm and 20.7 nm for soft, mid-stiffness and hard cantilevers, respectively, which are close to the manufacturer reported values of < 25 nm, < 25 nm and < 50 nm, respectively. The Hamaker's constant of PtIr was found as 224.7 zJ, which is in the 200-400 zJ range of reported values of Hamaker's constant for platinum [118, 129, 133]. Both simulation and experiment results for the hard cantilever shows no snap-into contact behavior hence the snap-into contact distances for every voltage value is equal to the inter-atomic distance value of 0.288 nm. The reason behind the hard cantilever not snapping-into contact is simply the fact that the gradient of the probe-sample force does not reach the high cantilever stiffness, hence does not cause any instability. On the other hand, for soft and mid-stiffness cantilevers, the stiffness values of the cantilevers are not high enough to ensure stability. Considering only 0.0 V and 4.0 V points of each plot are used for fitting the tip radii, the fact that the model predicts both the shape and the magnitude of voltage versus snap-into contact distance curves successfully is

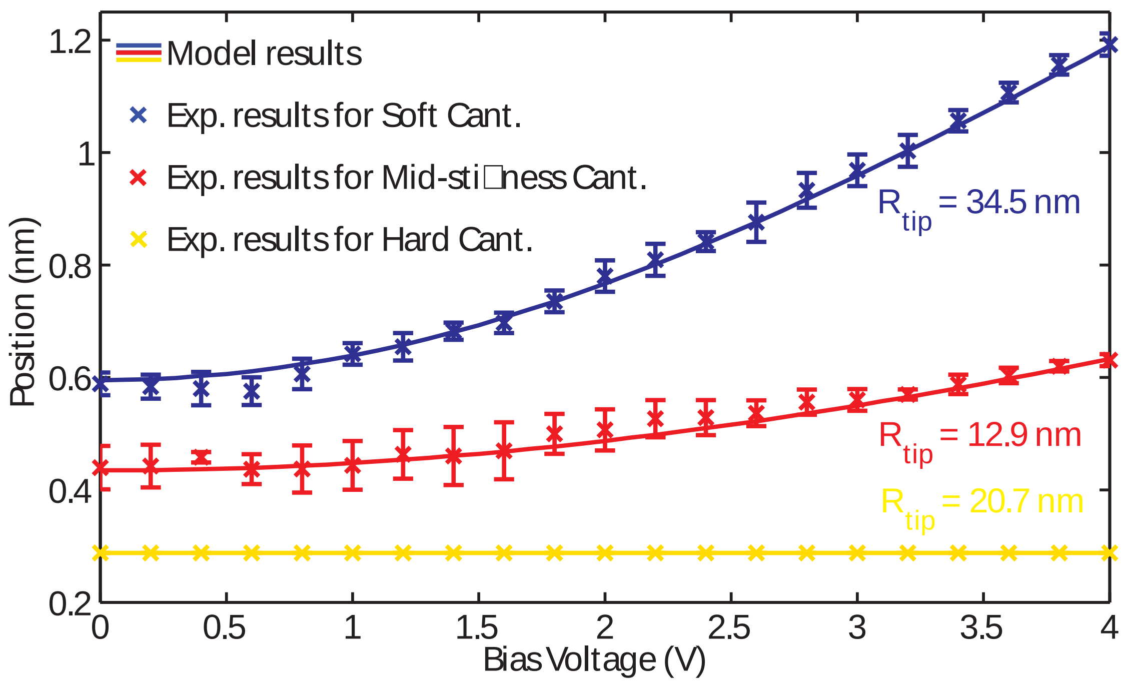

Figure 4.32: Experiment results (10 data points at each error bar) and their comparison with model. The tip radius values are fitted to the model and the resulting radii are also shown in the figure.

the indication that the model is accurate.

4.7.4 Effects of Oxidation Parameters on Titanium Manipulation

In addition to the proof of concept experiments presented in 4.7.2 that shows the capabilities of our system in terms of LAO on titanium surfaces, we conducted a series of experiments to investigate the effects of normal force applied during CAFM mode oxidation and manipulation voltage applied during STM mode oxidation on oxide feature properties.

The first set of experiments that we conducted was done in CAFM mode using a 35.5 N/m CAFM probe with a diamond coated tip (Bruker Probes, DDESP) on 5-6 nm thick, 2 μm wide rectangular titanium regions deposited on silicon dioxide. The cantilever stiffness is found using Sader's method. We used custom control system and RHK SPM operating under ambient conditions with 50%-65% humidity. The samples were imaged, then a linear path on the titanium is oxidized, and an "after" image is taken under -1 V bias voltage. Oxide line widths, oxidization current values, oxide resistance and resistivity values are found as described in 4.7.2. Manipulation voltage was held at 10 V for each run and a tip speed value of 100 nm/s is used. 5 different set-point normal force values were used for CAFM oxidization experiments which were 229 nN, 343 nN, 458 nN, 572 nN and 687 nN. These values correspond to 10 mV, 15 mV, 20 mV, 25 mV and 30 mV laser deflection readings. 4 experiments are conducted at each set-point normal force value. The results of these experiments are shown in Fig. 4.33.

We could not find any relation between the normal set-point and the oxide line width and oxidization current, as can be seen from Figs. 4.33(a) and 4.33(b), consecutively. Oxide line width values were high and seem not to vary significantly with different normal force set-point values which led us believe that the oxidization width is mostly a function of the tip radius rather than the set-point. On the other hand, we found an inverse relation between the normal force set-point value and the oxide resistance and resistivity, as can be seen from Figs. 4.33(c) and 4.33(d); respectively. We believe the reason of such relation is the fact that LAO needs the water

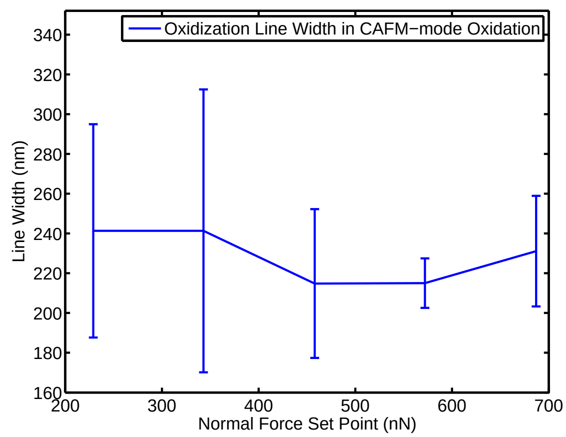

(a)

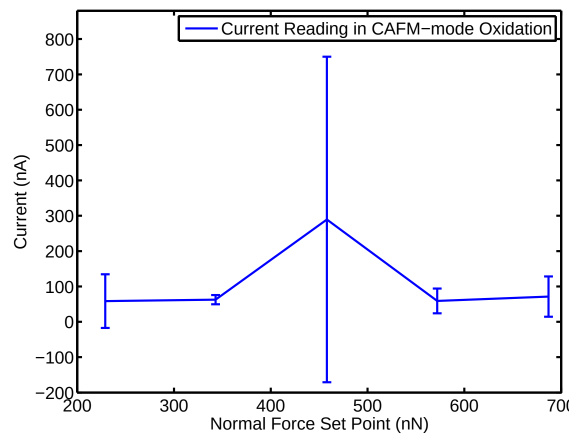

(b)

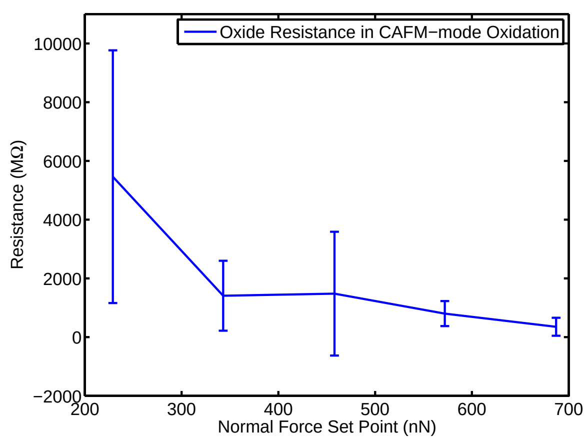

(c)

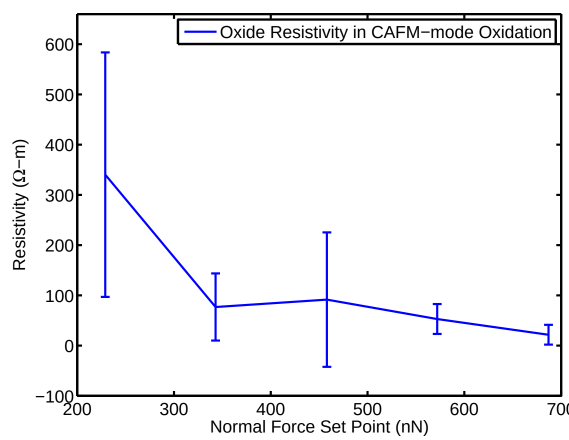

(d)

Figure 4.33: Analysis of the lines written on a titanium dog-bone structure using a conductive AFM probe in CAFM mode. Every error bar is calculated from 4 data points. Oxidization voltage was 10 V and cantilever stiffness was 35.5 N/m. (a) Oxidization line width with respect to different normal force set-points. (b) Oxidization current with respect to different normal force set-points. (a) Oxide resistance with respect to different normal force set-points. (a) Oxide resistivity with respect to different normal force set-points.

meniscus to oxidize the surface; however, the meniscus is pushed away from the contact as the cantilever is pressed more and more into the surface.

The second set of experiments was conducted in STM mode using the same CAFM probe on the same surface. We used custom control system and RHK SPM operating under ambient conditions with 50%-65% humidity. The samples were imaged in AFM mode, then a circular path on the titanium is oxidized in STM mode, and an "after" image is taken in AFM mode under -1 V bias voltage. Oxide circle widths, oxidization force values, oxide resistance and resistivity values are found as described in 4.7.2. Manipulation current was held at 1.5 nA for each run and a tip speed value of 50 nm/s is used. 5 different manipulation voltage values were used for STM oxidization experiments which were 3.5 V, 4.5 V, 5.5 V, 6.5 V and 7.5 V. 4 experiments are conducted at each manipulation voltage value. The results of these experiments are shown in Fig. 4.34.

We found linear relation between the manipulation voltage in STM mode and every analyzed oxide feature property, namely line width, oxidization force, oxide resistance and oxide resistivity, as can be seen from Figs. 4.34(a), 4.34(b), 4.34(c), and 4.34(d); respectively. The results show that as the manipulation voltage increases the line widths of the oxide patterns increase. We believe this is due to the increase in the electron beam radius during STM oxidization. The resistance and the resistivity of the oxide features also increase with increased manipulation voltage, which means the quality of the oxidization is better.

The most surprising result among all these experiments were the oxidization force with respect to the oxidization voltage. These force values are net values calculated by subtracting the mean force during STM operation at bias voltage from STM operation at manipulation voltage. Our results show that at low manipulation voltage values, CAFM probe experiences an attractive force during oxidation. However at 6.5 V and 7.5 V values, CAFM probe starts experiencing a more repulsive force. In other words, CAFM probe experiences a more repulsive force during oxidation as the manipulation voltage increases. We believe the reason for this behavior is the

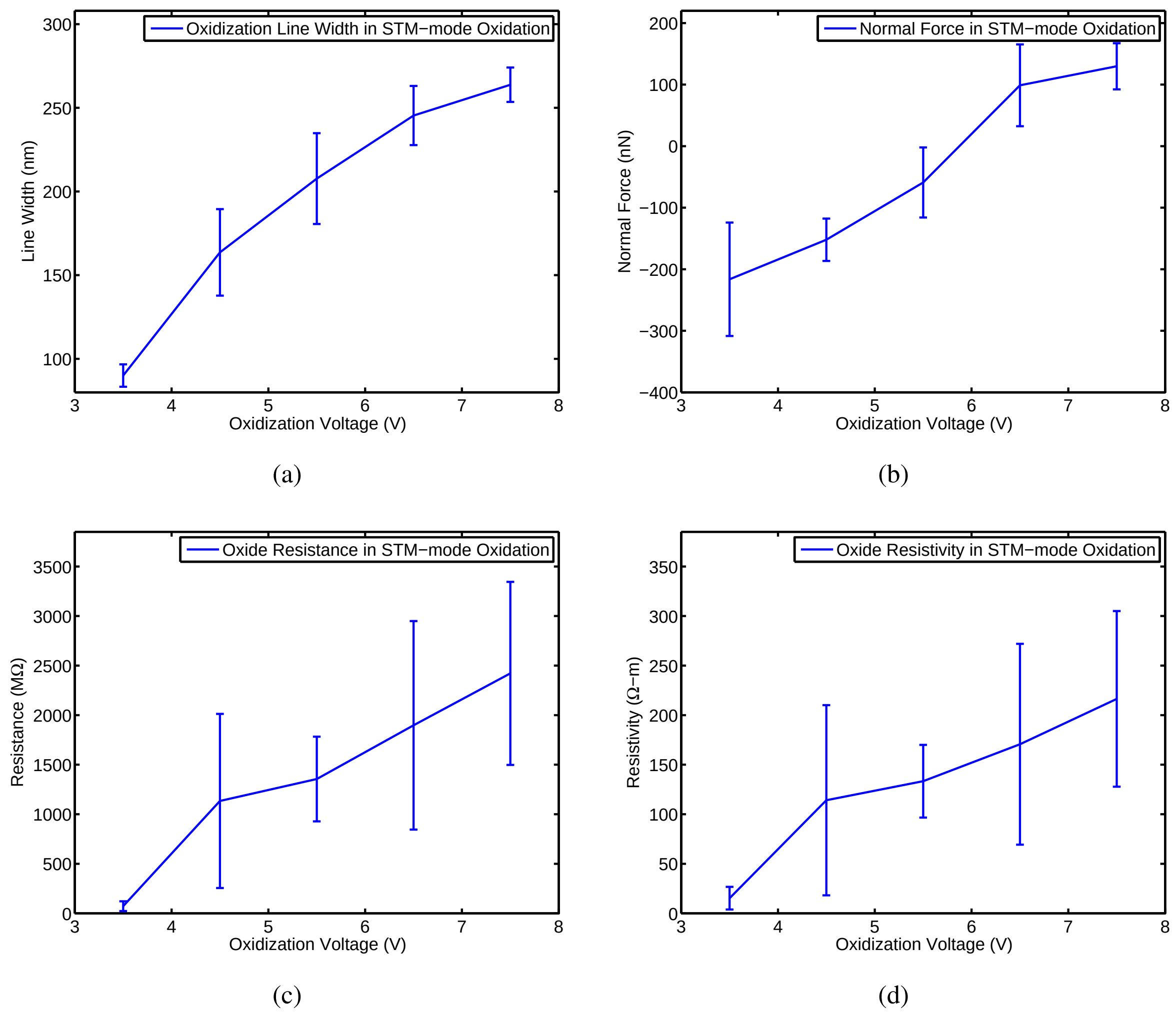

Figure 4.34: Analysis of the lines written on a titanium dog-bone structure using a conductive AFM probe in STM mode. Every error bar is calculated from 4 data points. Current set-point during writing was 1.5 nA and cantilever stiffness was 35.5 N/m. (a) Oxidization line width with respect to different oxidization voltages. (b) Oxidization force with respect to different oxidization voltages. (a) Oxide resistance with respect to different oxidization voltages. (a) Oxide resistivity with respect to different oxidization voltages.

increase in the resistivity of the region oxidized. The CAFM probe tip is touching the surface during oxidization operation however since the region is oxidized a lot of current does not flow through the contact; hence the controller can keep the current at the set-point value. As the manipulation voltage increases, the cantilever pushes itself more into the surface because the region oxidized has a higher resistivity. Therefore the CAFM probe experiences a more repulsive force with higher manipulation voltages.

The results also show that STM mode oxidation results in smaller structures at lower manipulation voltages. It also shows more controllability on oxide feature properties. CAFM mode oxidation has no advantage over STM mode oxidation other than being easier for most control systems to achieve since most commercial systems do not have instant switching capabilities that would allow them to operate on an electrically heterogeneous surface like ours.

4.8 Summary

This chapter demonstrated the procedure of electrical manipulation of surfaces using an SPM. Silicon samples are imaged using constant current mode STM and atomic resolution is achieved both with STM tip and CAFM probes as STM end-effectors. A custom control system is developed to control the SPM with more flexibility and faster control loop. Two different manipulation techniques are presented: manipulation of silicon surfaces using short electrical pulses under UHV and manipulation of titanium surfaces using high electric fields under ambient conditions. Both manipulation techniques are proven to work via experiments.

During manipulation using short electrical pulses, the silicon samples are passivated and patterns on the surface are formed. For demonstration, silicon surfaces and hydrogen masks are used; however the manipulation scheme can be applied to different conductive or semi-conductive substrates. These demonstrations are performed using STM tips as end-effectors. For manipulation using high electric fields, titanium samples are used in LAO technique. The manipulation scheme can be applied to different metals which can be oxidized using LAO. The demonstrations are performed using CAFM probes as end-effectors and in CAFM and STM operation modes. The effects of normal set-point force during CAFM mode oxidation and manipulation voltage during STM mode oxidation on oxide feature properties are experimentally investigated.

Moreover, a complete model of the STM system for imaging and pulsing, using STM tips or AFM cantilevers as end-effectors, is presented and used to analyze the feasibility of utilization of AFM cantilevers as STM end-effectors for imaging and manipulation of surfaces. The effects of several design and operation parameters of STM parts and CAFM probes to STM imaging and manipulation are investigated. The model is verified with experiments and then used to show that an optimal operating bias voltage can be found for STM operation using CAFM cantilevers. The model can also be used to find the minimum cantilever stiffness value for a given sample and operating bias voltage value. Given that the values of most of the parameters used in the model can be found from literature and cantilever stiffness values can be calculated using a normal stiffness calibration method, the only limitation of the model is seen as the uncertainty of the CAFM probe tip radius which we found by fitting the model to the experiments. This work could help researchers to choose an appropriate stiffness value for the end-effectors in a dual mode SPM that can work as either an STM or an AFM. Combined with the demonstration of atomic resolution STM imaging using AFM cantilevers, this is a step towards a multiple probe approach to increase the throughput of STM operation.

Demonstrating the possibility of a fast and reliable SPM based electrical manipulation system with high throughput would increase the use of SPM for micro/nano-manufacturing applications where SPM would be inexpensive than most of the techniques and machines, which are currently used for nanofabrication. With the increase in its throughput, SPM would be an invaluable tool for nanofabrication due to its capability of performing manipulation in nanometer to atomic scale. Hybrid manufacturing systems that use MEMS techniques to manufacture micron scale structures and SPMs to manufacture smaller scale structure can be built. Moreover, utilization of CAFM probes as STM end-effectors can lead to a dual mode SPM which can switch instantaneously between AFM and STM mode operations. This potential dual mode SPM can operate as an AFM or STM at a given time for nanoscale imaging or manipulation without changing the end-effector. Such an operation would enable researchers to image a heterogeneous surface with both insulating and conductive parts and pattern the same surface using STM principles for advanced tip based nanofabrication applications.

Chapter 5

Conclusions

5.1 Summary of Accomplished Work

This thesis focuses on tip directed mechanical and electrical manipulation. During this study, we have attempted to develop a faster and more reliable manipulation system using SPMs. We have selected AFM based automated nanoparticle manipulation and STM based electrical manipulation of surfaces as two case studies, to show the feasibility of the ideas that we presented. Below is a list that itemizes the progress achieved toward a more reliable and faster manipulation system during this work:

- Presented a nanoparticle manipulation system with automated operation capability to increase the speed and reliability of the nanoparticle manipulation by significantly decreasing operator interaction time and human error during the operation.
- Demonstrated contact loss detection and particle center detection algorithms for nanoparticle manipulation. These algorithms increased the reliability of the nanoparticle manipulation and enabled the automation of the procedure.
- Demonstrated physical model of the AFM based nanoparticle manipulation which helps us investigate the underlying principles of nanoparticle manipulation and enables us to choose

optimal cantilevers required to achieve the manipulation operation.

- Investigated the speed and reliability of the automated nanoparticle manipulation system by conducting a series of experiments with different pushing angles and for different distances, and presented that the reliability is not affected by the pushing angle and the relative speed increases with the increase in distance.
- Developed a multiple particle manipulation algorithm that significantly improves the overall speed of the nanoparticle manipulation process for tasks that involve manipulating more than one particle to form assemblies or patterns.
- Presented the design of a new SPM control system and software, which enabled us to access all the signals anytime they are needed. It was faster and more flexible than the commercial controller of the SPM used for electrical manipulation case study.
- Demonstrated the possibility of atomic resolution imaging using AFM cantilevers as end-effectors in STM mode. This is considered as a step towards multiple probe imaging and manipulation in using STM that can be utilized to increase the throughput.
- Demonstrated the ability of surface modification via electrical pulses and high electric fields between the STM end-effector and the surface using STM tips and CAFM probes. This step forms the basis of the second case study, STM based electrical surface manipulation.
- Introduced a complete dynamics model of the electrical non-contact manipulation system for both imaging and pulsing operations, using STM tips and AFM cantilevers as end-effectors with three, different bandwidth, vertical positioning stages. This dynamics model is also verified by comparing and showing the agreement of the snap into contact distance results of the dynamics model with the results obtained from contact stiffness (i.e. energy balance) equations.
- Verified the force model for using CAFM probes as STM end-effectors for operation and

manipulation through snap-into contact experiments ran with 3 different stiffness cantilevers under different bias voltages.

- Investigated the effects of several parameters such as cantilever stiffness, tip radius, noise and stage bandwidth on STM imaging using AFM cantilevers via the dynamics model of STM operation using AFM cantilevers. The model also verified the feasibility of the idea, using AFM cantilevers as STM end-effectors for imaging.
- Investigated the effects of several parameters such as cantilever stiffness, tip radius, pulse time, pulse voltage, bias voltage and pulse rise-time on STM based manipulation by electrical pulses using AFM cantilevers via the dynamics model of STM manipulation using AFM cantilevers. The model also verified the feasibility of the idea, using AFM cantilevers as STM end-effectors for pulsing.
- Investigated the effects of set-point normal force and manipulation voltage on the properties of written features for conductive AFM mode and STM mode electrical manipulation of surfaces using conductive AFM probes for high electric fields.

5.2 Future Directions

5.2.1 Automated Mechanical Contact Manipulation of Nanoparticles

For autonomous nanoparticle manipulation, combining a Kalman filter or particle filter based drift compensation algorithm with the current system is the first step to build structures that consist of more than a few nanoparticles. After this addition, the manipulation of smaller subunits such as CNTs or nanoparticles of smaller diameter (5-30 nm) can also be attempted. For this task, AFM systems with better noise levels should be utilized.

If one uses a 3-D force sensing AFM probe, estimating the particle position online becomes possible for better speed and reliability. Also, other methods of manipulation such as a pick-and place operation can be investigated. Finally, an application of nanoparticle manipulation can be studied. Possible candidates include plasmonic circuit elements, micro/nanoscale mask or mold making for fabrication, or gluing/soldering applications.

Plasmonic applications might be the most interesting possibility. When a conductive nanoentity is exposed to light at a certain wavelength that is determined by its geometry and material properties, its free electron cloud can be excited to oscillate. This excitation can be transferred, focused, or even branched if these nanostructures can be placed at precise locations to form certain patterns. Making use of this phenomenon, one can build plasmonic elements of very small size to transfer information with fast speed.

Gluing or soldering micro/nanostructures using manipulated nanoparticles seems to be a possible short term application. For instance, while CNTs can offer high conductivity, their usage in future nanocircuits as interconnects may suffer from high contact resistances. This contact resistance problem can be reduced to acceptable levels by soldering metallic nanoparticles at the contact point by melting with high electrical currents. Similarly, produced simple nano-objects can be glued in position to form and assemble complex structures.

5.2.2 Electrical Non-contact Manipulation of Surfaces

The first future task that should be achieved is the implementation of a more complete model for titanium oxidation using CAFM probes as end effectors. The model that I implemented in previous chapter is a comprehensive model that includes the forces that are in play during UHV operation. On the other hand, titanium oxidation process occurs in ambient conditions where capillary forces exist. This difference is discussed in the modeling and simulation section of previous chapter; however the model is not fully implemented and simulated. The force equations are given for future researchers' convenience. The following studies on this topic should include the capillary forces to the model to implement a more comprehensive model of the titanium oxidation and snap into contact distances should be recalculated with the new force model for titanium oxidation studies.

In addition, to increase the speed and the precision of the electrical non-contact manipulation of surfaces using STM, an open-loop, model based, lateral control of the STM scanner should be implemented and an algorithm that would operate the STM autonomously during manipulation should be designed. In order to achieve this, non-linearity compensation based on open-loop, inverse model control is a good candidate. This control algorithm can be designed to characterize and compensate non-linearities by using image data other than using positioning sensor data as the feedback, since positioning sensors are not available in every system. In order to design this control algorithm, the scanner should be characterized using images of known patterns such as calibration patterns or atomic resolution silicon images. Repetitive control for manipulation tasks can also be investigated since manipulating the surface requires the scanner to follow paths repetitively, that would enable the use of iterative learning or repetitive control methods.

Moreover, electrical manipulation and STM operation using CAFM probe arrays should be investigated further. As a first step towards a multiple probe STM based electrical surface manipulation approach to increase the throughput of SPM based nanomanipulation tasks, we showed STM operation and manipulation using AFM cantilevers. So far, we have demonstrated atomic resolution imaging using stiff AFM cantilevers and presented proof-of-concept STM imaging and manipulation simulations and experiments that used CAFM probes as end-effectors. In order to take these results one step further, conductive AFM probe arrays should be manufactured and parallel STM operation and manipulation should be shown. Such a demonstration would have a big impact on tip based nanomanipulation research since it is a direct solution to the speed and throughput problems of these systems.

Last but not least, device applications using electrical manipulation of surfaces should be studied further. Several studies suggested single electron transistors [77] and metal-insulator-metal diodes [76] can be manufactured using tip based manipulation. If such devices can be manufactured with a high yield rate at higher speeds, the significance of tip based manufacturing will be demonstrated. Also, advantages like the precision and the device size of the tip based manufacturing process will make the tip based manufacturing systems a viable option for manufacturing such devices.

5.2.3 Custom Control System and Oscan V2.0

Before continuing with the improvement suggestions, one problem should be noted that might prevent future researchers to achieve a better controller implementation in RHK SPM and the custom control system. The FPGA on the DAQ board, which has the lower level coding on it, ran out of space. Therefore, implementation of any new algorithms is on hold at this point. The solution for this problem is to buy an identical FPGA based DAQ board and divide the low level code into two pieces. Such a solution requires funding but very little effort because the low level code already is in two pieces: lateral loop and the vertical loop. These two loops can easily be run on two separate FPGAs. The only change that should be made is the synchronization of two DAQ boards.

Another good feature to have in the control system would be a logarithmic feedback. Tunneling current generated during STM operation is exponentially dependent on the tip-sample separation and this current value is used to control the tip height. In other words, the system is non-linear but is controlled with a linear PI controller. The easiest solution to this problem is to make the system linear by passing the current reading through a logarithm function. Since an exponential function will be fed to a logarithm, the resulting values would have a linear relation with tip-sample separation. In this case, the linear PI controller is expected to work in a better, more stable manner.

Appendix A

Custom Control System and Oscan V2.0 Software User Manual

I have written this user manual for the control system developed in Tip-directed Field emission Assisted Nanofabrication (TFAN) project. The control system is custom built from electronics purchased and software is written mostly by me. If you are a new user, read this manual completely and carefully because I tried to write the manual as detailed as possible. If you are a new developer that is trying to make changes on the software or hardware, feel free to contact me with your questions after reading this manual.

A.1 Custom Control System Hardware

This part of the manual covers the hardware used to build the custom control system. Custom control system generates all the signals necessary to drive the actuators on the system (except z-modulation actuator which provides high frequency oscillations to the cantilever for non-contact/tapping mode) and acquires all the signals that should be read for imaging. A schematic of the control system is shown in Fig. A.1

In order to understand how the hardware is selected and connected, we should first explain

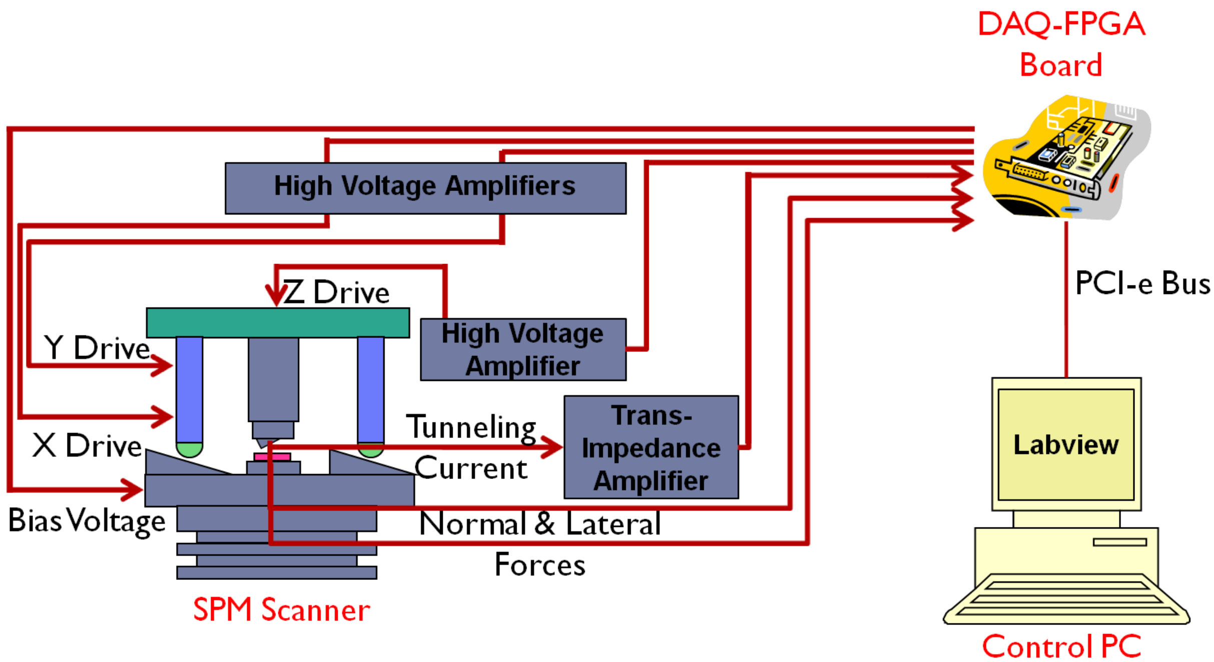

Figure A.1: A schematic of the control system.

how the system works. The scanner is a beetle walker that is engaged on a sample holder with ramps on the side. In order to achieve coarse positioning, the beetle walks up, down or lateral; which is achieved by applying a saw-tooth wave to the scanner legs. In order to achieve fine positioning for imaging, the beetle bends its legs; which is achieved by applying a triangular wave to the scanner legs. A schematic of this motion modes are shown in Fig. A.2

There are a total of 17 actuators on a RHK beetle scanner. It has 3 legs which has 5 actuators each and 2 additional vertical actuators. The legs are individual tube scanners, which means they have actuation in x and y by employing 2 actuators in each direction and an additional vertical actuator in the middle of these legs. The 2 vertical actuators that are located at the center of gravity of the beetle are the z-modulation and z-scan actuators. Z-modulation is a single stack piece which can achieve high frequency vertical motion in order to oscillate the cantilever for dynamic AFM modes. Z-scan is a double stack piece which can achieve fast vertical motion and is used for imaging. The three vertical actuators located at the center of each tube scanner are electrically shorted to each other, and they are named z-offset. Z-offset actuators have almost

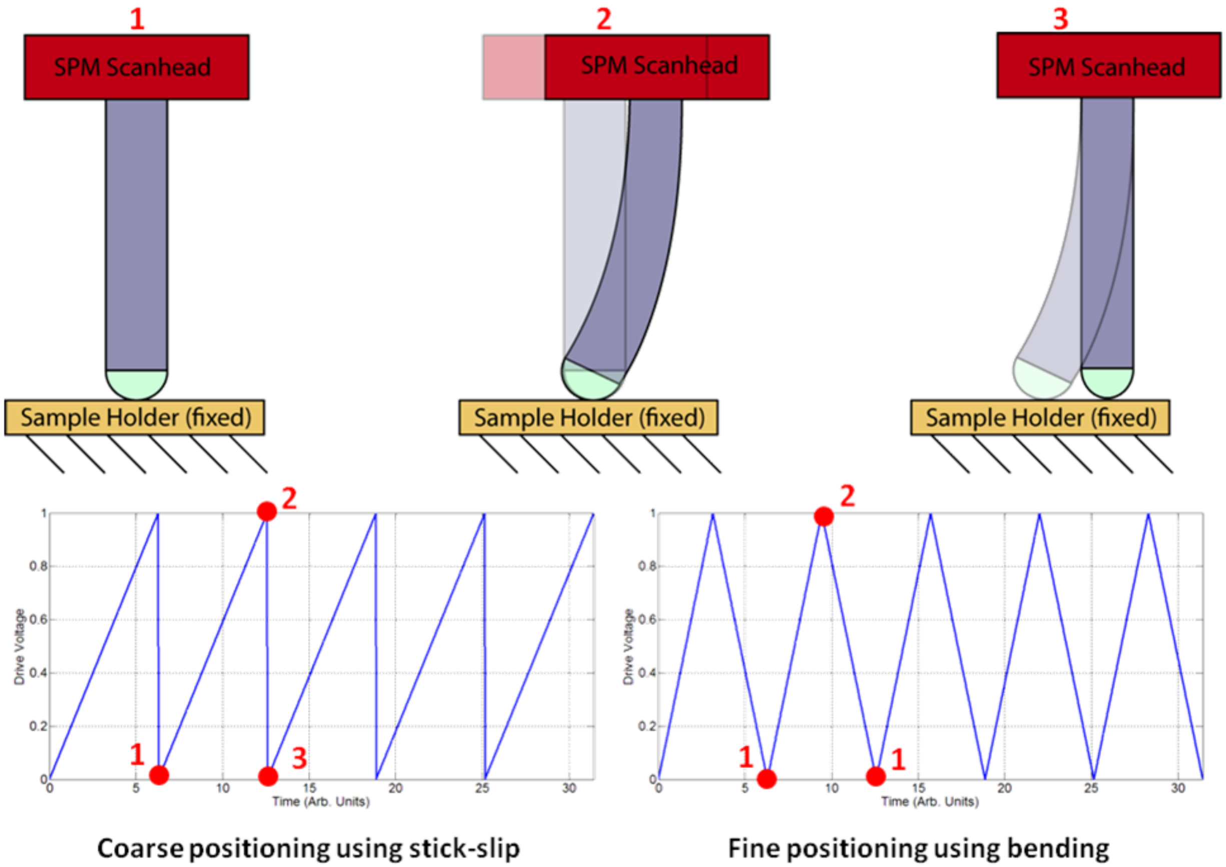

Figure A.2: How the coarse and fine positioning motions are achieved with the scan head.

double the range of z-scan and they are used to adjust the z-scan actuator to the middle of its range when desired. The remaining 12 actuators are used for coarse and fine positioning of the tip in x and y directions. A diagram of the beetle scanner actuators are shown in Fig. A.3.

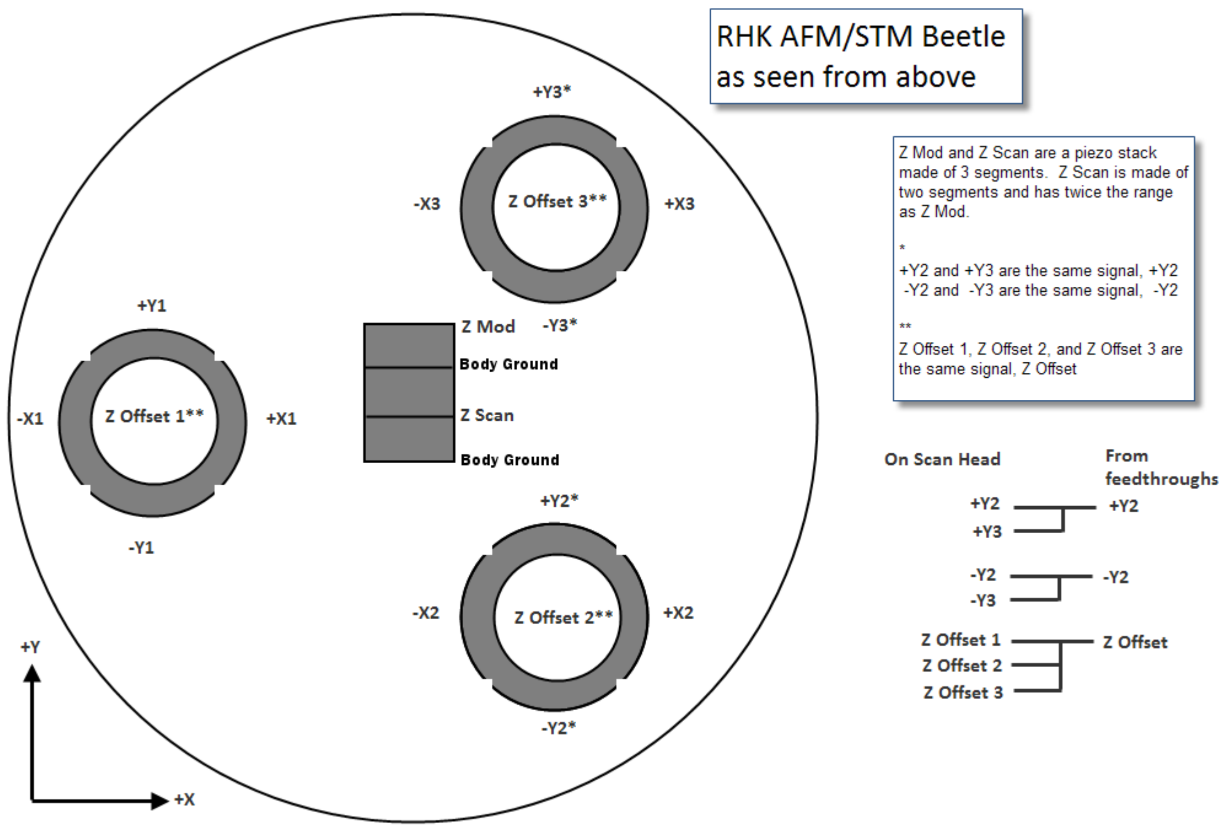

Figure A.3: Actuators located on the beetle scanner.

In order to control the 12 actuators that controls the x and y positioning, normally one would need to generate 12 signals, which is hard to achieve with a DAQ board. Instead, we purchased a programmable relay box, called PPC 200, from RHK that has 5 programs built in. This box takes only 4 high voltage signals (x+, x-, y+, y-) and distributes these 4 signals on the 12 signals needed to drive the piezo legs. We drive the z-scan and z-offset directly from DAQ board after amplifying the voltage via another 2 high voltage amplifiers. Because we drive the z actuators directly from DAQ board, we wanted the control loop to be as fast as possible. Therefore we chose a DAQ board with an embedded processor on it. We investigated our options and purchased a rather affordable but fast DAQ board from NI with an FPGA. We also purchased a fast PC for the time (Intel Core 2 Quad processor), to control all the rest of the hardware. A list of the components is shown below in table A.1 and a picture of the overall control system and its subcomponents are shown in Fig. A.3.

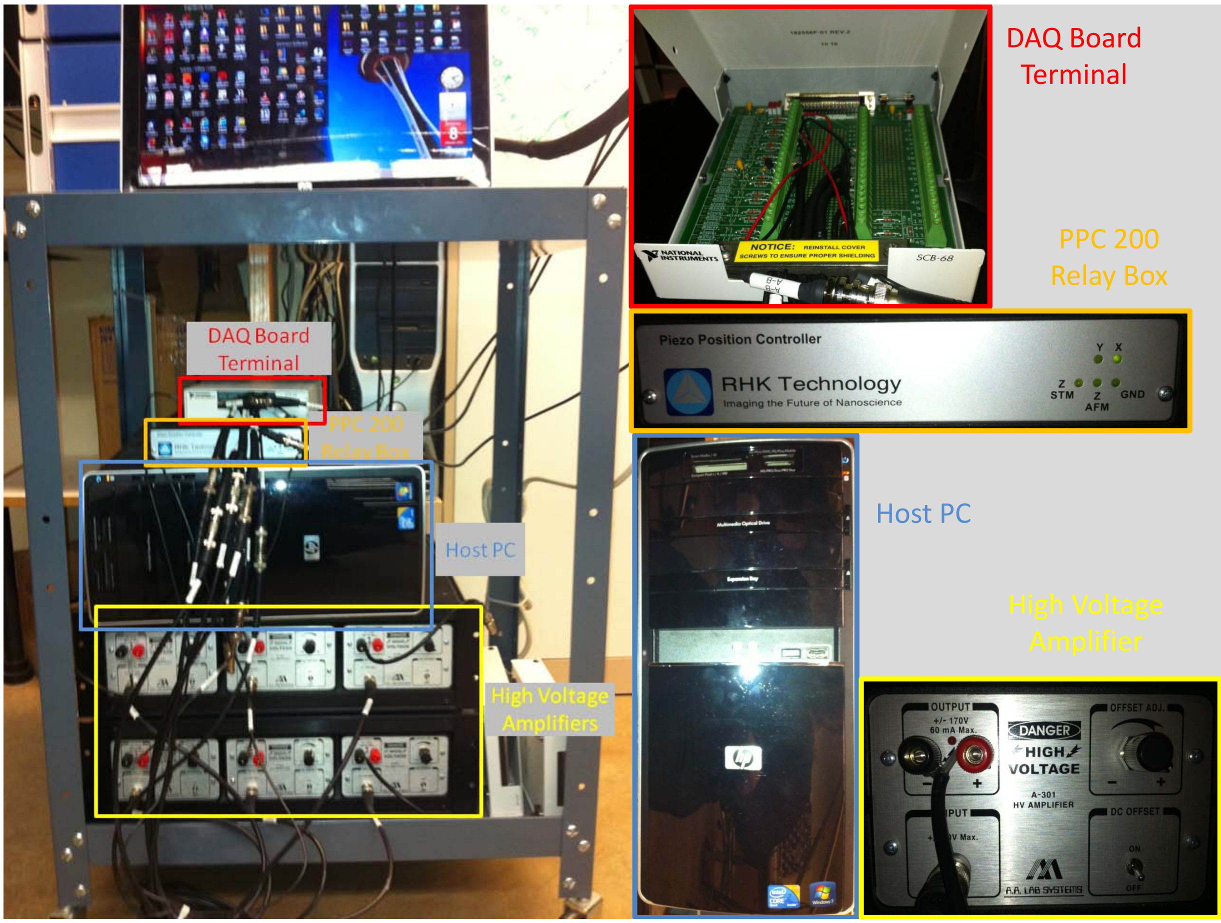

Figure A.4: A picture of the overall control system. DAQ board cannot be seen directly as it is plugged into the computer via PCI-express slot. The only visible part of the DAQ board is the terminal box where input and output connections are made.

There are a total of 3 inputs received by the host computer via DAQ board. Among these inputs, tunneling current is connected to the preamp monitor on SPM1000's back panel and lateral force and normal force are connected to the channel 2 and channel 3 on PLLPro's back panel. We take the readings directly from the RHK controllers in order to use their filters directly.

There are a total of 7 outputs generated by the host computer via DAQ board. 6 of these

Table A.1: Component list for the custom control system

Item	QTY	Description	Details
1	1	UHV SPM Controller-to-Scan-Head Cable Set - UHV subsystem interconnecting cables (12')	The cable set that we use now to connect the signals to scan head - **From RHK**
2	6	High Voltage Amplifers	From **AA Lab Systems**
3	2	17" Rack Enclosure for HV Amplifiers	From **AA Lab Systems**
4	1	PPC 200 Computer Controlled Piezo Position Control Interface Module	Relay box for distributing the signals - **From RHK**
5	1	NI PCIe-7852R Virtex-5 LX50 R Series Multifunc. RIO Device(8 AI,8 AO,96 DIO) 750kS/sec for LabVIEW FPGA	The FPGA based DAQ board that we use now - **FROM NI**
6	1	SHC68-68-RMIO Shielded Cable, 68 pin D-Type to 68 pin VHDCI, 1m Offset,1m	Cables for the DAQ Board - **FROM NI**
7	3	SCB-68 Noise Rejecting, Shielded I/O Connector Block	Screw Terminals for the DAQ Board - **FROM NI**
8	2	SHC68-68-RDIO Shielded Cable, 68 pin D-Type to 68 pin VHDCI, 1m	Cables for the DAQ Board - **FROM NI**
9	1	HP Pavilion Elite h8-1050 Desktop PC Intel Core i7 2600(3.40GHz) 10GB DDR3	A Fast PC I chose **From Newegg**
10	1	LCD Monitor	An LCD monitor **From Newegg**

outputs (x+, x-, y+, y-, z-scan, z-offset) are first amplified using the high voltage amplifiers. The 7th output, which is bias, is not amplified and connected directly to the sample. A list of inputs and outputs are shown below in table A.2.

Table A.2: I/O list for the FPGA based DAQ board. All the inputs and outputs are analog

Channel	Type	Description	Path to/from the Scanner
AO0	Out	X Voltage +	AO0 → HV Amplifier → PPC 200 → Scanner
AO1	Out	X Voltage -	AO1 → HV Amplifier → PPC 200 → Scanner
AO2	Out	Y Voltage +	AO2 → HV Amplifier → PPC 200 → Scanner
AO3	Out	Y Voltage -	AO3 → HV Amplifier → PPC 200 → Scanner
AO4	Out	Z-Scan Voltage	AO4 → HV Amplifier → Scanner
AO5	Out	Z-Offset Voltage	AO5 → HV Amplifier → Scanner
AO6	Out	Bias Voltage	AO6 → Scanner
AI0	In	Normal Force	Scanner → PLL Pro Input → PLL Pro Output Channel 3 → AI0
AI1	In	Lateral Force	Scanner → PLL Pro Input → PLL Pro Output Channel 2 → AI0
AI2	In	External PID	Scanner → Ext. Controller → AI2 → AO4 → HV Amplifier → Scanner
AI3	In	Tunneling Current	Scanner → SPM 1000 Input → SPM 1000 Preamp Monitor → AI0

The wiring between the scanner and other components are done using standard RHK cables as it makes the life easier for the user since all of the connectors on the scanner end and the connector on the PPC 200 end are already there. The other connectors on the standard RHK cables are all BNC, so we connected BNC connectors to the DAQ board outputs and HV amplifier outputs, to use standard BNC cables for the connections. All of the connections are done as described in the Table A.2, column “Path to/from the Scanner”.

Maintaining the DAQ board

The channels on the DAQ board slowly drift in time; hence cause the readings to have an offset value. This can be observed if all of the connections are disconnected but the input signal levels are not zero. In order to solve this problem, there is a maintenance procedure (takes about 5 minutes) that should be conducted periodically (Once in 2-4 weeks). If the maintenance is not done, it will not cause the DAQ board to break down, but it will cause false readings and outputs, and it might damage the scan head during driving.

Before starting the maintenance, all of the cables should be disconnected from the DAQ board end. After disconnecting all the cables, the user should run: "Calibrate 78xxR Device" that can be found under: "Start $\rightarrow$ Programs $\rightarrow$ National Instruments $\rightarrow$ NI RIO $\rightarrow$ R Series". After running this program, the user should select "RIO0" from "Select a device" dropdown menu and should click Self-Calibrate. The maintenance will be complete when the Self-Calibration is finished. You can now reconnect the cables and start the software.

A.2 Oscan V2.0 Software Introduction

The software that commands the control hardware is written in Labview since it is an easy to follow and code environment. Another advantage of using Labview for this project is the choice of DAQ board. We use a DAQ board produced by National Instruments which makes it easier to integrate to Labview.

The software is located on the Desktop of the control PC under the folder: "OScan V2.0". In order to open the software, one should double click the file named: "NanolabSTM_vers2.0.lvproj", which is the only Labview Project file that is located in that directory. One subdirectory of this folder is named "Datafiles" where all of the saved files are located. The software does not allow the user to select any folder other than the "Datafiles" folder to save the data. The user is only allowed to change the file name. Another subdirectory of the "OScan V2.0" folder is "Dependencies" in which almost all the subVIs and the .dll files used in this code are located.

After double clicking the "NanolabSTM_vers2.0.lvproj" file, the first window that appears is shown in Fig. A.5.

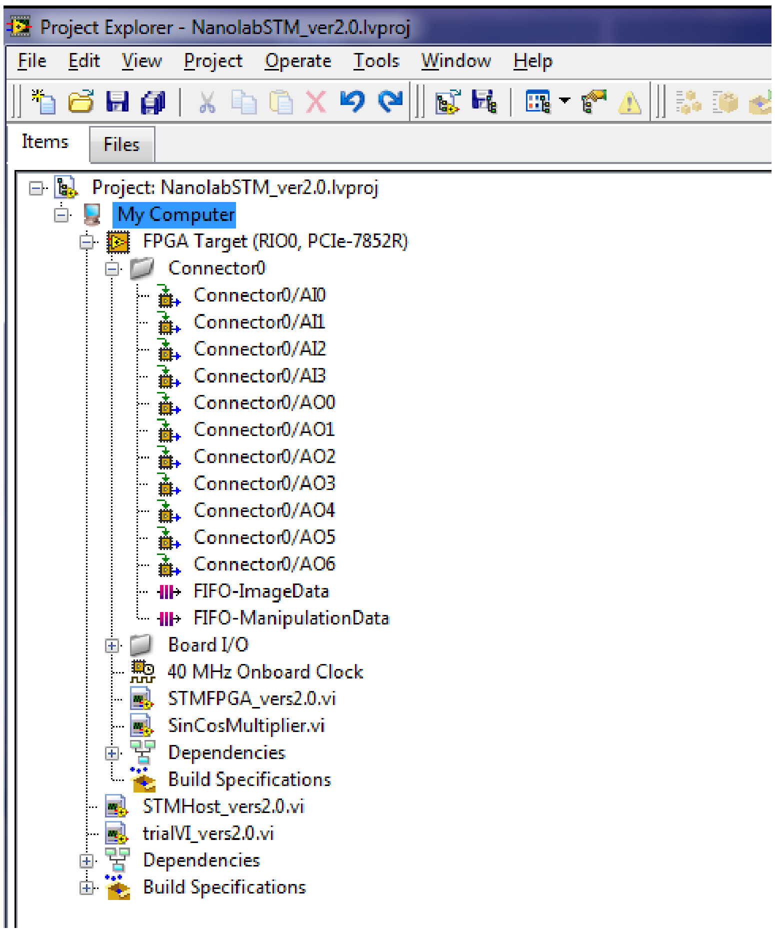

Figure A.5: Labview Project Window.

Connector0 folder that is defined under FPGA target includes the analog input and output channels used by the FPGA. The two FIFOs defined under the same folder are the two first in first out type buffers that is used to transfer large data streams between FPGA and the Host code pieces. “FIFO-ImageData” is the buffer used to transfer data from FPGA to Host during imaging and manipulation, and “FIFO-ManipulationData” is the buffer used to transfer manipulation parameters from Host to FPGA prior to the start of manipulation. The configurations of these buffers are shown below in Fig. A.6.

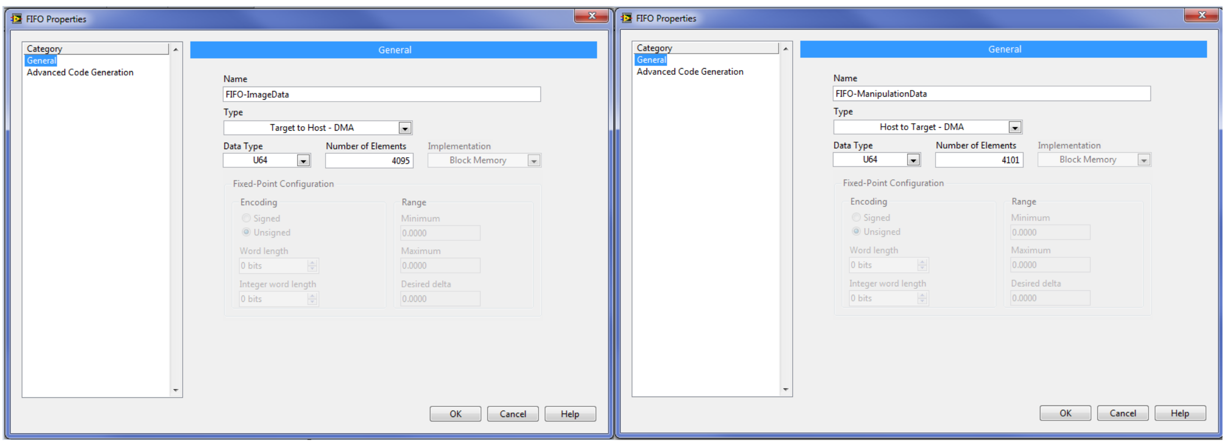

Figure A.6: First In First Out buffer configurations.

“STMFPGA_vers2.0.vi” located under FPGA target is the main code that runs in FPGA. SinCosMultiplier.vi and the other VIs located under Dependencies in the FPGA target are all subVIs of the main code “STMFPGA_vers2.0.vi”. “STMHost_vers2.0.vi” is the main code that runs on host PC. “trialVI_vers2.0.vi” is a VI that runs on the computer but has some of the functions from the FPGA code. This trial VI is not called in any other place and only used to try some of the functions that exist on FPGA without changing or running the FPGA code, which requires a 2-hour-long compilation after every small change. This manual will only describe the host code “STMHost_vers2.0.vi” and the FPGA code “STMFPGA_vers2.0.vi” because those are the two functions that are used to command the control system.

As described above, the software that commands the control hardware is in two pieces:

1. **The Host Code:** This part of the software runs on the host PC’s processor. It includes

all the high level commands and the front panels where the user interacts with the control system.

2. **The FPGA Code:** This part of the software runs on the FPGA that is located on the DAQ board connected to the PC via the PCI-express slot. It includes the low level commands and its front panel is not functional since the controls and indicators that locate on this front panel are controlled by the host code.

Example: For scanning, the user enters the scanning region and the speed to the front panel of the host code. Host code converts the scan size value to the voltage range that has to be generated by the FPGA and speed to the number of FPGA clock ticks that corresponds to one cycle of the voltage sweep generated by FPGA. Host code sends these values to FPGA front panel where the FPGA code reads these values from. After receiving these values, FPGA does all the rest of the work which is generating the actual waveform from these two values.

Almost all of the control system functions follow the same pattern. The conversions are carried by the Host regardless of the data transfer direction (i.e. even when FPGA reads topography and Host displays the image, the FPGA transfers the data to Host, where it is process afterwards). Waveform generations and main control loops are implemented in FPGA part of the software.

The rest of this manual will analyze the front panel of the host code, actual host code itself and FPGA code. I will not describe the FPGA front panel, as it is not used for any operation. This front panel only exists because Labview requires it to exist.

A.3 Oscan V2.0 Software Parameters and Front Panel

The aim of this part of the manual is to give insight on the front panel of the Oscan V2.0 custom control software and the controls and indicators that exist in the front panel. The front panel is where the user enters the values of the parameters for any operation; simply it is the main part where the user interacts with the control system.

The front panel consists of 5 tabs: Imaging, approach/ coarse positioning, writing/ manipulation, general parameters, and debug.

A.3.1 Imaging Tab

Imaging tab is the tab where the software starts. It is the tab mainly used for imaging, but some of the controls that can be used during any other operation such as X-Offset, Y-Offset and set-points are only located in this tab, as well. A screen shot of the imaging tab is shown in Fig. A.7. We will analyze this tab in 7 sections that are separated on Fig. A.7 with different colored borders.

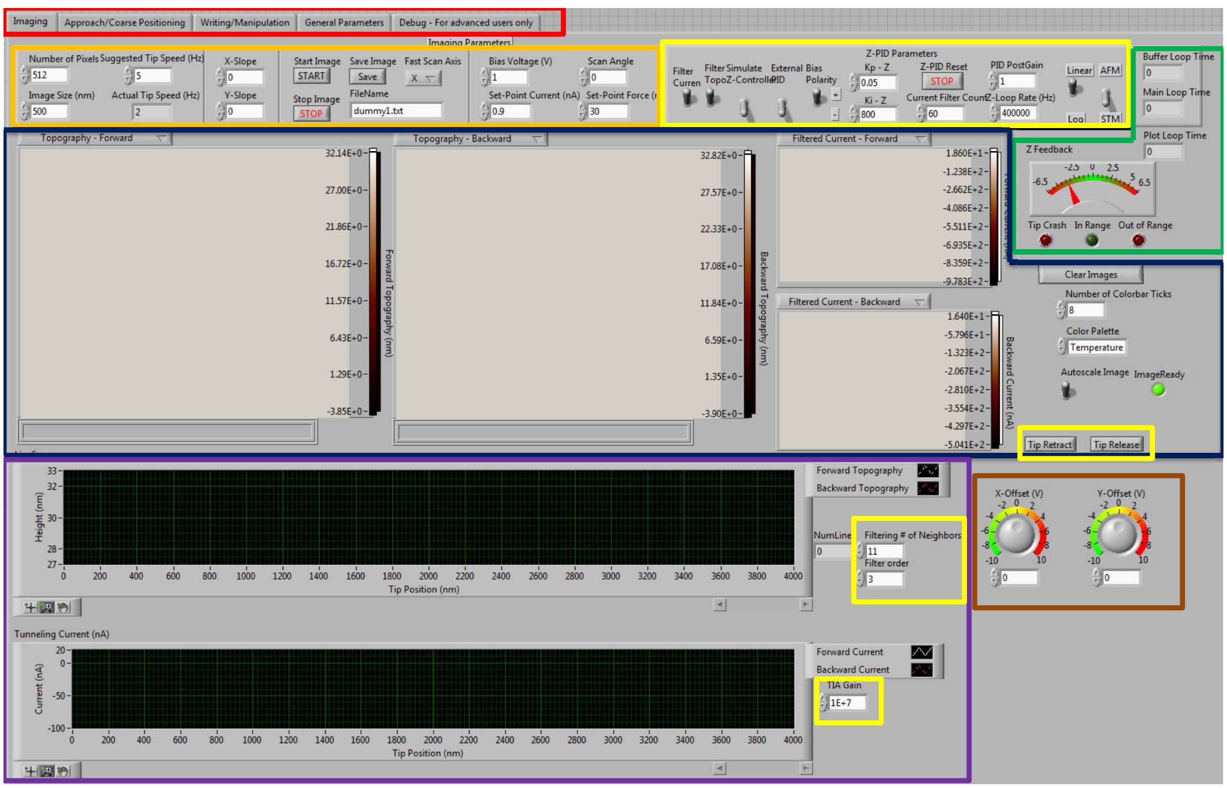

Figure A.7: A screen shot of the imaging tab.

The controls within the **red** borders are the tabs. Clicking to the tab controls makes the user to switch between the tabs. This is the part where the navigation within the software occurs.

The **orange** borders encapsulate the main imaging parameters. Their descriptions are given below:

Number of Pixels (default 512): Any number can be entered here to change the resolution of the image. It should be noted that as the number of pixels increase the host code slows down, causing missing lines in the image taken due to the limited time that the code has to transfer a large number of readings.

Image Size (default 500): This controls the size of the image. The unit is nanometers. For STM operation this value should be kept as small as possible, since it is hard for the controller to achieve stable operation at large regions. However we often image 3-4 um regions in AFM mode without suffering from any stability issues. On the other hand, increasing the image size also means increasing the effect of hysteresis on the images.

Suggested Tip Speed (default 5): This control changes the speed that the tip is run. It also changes the speed the front page is updated and the speed of the data transfer between the host and FPGA. Using 512 pixels, the highest speed that the host code can handle is 5 Hz, due to a large number of image matrices that it stores in its memory.

Actual Tip Speed: This indicator shows the actual speed that the tip will be moving during imaging. The small difference between this indicator and the suggested speed is because of the fact that FPGA runs with a 40 MHz clock (25 nanosecond periods) and can only achieve integer multiplies of this rate for any given loop.

X-Slope (default 0): This is the scanning slope in x direction. During the tips movement, the vertical position of the tip is changed with X-Slope*X-Position before calculating the topography to compensate for the slope of the sample scanned.

Y-Slope (default 0): This is the scanning slope in y direction. During the tips movement, the vertical position of the tip is changed with Y-Slope*Y-Position before calculating the topography to compensate for the slope of the sample scanned.

Start Image: This is the button that starts imaging.

Stop Image: This is the button that stops imaging.

Save Image: This is the button that saves the current image data. This is an instantaneous operation. It should not be pressed during imaging. It creates a .txt files that can be read from Matlab with the codes given in this manual.

FileName (default dummy1.txt): This is the name of the file that the image data would be saved.

Fast Scan Axis (default X): This control specifies the scan direction.

Bias Voltage (default 1): This control specifies the bias voltage. Its unit is Volts. You can still apply a bias voltage in AFM mode.

Set-Point Current (default 0.9): This control specifies the imaging current. Its unit is nanoamperes. It does not function when the system is in AFM mode. We often use 0.5 nA for imaging.

Scan Angle (default 0): It controls the rotation of the imaging square in order to image in arbitrary directions.

Set-Point Force (default 30): This control specifies the imaging force. Its unit is mV. It does not function when the system is in STM mode. We often use 30 mV for soft and 10-20 mV for hard cantilevers.

The 4 **yellow** rectangles on the imaging tab encapsulate the main z-control loop parameters. Z-control loop is almost always active hence this part of the controls is carried to every single tab. Any change that is done in one tab is carried to other tabs, as well. The descriptions of the parameters within the yellow borders are given below:

Filter Current (default True): Since FPGA is very fast and imaging is not that fast, and the current reading is noisy, we tend to filter the current during operation. This switch simply triggers a moving average filter on the FPGA end, and the current is filtered before it enters PI controller.

Filter Topo (default True): We tend to filter the topography after reading the data on the host end. This switch simply triggers a savitzky-golay filter on the host end, and only changes the smoothness of the topography displayed/saved.

Simulate Z-Controller (default False): When triggered, this controller changes the input of the PI controller from tunneling current/force to a sine wave generated by FPGA. This is used for testing some of the features of the software without the need of engaging the tip.

External PID (default False): When external PID is true, z output going to the piezo becomes 0, however the control system still drives the x and y positions. The z-piezo should be driven by an external controller and should be fed to the system via the specified port (labeled external PID on the terminal) in order to create an image.

Bias Polarity (default +): It changes the polarity of the bias voltage. It also changes sign of the current reading.

Kp-Z (default 0.05): Proportional control constant. Default value usually gives good results for STM. 0.1 is a good value for AFM. Values with the same order of magnitude as the default value should be used.

Ki-Z (default 800): Integral control constant. Default value usually gives good results for STM. 1000 is a good value for AFM. Values with the same order of magnitude as the default value should be used.

Z-PID Reset: This button flushes the integral term and resets the controller output to 0. It is a good practice to reset the PID after the tip crashes, since within the given time the integral controller usually grows too much.

Current Filter Count (default 60): This input controls the window size of the moving average filter. It should be adjusted to get the best imaging quality.

PID Post Gain (default 1): This is an option to multiply the output of the PID. It is not a commonly used control and should be left at 1 as much as possible.

Z-Loop Rate (default 400k): This is the loop rate of the z-control loop at the FPGA. Its unit is hertz. It means that every 2.5 microseconds FPGA reads a new input and generates a new control output. The best is to leave it at 400k but can be adjusted down if decreasing this seems to increase the image quality. (This can happen occasionally).

Linear/Log (default Linear): This switch is inactive at this point. It is not connected to anything in the code.

AFM/STM (default STM): This controls the operation type. The major difference is the change of the control input. Although all of the signals are read and recorded for any type of operation, switching to AFM from STM changes the input of the controller to normal force reading from tunneling current.

Tip Retract: When this button is pressed, the z-controller is interrupted and the piezo voltage is automatically set to -130 V, which is the fully retracted position.

Tip Release: When this button is pressed, the retracted piezo is returned to normal operation. Z-controller takes over.

Filtering # of Neighbors (default 11): This input controls the savitzky-golay filter window size for the topography reading. Increasing this number makes the topography smoother.

Filter order (default 3): This input controls the savitzky-golay filter order. A high number will over fit hence will end up with no improvement and a very low number will make the system loose important but small features.

TIA Gain (default 1E7): This input should match to the gain of the TIA used on the system. It adjusts the current reading values accordingly.

The **green** borders encapsulate the main indicators of this tab. Their descriptions are given below:

Buffer Loop Time: This indicator shows the loop time for the buffer reading operation in milliseconds. The buffer is read every once in $1/4$ lines, i.e. if the imaging speed is 1Hz, buffer is read with 4Hz speed or once in every 250 msec. The reason why we do this 4 times every line instead of once every line is the fact that the time relation between number of elements read and the data transfer time is non-linear. Therefore we do not want the number of elements to grow too much before reading the buffer.

Main Loop Time: This indicator shows the loop time for the main data transfer and user input operations in milliseconds. The value of this is set to be the same with the buffer loop since the operations in this loop are not very time consuming.

Plot Loop Time: This indicator shows the loop time for updating the charts, graphs and figures in milliseconds. The value of this is set to be four times the buffer loop, i.e. once in every line, since the operations in this loop are time consuming. This helps us relieve the processor.

Z Feedback: This dial shows where the piezo is with respect to its range. When the piezo voltage is close to -6.5, piezo is almost retracted all the way and the tip is about to crash to the surface if a feature on the surface is too high. In a similar fashion, when the dial is close to +6.5 volts, piezo is almost extended all the way and the scan is about to go out of range if a feature on the surface is too low.

Tip Crash: This lamp turns on if the piezo is retracted all the way.

In Range: This lamp turns on if the controller output to the piezo is within the voltage range of piezo.

Out of Range: This lamp turns on if the piezo is extended all the way.

The **brown** borders encapsulate the controls for X-Offset and Y-Offset. Their descriptions are given below:

X-Offset (default 0): This dial input controls the offset voltage amount on x voltage. During a normal scan, x voltage is a triangular wave around 0 V. When x-offset is set to a non-zero value, this changes the offset on the triangular wave.

Y-Offset (default 0): This dial input controls the offset voltage amount on y voltage. During a normal scan, y voltage is a triangular wave around 0 V. When y-offset is set to a non-zero value, this changes the offset on the triangular wave.

The **blue** borders encapsulate the figures and controls related to these figures. Their descriptions are given below:

The four menu selectors above each image: These selectors enable the user to display whatever images he wants to display on these figure windows. These are implemented because we wanted to limit the number of images displayed at a given time in order to relieve the processor.

Clear Images: This button initializes the elements of image matrices to 0.

Number of Colorbar Ticks (default 8): This input controls the number of ticks displayed on the color bar of the images.

Color Palette (default Temperature): This input controls the color scheme of the figures displayed.

Autoscale Image (default True): Whenever this switch is on, the color bar of all of the displayed images are scaled to minimum-maximum value of the topography reading.

Image ready: This indicator comes on when an image is finished and is reset to off when an image is started. The purple borders encapsulate the line-scans and one indicator related to these line-scans. Their descriptions are given below:

LineScan: This chart shows the data of the two big images from the last line.

Tunneling Current (nA): This chart shows the data of the two small images from the last line.

NumLine: This indicator shows the line the imaging operation is at. It starts from 0 and counts up to number of pixels.

A.3.2 Approach/ Coarse Positioning Tab

Approach/Coarse Positioning tab is the tab where all of the stepping and coarse motions are controlled. A screen shot of this tab is shown below in Fig. A.8. We will analyze this tab in 5 sections that are separated on Fig. A.8 with different colored borders.

The controls within the **orange** borders are the buttons that control the vertical z-motion. Their descriptions are given below:

Approach: This button starts the approach motion. Approach can only stop if cancel all stepping is clicked or the control input (normal force or tunneling current) reaches its set-point.

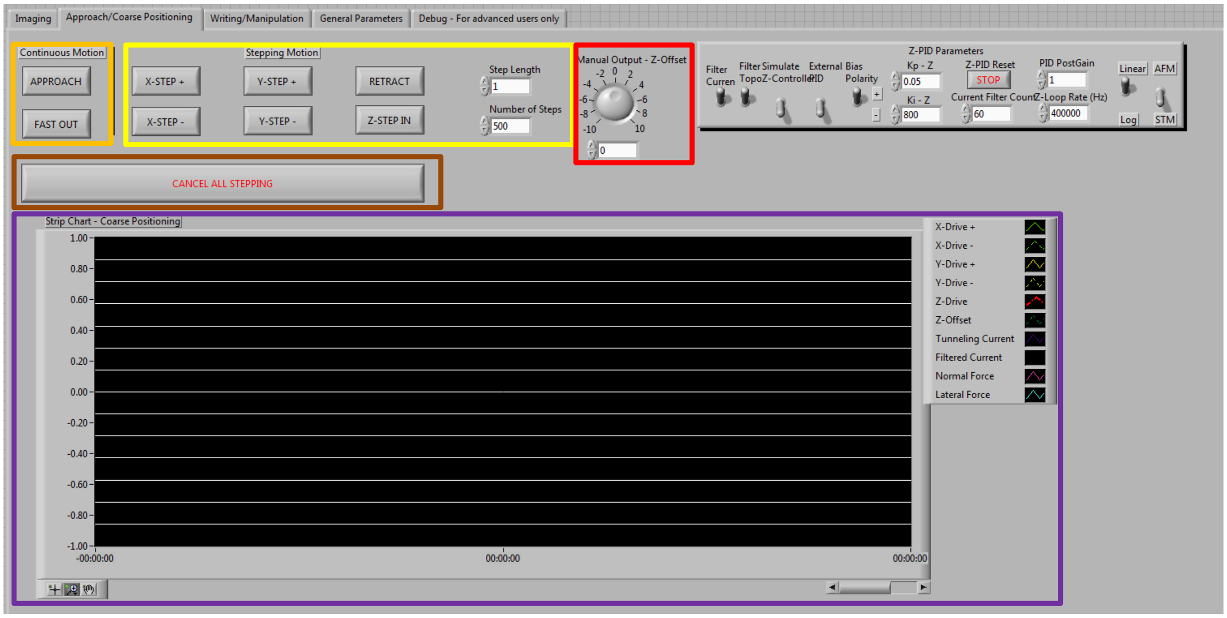

Figure A.8: A screen shot of the approach/coarse positioning tab.

The step size of this motion is controlled by Step Length input.

Fast Out: This button starts the fast out motion. Fast out only stops if cancel all stepping is clicked. This means there is no fail safe; hence the beetle can walk itself off the ramps if not stopped after the beetle is all the way up.

The **yellow** borders encapsulate the controls for coarse positioning motion. Their descriptions are given below:

X-Step +: This button starts the beetle stepping in X+ direction for the number of steps specified in Number of Steps control with the step length specified in Step Length control. This motion can only stop if cancel all stepping is clicked or the number of steps taken reaches the number of steps control.

X-Step -: This button starts the beetle stepping in X- direction for the number of steps specified in Number of Steps control with the step length specified in Step Length control. This motion can only stop if cancel all stepping is clicked or the number of steps taken reaches the number of steps control.

Y-Step +: This button starts the beetle stepping in Y+ direction for the number of steps specified in Number of Steps control with the step length specified in Step Length control. This motion can only stop if cancel all stepping is clicked or the number of steps taken reaches the number of steps control.

Y-Step -: This button starts the beetle stepping in Y- direction for the number of steps specified in Number of Steps control with the step length specified in Step Length control. This motion can only stop if cancel all stepping is clicked or the number of steps taken reaches the number of steps control.

Retract: This button starts the beetle stepping in fast out direction for the number of steps specified in Number of Steps control with the step length specified in Step Length control. This motion can only stop if cancel all stepping is clicked or the number of steps taken reaches the number of steps control.

Z-Step In: This button starts the beetle stepping in approach direction for the number of steps specified in Number of Steps control with the step length specified in Step Length control. This motion can only stop if cancel all stepping is clicked or the number of steps taken reaches the number of steps control.

Step Length (default 1): This control specifies the maximum voltage used during stepping, approach and fast out. If it is 1, it uses the maximum voltage allowed to the legs.

Number of Steps (default 500): This control specifies the number of steps that will be taken during stepping.

The **brown** borders encapsulate the button named "Cancel All Stepping" that stops the stepping motion immediately after being pressed. This is sort of an emergency stop for any type of movement in x and y directions.

The **red** borders encapsulate the "Manual Output Z-Offset" control. This dial controls the output going to the z-offset port. Z-offset is connected to the vertical actuators located at the center of the legs and controls the coarse position of the tip. This dial is used to bring the tip closer to or further away from the surfaces as needed.

The **purple** borders encapsulate the "Strip Chart-Coarse Positioning" graph. This graph shows all of the voltages read by the host at any given time. The update rate of this chart is the same as the main loop rate, i.e. four times the line speed.

A.3.3 Writing/Manipulation Tab

Writing/Manipulation tab is the tab where all of the writing, oxidization and spectroscopy operations are carried. A screen shot of this tab is shown below in Fig. A.9. We will analyze this tab in 6 sections that are separated on Fig. A.9 with different colored borders.

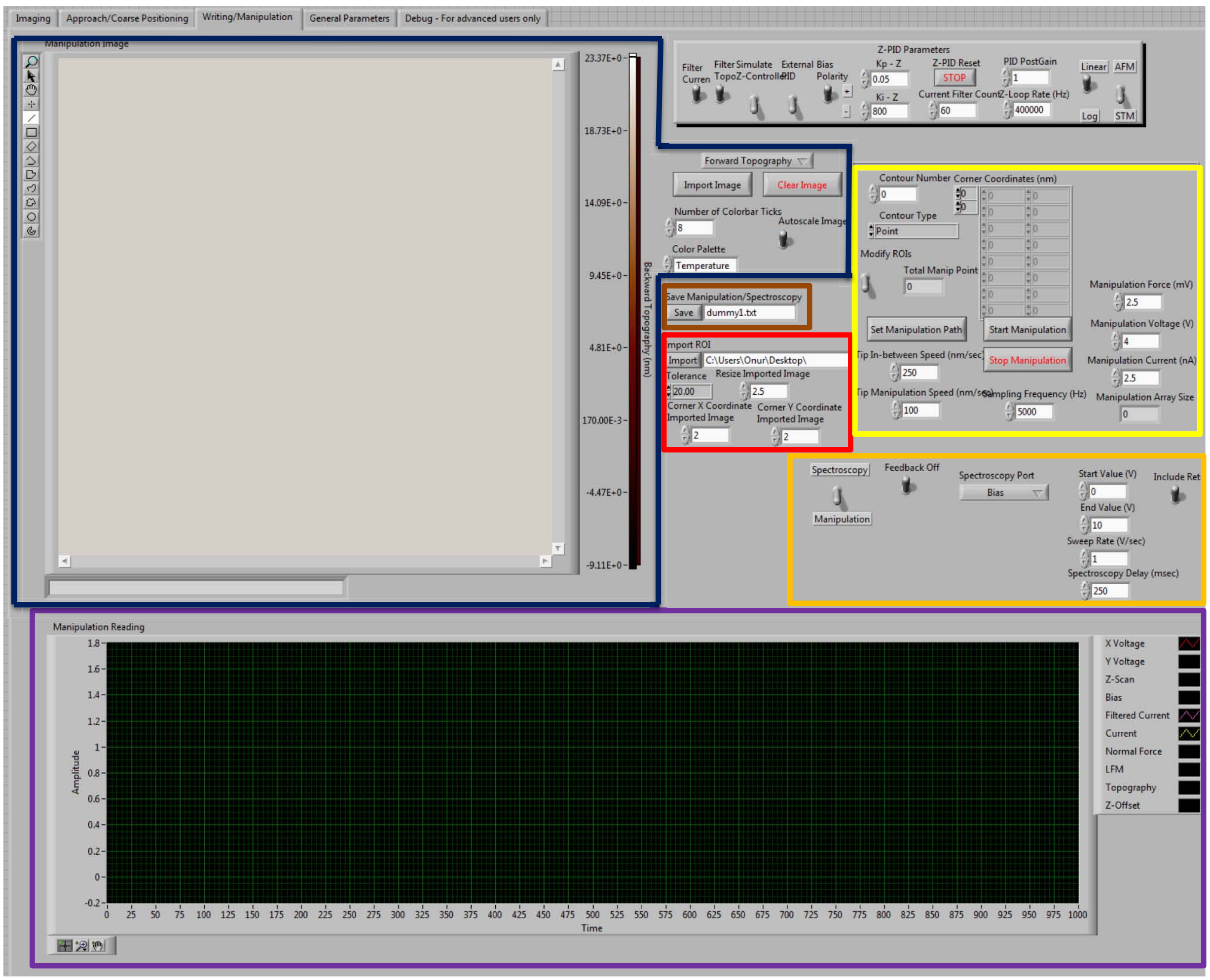

Figure A.9: A screen shot of the writing/manipulation tab.

The **blue** borders encapsulate the figure that the manipulation will be done on and controls related to this figure. Their descriptions are given below:

Manipulation Image: This is the display where the image that is imported from the imaging tab is shown and manipulation path can be defined on. The manipulation paths are defined as Region Of Interests (ROI), where the host code then finds the pixels that intersects the ROIs and converts them to x and y voltages. The ROIs can be drawn on the image using the pane on the left hand side of the image. If multiple ROIs will be defined, the user must hold the ctrl button pressed during drawing the ROIs after the first one.

The menu selector on the side of the image: This selector enables the user to select whatever image he wants to import from the imaging tab.

Import Image: This button imports the image specified at the selector from the imaging tab.

Clear Image: This button initializes the elements of manipulation image matrix to 0.

Number of Colorbar Ticks (default 8): This input controls the number of ticks displayed on the color bar of the manipulation image.

Color Palette (default Temperature): This input controls the color scheme of the manipulation figure displayed.

Autoscale Image (default True): Whenever this switch is on, the color bar of the displayed image is scaled to minimum-maximum value of the imported image.

The **brown** borders encapsulate the button named “Save Manipulation/Spectroscopy” that saves the signals read during manipulation or spectroscopy operation into the file whose name is specified in the string input box right next to the “Save Manipulation/Spectroscopy” button.

The **red** borders encapsulate the controls for importing a manipulation path from a given bitmap file. Their descriptions are given below:

Import ROI: This button imports the bitmap file whose name is specified in the string input box right next to the “Import” button.

Tolerance: After importing the bitmap from the file, the host code finds the edges on the bitmap file. Tolerance input is used while finding the edges. It controls the color difference tolerance between the adjacent pixels.

Resize Imported Image: This input changes the size the input bitmap file when importing. The value of this control is multiplied with the resolution of the input image to resize the image.

Corner X Coordinate Imported Image: This input moves the imported bitmap on the manipulation image in x direction. The upper left corner of the imported image is moved in x direction with the amount specified in this input.

Corner Y Coordinate Imported Image: This input moves the imported bitmap on the manipulation image in y direction. The upper left corner of the imported image is moved in y direction with the amount specified in this input.

The **yellow** borders encapsulate the controls for modifying a manipulation path and other manipulation parameters. Their descriptions are given below:

Modify ROIs (default False): When this input is switch on, the user can modify the manipulation path by entering values to the corner coordinates array. Manual modification of the manipulation path can only be done when the switch is True, however when this is the case, the user cannot draw new paths on the image or import a bitmap. When the switch is False, modification of the path can only be done through drawing the pattern on the image or by importing the manipulation path from a bitmap.

Contour Type: This indicator shows the type of the contour whose number is selected via Contour number.

Contour Number (default 0): This input controls which contour is selected and displayed at the corner coordinates array display.

Corner Coordinates: This array displays the corner coordinates of the contour whose number is selected via contour number input. When the Modify ROIs switch is turned on, the user can modify the manipulation path by changing the coordinates specified here.

Total Manip Points: This indicator shows the number of points on a defined manipulation path.

Tip In-between Speed (default 250): This input controls the speed of the tip while the tip is in between contours, i.e. not manipulating the surface. Its unit is nanometers per seconds.

Tip Manipulation Speed (default 100): This input controls the speed of the tip while the tip is on manipulation path, i.e. on the contours. Its unit is nanometers per seconds.

Manipulation Force (default 2.5): This input controls the force set-point during AFM mode manipulation where feedback control is on. Its unit is millivolts.

Manipulation Current (default 2.5): This input controls the current set-point during STM mode manipulation where feedback control is on. Its unit is nanoamperes.

Manipulation Voltage (default 4): This input controls the voltage that will be applied on the surface during manipulation when the tip is on the contours. When the tip is not on contours the voltage is switched back to bias voltage. Its unit is volts.

Manipulation Array Size: This indicator shows the number of points on a defined manipulation path.

Sampling Frequency (default 5000): This input controls the frequency at which the DAQ board will read the channels (input and output) during manipulation. DAQ board then transfers this data to host PC once in every 250 data points. Its unit is Hertz.

Set Manipulation Path: After every change in the manipulation path or parameters, this button has to be pressed in order for the changes to take effect. This button generates the manipulation array.

Start Manipulation: Starts the transfer of manipulation array from host PC to FPGA and data from FPGA to host PC back. It also starts the manipulation operation.

Stop Manipulation: Stops the manipulation operation immediately.

The **orange** borders encapsulate the controls for spectroscopy parameters. Their descriptions are given below:

Spectroscopy/Manipulation (default Manipulation): Spectroscopy mode is used for taking I-V, I-z, or F-d curves whereas manipulation mode is used for moving the tip on a selected path with a known voltage and set-point value.

Feedback Off (default True): While the switch is true, the feedback is turned off during manipulation/spectroscopy.

Spectroscopy Port (default Bias): This menu selector is used during spectroscopy operation to specify which port the ramp output will be applied. If bias is selected the resulting spectroscopy will be I-V, if z-offset or z-scan is selected the resulting spectroscopy will be F-d or I-z.

Start Value (default 0): This input controls the start value of the spectroscopy ramp generated by the FPGA. Its unit is volts.

End Value (default 10): This input controls the end value of the spectroscopy ramp generated by the FPGA. Its unit is volts.

Sweep Rate (default 1): This input controls the sweep rate/speed of the spectroscopy ramp generated by the FPGA. Its unit is volts/seconds.

Spectroscopy Delay (default 250): This input controls the delay between two spectroscopies that will be applied on the same surface at two different positions. Its unit is milliseconds.

Include Return (default True): While the switch is true, the spectroscopy ramp will start from start value, will go to the end value and then come back to start value. While it is false, it will start from start value and then end at end value.

The **purple** borders encapsulate the "Manipulation Reading" chart. This graph shows all of the voltages read by the host during manipulation. All of the displayed signals are the voltage readings received by the DAQ board.

A.3.4 General Parameters Tab

General Parameters tab is the tab where some of the controls and indicators of parameters that effect the general operation are located. A screen shot of this tab is shown below in Fig. A.10. We will analyze some of the crucial controls on this tab because some of them cannot be used to control the software and only exist for debugging purposes.

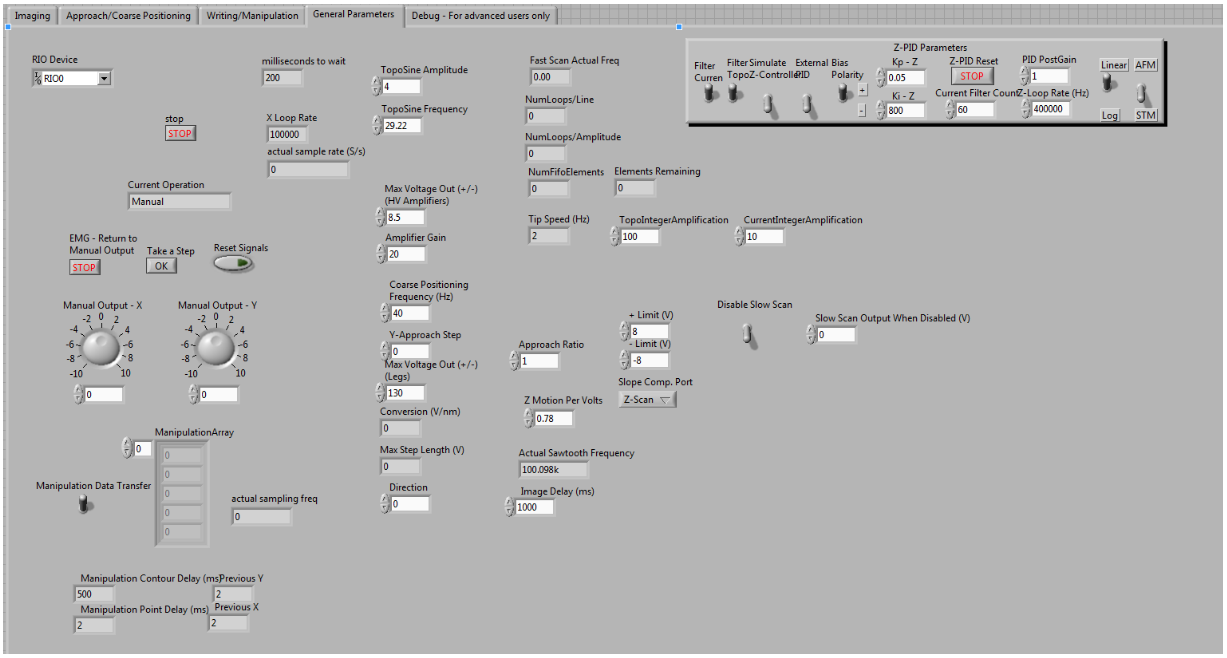

Figure A.10: A screen shot of the general parameters tab.

Reset Signals: This control is used in the host code automatically to reset the output signals of the DAQ board and start some of the operations. If some function does not work properly, this button can be used to reset the function.

Max Voltage Out (+/-) (HV Amplifiers) (default 8.5): This control is used to limit the output voltages generated by the DAQ board in order not to feed too high signals to the high-voltage amplifiers that might damage them.

Amplifier Gain (default 20): This value should be the same as the high voltage amplifiers used in the control system hardware.

Max Voltage Out (+/-) (Legs) (default 130): This control is used to limit the output voltages generated by the high voltage amplifiers in order not to feed too high signals to the piezo legs that might damage them.

Z-motion per volts (default 0.78): This value is the conversion factor between the piezo voltage and the topography reading.

+ Limit (default 8): This value is the upper limit of the z-piezo voltage generated from DAQ board (160 Volts actual). Its unit is volts.

- Limit (default -8): This value is the lower limit of the z-piezo voltage generated from DAQ board (-160 Volts actual). Its unit is volts.

TopoIntegerAmplification (default 100): This control is used as a way of amplifying the topography signal before displaying the image. The actual values of the signals displayed and saved do not change with this value, only the contrast of the images change.

CurrentIntegerAmplification (default 10): This control is used as a way of amplifying the rest of the signals before displaying them on the images. The actual values of the signals displayed and saved do not change with this value, only the contrast of the images change.

Slope Comp. Port (default Z-Scan): This menu selector has the options of selecting z-scan or z-offset. Slope compensation signal (X Slope*X Voltage + Y Slope*Y Voltage) is added to the value of the port specified in this selection.

Disable Slow Scan (default False): When this switch is true, slow scan is disabled and the image is taken on the same line.

Slow Scan Output When Disabled (default 0): The value of this control is fed directly to the slow scan port when the slow scan output is disabled. Its unit is volts.

A.3.5 Debug Tab

Debug tab is the tab where the rest of the indicators that is not used during any other operation are located. A screen shot of this tab is shown below in Fig. A.11. The indicators in this tab are dummy parameters mostly used as middle parameters during calculations. They exist in the front panel because it is required by the Labview but they are almost completely useless. Therefore we will not discuss any of the parameters located in this tab.

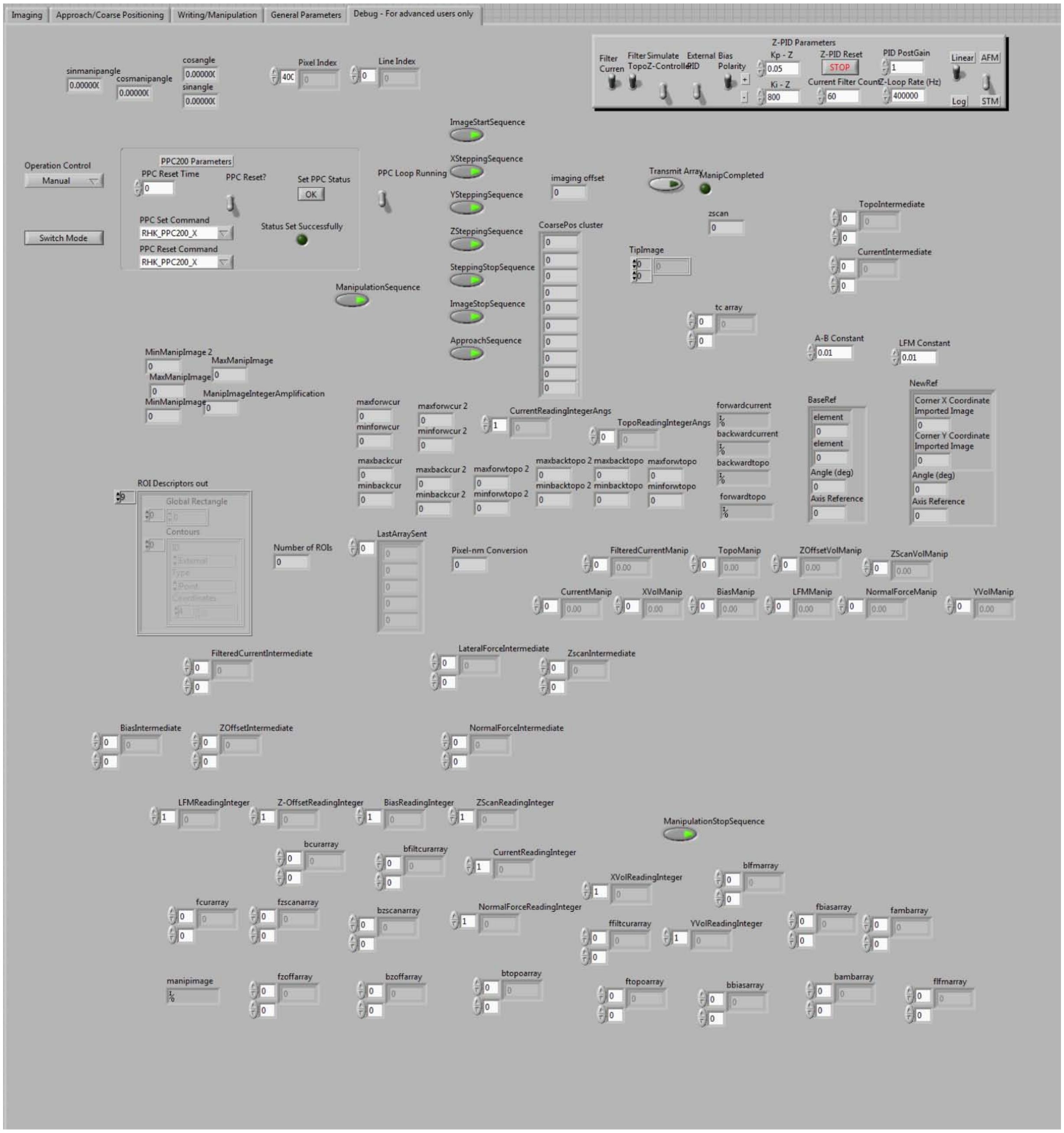

Figure A.11: A screen shot of the debug tab.

A.4 How To Use the System

This part of the manual lists the procedures to achieve most common tasks using OScan V2.0. The procedures are detailed however the explanations of most of the controls are not included in this section. For detailed explanation on the controls in a certain tab, please refer to Parameters and Front Page section. We have listed every useful control and indicator in that section and given details on how they work and what they affect.

A.4.1 Running the software

1. Turn on high voltage amplifiers using the switch that is located on the back panel of HV amplifier rack.
2. Double click on the “Oscan V2.0” folder, which is located on desktop.
3. Run the Labview project file, named: “NanolabSTM_vers2.0.vi”. Project window will appear.
4. Double click on STMHost_vers2.0.vi to open the front panel of host code.
5. Double click on STMFPGA_vers2.0.vi located under FPGA Target to open the front panel of the FPGA code.
6. Try running the STMFPGA_vers2.0.vi by clicking the arrow located on the top left corner.
7. Step 5 might result with an error message. Don’t be alarmed. Try running the STMHost_vers2.0.vi, even step 5 resulted with an error message. Regardless of the outcome of step 5, the host code should start running.
8. If you received an error message at step 5, go back to the FPGA front panel again and run the code by clicking the arrow. It should start this time.
9. The code is now running and functional. You can start operation.

A.4.2 Stopping the software

1. Click the red stop sign two buttons right to the arrow on the STMHost_vers2.0.vi.
2. Click the red stop sign two buttons right to the arrow on the STMFPGA_vers2.0.vi.
3. You can now close all the windows and quit Labview.
4. If you won't be using the system for a few hours, it is a good practice to turn off high voltage amplifiers. This can be done using the switch that is located on the back panel of HV amplifier rack.

A.4.3 Engaging Tip to the Surface

1. Set the set-point current (for STM), set-point force (for AFM) and the bias to the desired values. For STM start with a medium tunneling current such as 0.5 nA and a low bias voltage such as 1 V. For AFM, the set-point force value will depend on the stiffness of the cantilever. If you are using a soft cantilever (below 10 N/m) you can start with high values such as 30 mV. If you are using a hard cantilever, start with smaller forces like 10-15 mV.
2. Make sure that the Kp and Ki values make sense. A good set of values for Kp and Ki are 0.05 and 800 respectively. I observed that 0.1 and 1000 also works well.
3. Make sure that simulate z-controller is switched to off.
4. Press the button Tip Release in order to make sure that the piezo is not retracted.
5. Press the button Z-PID Reset in order to make sure that the integral controller did not overflew.
6. Make sure that "Out of Range" lamp is on and tip crash and in range are off.
7. After completing steps 1-6, switch to "Approach/Coarse Positioning" tab.
8. Set the step length to the desired value (1 is usually pretty fast and we use this value, but the range of this input is 0-1. So if needed the approach can be slowed down using this

control).

9. Click Approach.
10. When approach is complete, a message will be displayed on the front panel stating that the tip is retracted. Click "Tip Release" on that window.
11. Adjust the Z-Offset after releasing the tip to bring the Z-Scan voltage as close to zero as possible.

A.4.4 Coarse Positioning

1. Set the step length to the desired value. If you want to take small steps (10s of um), the step length value should be set to 0.2-0.3.
2. Set the number of steps to the desired value. If you want to move the tip a small amount, set it to 1, if you want to move the tip continuously set to a high value like 5000 and stop it during the movement.
3. If the step length value is smaller than 0.3 and the number of steps is 1, the user can skip this step. If the motion of the tip would be larger than the user should retract or fast out the tip before doing any coarse positioning, to prevent tip crashing into the surface.
4. Click on the stepping button that represents the direction you want the tip to move.
5. The motion stops only if the number of steps is reached or if cancel all stepping is clicked.
6. When the coarse positioning is complete, click cancel all stepping one more time to let the FPGA know that the coarse positioning stage is finished.
7. If you have retracted the tip or fasted out before the coarse positioning, tip should be reengaged to the surface. Follow the directions above to achieve reengagement.

A.4.5 Taking an STM Image

1. Flip the AFM/STM switch to STM direction.
2. Set the desired set-point current value.
3. Set the desired bias voltage.
4. Make sure that the z-feedback is in range. The dial should be around 0, which is the safest when starting a new image and the in range light should be on.
5. Make sure that the z-scan signal is not oscillating too much. To check this switch to approach/coarse positioning tab and check how the z-scan behaves. Tweak the controller parameters in order to achieve small/no oscillation.
6. Set the number of pixels to the desired value. Be aware that high values in this control slows down the Labview and causes imaging problems. The best practice is to leave this control at 512.
7. Set the suggested tip speed. For STM the speed should be low, i.e. 1-2 Hz. If you feel the surface is smooth and the controller is doing a good job imaging, you can increase the speed.
8. Start imaging by clicking the Start Image button.
9. Adjust the x slope while imaging in x direction (i.e. Fast Scan Axis selected as X). Then switch the Fast Scan Axis to Y and adjust the y slope.
10. You can leave the autoscale image switch on, or switch it off and scale the color bar of the image by simply double clicking on the number on the color bar and typing in the desired value.
11. Imaging is going to stop once Stop Image is clicked or the image is finished.
12. You can save the image by typing in the FileName and clicking Save Image button. It will ask for your confirmation if a file with the name specified exists, as a failsafe to overwriting

the already saved data.

A.4.6 Taking an AFM Image

1. Flip the AFM/STM switch to AFM direction.
2. Set the desired set-point force value.
3. Set the desired bias voltage for conductive AFM imaging. You should set this to 0 for regular AFM operation.
4. Make sure that the z-feedback is in range. The dial should be around 0, which is the safest when starting a new image and the in range light should be on.
5. Make sure that the z-scan signal is not oscillating too much. To check this switch to approach/coarse positioning tab and check how the z-scan behaves. Tweak the controller parameters in order to achieve small/no oscillation.
6. Set the number of pixels to the desired value. Be aware that high values in this control slows down the Labview and causes imaging problems. The best practice is to leave this control at 512.
7. Set the suggested tip speed. For AFM the speed can be higher than the STM, i.e. 3-4 Hz. If you feel the surface is smooth and the controller is doing a good job imaging, you can increase the speed.
8. Start imaging by clicking the Start Image button.
9. Adjust the x slope while imaging in x direction (i.e. Fast Scan Axis selected as X). Then switch the Fast Scan Axis to Y and adjust the y slope.
10. You can leave the autoscale image switch on, or switch it off and scale the color bar of the image by simply double clicking on the number on the color bar and typing in the desired value.

11. Imaging is going to stop once Stop Image is clicked or the image is finished.
12. You can save the image by typing in the FileName and clicking Save Image button. It will ask for your confirmation if a file with the name specified exists, as a failsafe to overwriting the already saved data.

A.4.7 Performing a Manipulation Task

1. Switch to “Writing/Manipulation Tab”.
2. Choose the image that you want to import from the drop down menu next to the image.
3. Click Import Image button to import the image.
4. Define the manipulation path. There are two ways of doing this:

   Draw the manipulation path manually as a region of interest (ROI) using the tools given on the left side of the manipulation image.

   Import a ROI by entering the filename to the text box next to the Import ROI button and click the import button.

   After importing or drawing the ROI, you can modify these ROIs by simply switching on the Modify ROIs switch and changing the corner coordinates array elements.

   For detailed information on the controls that exist in this tab and how they work, refer to the Parameters & Front Page section, writing/manipulation tab subsection.
5. After entering the desired path, enter the manipulation force (for AFM manipulation), manipulation current (for STM manipulation) and manipulation voltage.
6. Enter the desired sampling frequency. If the number of manipulation points is too high and the manipulation is slow, enter a low number like 500 Hz, to make sure that the Labview will not slow down or crash during manipulation due to the large array size.
7. Enter the desired tip in-between speed and tip manipulation speed.

8. Turn the manipulation/spectroscopy switch to manipulation.

9. Turn the Feedback off switch to False, since manipulation is often done while the feedback is on.

10. Click set manipulation path to generate the array that should be sent to FPGA.

11. Click start manipulation and observe the tip movement on the manipulation image.

12. Manipulation will only stop if Stop Manipulation is clicked or the manipulation is completed.

13. After the manipulation is completed, save the data using save manipulation/spectroscopy controls.

A.4.8 Performing a Spectroscopy Task

1. Switch to "Writing/Manipulation Tab".

2. Choose the image that you want to import from the drop down menu next to the image.

3. Click Import Image button to import the image.

4. Define the spectroscopy points. The easiest way of doing this is to use the tools given on the left side of the manipulation image.

5. After entering the desired spectroscopy points, enter the start value, end value, sweep rate, and spectroscopy delay that should be used to generate the spectroscopy ramp.

6. Enter the desired sampling frequency. If the number of spectroscopy points is too high or the spectroscopy is slow, enter a low number like 500 Hz, to make sure that the Labview will not slow down or crash during spectroscopy due to the large array size.

7. Choose if you want to generate a one way or two way ramp using Include Return. If you select include return, the ramp generated will start from start value, go to the end value and then come back to the start value. If include return is not selected, the ramp will stop at the

end value.

8. Turn the manipulation/spectroscopy switch to spectroscopy.
9. Turn the Feedback off switch to the desired position. Feedback is mostly off during spectroscopy so in most cases it should be True.
10. Choose the spectroscopy port from the dropdown menu. This specifies the port where the ramp will be output from.
11. Click set manipulation path to generate the array that should be sent to FPGA.
12. Click start manipulation and observe the tip movement on the manipulation image.
13. Spectroscopy will only stop if Stop Manipulation is clicked or the manipulation is completed.
14. After the spectroscopy is completed, save the data using save manipulation/spectroscopy controls.

A.4.9 Importing Images/Data to Matlab as a Struct

We have written the following code in Matlab to import the images or manipulation/spectroscopy data saved using OScan v2.0. The .m file that imports data automatically reads every data point specified in the image and also the imaging parameters, and creates a Matlab struct type variable that includes the image/data information. The .m file is given below:

```
function imagestruct = importimagedata(fname)

close all
clc

imagename = fname;
filename = sprintf('%s%s',imagename,'.txt');
```

```
fid = fopen(filename);
index = 1;
imagefile = 1;
while ¬feof(fid)
    text{1,index} = textscan(fid,'%s',1,'Delimiter',':','BufSize',1e6);
    if isempty(strfind(text{1,index}{1,:}{1,:},'anipulation'))
    else
        imagefile = 0;
    end
    data{1,index} = textscan(fid,'%f');
    lenmatrix = length(data{1,index}{:});
    if lenmatrix == 1
        eval(['image.' genvarname(text{1,index}{1,:}{1,:}) '=' ...
            num2str(data{1,index}{:}) ';'])
    else
        data1 = data{1,index};
        data1_2 = cell2mat(data1);
        eval(['image.' genvarname(text{1,index}{1,:}{1,:}) 'array = ...
            data1_2;'])
        if imagefile == 1
            numpix = sqrt(length(data1_2(:,1)));
            data1_3 = reshape(data1_2,numpix,numpix)';
            data1_3 = data1_3(end:-1:1,:);
        else
            data1_3 = data1_2;
        end
        eval(['image.' genvarname(text{1,index}{1,:}{1,:}) '= data1_3;'])
    end
    index = index + 1;
end
fclose(fid);
if imagefile == 1
```

```
    image.NumberOfPixels = numpix;
end

imagestruct = image;
```

The only input to this .m file is the filename, which should be entered without the file extension .txt. For example, if your file name is “ILoveOscan.txt”, you should call this function from the command window as: data = importimagedata(’ILoveOscan’);

A.4.10 Plotting Images in Matlab

We have written the following code in Matlab to import the images saved using OScan v2.0 and to display them. The .m file uses the importimagedata.m function directly to import the images and then displays them. The .m file is given below:

```
function result = imagedisplay(fname, SaveImages, stdrange_topo, ...
    stdrange_current)

close all
clc

imagename = fname;
image = importimagedata(fname);

numpix = image.NumberOfPixels;

ftopo = image.ForwardTopography;
btopo = image.BackwardTopography;
fcur = image.ForwardTunnelingCurrent;
bcur = image.BackwardTunnelingCurrent;
imagesize = image.ImageSize;
```

```
x=1:1:numpix;
y=1:1:numpix;
x_actual = x*imagesize/numpix;
y_actual = y*imagesize/numpix;

fttoshow = ftopo;
bttoshow = btopo;
fctoshow = fcur;
bctoshow = bcur;

meantopo = mean([mean(mean(fttoshow)) mean(mean(bttoshow))]);
stdtopo = max([std(mean(fttoshow)) std(mean(bttoshow))]);
meancur = mean([mean(mean(fctoshow)) mean(mean(bctoshow))]);
stdcur = max([std(mean(fctoshow)) std(mean(bctoshow))]);
stdrangetopo = stdrange_topo;
stdrangecur = stdrange_current;

maxtopolim = min([meantopo+stdrangetopo*stdtopo ...
    max([max(max(fttoshow)) max(max(bttoshow))])]);
mintopolim = max([meantopo-stdrangetopo*stdtopo ...
    min([min(min(fttoshow)) min(min(bttoshow))])]);
maxcurlim = min([meancur+stdrangecur*stdcur max([max(max(fctoshow)) ...
    max(max(bctoshow))])]);
mincurlim = max([meancur-stdrangecur*stdcur min([min(min(fctoshow)) ...
    min(min(bctoshow))])]);

topolimarray = [mintopolim maxtopolim];
curlimarray = [mincurlim maxcurlim];

h1 = figure;
imagesc(x_actual,y_actual,fttoshow);
```

```
C = hot(100);
colormap(C);
cbar = colorbar('FontSize',16,'YLim',topolimarray);
set(get(cbar,'ylabel'),'String', 'Topography (nm)','FontSize',16);
caxis(topolimarray);
axis([min(x_actual) max(x_actual) min(y_actual) max(y_actual)])
axis image
axis xy
xlabel('X-Position (nm)','FontSize',16);
ylabel('Y-Position (nm)','FontSize',16);
set(gca,'LineWidth',2,'FontSize',16);
set(gcf,'Position',[10 50 900 600],'Color','w');

h2 = figure;
imagesc(x_actual,y_actual,bttoshow);
colormap(C);
cbar = colorbar('FontSize',16,'YLim',topolimarray);
set(get(cbar,'ylabel'),'String', 'Topography (nm)','FontSize',16);
caxis(topolimarray);
axis([min(x_actual) max(x_actual) min(y_actual) max(y_actual)])
axis image
axis xy
xlabel('X-Position (nm)','FontSize',16);
ylabel('Y-Position (nm)','FontSize',16);
set(gca,'LineWidth',2,'FontSize',16);
set(gcf,'Position',[10 50 900 600],'Color','w');

h3 = figure;
imagesc(x_actual,y_actual,fctoshow);
C = hot(100);
colormap(C);
cbar = colorbar('FontSize',16,'YLim',curlimarray);
```

```
set(get(cbar,'ylabel'),'String', 'Current (nA)','FontSize',16);
caxis(curlimarray);
axis([min(x_actual) max(x_actual) min(y_actual) max(y_actual)])
axis image
axis xy
xlabel('X-Position (nm)','FontSize',16);
ylabel('Y-Position (nm)','FontSize',16);
set(gca,'LineWidth',2,'FontSize',16);
set(gcf,'Position',[10 50 900 600],'Color','w');

h4 = figure;
imagesc(x_actual,y_actual,bctoshow);
colormap(C);
cbar = colorbar('FontSize',16,'YLim',curlimarray);
caxis(curlimarray);
set(get(cbar,'ylabel'),'String', 'Current (nA)','FontSize',16);
axis([min(x_actual) max(x_actual) min(y_actual) max(y_actual)])
axis image
axis xy
xlabel('X-Position (nm)','FontSize',16);
ylabel('Y-Position (nm)','FontSize',16);
set(gca,'LineWidth',2,'FontSize',16);
set(gcf,'Position',[10 50 900 600],'Color','w');

if SaveImages == 1
    curdir = pwd;
    imagedir = sprintf('%s%s',pwd,'\Images');
    mkdir(curdir,'Images');
    ftname = sprintf('%s%s%s%s',imagedir,'\',imagename,'_topoforw');
    btname = sprintf('%s%s%s%s',imagedir,'\',imagename,'_topoback');
    fcname = sprintf('%s%s%s%s',imagedir,'\',imagename,'_currentforw');
    bcname = sprintf('%s%s%s%s',imagedir,'\',imagename,'_currentback');
```

```
    saveas(h1,ftname,'jpg');
    saveas(h1,ftname,'fig');
    saveas(h2,btname,'jpg');
    saveas(h2,btname,'fig');
    saveas(h3,fcname,'jpg');
    saveas(h3,fcname,'fig');
    saveas(h4,bcname,'jpg');
    saveas(h4,bcname,'fig');
end

imageraw = image;
imageraw.ForwardTopography = fttoshow;
imageraw.BackwardTopography = bttoshow;
imageraw.ForwardTunnelingCurrent = fctoshow;
imageraw.BackwardTunnelingCurrent = bctoshow;
imageraw.XPositionArray = x_actual;
imageraw.YPositionArray = y_actual;

result = imageraw;
```

There are four inputs to this .m file. The first one is the filename, which should be entered without the file extension .txt. For example, if your file name is “ILOVEOSCAN.txt”, you should call this function from the command window as: data = importimagedata('ILOVEOSCAN');. The second input is the option for saving the images. If you enter 1 here as the value, it will save the images generated. A 0 input will skip the image saving step. The third input is the range for the standard deviation on the topography for display purposes. Before displaying the images, the code first generates a color bar appropriate for the image. To do that, the code finds the mean value of the topography, then it sets the limits of the color bar at mean(topography) +/- standard deviation(topography)*third input. The fourth input is almost the same as the third input except it is for the current images.

A.4.11 Processing Images in Matlab

We have written the following code in Matlab to import the images saved using OScan v2.0, process the imported images and then display them. There are two processing steps: plane fitting and smoothening. The plane fitting part simply fits a plane to the images using the least squares method and then subtracts that plane from the image. The smoothening filter is the second step, which includes the application of a smoothening filter on the image. The .m file uses the importimagedata.m function directly to import the images and the same functions described above to display them. The .m file is given below:

```
function result = imageprocess(fname, SaveImages, stdrange_topo, ...
    stdrange_current)

close all
clc

imagename = fname;
image = importimagedata(fname);

numpix = image.NumberOfPixels;

ftopo = image.ForwardTopography;
btopo = image.BackwardTopography;
fcur = image.ForwardTunnelingCurrent;
bcur = image.BackwardTunnelingCurrent;
imagesize = image.ImageSize;

x=1:1:numpix;
y=1:1:numpix;
x_actual = x*imagesize/numpix;
```

```
y_actual = y*imagesize/numpix;

dum = 1:numpix*numpix;
xarray = mod(dum-1,numpix)+1;
yarray = ceil(dum/numpix);
ftopoarray = image.ForwardTopographyarray;
btopoarray = image.BackwardTopographyarray;
fcurarray = image.ForwardTunnelingCurrentarray;
bcurarray = image.BackwardTunnelingCurrentarray;
[ft_mean slope_ft] = lsplane([xarray' yarray' ftopoarray]);
[bt_mean slope_bt] = lsplane([xarray' yarray' btopoarray]);
[fc_mean slope_fc] = lsplane([xarray' yarray' fcurarray]);
[bc_mean slope_bc] = lsplane([xarray' yarray' bcurarray]);

xmat = reshape(xarray,numpix,numpix)';
xmat = xmat(end:-1:1,:);
ymat = reshape(yarray,numpix,numpix)';
ymat = ymat(end:-1:1,:);

ft_plane = ...
    (-slope_ft(1,1)/slope_ft(3,1))*(xmat-ft_mean(1,1))+(-slope_ft(2,1)...
.../slope_ft(3,1))*(ymat-ft_mean(2,1))+ft_mean(3,1);
bt_plane = ...
    (-slope_bt(1,1)/slope_bt(3,1))*(xmat-bt_mean(1,1))+(-slope_bt(2,1)...
.../slope_bt(3,1))*(ymat-bt_mean(2,1))+bt_mean(3,1);
fc_plane = ...
    (-slope_fc(1,1)/slope_fc(3,1))*(xmat-fc_mean(1,1))+(-slope_fc(2,1)...
.../slope_fc(3,1))*(ymat-fc_mean(2,1));
bc_plane = ...
    (-slope_bc(1,1)/slope_bc(3,1))*(xmat-bc_mean(1,1))+(-slope_bc(2,1)...
.../slope_bc(3,1))*(ymat-bc_mean(2,1));

```

```
ftopo2 = ftopo - ft_plane;
btopo2 = btopo - bt_plane;
fcur2 = fcur - fc_plane;
bcur2 = bcur - bc_plane;

n = 5;
h = ones(n,n) / n^2;
ftopo3 = imfilter(ftopo2,h);
btopo3 = imfilter(btopo2,h);
fcur3 = imfilter(fcur2,h);
bcur3 = imfilter(bcur2,h);

fttoshow = ftopo3;
bttoshow = btopo3;
fctoshow = fcur3;
bctoshow = bcur3;

meantopo = mean([mean(mean(fttoshow)) mean(mean(bttoshow))]);
stdtopo = max([std(mean(fttoshow)) std(mean(bttoshow))]);
meancur = mean([mean(mean(fctoshow)) mean(mean(bctoshow))]);
stdcur = max([std(mean(fctoshow)) std(mean(bctoshow))]);
stdrangetopo = stdrange_topo;
stdrangecur = stdrange_current;

maxtopolim = min([meantopo+stdrangetopo*stdtopo ...
    max([max(max(fttoshow)) max(max(bttoshow))])]);
mintopolim = max([meantopo-stdrangetopo*stdtopo ...
    min([min(min(fttoshow)) min(min(bttoshow))])]);
maxcurlim = min([meancur+stdrangecur*stdcur max([max(max(fctoshow)) ...
    max(max(bctoshow))])]);
mincurlim = max([meancur-stdrangecur*stdcur min([min(min(fctoshow)) ...
    min(min(bctoshow))])]);
```

```

topolimarray = [mintopolim maxtopolim];
curlimarray = [mincurlim maxcurlim];

h1 = figure;
imagesc(x_actual,y_actual,fttoshow);
C = hot(100);
colormap(C);
cbar = colorbar('FontSize',16,'YLim',topolimarray);
set(get(cbar,'ylabel'),'String', 'Topography (nm)','FontSize',16);
caxis(topolimarray);
axis([min(x_actual) max(x_actual) min(y_actual) max(y_actual)])
axis image
axis xy
xlabel('X-Position (nm)','FontSize',16);
ylabel('Y-Position (nm)','FontSize',16);
set(gca,'LineWidth',2,'FontSize',16);
set(gcf,'Position',[10 50 900 600],'Color','w');

h2 = figure;
imagesc(x_actual,y_actual,bttoshow);
colormap(C);
cbar = colorbar('FontSize',16,'YLim',topolimarray);
set(get(cbar,'ylabel'),'String', 'Topography (nm)','FontSize',16);
caxis(topolimarray);
axis([min(x_actual) max(x_actual) min(y_actual) max(y_actual)])
axis image
axis xy
xlabel('X-Position (nm)','FontSize',16);
ylabel('Y-Position (nm)','FontSize',16);
set(gca,'LineWidth',2,'FontSize',16);
set(gcf,'Position',[10 50 900 600],'Color','w');
```

```
h3 = figure;
imagesc(x_actual,y_actual,fctoshow);
C = hot(100);
colormap(C);
cbar = colorbar('FontSize',16,'YLim',curlimarray);
set(get(cbar,'ylabel'),'String', 'Current (nA)','FontSize',16);
caxis(curlimarray);
axis([min(x_actual) max(x_actual) min(y_actual) max(y_actual)])
axis image
axis xy
xlabel('X-Position (nm)','FontSize',16);
ylabel('Y-Position (nm)','FontSize',16);
set(gca,'LineWidth',2,'FontSize',16);
set(gcf,'Position',[10 50 900 600],'Color','w');

h4 = figure;
imagesc(x_actual,y_actual,bctoshow);
colormap(C);
cbar = colorbar('FontSize',16,'YLim',curlimarray);
caxis(curlimarray);
set(get(cbar,'ylabel'),'String', 'Current (nA)','FontSize',16);
axis([min(x_actual) max(x_actual) min(y_actual) max(y_actual)])
axis image
axis xy
xlabel('X-Position (nm)','FontSize',16);
ylabel('Y-Position (nm)','FontSize',16);
set(gca,'LineWidth',2,'FontSize',16);
set(gcf,'Position',[10 50 900 600],'Color','w');

if SaveImages == 1
    curdir = pwd;
```

```
    imagedir = sprintf('%s%s',pwd,'\Images');
    mkdir(curdir,'Images');
    ftname = sprintf('%s%s%s%s',imagedir,'\',imagename,'_topoforw');
    btname = sprintf('%s%s%s%s',imagedir,'\',imagename,'_topoback');
    fcname = sprintf('%s%s%s%s',imagedir,'\',imagename,'_currentforw');
    bcname = sprintf('%s%s%s%s',imagedir,'\',imagename,'_currentback');
    saveas(h1,ftname,'jpg');
    saveas(h1,ftname,'fig');
    saveas(h2,btname,'jpg');
    saveas(h2,btname,'fig');
    saveas(h3,fcname,'jpg');
    saveas(h3,fcname,'fig');
    saveas(h4,bcname,'jpg');
    saveas(h4,bcname,'fig');
end

imageprocessed = image;
imageprocessed.ForwardTopography = fttoshow;
imageprocessed.BackwardTopography = bttoshow;
imageprocessed.ForwardTunnelingCurrent = fctoshow;
imageprocessed.BackwardTunnelingCurrent = bctoshow;
imageprocessed.XPositionArray = x_actual;
imageprocessed.YPositionArray = y_actual;

result = imageprocessed;
```

There are four inputs to this .m file. The first one is the filename, which should be entered without the file extension .txt. For example, if your file name is “ILOVEOSCAN.txt”, you should call this function from the command window as: data = importimagedata('ILOVEOSCAN');. The second input is the option for saving the images. If you enter 1 here as the value, it will save the images generated. A 0 input will skip the image saving step. The third input is the range for the standard deviation on the topography for display purposes. Before displaying the images, the code first generates a color bar appropriate for the image. To do that, the code finds the mean value of the topography, then it sets the limits of the color bar at mean(topography) +/- standard deviation(topography)*third input. The fourth input is almost the same as the third input except it is for the current images.

A.5 Oscan V2.0 Host Code

The host code is the main software piece that almost all the plotting and data manipulation is conducted. It can be grouped under 1 loop (for z-feedback range indicators: the needle and the indicator lamps) and a two-window sequence structure. The first window of the sequence structure is reserved for initializations and the second window of the sequence structure is reserved for 4 other loops, which are the main loop, data transfer loop, manipulation path generation loop and the plotting loop. A schematic that shows the general flow of the code is shown below in Fig. A.12.

The loop outside of the two-window sequence structure is the smallest loop in the code. It simply takes the z-scan value (which is read from FPGA front panel in main loop) and turns on the appropriate lamp and also feeds this to the needle indicator, which are all located in the imaging window. A screen shot of this loop with comments are shown below in Fig. A.13.

The first window of the two-window sequence structure is the initialization window. The code starts in this window and executes everything in this window only once, at the start of the run. After everything in this window is executed, code enters the second window of the sequence structure, where it enters infinite loops and never come back to this part again. Hence, any type of initialization that should be done at the start of the code should be done here. The commented code that is located in this window is shown below in Figures A.14 and A.15.

After initialization, the code enters the second window of the two-window sequence, in which is spends the rest of its run-time. Before the code enters the infinite loops in the second window,

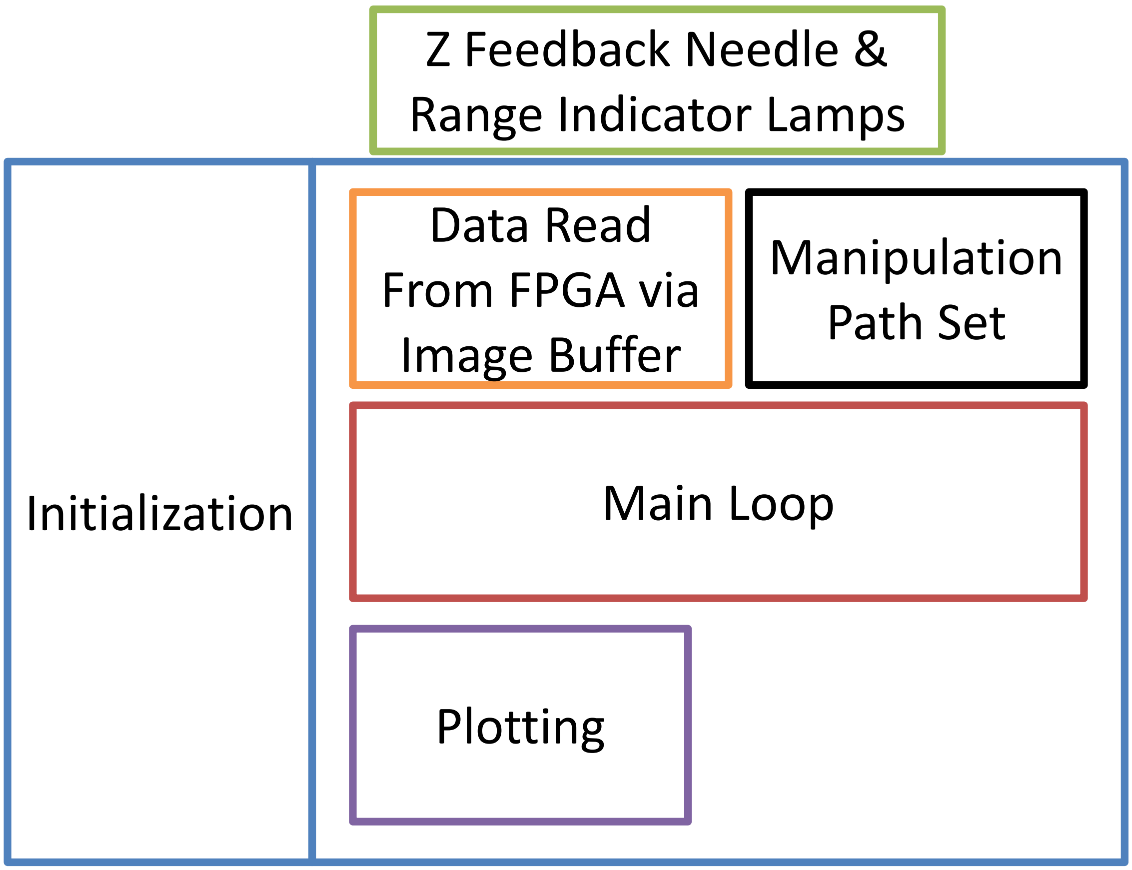

Figure A.12: The general structure of the host code. The two window blue structure is a sequence structure, in which the code initializes and then runs the 4 main loops of the code: data transfer, manipulation path generation, main and plotting loops.

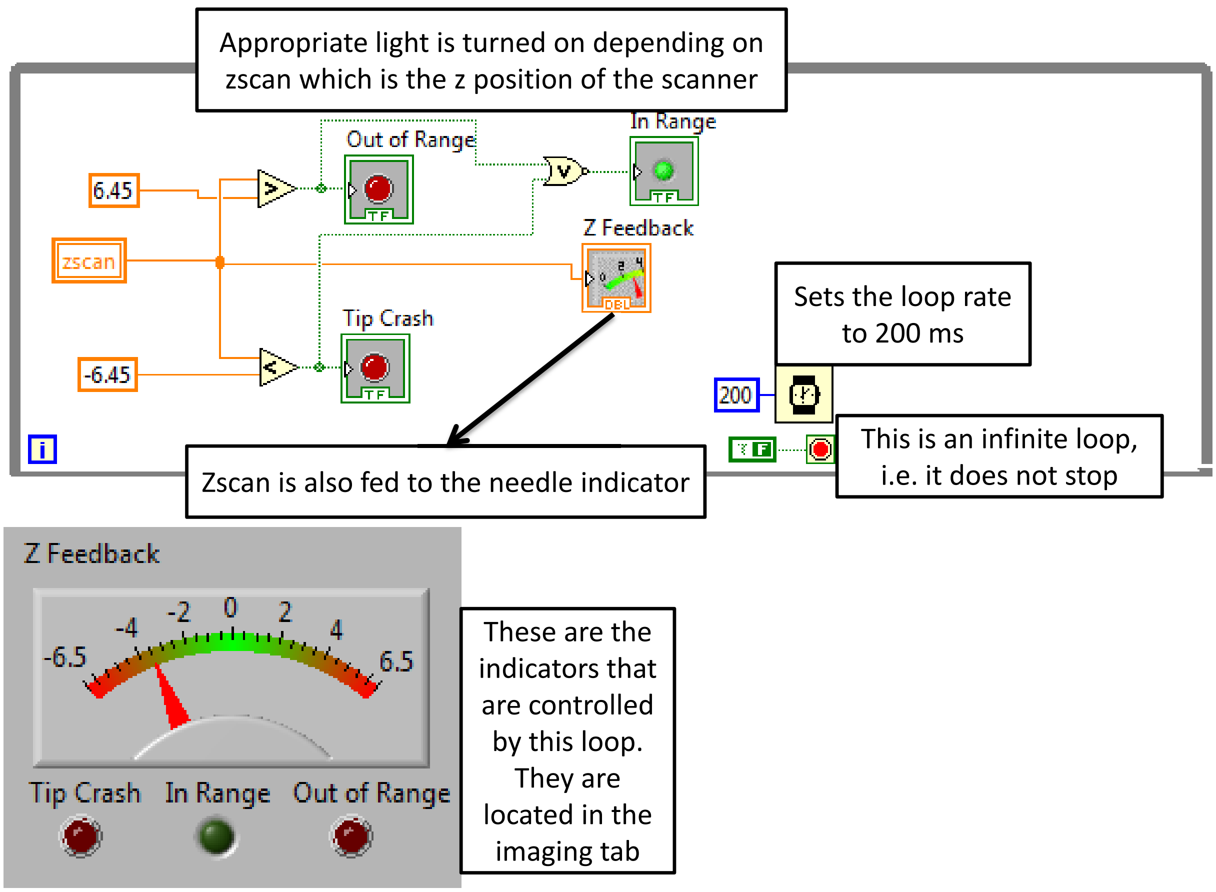

Figure A.13: The commented code that is located in the green loop from Fig. A.12

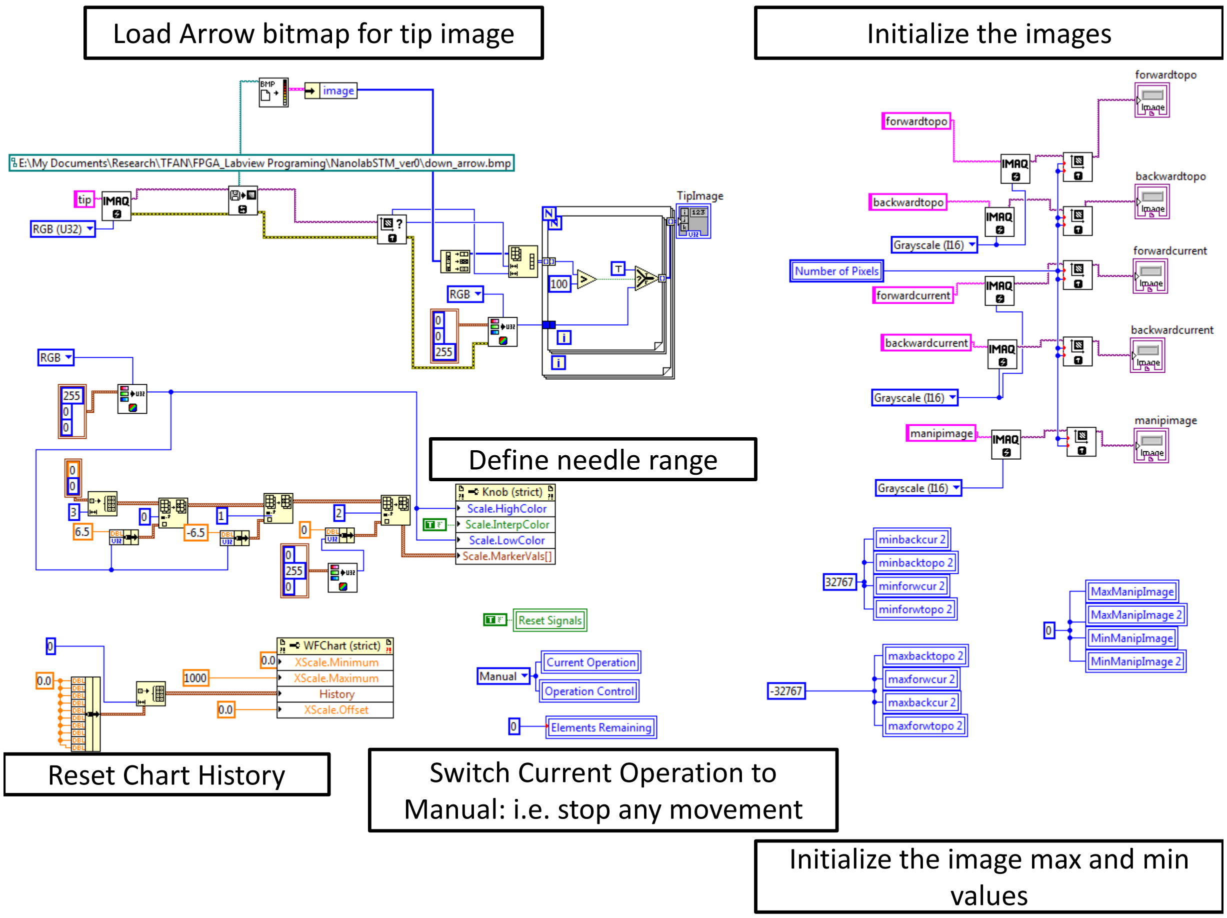

Figure A.14: Part of the commented code that is located in the first window (initialization window) of the two-window sequence structure. Only initializations should be located here.

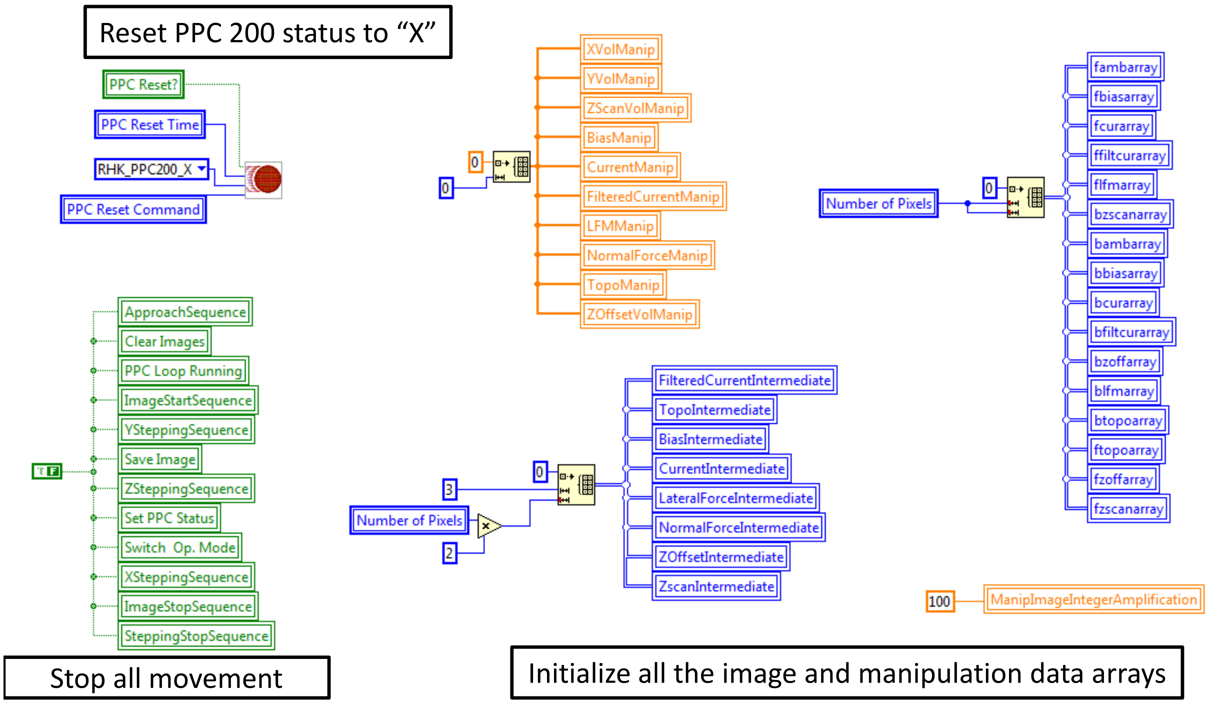

Figure A.15: The rest of the commented code that is located in the first window (initialization window) of the two-window sequence structure.

the code starts with selecting the DAQ board that will be used. It then loads the FPGA code in the device and runs the code. All of the codes that are written for this DAQ board should follow this procedure, in order to function properly. In addition to the FPGA related operations, an occurrence is also created here which is then set in data transfer loop and read at data display loop. This occurrence synchronizes the data transfer and plotting loops. A screen shot of this piece of code is shown in Fig. A.16.

Before describing the remaining 4 loops further, we should first described the two most commonly used block diagram that coverts the voltage values (-10-10V) that is read to DAQ board channels to 16 bit signed integer values (-32768-32767) which is the type that FPGA reads these values into and vice versa.

FPGA does not allow the users to store variables using floating point numbers (which are 64 bit numbers) due to the limited allocation and calculation space on the FPGA. It only allows the user to do calculations and store variables in integers. In addition to this, the entire analog

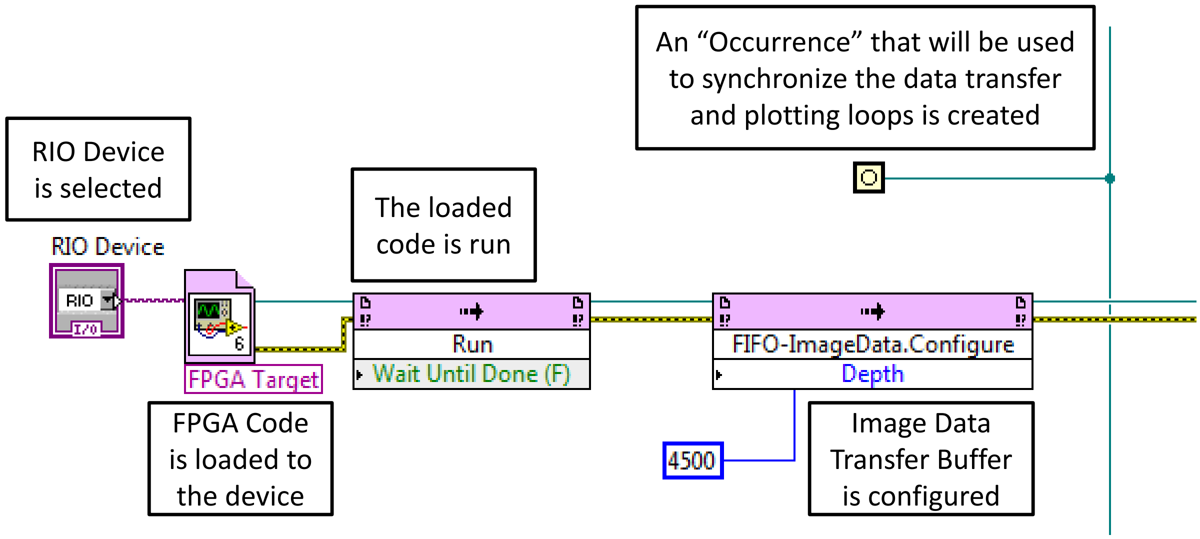

Figure A.16: The commented code piece that is located in the second window of the two-window sequence structure before the infinite loops. This code starts the FPGA operation and creates an occurrence for the synchronization of the data transfer and display.

channels read or written by the FPGA use 16 bit signed integer values. For example, a 10 volt input is written as a 16 bit integer whose value is 32767 and a -10 volt output must be written as -32768. Therefore, we try to conduct all of the operations that are done on FPGA using integers and we do all the conversions on the host code, in order to relieve FPGA from extra processing burden. The blocks that achieve these conversions are shown below in Fig. A.17.

Data transfer loop is one of the most crucial loops in the software. This loop is the backbone of the data transfer from FPGA to the host computer. It is the loop that reads the image buffer while imaging, manipulation and spectroscopy (the buffer name is imaging buffer but actually it is used to transfer data during imaging, manipulation and spectroscopy operations from FPGA to Host). This loop only runs while imaging, manipulation and spectroscopy and reads the buffer elements into a large array. This array is then separated to its channels using "Extract-FromDMA.vi". All of the channels resolved in the previous step are then converted to voltage values and multiplied by "CurrentIntegerAmplification" in order to change the parameters to integer values and amplify. This is done for mere visualization purposes and the data is not saved this way. While this is happening, a counter counts the iterations and sets the occurrence after

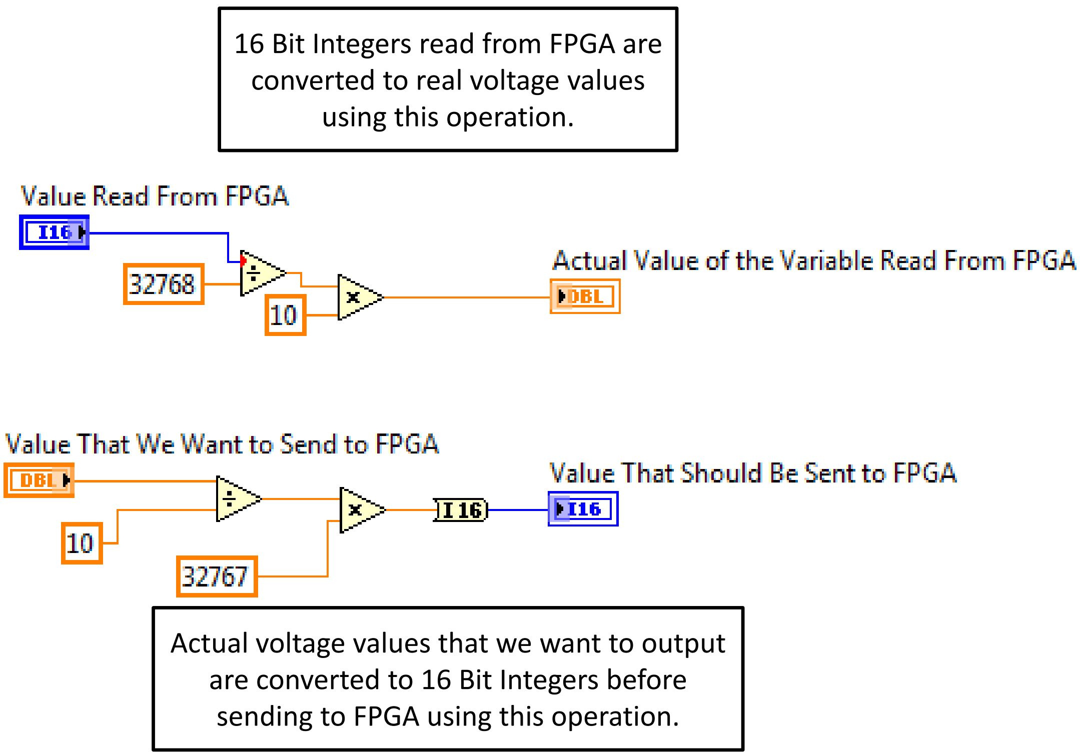

Figure A.17: The commented code pieces that are used to convert actual voltage values to FPGA integers and vice versa. These blocks are used commonly throughout the code and will not be explained again.

the fourth iteration and resets the counter, because in an iteration of the loop, 1/4th of a line is transferred to host. This occurrence is going to trigger the plotting loop, and the images will be updated once in a line. Topography is also filtered here, if the ”filter topo” switch is True, by using a built-in Labview function. A schematic of the data transfer loop is shown below in Fig. A.18.

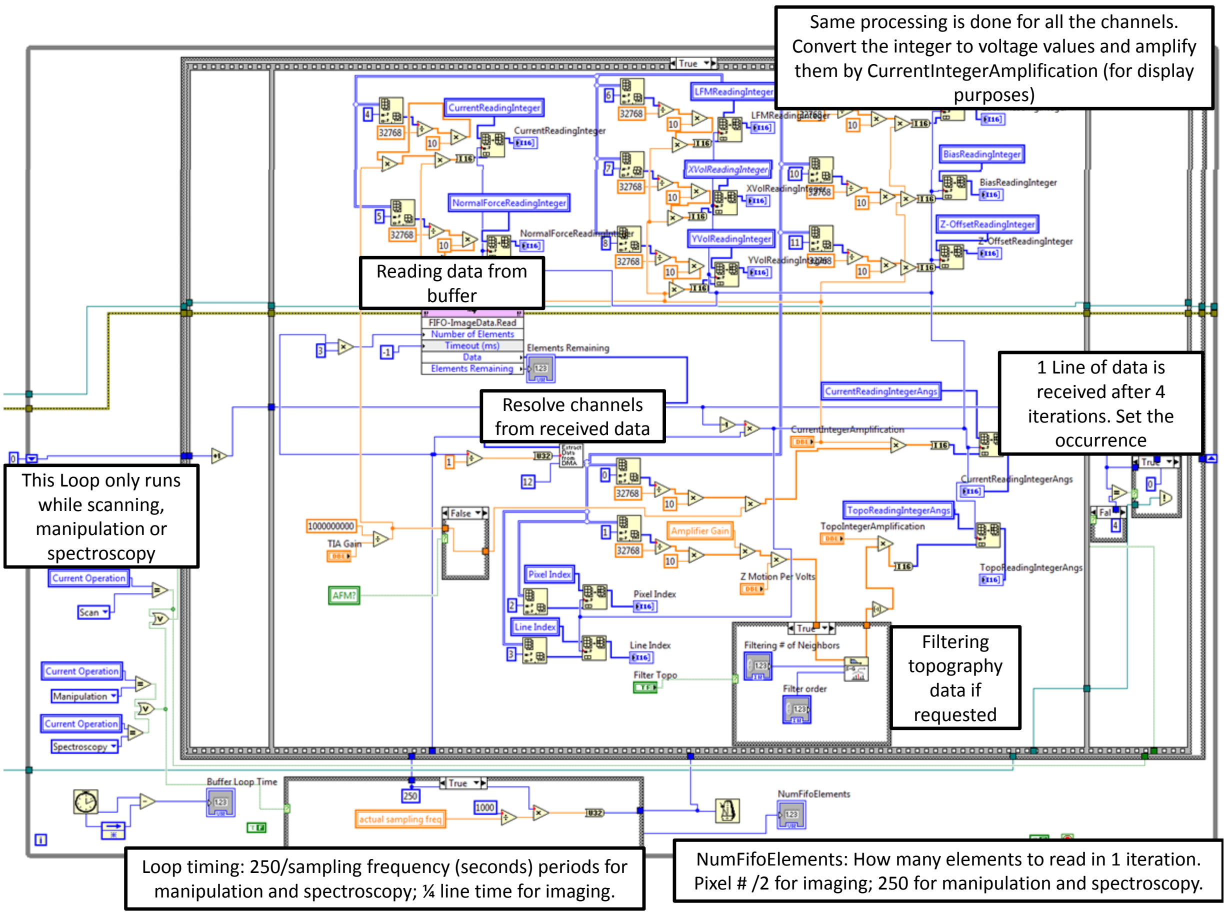

Figure A.18: The commented data transfer loop. Image/manipulation/spectroscopy data generated/read by the DAQ board is transferred to host computer through this loop. It is written to intermediate arrays which will then be processed.

Another loop that is located in the second window of the sequence structure is ”Manipulation Path Set” loop. This loop is active when the user is viewing the manipulation tab and includes all the code pieces that command the manipulation tab operations such as importing the manipulation image, scaling the manipulation image, defining or importing region of interests (ROIs) on the manipulation image, creating actual manipulation path from ROIs and generating ROI parameters in real world coordinates for user convenience, such as center coordinates or ROI radius. A schematic of the structure of manipulation path set loop is shown in Fig. A.19.

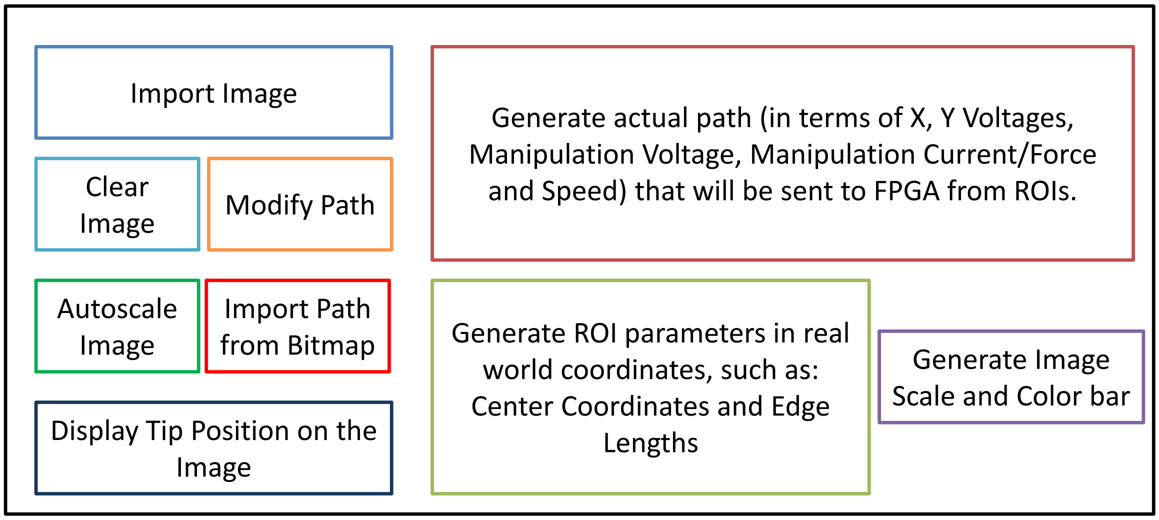

Figure A.19: A schematic of the manipulation path set loop. It is consisted of several sub-loops that carry all the functions in the manipulation tab.

The first part of the manipulation path set loop includes functions related to the manipulation image. Using these functions a selected image can be imported from the imaging tab, the image can be cleared or its color bar can be scaled. It also includes importing ROIs from a bitmap image and modifying the imported or defined ROIs. Another loop that is located at this part of the loop is the display tip position on the image loop, where the previously imported tip image (an arrow) is shown on the manipulation image at the position where the tip is currently located. The commented version of this part of the code is shown in Fig. A.20.

Another loop located in the manipulation path set loop is the code that is used to generate ROI parameters in world coordinates for user convenience. The code located in this loop, takes each ROI, finds and displays its type, corner coordinates, edge length, rotation angle, radius, and center position in nanometers. It is mostly used for monitoring purposes however it is proven useful while modifying manipulation path as well since during some manipulations we want exact shapes that can be written on the surface. The code is shown below in Fig. A.21.

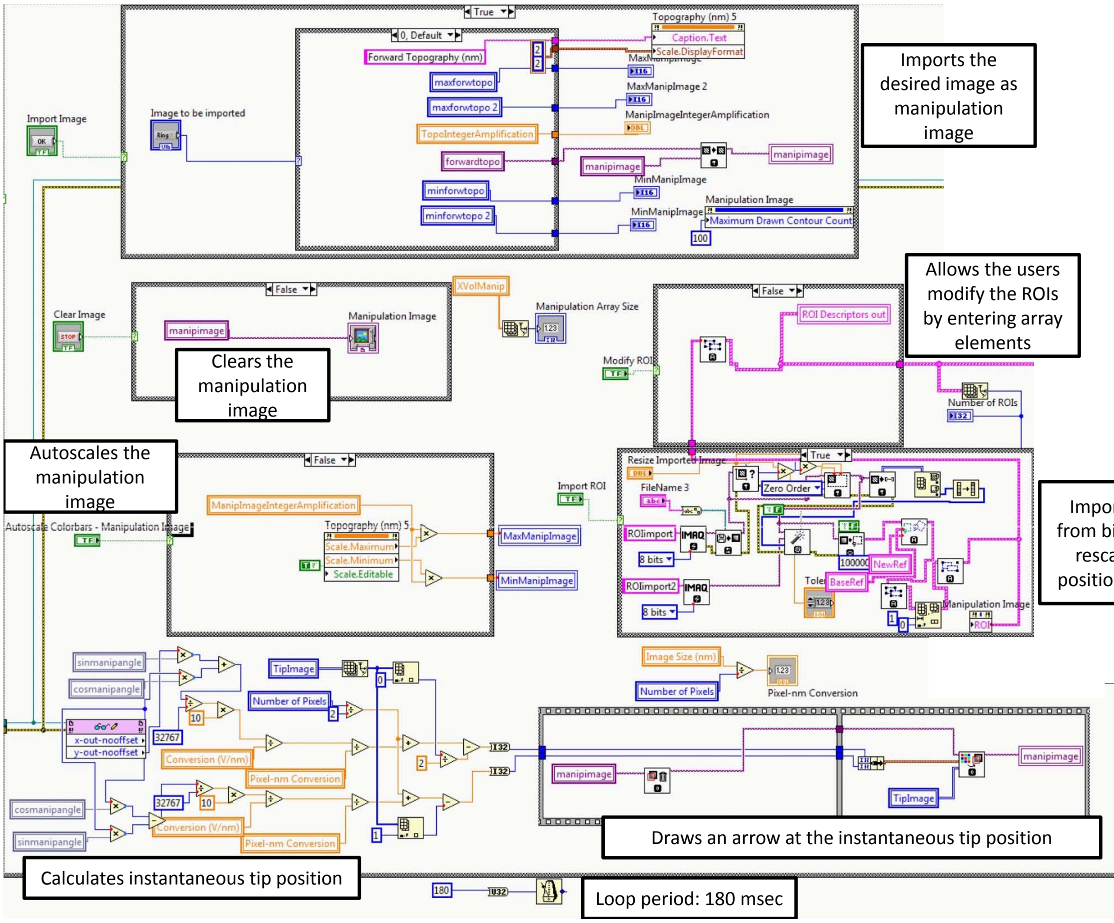

Figure A.20: The commented code that is located in the rightmost part of the manipulation path set loop.

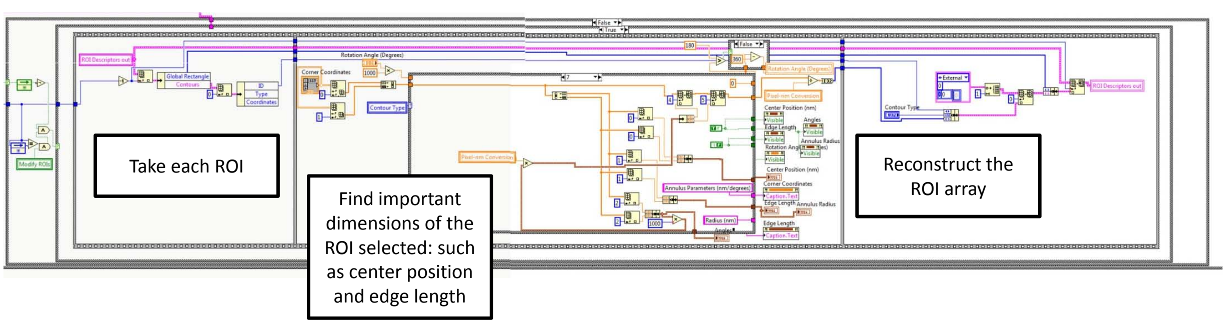

Figure A.21: The commented code that is used to generate ROI parameters in world coordinates.

The manipulation path set loop also includes a piece of code that is used to create a color bar for the manipulation image. This piece of code is standard and used for every image display in this software. It simply generates a color bar with the user defined palette type, and user defined number of ticks within the maximum and minimum value of the image pixels. The limits can also be manually changed by the user. The code is commented and shown below in Fig. A.22.

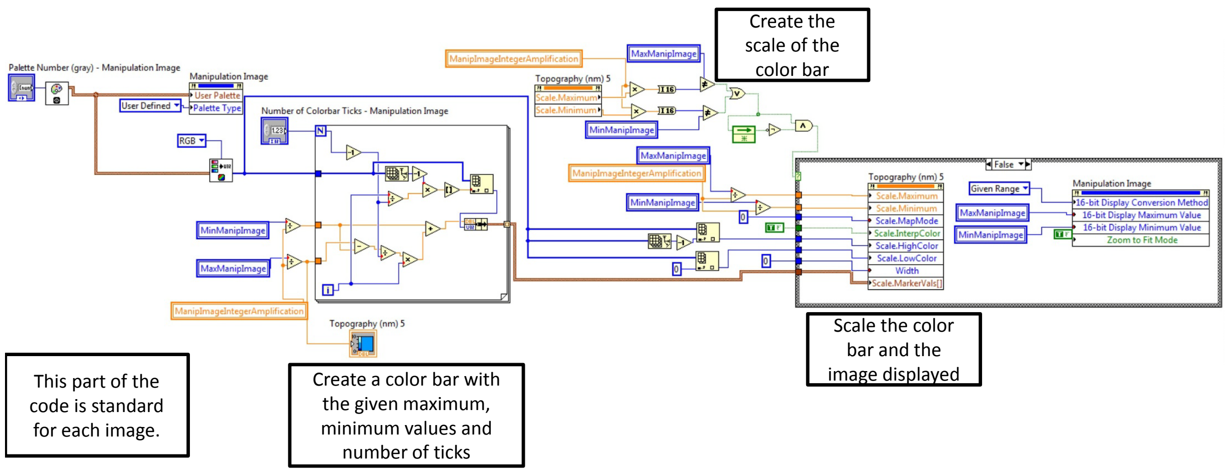

Figure A.22: The commented code that is used to generate and modify the color bar of the manipulation image.

The remaining and the most important part of the manipulation path set loop is the actual manipulation path generation loop which simply generates the manipulation path using the ROIs, speeds and manipulation force/voltage/current values. The loop starts with initializing the manipulation path array and then reads the ROIs one by one and point by point. Every point is converted to voltage values for x and y actuators and then assigned a voltage, set point and speed value. The manipulation array is then constructed from these points one last time. Therefore, every manipulation/spectroscopy point includes 5 coordinates. For manipulation, a point is defined as: (X Voltage, Y Voltage, Voltage, Set-point Current/Force, and Speed) and for spectroscopy, a point is defined as: (Spectroscopy Port Voltage, Y Voltage, Bias, X Voltage, and Speed). If spectroscopy port is bias, then the 4th coordinate of the spectroscopy point is not used. A commented version of this loop is shown below in Fig. A.23.

Another loop located in the second window of the sequence structure is the plotting loop.

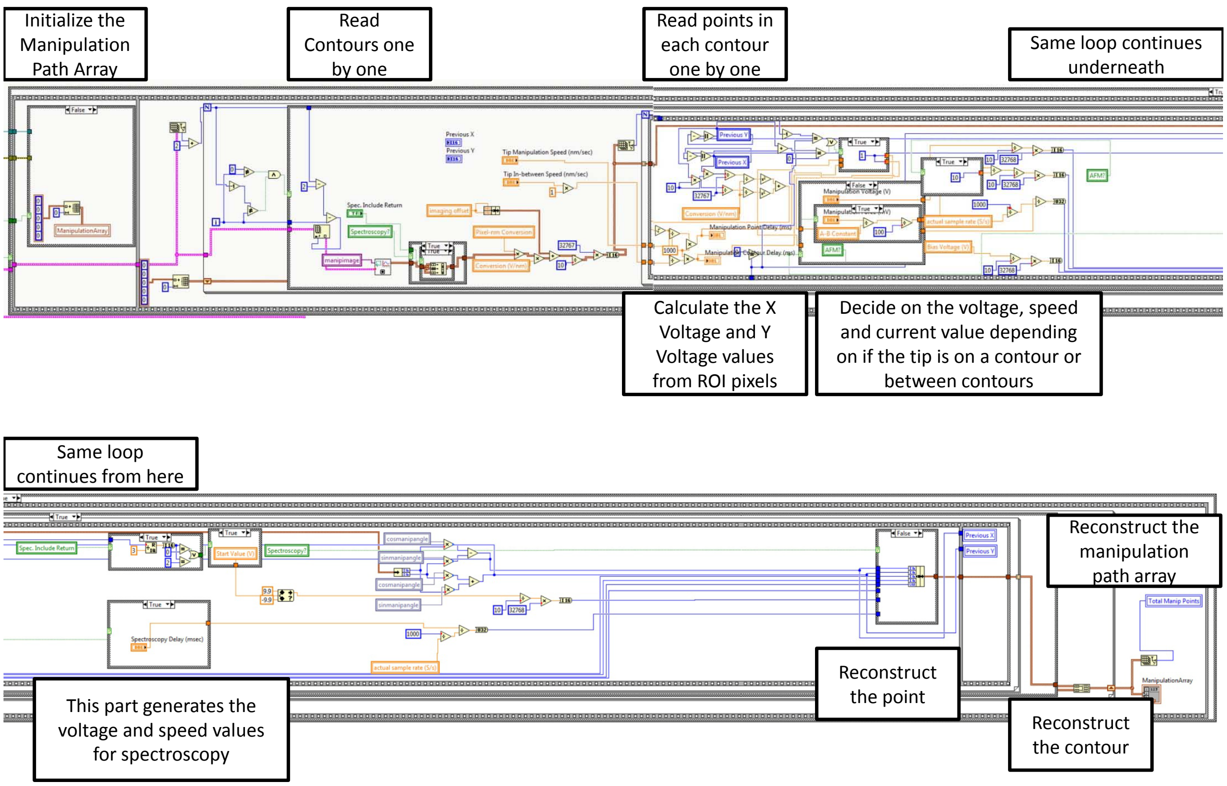

Figure A.23: The commented code that is used to generate manipulation path array.

This loop is called when there is data available to plot. This is determined using an occurrence set in the data transfer loop. An occurrence is created in the second window of the sequence structure and its set command is carried in the data transfer loop when each line data is created. The occurrence is read by the plotting loop and the plotting loop is started. It is run once after each line is read. Its purpose is to form data matrices or arrays. It only works when current operation is imaging or manipulation/spectroscopy. It consists of a case structure which chooses between imaging or manipulation/spectroscopy modes. Within the case structure, there are two main loops (one for each case) where the data plotting operations are conducted. Its structure is shown in Fig. A.24.

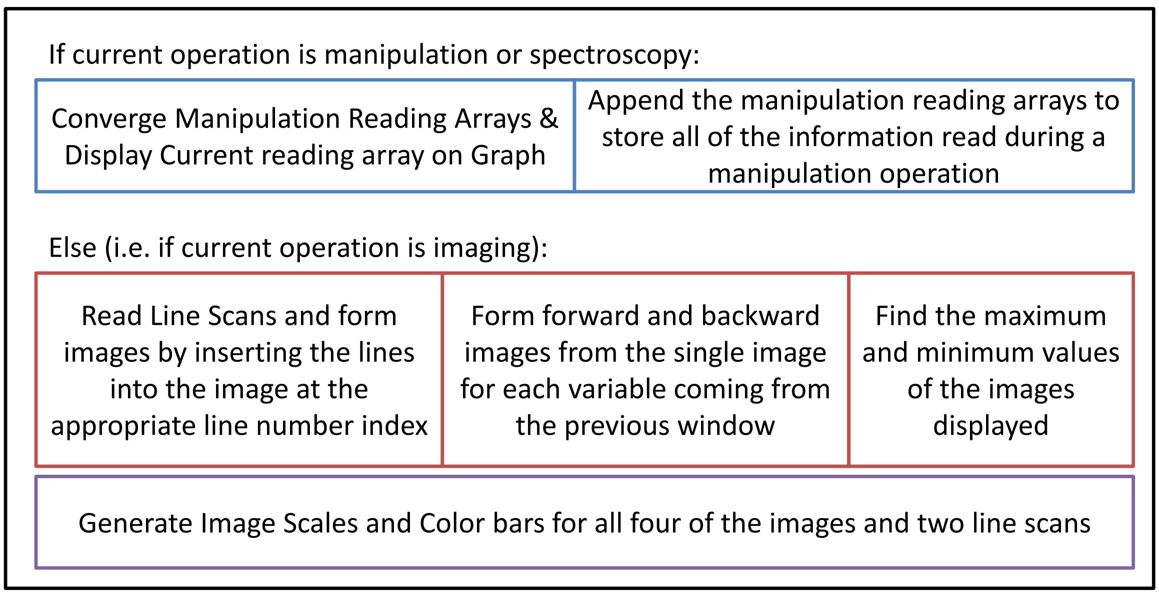

Figure A.24: A schematic of the plotting loop. It is consisted of a case structure where it selects between manipulation/spectroscopy and imaging operations and each case consists of a sequence structure. An additional image scaling loop is located in the imaging case.

For manipulation/spectroscopy case, the loop is fairly simple. The plotting loop takes the last sent data array. Outputs the last sent current reading array to the graph located in the manipulation tab. It also forms the arrays where all of the data for the manipulation/spectroscopy arrays are stored. The commented code for this operation is shown in Fig. A.25.

For imaging case, the loop is somewhat more complicated. This case consists of a three

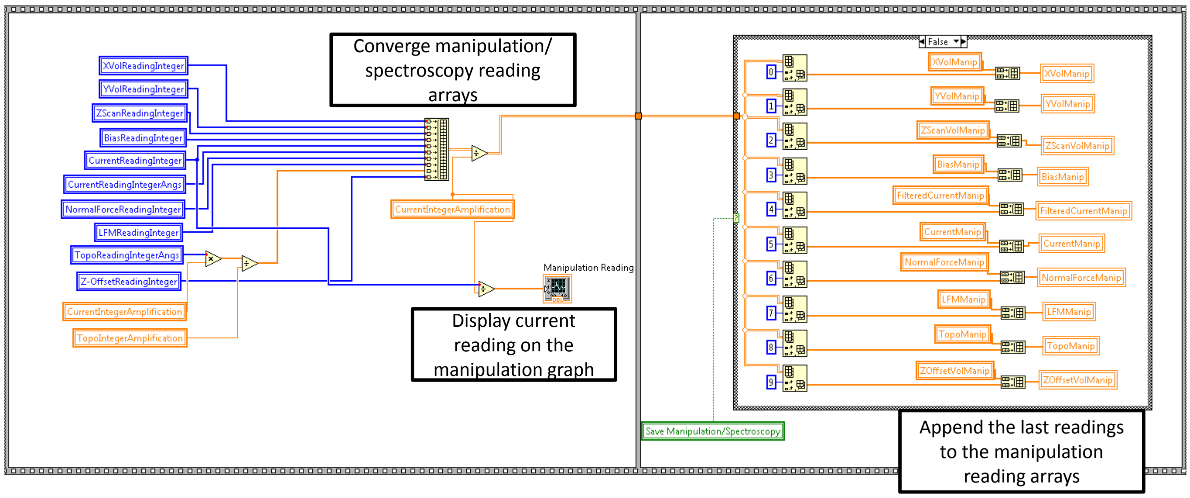

Figure A.25: The commented code that is used to generate manipulation/spectroscopy data arrays.

window sequence structure and a color bar adjusting code piece located outside the sequence structure. The color bar generation and adjusting code piece is the standard function that was also used in manipulation path set loop, only implemented here for all four of the images separately. The commented code for this color bar generation is shown in Fig. A.26.

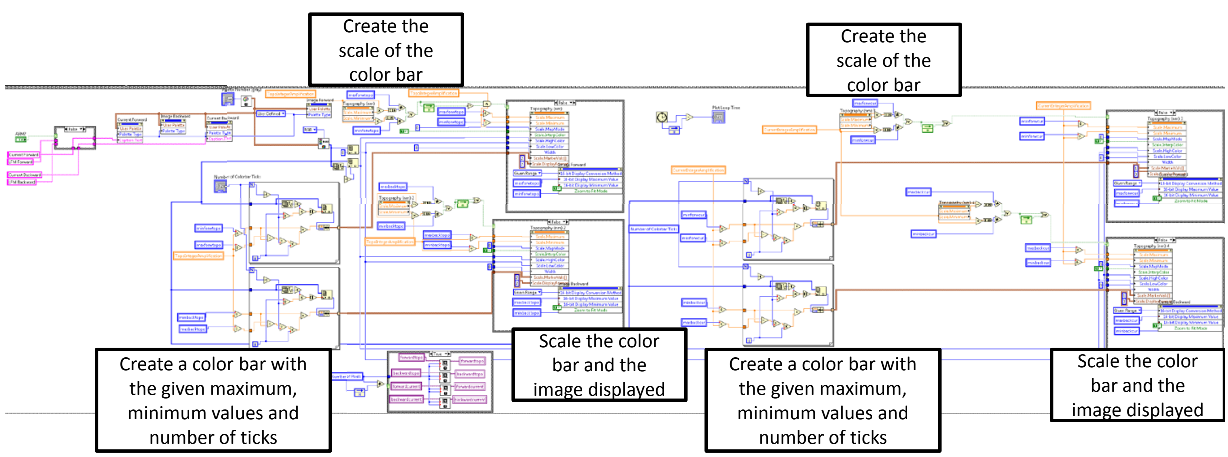

Figure A.26: The commented code that is used to generate color bars of image displays.

The sequence structure located in the imaging case of the plotting loop is implemented in order to form the image matrices. In this three window sequence structure, the first window has a for-loop located in it. This for-loop reads the data coming in arrays point by point, and assigns each point to an intermediate image matrix. Each data has its own matrix and the matrices are forward and backward direction combined. For example, 12th topography line of a 512x512 pixel image is read as a 1x1024 array and transferred to the plotting loop. Plotting loop reads every point and fills in the 12th row of the topography intermediate array which is 512x1024. The commented code for this operation is shown in Fig. A.27.

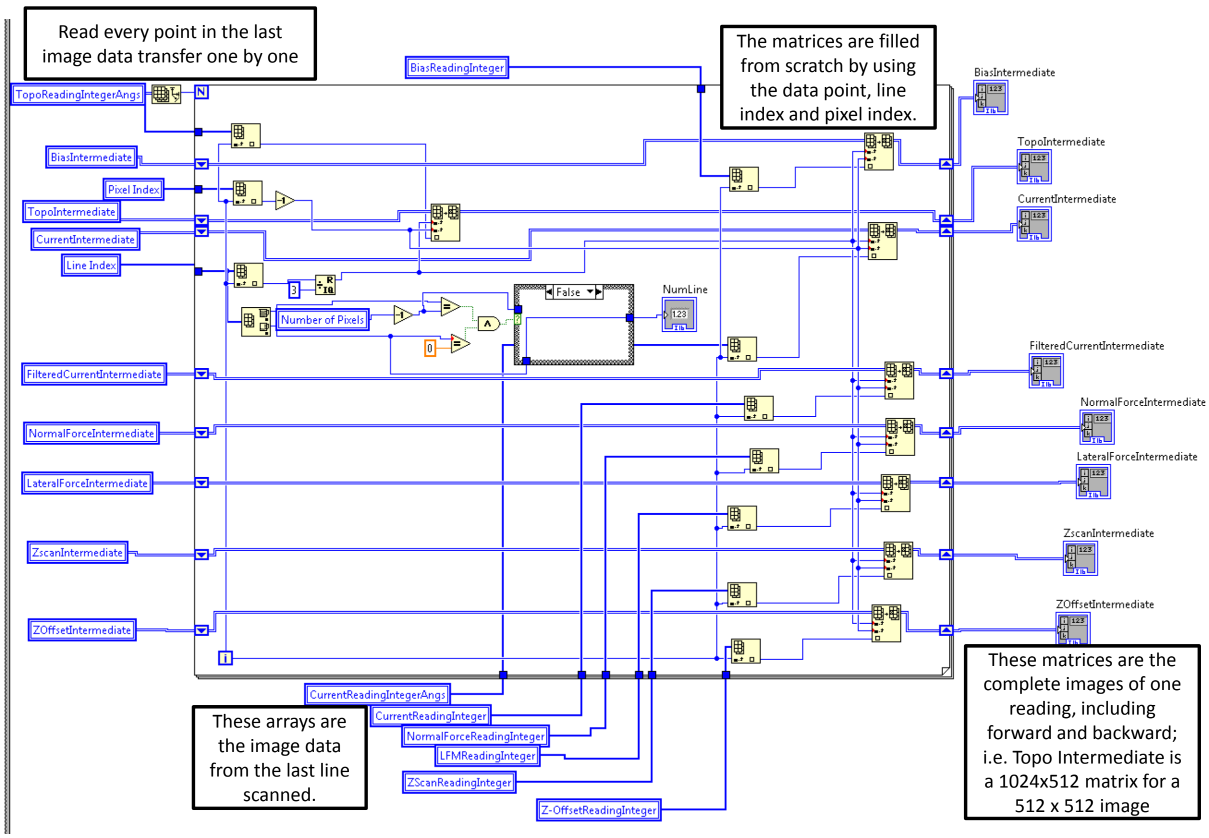

Figure A.27: The commented code that is used to generate intermediate image matrices.

The second window of the three window sequence structure takes these intermediate arrays and divides them into two arrays, forward and backward. It also reverses the backward image in order to make sure the matrices appear the same, not symmetric. To continue the previous example, the topography intermediate matrix (1024x512) defined in the previous window is divided into two 512x512 matrices in this window and the backward topography matrix is then reversed with respect to y axis. A commented code for this operation is shown in Fig. A.28.

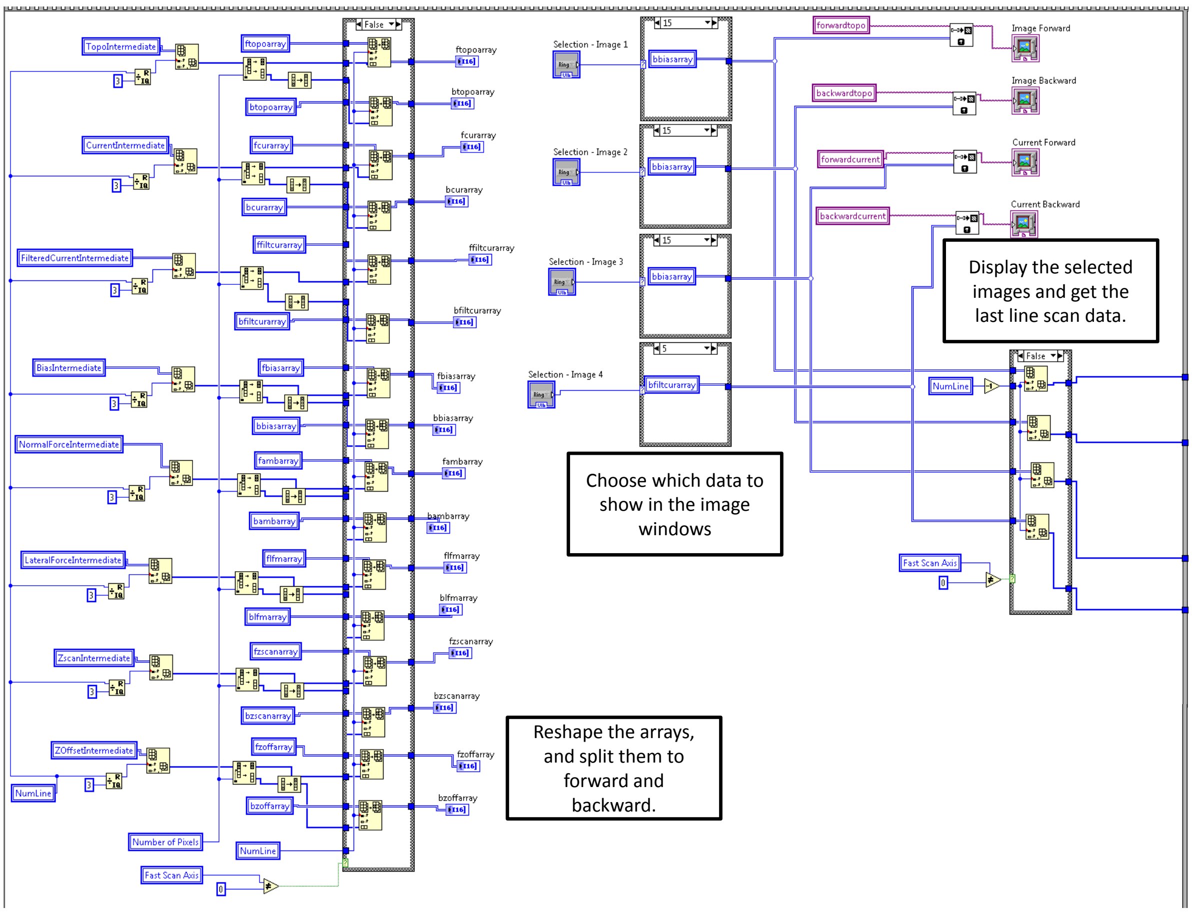

Figure A.28: The commented code that is used to generate actual image matrices.

In the third and last window of this sequence structure, minimum and maximum values of the matrices are found to adjust the color bar. Line scans are also displayed here in the imaging tab graphs. Commented code for this operation is shown in Fig. A.29.

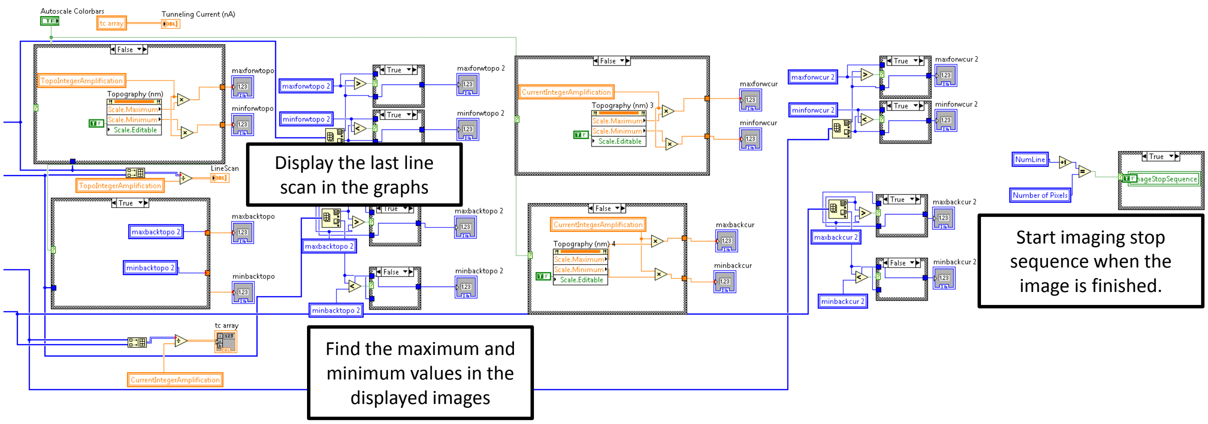

Figure A.29: The commented code that is used to find maximum and minimum pixel values of the images displayed for the generation of the color bar.

The last part of the code that is left is the main loop structure. This main loop is the part where most of the operation is commanded. It consists of 2 code pieces, one for setting the FPGA speeds and the other one for handling errors generated by FPGA-Host Code communication. Between these two code pieces, there is a stacked sequence structure, where most of the procedures are coded. A schematic of the main loop is shown in Fig. A.30.

The code piece that is used to set the FPGA loop rates is straightforward. A built in function for FPGA operations is used to convert the desired loop rate a value that FPGA can understand, and then it is fed to the FPGA side of the code using FPGA Write function. This code piece only runs when the loop rates are changed. A commented version of this operation is shown in Fig. A.31.

The first window of the stacked sequence structure is used to calculate the achievable tip speed using the actual loop rate. It also has code that sets up the host code loop rate and calculates the V/nm conversion constant for lateral positioning. A commented version of this operation is shown in Fig. A.32.

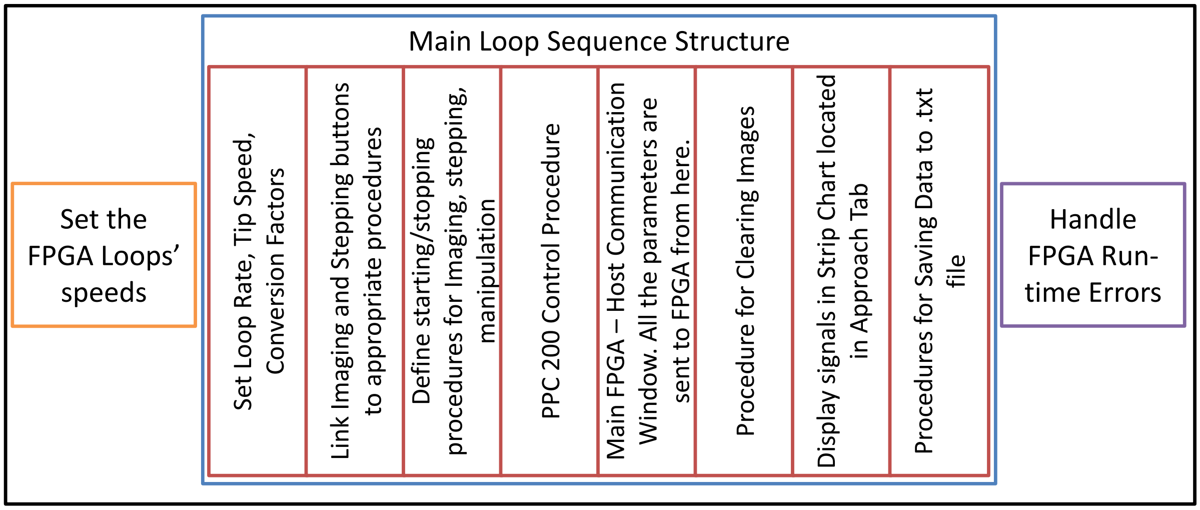

Figure A.30: A schematic of the main loop. It is consisted of two code pieces outside of a stacked sequence structure. The code pieces outside is used to set the FPGA loop speeds and handle the errors. The stack sequence is where the main operation is commanded.

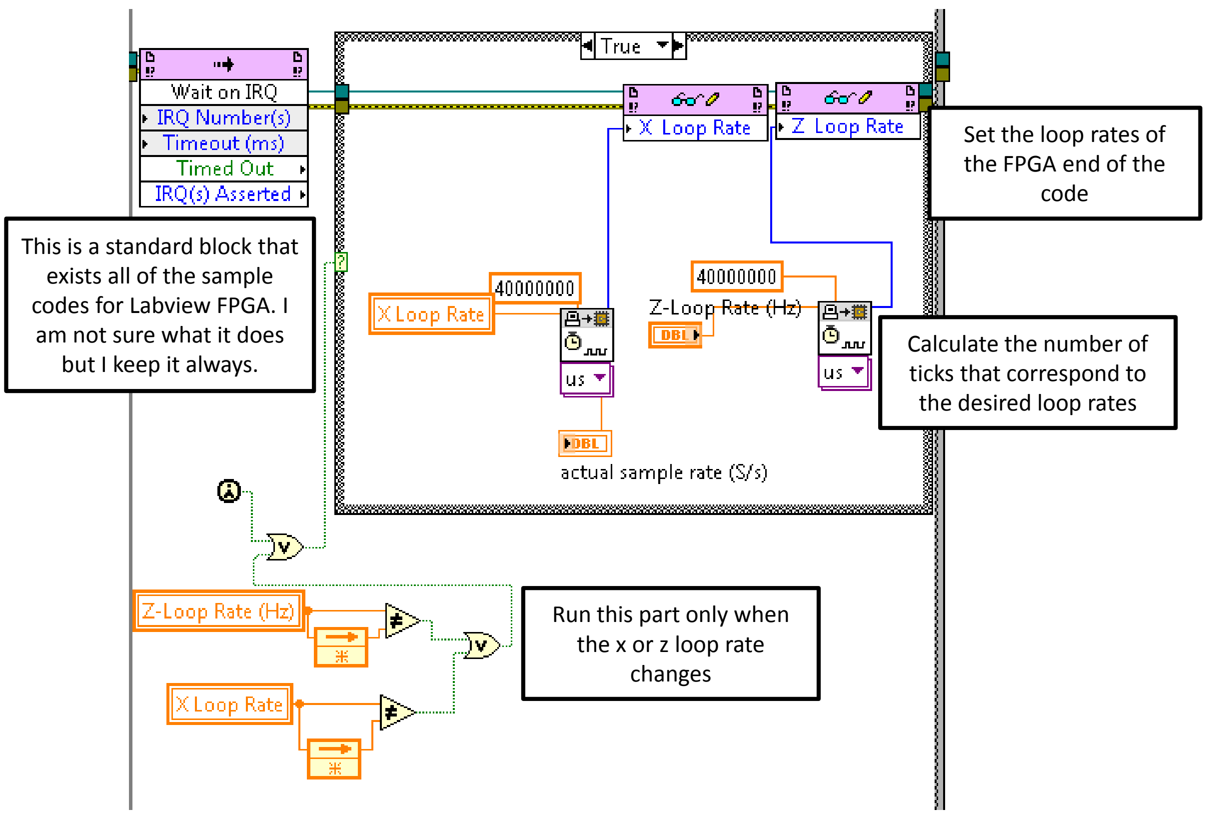

Figure A.31: The commented code that is used to set the FPGA loop rates.

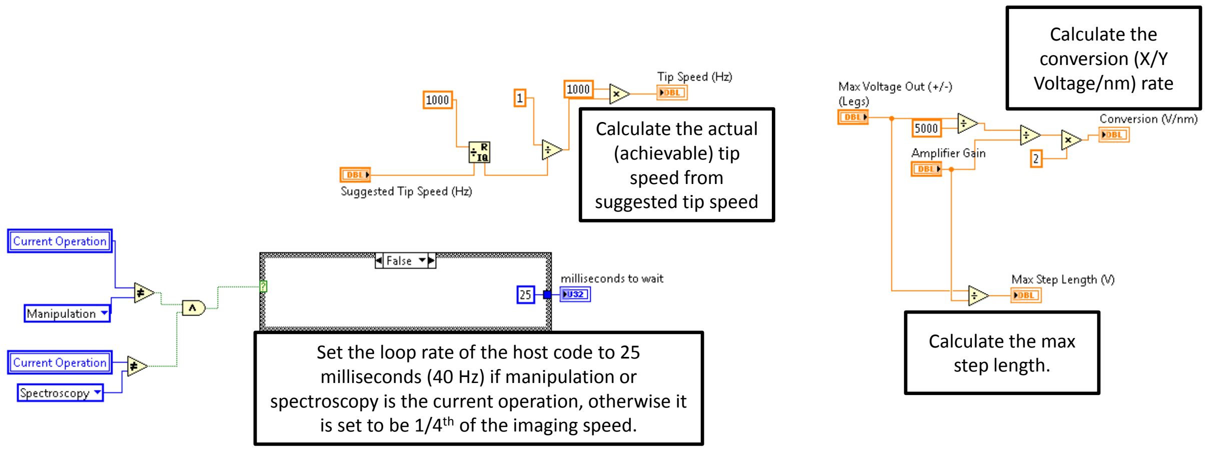

Figure A.32: 1st window of the stacked sequence structure. This window is used to calculate tip speed and update rate of the host code.

The second window of the stacked sequence structure is reserved for button definitions. When each start or stop button is pressed, the host code calls a procedure. In this window these buttons are assigned to their procedures. A commented version of this code is shown in Fig. A.33.

The third window of the stacked sequence structure is where these start or stop procedures are defined. Each procedure follows the same routine. The new operation name is written to the current operation ring, PPC200 loop is called to change the PPC200's status to the new status current operation requires, reset the signals and initialize variables. A commented version of this operation is shown in Fig. A.34.

The fourth window of the stacked sequence structure is where PPC200 loops are located. The code in this window is used to change the status of PPC 200. One loop is taken directly from RHK's codes, which communicates with PPC200 over USB and sends it the new status. The other loop controls the RHK's loop, sends it when to run and what to send to PPC200 as the new status by analyzing current operation. A commented code for this operation is shown in Fig. A.35.

The fifth window of the stacked sequence is the most crowded window and will seem as the most complicated one. However this window is also very straightforward. This window simply establishes the communication with FPGA front panel and writes and reads the parameter from

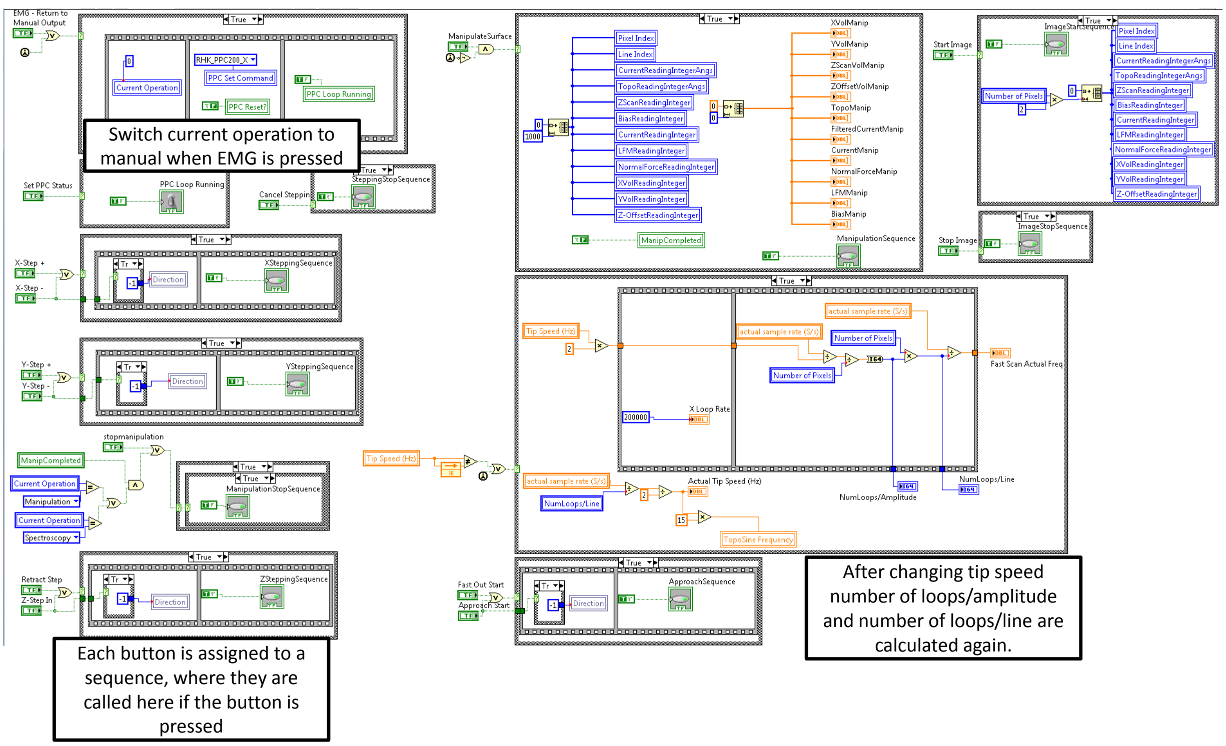

Figure A.33: 2nd window of the stacked sequence structure. This window is used to assign the action buttons to appropriate procedures.

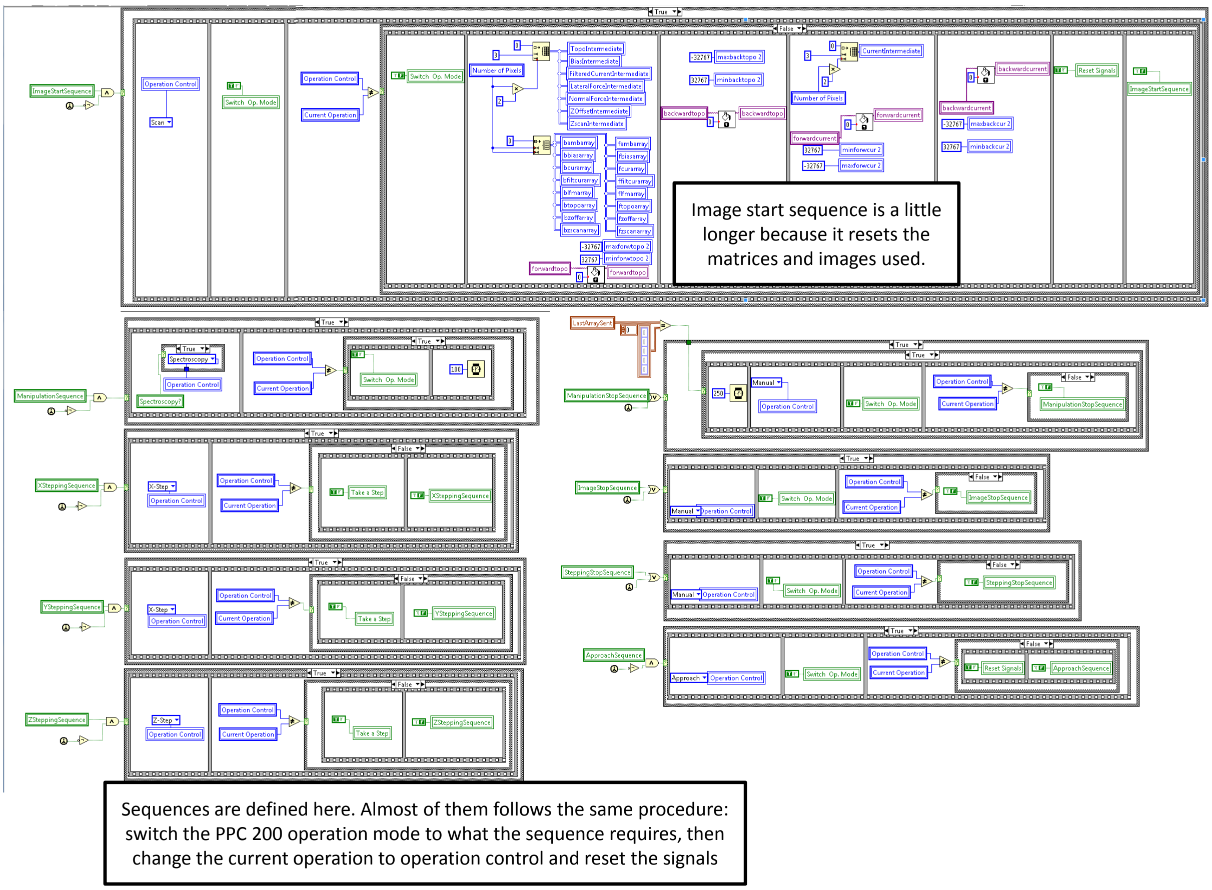

Figure A.34: 3rd window of the stacked sequence structure. This window is used to define the procedures for starting operations such as imaging, coarse positioning, etc.

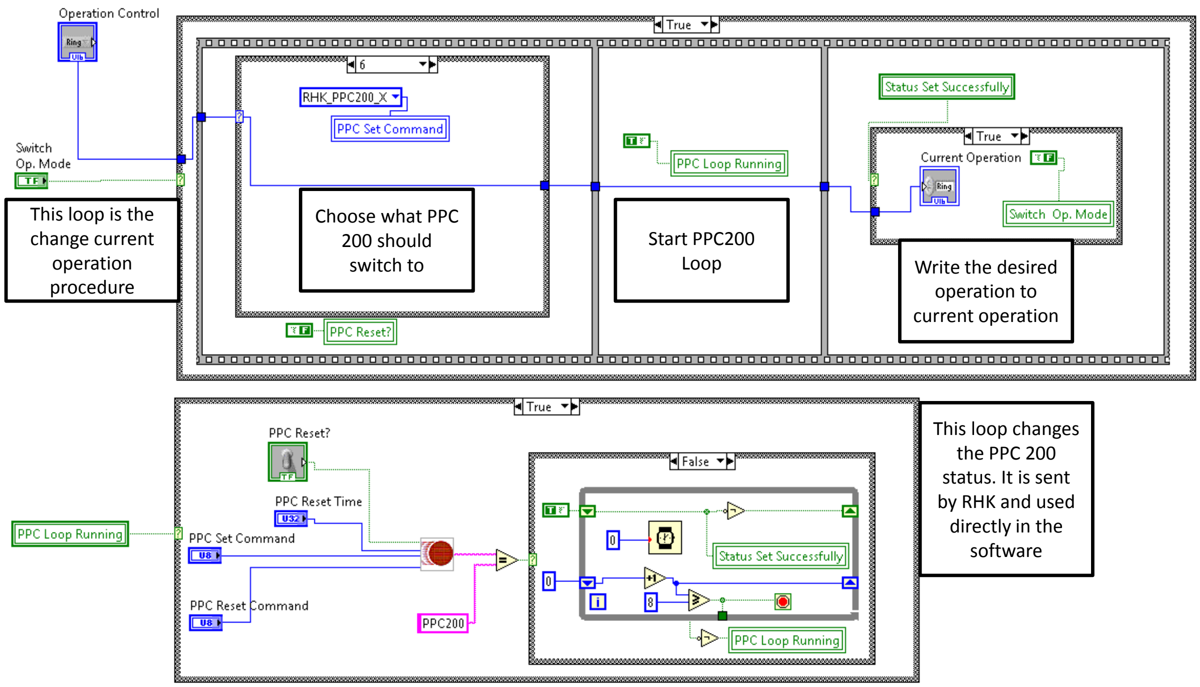

Figure A.35: 4th window of the stacked sequence structure. This window is used to switch the current operation mode and the PPC 200 status.

the FPGA front panel. All of the parameters for any operation are sent to FPGA in this window and all of the instantaneous, low speed data reading from FPGA occurs in this window. (High speed data readings occur through buffers and in the data transfer loop located outside of the main loop as discussed before.) A commented version of this code is shown below in Fig. A.36.

The sixed window of the stacked sequence structure is used to clear images and data matrices/arrays. When clear images button that is located in the imaging tab is pressed, the loop runs and initializes the images, matrices and arrays in host code. A commented version of the code is shown in Fig. A.37.

In the seventh window of the stacked sequence, instantaneous data readings from the fifth window are displayed on the graph located in the approach/coarse positioning tab. X-axes of this plot and two line scan plots in the imaging tab are also generated here. A commented version of this code is shown in Fig. A.38.

The eighth and last window of the stacked sequence structure is reserved for saving data to

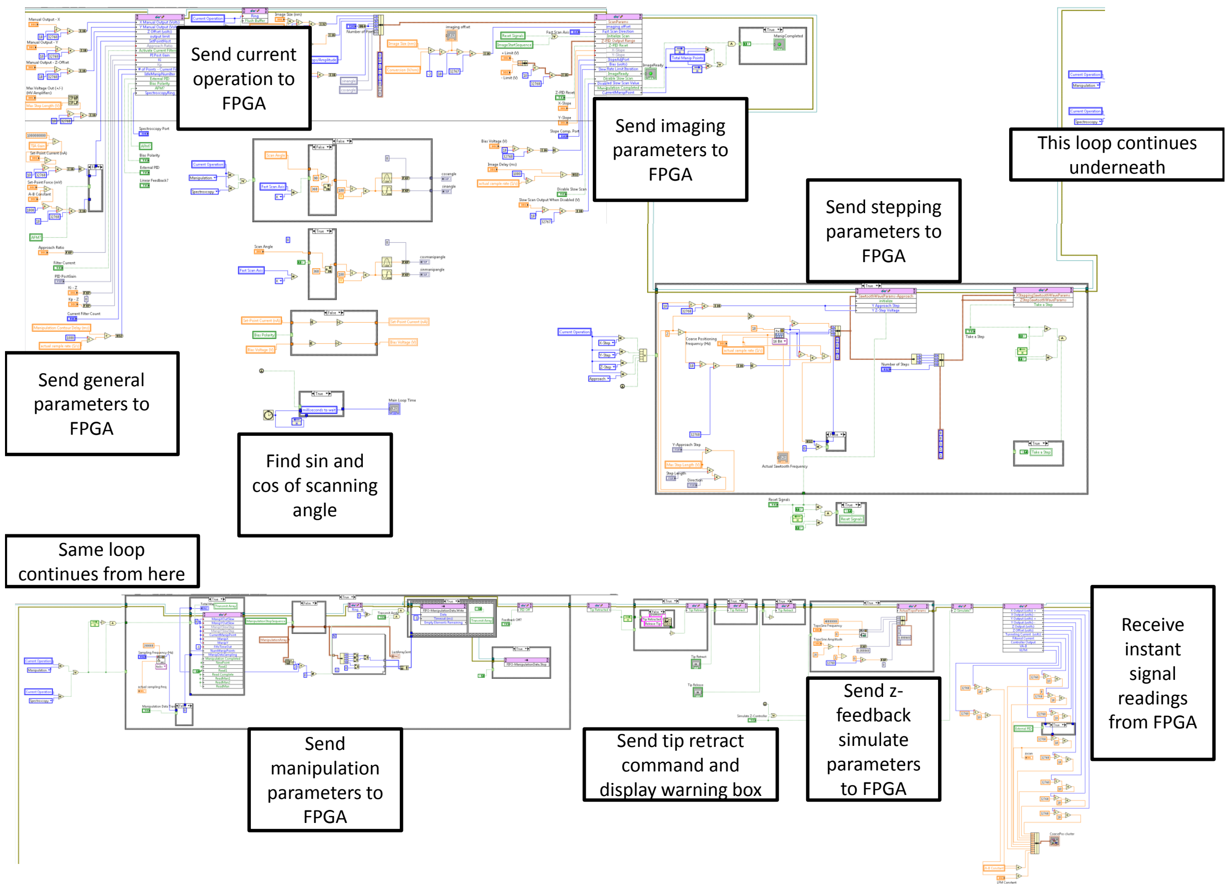

Figure A.36: 5th window of the stacked sequence structure. This window is used to establish the communication between the FPGA and the Host code to send parameters and receive instantaneous readings.

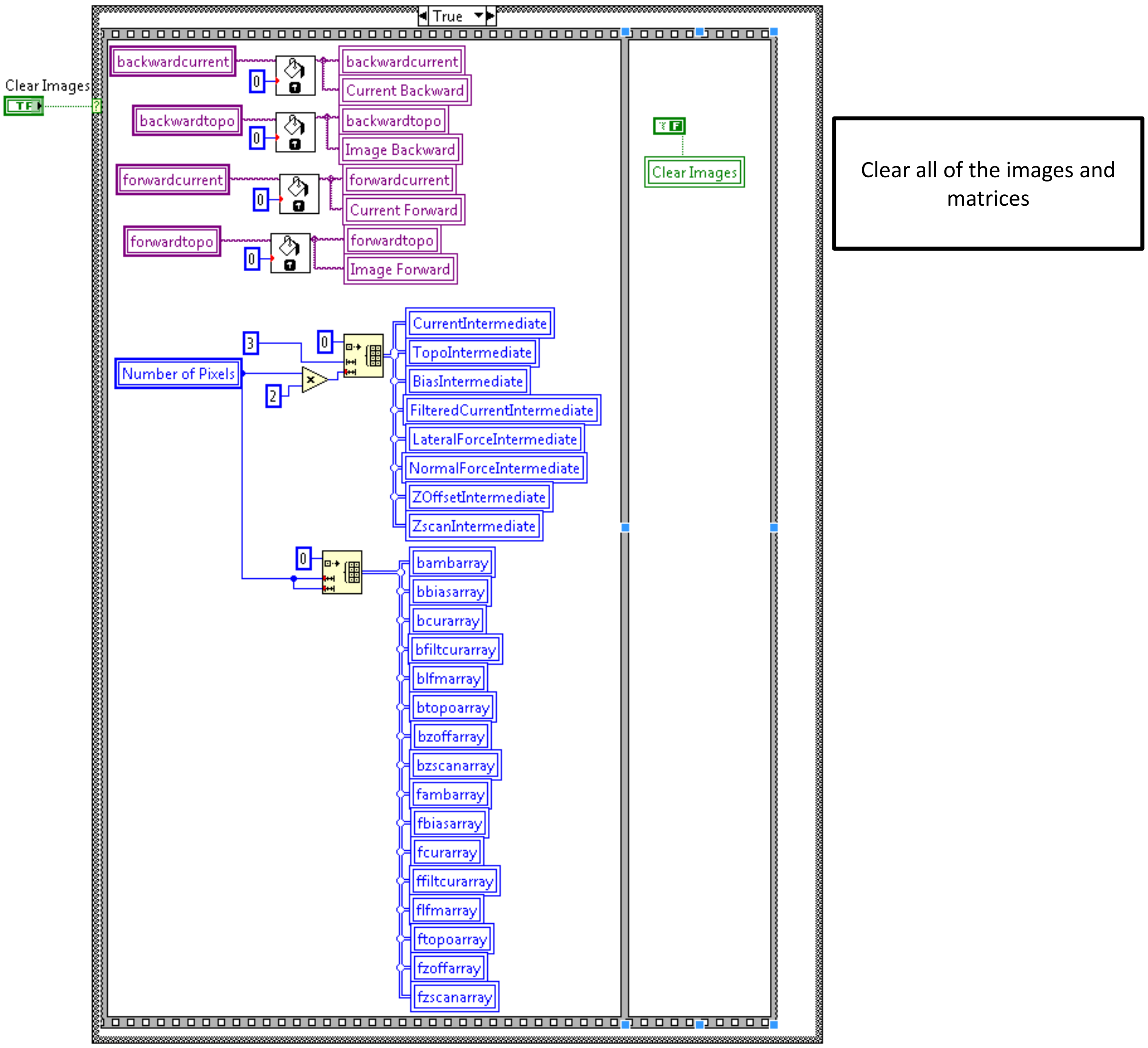

Figure A.37: 6th window of the stacked sequence structure. This window is used to clear the images and the image matrices.

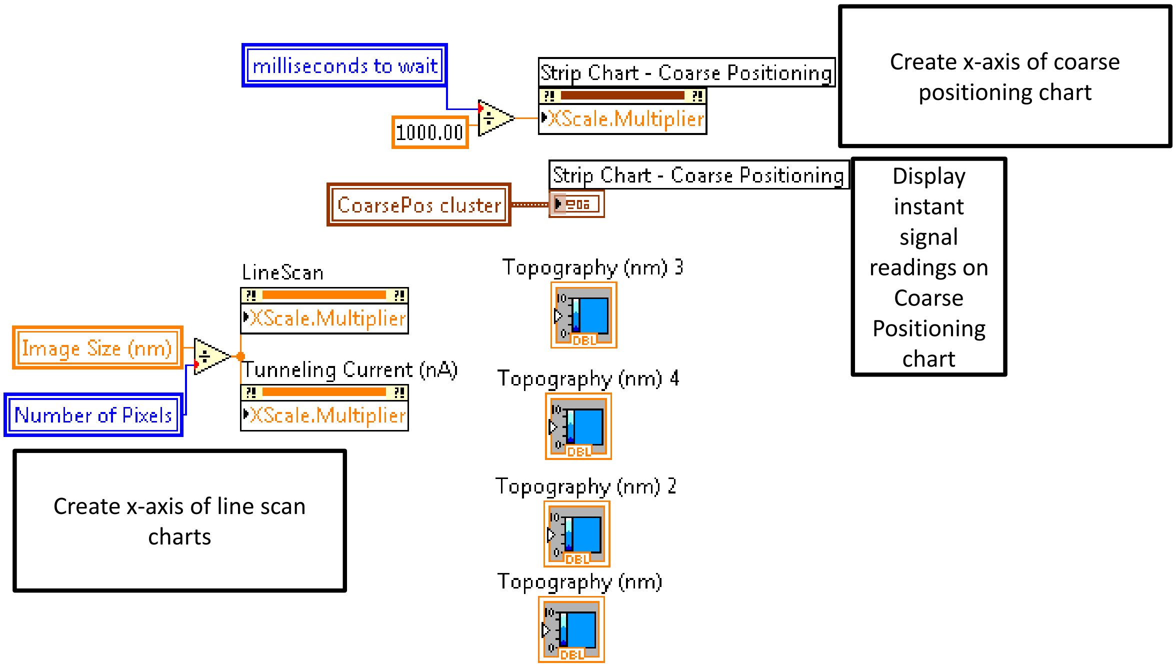

Figure A.38: 7th window of the stacked sequence structure. This window is used to display the instantaneous readings and create x-axes for the graphs.

file functions. In this window, there are two main loops. One of them is activated when saving an image data into a file and the other one is activated when saving a manipulation/spectroscopy data into a file. The file format is ASCII and extensions should be .txt. Both loops are almost identical, with some minor changes in the variable names. Simply all of the variables are converted to spreadsheet strings and then written into the files whose names are specified by the user. A commented version of this code is shown in Fig. A.39.

A.6 Oscan V2.0 FPGA Code

The FPGA code is the main software piece located on the FPGA that all the wave generation and input/output functions are conducted. It can be grouped under 2 parallel loops: (vertical) z-positioning loop and (lateral) x-positioning loop. The first window of both loops set the loop rates for their respective loops. The second windows of both loops have main input/output operations

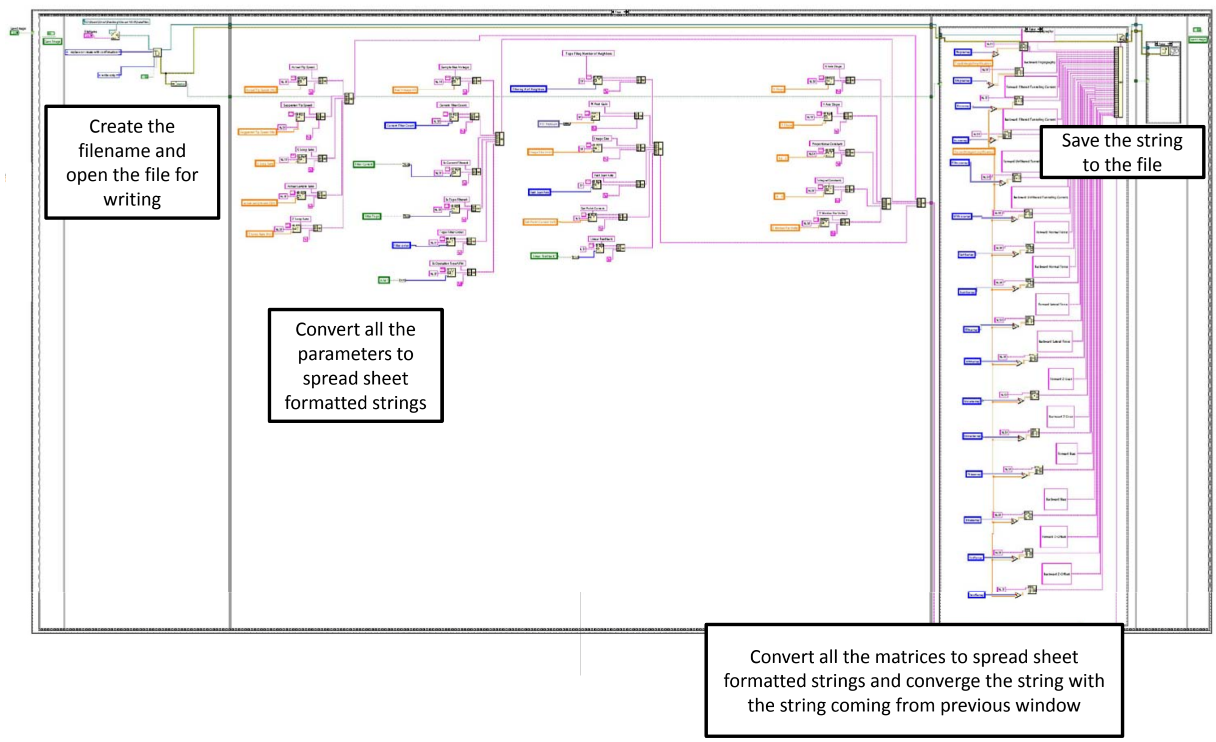

Figure A.39: 8th window of the stacked sequence structure. This window is used to save image or spectroscopy/manipulation data into a .txt file.

and calculations. A third window is located in lateral positioning loop which handles the data transfer from FPGA to Host PC via image buffer. A schematic that shows the general flow of the code is shown below in Fig. A.40.

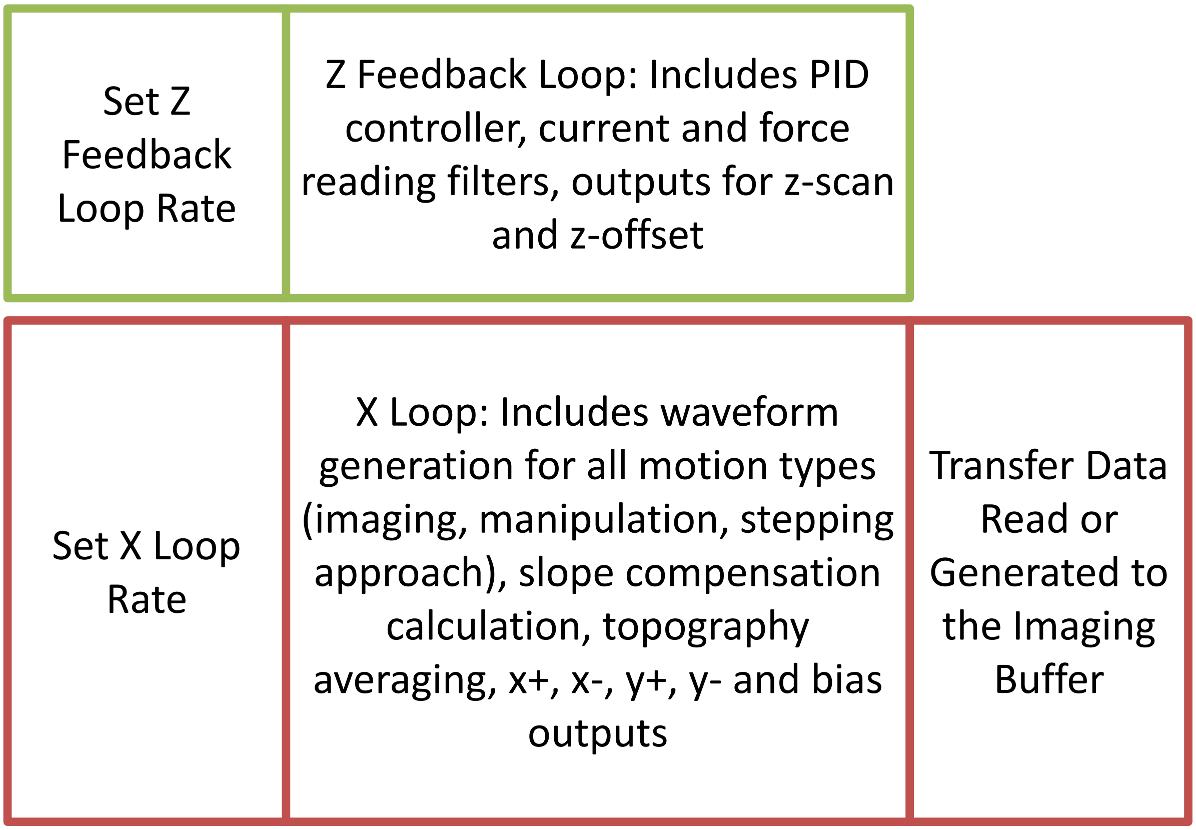

Figure A.40: A schematic of the FPGA code. It is consisted of two parallel loops that run at their specified rates. The first loop controls the vertical position of the tip and the second loop controls the lateral position of the tip.

The vertical positioning loop is the loop where PI controller is located. This loop reads tunneling current, normal force and lateral force from input channels. It then selects the feedback signal depending on if the operation mode is AFM (normal force), STM (tunneling current) or z-feedback simulate (a simulated sine wave). It passes these signals through a PI controller and writes the output of this controller to the variable ”controller output”. It adds the slope compensation to this output and outputs the signal from z-scan output after saturating it at the user defined limits. This loop also controls the z-offset signal which is commanded directly by the user. Tip retract and external PID functions are also located in this loop. During tip retract case, the connection between the z-scan and the PID is broken and z-scan is fed the maximum available voltage directly. During external PID, the connection between the z-scan and the internal PID is severed just like tip retract case, but this time, the external PID input is directly fed to controller output variable and z-scan signal. A commented version of this loop is shown below in Fig. A.41.

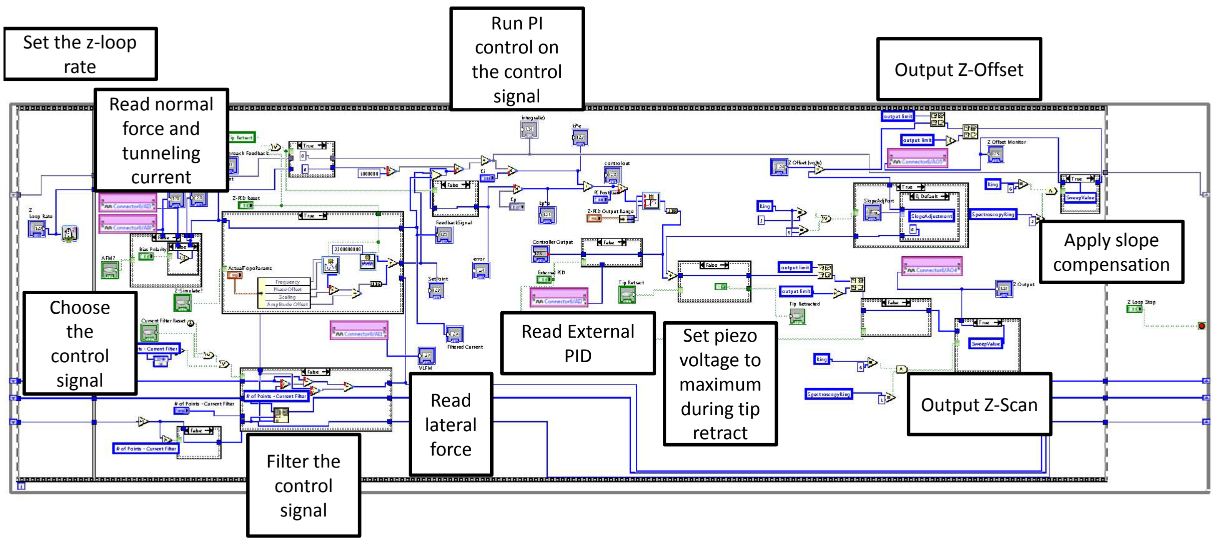

Figure A.41: The commented z-loop that controls the vertical position actuators z-scan and z-offset. PI loop also runs in this loop.

The lateral positioning loop is the loop where x and y actuator outputs are located. The main function of this loop is to generate the waveforms required by different operations. There is a case structure in this loop where the waveform generation is implemented. The case structure generates an x voltage and y voltage output which are fed to x+, x-, y+ and y- outputs. In addition to this case structure, there is a code piece for initializing variables. Controller output generated in the vertical loop is also read here and topography reading is generated via a running average filter. Bias output is also controlled in this loop. The last window of this loop is where all the readings are written to the image buffer for the host code to receive on the other end of the buffer. A commented version of this loop is shown below in Fig. A.42.

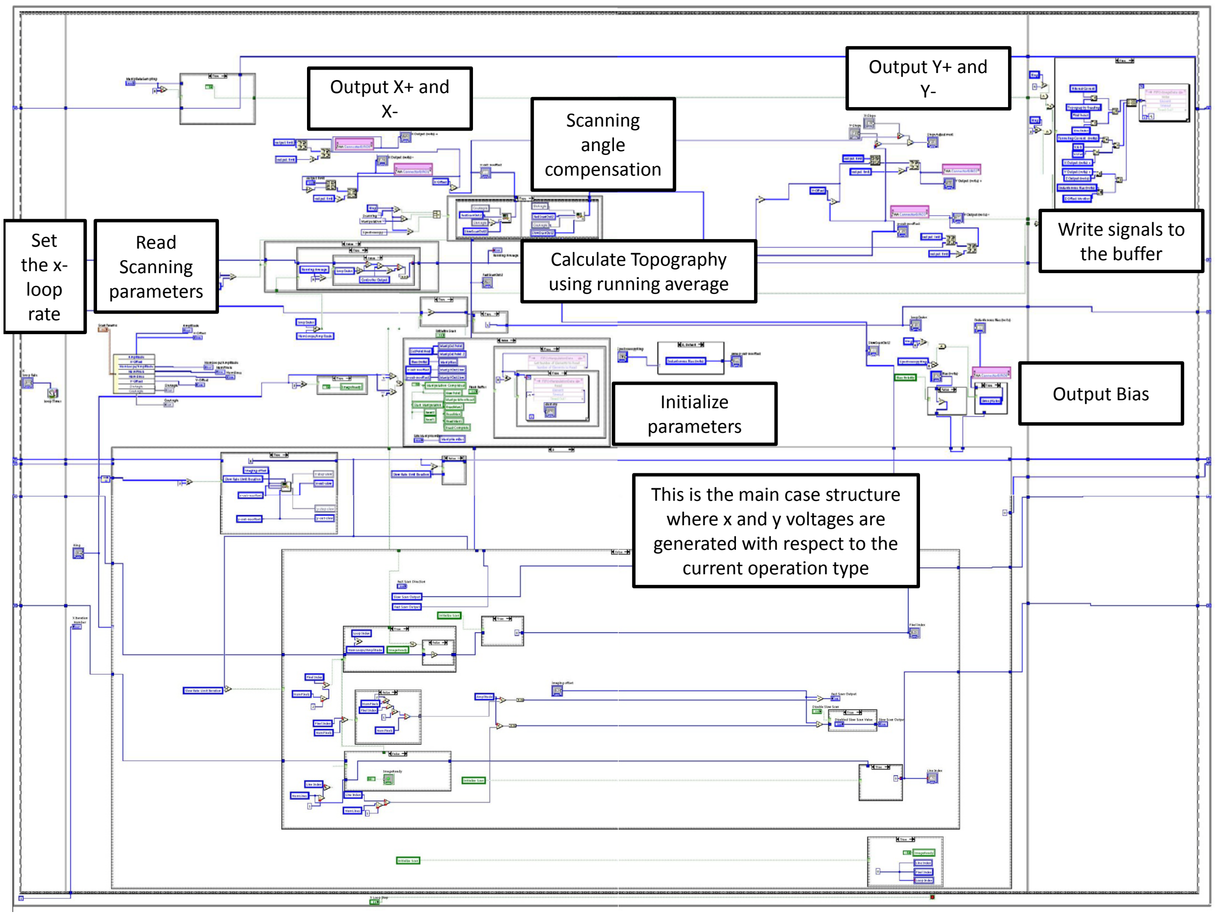

Figure A.42: The commented x-loop that controls the lateral position actuators x+, x-, y+, and y-. Bias is also controlled in this loop and data transfer is conducted at the third window through a buffer.

The first case in the case structure is manual operation. In this operation, x and y voltage values are set to the values sent from the host code after passing a slew rate limit. The x and y voltages are not allowed to jump directly as this may cause the scanner the take a step. Instead the slew rates are limited in most of the cases in this case structure. A commented version of this operation is shown below in Fig. A.43.

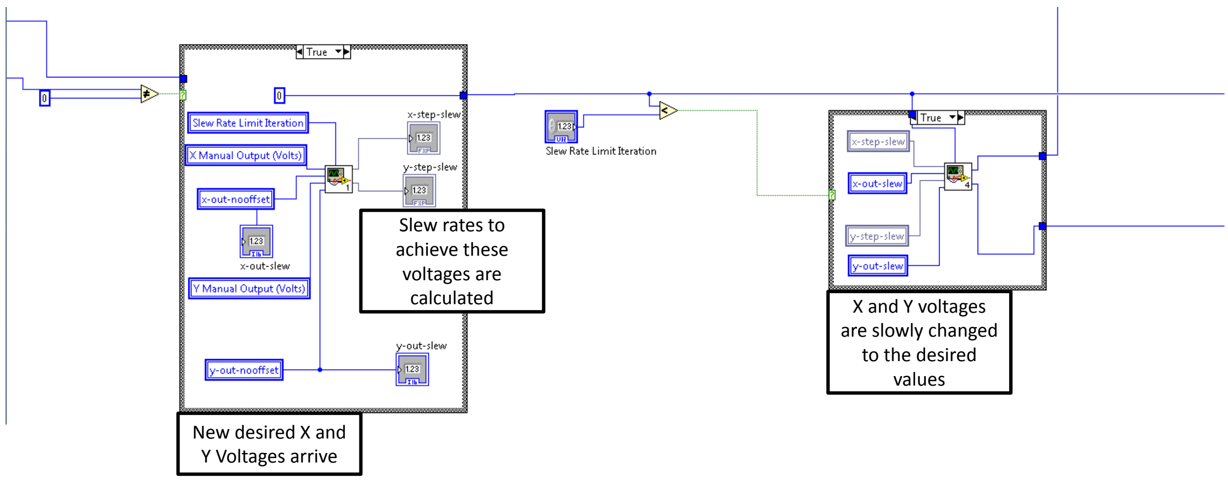

Figure A.43: 1st case of the case structure in the lateral positioning loop: Manual Output. This case outputs voltages to x and y actuators with a slew rate limitation.

The second case of the case structure is where the waveform for approach and fast out operation is generated. The waveform for this operation is a delayed sawtooth wave, i.e. the output is zero for 1/5th of the operation and it is the full swing saw tooth for the remaining 4/5th of the cycle. It is implemented this way because in the 1/5th of the cycle when the output is zero, there is very little oscillations in the feedback signal and it is easier to detect if approach is completed or not. A commented version of this case is shown in Fig. A.44.

The third case of the case structure is used for imaging. Two triangular waves are generated for this operation, one at the line speed, the other at the line speed/number of pixels, i.e. if tip speed is 5 Hz and number of pixels are 512, one triangular wave is at 5 Hz and the other is at 5/512 Hz. The triangular waves are then offset and amplified to the desired image size. The fast triangular wave is fed to the fast scan direction and the other wave is fed to the perpendicular

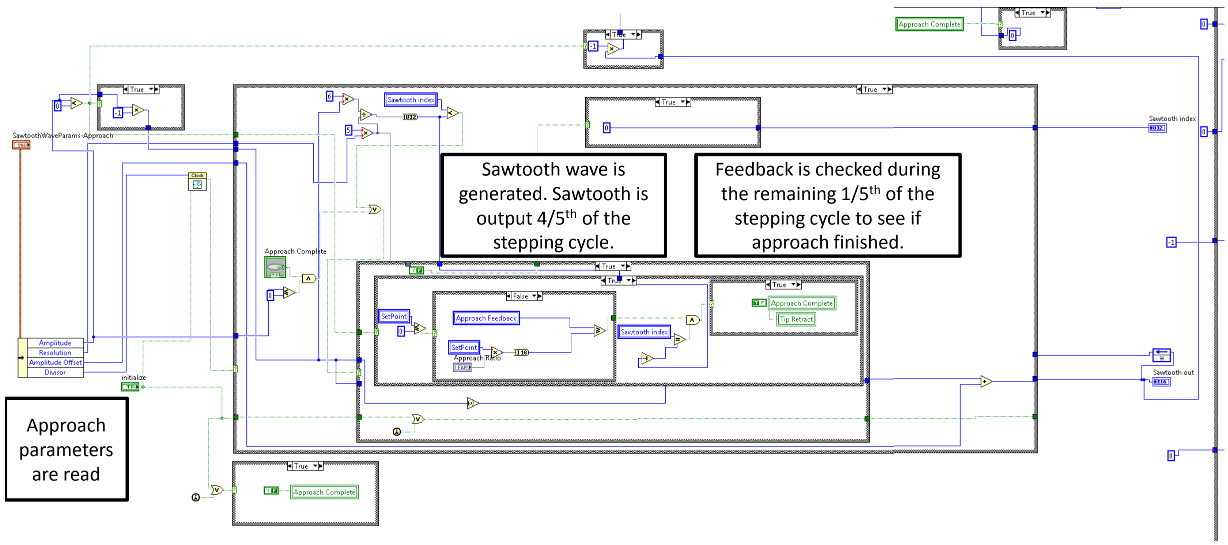

Figure A.44: 2nd case of the case structure in the lateral positioning loop: Approach. This case outputs sawtooth waves to x actuator.

direction. A commented version of this case is shown in Fig. A.45.

The fourth case of the case structure is X-Stepping. This is used for stepping in x or y direction in forward or backward directions. Unlike approach and fast out waveform, the waveform generated here is a pure sawtooth wave. It reads the parameters for the waveform from its front panel (these parameters are sent by the Host code) and scales the amplitude of the waveform with step length defined in the host front panel by the user. It counts the steps it takes along the wave and stops the waveform when number of steps taken is equal to the desired number of steps. A commented version of this case is shown below in Fig. A.46.

The fifth case of the case structure is Z-Stepping. This is used for stepping in z direction in forward or backward directions. Similar to approach and fast out waveform, the waveform generated here is a delayed sawtooth wave. It reads the parameters for the waveform from its front panel (these parameters are sent by the Host code) and scales the amplitude of the waveform with step length defined in the host front panel by the user. It counts the steps it takes along the wave and stops the waveform when number of steps taken is equal to the desired number of steps. A commented version of this case is shown below in Fig. A.47.

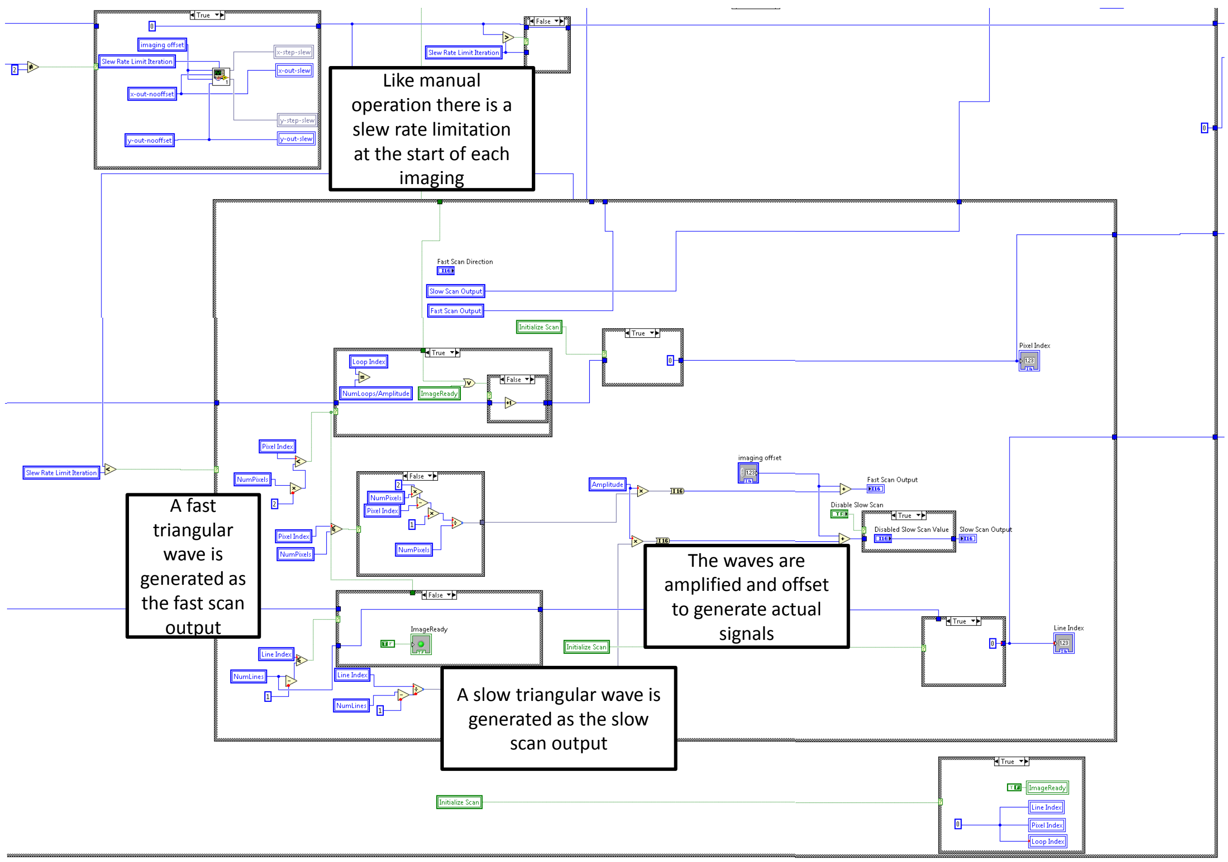

Figure A.45: 3rd case of the case structure in the lateral positioning loop: Scanning. This case outputs triangular waves to x and y actuators.

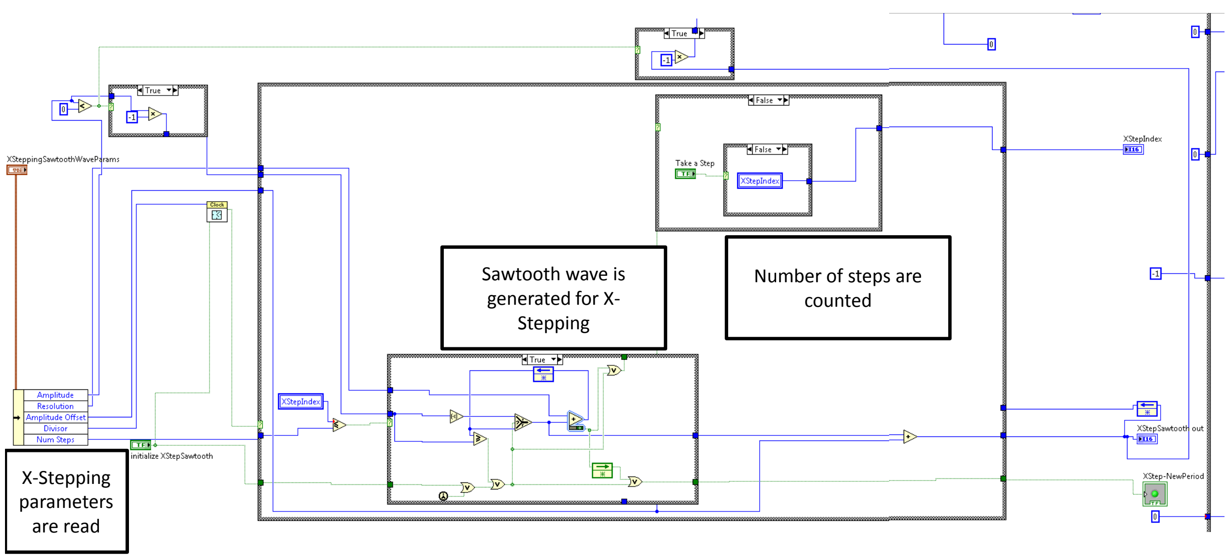

Figure A.46: 4th case of the case structure in the lateral positioning loop: X-Stepping. This case outputs sawtooth waves to x actuators.

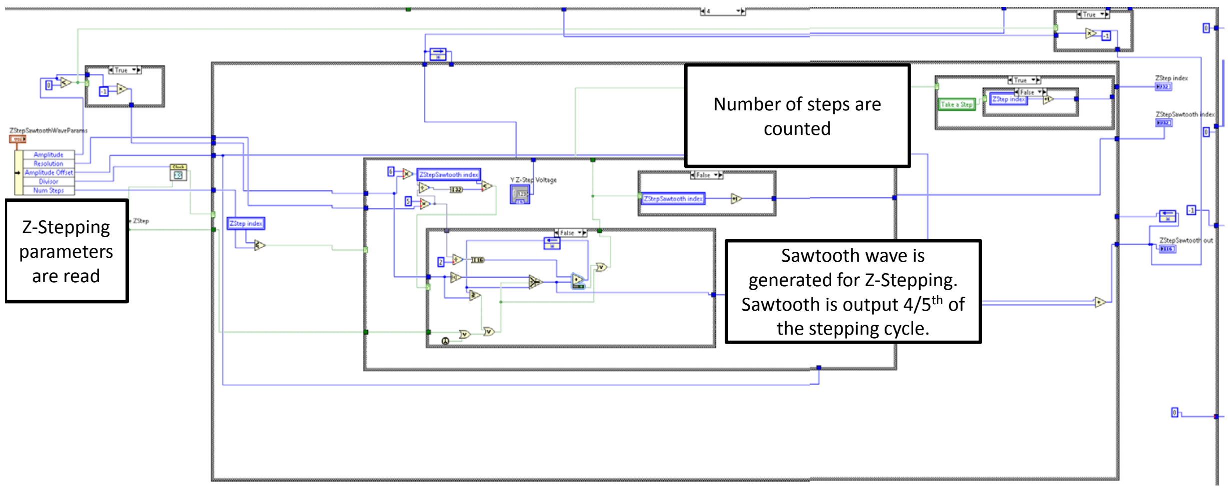

Figure A.47: 5th case of the case structure in the lateral positioning loop: Z-Stepping. This case outputs sawtooth waves to x actuators.

The sixth case of the case structure is used for manipulation. In this case, the variables are first initialized. Then FPGA reads the manipulation points from the manipulation buffer. The manipulation points have 5 coordinates: x voltage, y voltage, bias, current/force and speed. Using speed, x voltage and y voltage values, slew rates are calculated. After receiving all of the coordinates and calculating the slew rates, reception of a new point is confirmed. Upon this confirmation, the bias voltage is changed to the voltage of current manipulation point, the set point is changed to the set-point current/force of the current manipulation point and the x and y voltages are changed according to the slew rates they calculated. A commented version of this case is shown in Fig. A.48.

The seventh and last case of the case structure is used for spectroscopy. In this case, the variables are first initialized. Then FPGA reads the spectroscopy points from the manipulation buffer. The spectroscopy points have 5 coordinates: spectroscopy voltage, y voltage, bias, x voltage and speed. Using speed and spectroscopy voltage, slew rate of the spectroscopy is calculated. After receiving all of the coordinates and calculating the slew rate, reception of a new point is confirmed. Upon this confirmation, the bias voltage is changed to the voltage of current spectroscopy point (if spectroscopy port is not bias, i.e. this is not an IV curve), the x and y volt-

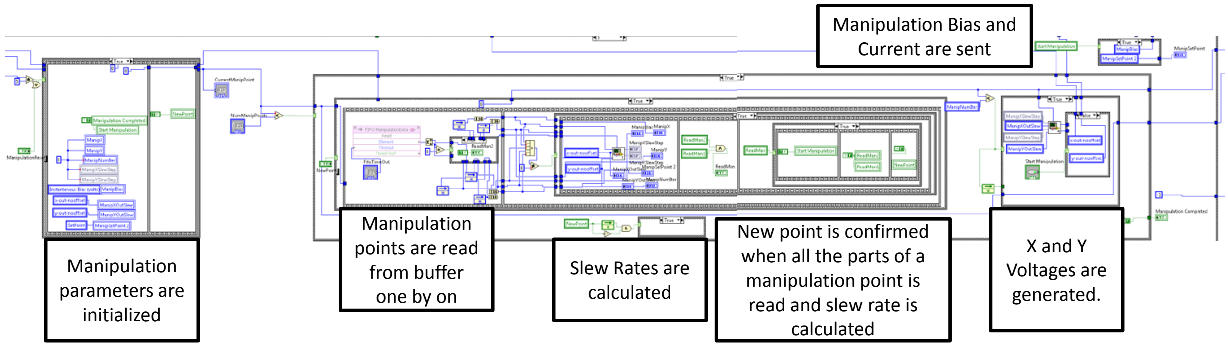

Figure A.48: 6th case of the case structure in the lateral positioning loop: Manipulation. This case receives the manipulation parameters from host code and applies the voltages to x and y actuators with the slew rate specified as speed in the manipulation point.

ages are changed to the x and y voltage of the current spectroscopy point, and the spectroscopy voltage is changed according to the slew rate calculated. A commented version of this case is shown in Fig. A.49.

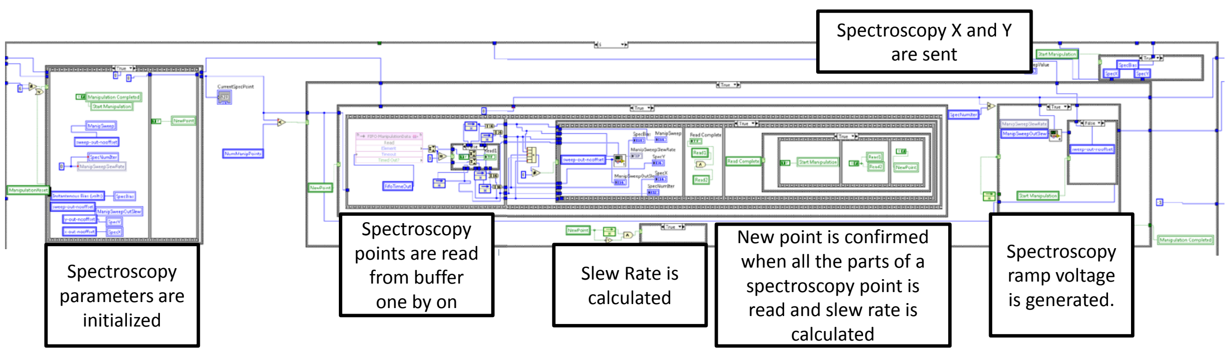

Figure A.49: 7th case of the case structure in the lateral positioning loop: Spectroscopy. This case receives the spectroscopy parameters from host code and applies the voltages to x and y actuators and spectroscopy port with the slew rate specified as speed in the spectroscopy point.

Bibliography

[1] Khalid Abidi and Asif Sabanovic. Sliding-mode control for high-precision motion of a piezostage. *Industrial Electronics, IEEE Transactions on*, 54(1):629 –637, feb. 2007. ISSN 0278-0046. doi: 10.1109/TIE.2006.885477. 1.2.3

[2] D.Y. Abramovitch, S.B. Andersson, L.Y. Pao, and G. Schitter. A tutorial on the mechanisms, dynamics, and control of atomic force microscopes. In *Proc. Amer. Ctrl. Conf*, pages 3488–3502. Citeseer, 2007. 1.2.3

[3] S. Aphale, AJ Fleming, and SOR Moheimani. High speed nano-scale positioning using a piezoelectric tube actuator with active shunt control. *Micro & Nano Letters*, 2(1):9–12, 2007. 1.2.3

[4] L. Bartels, G. Meyer, and K.H. Rieder. Basic steps of lateral manipulation of single atoms and diatomic clusters with a scanning tunneling microscope tip. *Physical Review Letters*, 79(4):697–700, 1997. ISSN 1079-7114. 1.2.2

[5] C. Baur, B. C. Gazen, B. Koel, T. R. Ramachandran, A. A. G. Requicha, and L. Zini. Robotic nanomanipulation with a scanning probe microscope in a networked computing environment. volume 15, pages 1577–1580. AVS, 1997. doi: 10.1116/1.589404. 1.2.2, 3.1, 3.2, 3.3

[6] C. Baur, A. Bugacov, BE Koel, A. Madhukar, N. Montoya, TR Ramachandran, AAG Requicha, R. Resch, and P. Will. Nanoparticle manipulation by mechanical pushing: underlying phenomena and real-time monitoring. *Nanotechnology*, 9:360, 1998. 3.1

[7] TM Bernhardt, B. Kaiser, and K. Rademann. Formation of superperiodic patterns on highly oriented pyrolytic graphite by manipulation of nanosized graphite sheets with the stm tip. *Surface Science*, 408(1-3):86–94, 1998. ISSN 0039-6028. 1.2.2

[8] B. Bhikkaji and S.O. Moheimani. Integral resonant control of a piezoelectric tube actuator for fast nanoscale positioning. *Mechatronics, IEEE/ASME Transactions on*, 13(5):530 – 537, oct. 2008. ISSN 1083-4435. doi: 10.1109/TMECH.2008.2001186. 1.2.3

[9] B.. Bhikkaji, M.. Ratnam, A.J. Fleming, and S.O.R. Moheimani. High-performance control of piezoelectric tube scanners. *Control Systems Technology, IEEE Transactions on*, 15(5):853 –866, sept. 2007. ISSN 1063-6536. doi: 10.1109/TCST.2007.902947. 1.2.3

[10] B. Bhushan. *Handbook of Micro/Nano Tribology, 2nd ed.* CRC Press, 1999. 1.2.1

[11] B. Bhushan. *Springer Handbook of Nanotechnology*. Springer Press, 2004. 1.2.2, 4.5.2

[12] B. Bhushan. *Springer handbook of nanotechnology*, volume 1. (Springer-Verlag, Berlin Heidelberg), 3 edition, 2004. ISBN 9783540012184. 2.4

[13] G. Binnig, H. Rohrer, C. Gerber, and E. Weibel. Surface studies by scanning tunneling microscopy. *Physical Review Letters*, 49(1):57–61, 1982. ISSN 1079-7114. 1.2.1

[14] G. Binnig, H. Rohrer, Ch. Gerber, and E. Weibel. Tunneling through a controllable vacuum gap. *Applied Physics Letters*, 40(2):178–180, 1982. doi: 10.1063/1.92999. 1.2.1

[15] G. Binnig, C. F. Quate, and Ch. Gerber. Atomic force microscope. *Phys. Rev. Lett.*, 56(9): 930–933, Mar 1986. doi: 10.1103/PhysRevLett.56.930. 1.2.1

[16] Elmar Bonaccurso, Friedhelm Schonfeld, and Hans-Jurgen Butt. Electrostatic forces acting on tip and cantilever in atomic force microscopy. *Phys. Rev. B*, 74:085413, 2006. doi: 10.1103/PhysRevB.74.085413. 2.4

[17] T.R. Braun and R.C. Smith. High speed model implementation and inversion techniques for ferroelectric and ferromagnetic transducers. *Journal of Intelligent Material Systems and Structures*, 19(11):1295–1310, 2008. 1.2.3

[18] David Bullen and Chang Liu. Electrostatically actuated dip pen nanolithography probe arrays. *Sensors and Actuators A: Physical*, 125(2):504 – 511, 2006. ISSN 0924-4247. doi: DOI:10.1016/j.sna.2005.09.001. 1.2.3

[19] B. Cappella, P. Baschieri, C. Frediani, P. Miccoli, and C. Ascoli. Improvements in afm imaging of the spatial variation of force-distance curves: on-line images. *Nanotechnology*, 8:82, 1997. 1.2.1

[20] R.W. Carpick, DF Ogletree, and M. Salmeron. Lateral stiffness: A new nanomechanical measurement for the determination of shear strengths with friction force microscopy. *Applied Physics Letters*, 70:1548, 1997. 1.2.1

[21] Heping Chen, Ning Xi, and Guangyong Li. Cad-guided automated nanoassembly using atomic force microscopy-based nonrobotics. *Automation Science and Engineering, IEEE Transactions*, 3:208–217, July 2006. 3.1

[22] C.J. Chien, F.S. Lee, and J.C. Wang. Enhanced iterative learning control for a piezoelectric actuator system using wavelet transform filtering. *Journal of Sound and Vibration*, 299 (3):605–620, 2007. 1.2.3

[23] GM Clayton, S. Tien, AJ Fleming, SOR Moheimani, and S. Devasia. Inverse-feedforward of charge-controlled piezopositioners. *Mechatronics*, 18(5-6):273–281, 2008. 1.2.3

[24] D. Croft, D. McAllister, and S. Devasia. High-speed scanning of piezo-probes for nanofabrication. *Journal of Manufacturing Science and Engineering*, 120:617, 1998. 1.2.3

[25] D. Croft, G. Shed, and S. Devasia. Creep, hysteresis, and vibration compensation for piezoactuators: Atomic force microscopy application. *Journal of Dynamic Systems, Measurement, and Control*, 123:35, 2001. 1.2.3

[26] J.A. Dagata, J. Schneir, H. H. Harary, C. J. Evans, M. T. Postek, and J. Bennett. Modification of hydrogen passivated silicon by a scanning tunneling microscope operating in air. *Applied Physics Letters*, 56, 1990. 1.2.2

[27] S. Datta, W. Tian, S. Hong, R. Reifenberger, J.I. Henderson, and C.P. Kubiak. Current-voltage characteristics of self-assembled monolayers by scanning tunneling microscopy. *Physical Review Letters*, 79(13):2530–2533, 1997. ISSN 1079-7114. 1.2.1

[28] G. V. Dedkov. Friction on the nanoscale: new physical mechanisms. *Materials Letters*, 38:360–366, 1999. 1.2.2

[29] S. Devasia. Review of feedforward approaches for nano precision positioning in high speed spm operation. In *Proc. IFAC World Congress*, pages 9221–9229, Seul, Korea, July 2008. 1.2.3

[30] MJ Doktycz, CJ Sullivan, PR Hoyt, DA Pelletier, S. Wu, and DP Allison. Afm imaging of bacteria in liquid media immobilized on gelatin coated mica surfaces. *Ultramicroscopy*, 97(1-4):209–216, 2003. ISSN 0304-3991. 1.2.1

[31] G. Dujardin, A. Mayne, O. Robert, F. Rose, C. Joachim, and H. Tang. Vertical manipulation of individual atoms by a direct stm tip-surface contact on ge (111). *Physical Review Letters*, 80(14):3085–3088, 1998. ISSN 1079-7114. 1.2.2

[32] D.M. Eigler and E.K. Schweizer. Positioning single atoms with a scanning tunnelling microscope. *Nature*, 344(6266):524–526, 1990. ISSN 0028-0836. 1.2.2, 4.1

[33] A.J. Fleming and S.O.R. Moheimani. Sensorless vibration suppression and scan compensation for piezoelectric tube nanopositioners. *Control Systems Technology, IEEE Transactions on*, 14(1):33 – 44, jan. 2006. ISSN 1063-6536. doi: 10.1109/TCST.2005.860511. 1.2.3

[34] Halbritter J. Freund, J. and J. Hrber. How dry are dried samples? water adsorption measured by stm. *Microscopy Research and Technique*, 44:327338, 1999. doi: 10.1002/(SICI)1097-0029(19990301)44:5⟨327::AID-JEMT3⟩3.0.CO;2-E. 1.2.1

[35] G. Garcia et al. Atomic-scale manipulation in air with the scanning tunneling microscope. *Applied Physics Letters*, 60(16):1960–1962, 2009. ISSN 0003-6951. 1.2.2

[36] R. Garcia, M. Calleja, and F. Perez-Murano. Local oxidation of silicon surfaces by dynamic force microscopy: Nanofabrication and water bridge formation. *Applied Physics Letters*, 72-18, 1998. 1.2.2

[37] R. C. Gonzalez and R. E. Woods, editors. *Digital Image Processing*. Prentice Hall, 2002. 3.5, 3.6

[38] J.J. Gorman, Y.S. Kim, and N.G. Dagalakis. Control of mems nanopositioners with nanoscale resolution. In *ASME International Mechanical Engineering Congress and Exposition, ASME*, 2006. 1.2.3

[39] L. T. Hansen, A. Kuhle, A. H. Srensen, J. Bohr, and P. B. Lindelof. A technique for positioning nanoparticles using an atomic force microscope. *Nanotechnology*, 9:337–342, 1998. 1.2.2

[40] U. Hartmann. Magnetic force microscopy. *Annual Review of Materials Science*, 29(1): 53–87, 1999. ISSN 0084-6600. 1.2.1

[41] Y. Hasegawa and P. Avouris. Manipulation of the reconstruction of the au (111) surface with the stm. *Science*, 258(5089):1763, 1992. 1.2.2

[42] R Held, T Heinzel, P Studerus, and K Ensslin. Nanolithography by local anodic oxidation of metal films using an atomic force microscope. *Physica E: Low-dimensional Systems and Nanostructures*, 2(14):748 – 752, 1998. 4.4.2

[43] K.J.G. Hinnen, R. Fraanje, and M. Verhaegen. The application of initial state correction in iterative learning control and the experimental validation on a piezoelectric tube scanner. *Proceedings of the Institution of Mechanical Engineers, Part I: Journal of Systems and Control Engineering*, 218(6):503–511, 2004. 1.2.3

[44] S. Hong, H. Shin, J. Woo, and K. No. Effect of cantilever–sample interaction on piezoelectric force microscopy. *Applied Physics Letters*, 80:1453, 2002. 1.2.1

[45] S. Hosaka. Spm based recording toward ultrahigh density recording with trillion bit-

s/inch2. *IEEE Transactions on Magnetics*, 37-2:855–859, 2001. 1.2.2

[46] S. Hosaka, H. Koyanagi, A. Kikukawa, M. Miyamoto, R. Imura, and J. Ushiyama. Fabrication of nanometer-scale structures on insulators and in magnetic materials using a scanning probe microscope. *JVST B-Microelectronics and Nanometer Structures*, 13(3): 1307–1311, 1995. 1.2.2

[47] S. Hsieh, S. Meltzer, C.R.C. Wang, A.A.G. Requicha, M.E. Thompson, and B.E. Koel. Imaging and manipulation of gold nanorods with an atomic force microscope. *Journal of Physical Chemistry B*, 106(2):231–234, 2002. ISSN 1520-6106. 1.2.2, 3.1

[48] W. Hu, J. Gu, Z. George, and D. Ricketts. Directed scanning probe nanomanufacturing of lateral Ti-TiO_2-Ti junctions for low capacitance mim rectenna diodes. In *The 37th International Conference on Micro and Nano Engineering (MNE 2011), Berlin*, 2011. 4.4.2

[49] Sunan Huang, Kok Kiong Tan, and Tong Heng Lee. Adaptive sliding-mode control of piezoelectric actuators. *Industrial Electronics, IEEE Transactions on*, 56(9):3514 –3522, sept. 2009. ISSN 0278-0046. doi: 10.1109/TIE.2009.2012450. 1.2.3

[50] S. Hudlet, M. Saint Jean, C. Guthmann, and J. Berger. Evaluation of the capacitive force between an atomic force microscopy tip and a metallic surface. *The European Physical Journal B*, 2(1):5–10, 1998. ISSN 1434-6028. 2.4

[51] J.N. Israelachvili. *Intermolecular and Surface Forces: Revised Third Edition*. Elsevier Science, 2011. ISBN 9780123919274. 2.4

[52] R.V. Iyer, Xiaobo Tan, and P.S. Krishnaprasad. Approximate inversion of the preisach hysteresis operator with application to control of smart actuators. *Automatic Control, IEEE Transactions on*, 50(6):798 – 810, june 2005. ISSN 0018-9286. doi: 10.1109/TAC.2005.849205. 1.2.3

[53] T. Junno, K. Deppert, L. Montelius, and L. Samuelson. Controlled manipulation of

nanoparticles with an atomic force microscope. *Applied Physics Letters*, 66(26):3627–3629, 1995. doi: 10.1063/1.113809. 1.2.2, 3.1

[54] Florian Krohs, Cagdas D. Onal, Metin Sitti, and Sergei Fatikow. A probabilistic approach to drift compensation towards autonomous nanomanipulation using an atomic force microscope. *ASME Journal of Dynamic Systems, Measurement, and Control*, under review, 2009. 1.2.3

[55] A. V. Kulkarni and B. Bhushan. Nanoscale mechanical property measurements using modified atomic force microscopy. *Thin Solid Films*, 290-291:206–210, 1996. 1.2.2

[56] Jun Hong L. Nanomanipulation of extended single-dna molecules on modified mica surfaces using the atomic force microscopy. *Colloids Surf B Biointerfaces*, 39(4):177–180, Dec 2004. doi: 10.1016/j.colsurfb.2004.07.013. 3.1

[57] H. Ladjal, J.-L. Hanus, and A. Ferreira. H-inf robustification control of existing piezoelectric-stack actuated nanomanipulators. In *Robotics and Automation, 2009. ICRA '09. IEEE International Conference on*, pages 3353 –3358, may 2009. doi: 10.1109/ROBOT.2009.5152701. 1.2.3

[58] K.K. Leang and S. Devasia. Hysteresis, creep, and vibration compensation for piezoactuators: Feedback and feedforward control. In *Proc. 2nd IFAC Conf. Mechatron. Syst*, pages 283–289, 2002. 1.2.3

[59] K.K. Leang and S. Devasia. Iterative feedforward compensation of hysteresis in piezo positioners. In *Decision and Control, 2003. Proceedings. 42nd IEEE Conference on*, volume 3, pages 2626 – 2631 Vol.3, dec. 2003. doi: 10.1109/CDC.2003.1273019. 1.2.3

[60] Eunjeong Lee and Hyun Seok Hong. An integrated system of microcantilever arrays with carbon nanotube tips for bio/nano analysis: design and control. In Hyun Seok Hong, editor, *Proc. IEEE International Conference on Automation Science and Engineering*, pages 113–117, 2005. doi: 10.1109/COASE.2005.1506754. 1.2.3

[61] F.S. Lee, C.J. Chien, and J.C. Wang. Trajectory tracking of piezoelectric actuators using state-compensated iterative learning control. *Journal of intelligent material systems and structures*, 18(6):555, 2007. 1.2.3

[62] H. J. Lee and W. Ho. Single-bond formation and characterization with a scanning tunneling microscope. *Science*, 286(5445):1719–1722, 1999. doi: 10.1126/science.286.5445.1719. 1.2.2

[63] K.B. Lee, S. J. Park, C. A. Mirkin, J. C. Smith, and M. Mrksich. Protein nanoarrays generated by dip-pen nanolithography. *Science*, 295:1702–1705, 2002. 1.2.2

[64] Lennart and Bergstrom. Hamaker constants of inorganic materials. *Advances in Colloid and Interface Science*, 70(0):125 – 169, 1997. ISSN 0001-8686. doi: 10.1016/S0001-8686(97)00003-1. (document), 4.28

[65] Guangyong Li, Ning Xi, Mengmeng Yu, and Wai Keung Fung. 3d nanomanipulation using atomic force microscopy. In *Proc. IEEE International Conference on Robotics and Automation ICRA '03*, volume 3, pages 3642–3647, 2003. doi: 10.1109/ROBOT.2003.1242155. 1.2.2, 3.1

[66] Guangyong Li, Ning Xi, Heping Chen, C. Pomeroy, and M. Prokos. ”videolized” atomic force microscopy for interactive nanomanipulation and nanoassembly. 4(5):605–615, 2005. ISSN 1536-125X. doi: 10.1109/TNANO.2005.851430. 1.2.2, 3.1, 3.4

[67] Chien-Kuo Liu, Sanboh Lee, Li-Piin Sung, and Tinh Nguyen. Load-displacement relations for nanoindentation of viscoelastic materials. *Journal of Applied Physics*, 100(3):033503, 2006. doi: 10.1063/1.2220649. 3.1

[68] Zhiguo Liu, Zhuang Li, Gang Wei, Yonghai Song, Li Wang, and Lanlan Sun. Manipulation, dissection, and lithography using modified tapping mode atomic force microscope. *Microscopy Research and Technique*, 69(12):998–1004, 2006. 1.2.2

[69] YF Lu, ZH Mai, YW Zheng, and WD Song. Nanostructure fabrication using pulsed lasers

in combination with a scanning tunneling microscope: Mechanism investigation. *Applied Physics Letters*, 76:1200, 2000. 1.2.1

[70] J. W. Lyding, G. C. Abeln, T. C. Shen, C. Wang, and J. R. Tucker. Nanometer scale patterning and oxidation of silicon surfaces with an ultrahigh vacuum scanning tunneling microscope. *Journal of Vacuum Science Technology B: Microelectronics and Nanometer Structures*, 12(6):3735–3740, November 1994. ISSN 1071-1023. doi: 10.1116/1.587433. 1.2.2, 4.1, 4.3

[71] I.W. Lyo and P. Avouris. Field-induced nanometer-to atomic-scale manipulation of silicon surfaces with the stm. *Science*, 253(5016):173, 1991. 1.2.2

[72] S. F. Lyuksyutov, R. A. Vaia, P. B. Paramonov, S. Juhl, L. Waterhouse, R. M. Ralich, G. Sigalovand, and B. Sancaktar. Electrostatic nanolithography in polymers using atomic force microscopy. *Nature Materials*, 2:468–472, 2003. 1.2.2

[73] Marc J. Madou. *Fundamentals of Microfabrication The Science of Minituarization*. CRC Press, 2nd edition, 2002. 1.2.2

[74] SN Magonov, V. Elings, and M.H. Whangbo. Phase imaging and stiffness in tapping-mode atomic force microscopy. *Surface science*, 375(2-3):L385–L391, 1997. ISSN 0039-6028. 1.2.1

[75] M. Martin, L. Roschier, P. Hakonen, U. Parts, M. Paalanen, B. Schleicher, and E. I. Kauppinen. Manipulation of ag nanoparticles utilizing noncontact atomic force microscopy. *Applied Physics Letters*, 73(11):1505–1507, 1998. doi: 10.1063/1.122187. 1.2.2

[76] K. Matsumoto, S. Takahashi, M. Ishii, M. Hoshi, A. Kurokawa, S. Ichimura, and Ando A. Application of stm nanometer-size oxidation process to planar-type mim diode. *Japanese Journal of Applied Physics*, 34:1387–1390, 1995. 5.2.2

[77] K. Matsumoto, M. Ishii, K. Segawa, Y. Oka, B. J. Vartanian, and J. S. Harris. Room temperature operation of a single electron transistor made by the scanning tunneling mi-

croscope nanooxidation process for the TiO_x/Ti system. *Applied Physics Letters*, 68(1): 34–36, 1996. doi: 10.1063/1.116747. 4.4.2, 5.2.2

[78] K. Matsumoto, M. Ishii, K. Segawa, Y. Oka, BJ Vartanian, and JS Harris. Room temperature operation of a single electron transistor made by the scanning tunneling microscope nanooxidation process for the tio/ti system. *Applied Physics Letters*, 68:34, 1996. 1.2.2

[79] M. McEllistrem, G. Haase, D. Chen, and R. J. Hamers. Electrostatic sample-tip interactions in the scanning tunneling microscope. *Phys. Rev. Lett.*, 70(16):2471–2474, Apr 1993. doi: 10.1103/PhysRevLett.70.2471. 1.2.1

[80] G. Meyer, B. Neu, and K.H. Rieder. Controlled lateral manipulation of single molecules with the scanning tunneling microscope. *Applied Physics A: Materials Science & Processing*, 60(3):343–345, 1995. ISSN 0947-8396. 1.2.2

[81] S. O. Reza Moheimani. Invited review article: Accurate and fast nanopositioning with piezoelectric tube scanners: Emerging trends and future challenges. *Review of Scientific Instruments*, 79(7):071101, 2008. doi: 10.1063/1.2957649. 1.2.3

[82] B. Mokaberi and A. A. G. Requicha. Drift compensation for automatic nanomanipulation with scanning probe microscopes. *Automation Science and Engineering, IEEE Transactions on*, (3):199–207, July 2006. doi: 10.1109/TASE.2006.875534. 3.1

[83] B. Mokaberi and A.A.G. Requicha. Towards automatic nanomanipulation: drift compensation in scanning probe microscopes. In *Proc. IEEE International Conference on Robotics and Automation ICRA '04*, volume 1, pages 416–421 Vol.1, 2004. doi: 10.1109/ROBOT.2004.1307185. 1.2.2, 1.2.3, 3.1

[84] B. Mokaberi, Jaehong Yun, M. Wang, and A.A.G. Requicha. Automated nanomanipulation with atomic force microscopes. In *Proc. IEEE International Conference on Robotics and Automation*, pages 1406–1412, 2007. doi: 10.1109/ROBOT.2007.363181. 1.2.2, 3.1

[85] F. Moresco, G. Meyer, K.H. Rieder, H. Tang, A. Gourdon, and C. Joachim. Conforma-

tional changes of single molecules induced by scanning tunneling microscopy manipulation: a route to molecular switching. *Physical Review Letters*, 86(4):672–675, 2001. ISSN 1079-7114. 1.2.2

[86] M. Nakamura and H. Yamada. Electrostatic force microscopy. *Roadmap of Scanning Probe Microscopy*, pages 43–51, 2007. 1.2.1

[87] I.M. Nnebe, R.D. Tilton, and J.W. Schneider. Direct force measurement of the stability of poly (ethylene glycol)-polyethylenimine graft films. *Journal of colloid and interface science*, 276(2):306–316, 2004. ISSN 0021-9797. 3.4.2

[88] W.S. Oates and R.C. Smith. Nonlinear control design for a piezoelectric-driven nanopositioning stage, 2005. 1.2.3

[89] C.D. Onal and M. Sitti. Visual servoing-based autonomous 2-d manipulation of microparticles using a nanoprobe. *Control Systems Technology, IEEE Transactions on*, 15(5):842–852, 2007. ISSN 1063-6536. 3.4, 3.6

[90] Kenneth L Osborne III. Temperature-dependence of the contact angle of water on graphite, silicon, and gold. Master's thesis, Worcester Polytechnic Institute, 2009. 4.4

[91] A. Pantazi, A. Sebastian, H. Pozidis, and E. Eleftheriou. Two-sensor-based h-inf control for nanopositioning in probe storage. In *Decision and Control, 2005 and 2005 European Control Conference. CDC-ECC '05. 44th IEEE Conference on*, pages 1174 – 1179, dec. 2005. 1.2.3

[92] O. Pietrement and M. Troyon. General equations describing elastic indentation depth and normal contact stiffness versus load. *Journal of colloid and interface science*, 226(1): 166–171, 2000. ISSN 0021-9797. 2.4, 3.4.2

[93] R.D. Piner, J. Zhu, F. Xu, S. Hong, and C. A. Mirkin. Dip pen nanolithography. *Science*, 283:661–663, 1999. 1.2.2

[94] H. Pozidis, W. Haberle, D. Wiesmann, U. Drechsler, M. Despont, T.R. Albrecht, and

E. Eleftheriou. Demonstration of thermomechanical recording at 641 gbit/in/sup 2/. 40 (4):2531–2536, 2004. ISSN 0018-9464. doi: 10.1109/TMAG.2004.830470. 1.2.3

[95] Sabrina D. Puckett. *Select Nanofabricated Titanium Materials for Enhancing Bone and Skin Growth of Intraosseous Transcutaneous Amputation Prostheses*. PhD thesis, Brown University, 2010. 4.4

[96] T R Ramachandran, C Baur, A Bugacov, A Madhukar, B E Koel, A Requicha, and C Gazen. Direct and controlled manipulation of nanometer-sized particles using the non-contact atomic force microscope. *Nanotechnology*, 9(3):237–245, 1998. 1.2.1, 1.2.2, 3.1

[97] P. Rerkkumsup, N. T. Thinh, Y. Kozuma, M. Aketagawa, and K. Takada. Stabilization technique for atomic tracking control of scanning tunneling microscope tip by referring regular crystalline surface. *Seimitsu Kogakkai Taikai Gakujutsu Koenkai Koen Ronbunshu*, 2002:596, 2002. 4.6.3

[98] R. Resch, C. Baur, A. Bugacov, B. E. Koel, A. Madhukar, A. Requicha, and P. Will. Building and manipulating 3-d and linked 2-d structures of nanoparticles using scanning force microscopy. *Langmuir*, 14-23:6613–6616, 1998. 1.2.2

[99] C. Rotsch, F. Braet, E. Wisse, and M. Radmacher. Afm imaging and elasticity measurements on living rat liver macrophages. *Cell biology international*, 21(11):685–696, 1997. ISSN 1065-6995. 1.2.1

[100] John E. Sader, James W. M. Chon, and Paul Mulvaney. Calibration of rectangular atomic force microscope cantilevers. *Review of Scientific Instruments*, 70(10):3967–3969, 1999. doi: 10.1063/1.1150021. URL `http://link.aip.org/link/?RSI/70/3967/1`. 4.7.3

[101] S. Salapaka and A. Sebastian. Control of the nanopositioning devices. In *Decision and Control, 2003. Proceedings. 42nd IEEE Conference on*, volume 3, pages 3644 – 3649 Vol.3, dec. 2003. doi: 10.1109/CDC.2003.1273022. 1.2.3

[102] CT Salling and MG Lagally. Fabrication of atomic-scale structures on si (001) surfaces. *Science*, 265(5171):502, 1994. 1.2.2

[103] J.-P. Salvetat, J.-M. Bonard, N.H. Thomson, A.J. Kulik, L. Forr, W. Benoit, and L. Zuppiroli. Mechanical properties of carbon nanotubes. *Applied Physics A: Materials Science & Processing*, 69(3):255–260, 1999. 1.2.1

[104] D. Sarid. *Exploring scanning probe microscopy with Mathematica*. WILEY-VCH, second, completely revised and enlarged edition edition, 2007. ISBN 3527406174. 1.2.1

[105] D. M. Schaefer, R. Reifenberger, A. Patil, and R. P. Andres. Fabrication of two-dimensional arrays of nanometer-size clusters with the atomic force microscope. *Applied Physics Letters*, 66(8):1012–1014, 1995. doi: 10.1063/1.113589. 1.2.2, 3.1

[106] G. Schitter and A. Stemmer. Fast closed loop control of piezoelectric transducers. *Journal of Vacuum Science & Technology B: Microelectronics and Nanometer Structures*, 20:350, 2002. 1.2.3

[107] G. Schitter and A. Stemmer. Model-based signal conditioning for high-speed atomic force and friction force microscopy. *Microelectronic Engineering*, 67:938–944, 2003. 1.2.3

[108] G Schitter, F Allgöwer, and A Stemmer. A new control strategy for high-speed atomic force microscopy. *Nanotechnology*, 15(1):108–114, 2004. 1.2.3

[109] John G. Simmons. Electric tunnel effect between dissimilar electrodes separated by a thin insulating film. *Journal of Applied Physics*, 34(9):2581 –2590, 1963. ISSN 0021-8979. doi: 10.1063/1.1729774. 2.3.2

[110] M. Sitti. Atomic force microscope probe based controlled pushing for nanotribological characterization. 9(2):343–349, 2004. ISSN 1083-4435. doi: 10.1109/TMECH.2004.828654. 1.2.1, 3.4

[111] M. Sitti and H. Hashimoto. Controlled pushing of nanoparticles: Modeling and experiments, ieee. *ASME Trans. on Mechatronics*, 5(2):199–211, 2000. 3.4

[112] Metin Sitti. Lecture 4: Micro/nanoscale surface forces. Lecture Notes of Micro/Nano Robotics - Carnegie Mellon University, Mechanical Engineering Department, February 2008. 4.6.4, 4.6.4

[113] R.C. Smith, T. De, M.V. Salapaka, J. Smith, and A. Hatch. Model development and inverse compensator design for high speed nanopositioning, 2002. 1.2.3

[114] R.C. Smith, T. De, and A. Hatch. Model development for piezoceramic nanopositioners, 2003. 1.2.3

[115] G. Song, Jinqiang Zhao, Xiaoqin Zhou, and J.A. De Abreu-Garcia. Tracking control of a piezoceramic actuator with hysteresis compensation using inverse preisach model. *Mechatronics, IEEE/ASME Transactions on*, 10(2):198 –209, april 2005. ISSN 1083-4435. doi: 10.1109/TMECH.2005.844708. 1.2.3

[116] Robert W Stark, Francisco J Rubio-Sierra, Stefan Thalhammer, and Wolfgang M Heckl. Combined nanomanipulation by atomic force microscopy and uv-laser ablation for chromosomal dissection. *Eur Biophys J*, 32(1):33–39, Mar 2003. doi: 10.1007/s00249-002-0270-y. 3.1

[117] Dmitri B. Strukov, Gregory S. Snider, Duncan R. Stewart, and R. Stanley Williams. The missing memristor found. *Nature*, 453:80–83, 2008. 1.2.1

[118] Ram Subbaraman, Tom Zawodzinski, and J. A. Mann. Estimation of the hamaker coefficient for a fuel-cell-supported catalyst system. *Langmuir*, 24(15):8245–8253, 2008. doi: 10.1021/la800064a. 4.7.3

[119] Bilsay Sumer and Metin Sitti. Rolling and spinning friction characterization of fine particles using lateral force microscopy based contact pushing. *J. Adh. Scie. Techn.,*, art. in press, 2008. 1.2.1, 3.4

[120] A. Tafazzoli and M. Sitti. Dynamic modes of nanoparticle motion during nanoprobe-based manipulation. In *Proc. of 4th IEEE Conf. in Nanotechnology*, 2004. 1.2.2

[121] X. Tan and O. Bennani. Fast inverse compensation of preisach-type hysteresis operators using field-programmable gate arrays. In *Proceedings of the American Control Conference, Seattle, WA*, pages 2365–2370, 2008. 1.2.3

[122] H. Tanaka and T. Kawai. Scanning tunneling microscopy imaging and manipulation of dna oligomer adsorbed on cu (111) surfaces by a pulse injection method. *Journal of Vacuum Science & Technology B: Microelectronics and Nanometer Structures*, 15(3):602–604, 2009. ISSN 1071-1023. 1.2.2

[123] Xiaojun Tian, Niandong Jiao, Lianqing Liu, Yuechao Wang, Ning Xi, Wenjung Li, and Zaili Dong. An afm based nanomanipulation system with 3d nano forces feedback. In *Proc. International Conference on Intelligent Mechatronics and Automation*, pages 18–22, 2004. 1.2.2, 3.1

[124] T. Uchihashi, Y. Sugawara, T. Tsukamoto, M. Ohta, S. Morita, and M. Suzuki. Role of a covalent bonding interaction in noncontact-mode atomic-force microscopy on si (111) 7×7. *Physical Review B*, 56(15):9834–9840, 1997. ISSN 1550-235X. 1.2.1

[125] Y. Wang, M.J. Bronikowski, and R.J. Hamers. An atomically resolved scanning tunneling microscopy study of the thermal decomposition of disilane on si (001). *Surface Science*, 311(1-2):64–100, 1994. ISSN 0039-6028. 4.4.1

[126] LJ Whitman, J.A. Stroscio, R.A. Dragoset, and RJ Celotta. Manipulation of adsorbed atoms and creation of new structures on room-temperature surfaces with a scanning tunneling microscope. *Science*, 251(4998):1206–1210, 1991. 1.2.2

[127] Eric W. Wong, Paul E. Sheehan, and Charles M. Lieber. Nanobeam mechanics: Elasticity, strength, and toughness of nanorods and nanotubes. *Science*, 277(5334):1971–1975, 1997. 1.2.1

[128] S.S. Wong, A.T. Woolley, T.W. Odom, J.L. Huang, P. Kim, D.V. Vezenov, and C.M. Lieber. Single-walled carbon nanotube probes for high-resolution nanostructure imaging.

Applied Physics Letters, 73:3465, 1998. 1.2.1

[129] John T. Woodward and Joseph A. Zasadzinski. Height amplifications of scanning tunneling microscopy images inair. *Langmuir*, 10(5):1340–1344, 1994. doi: 10.1021/la00017a004. 4.7.3

[130] Bin Wu, Andreas Heidelberg, and John J. Boland. Mechanical properties of ultrahigh-strength gold nanowires. *Nature Materials Letters*, 4:525–529, 2005. 1.2.1

[131] Dewei Xu, Kenneth M. Liechti, and K. Ravi-Chandar. On the modified tabor parameter for the jkr-dmt transition in the presence of a liquid meniscus. *Journal of Colloid and Interface Science*, 315(2):772 – 785, 2007. ISSN 0021-9797. 2.4

[132] F. Yang, E. Wornyo, K. Gall, and W.P. King. Nanoscale indent formation in shape memory polymers using a heated probe tip. *Nanotechnology*, 18-285302, 2007. 1.2.2

[133] Choongho Yu, Sanjoy Saha, Jianhua Zhou, Li Shi, Alan M. Cassell, Brett A. Cruden, Quoc Ngo, and Jun Li. Thermal contact resistance and thermal conductivity of a carbon nanofiber. *Journal of Heat Transfer*, 128(3):234–239, 2006. doi: 10.1115/1.2150833. 4.7.3

[134] W. Zesch and R. S. Fearing. Alignment of microparts using force controlled pushing. In *Microrobotics and Micromanipulation. Conference, Boston MA*, volume 3519, pages 148–156, 1998. 1.2.2

[135] Jinghua Zhong and Bin Yao. Adaptive robust precision motion control of a piezoelectric positioning stage. *Control Systems Technology, IEEE Transactions on*, 16(5):1039 –1046, sept. 2008. ISSN 1063-6536. doi: 10.1109/TCST.2007.916319. 1.2.3

[136] Q. Zou, KK Leang, E. Sadoun, MJ Reed, and S. Devasia. Control issues in high-speed afm for biological applications: collagen imaging example. *Asian journal of control*, 6: 164–178, 2004. 1.2.3